NORTHWESTERN UNIVERSITY

Quantitative Three-Dimensional Analysis of Solid Oxide Fuel Cell Electrode Microstructure Using Focused Ion Beam – Scanning Electron Microscopy

A DISSERTATION

SUBMITTED TO THE GRADUATE SCHOOL IN PARTIAL FULFILLMENT OF THE REQUIREMENTS

for the degree

DOCTOR OF PHILOSOPHY

Field of Materials Science & Engineering

By

James Robert Wilson

EVANSTON, ILLINOIS

December 2008

ABSTRACT

Quantitative Three-Dimensional Analysis of Solid Oxide Fuel Cell Electrode Microstructure Using Focused Ion Beam – Scanning Electron Microscopy

James Robert Wilson

This thesis demonstrates the use of dual-beam focused ion beam - scanning electron microscopy (FIB-SEM) for making complete three-dimensional reconstructions of SOFC electrodes in order to better understand the links between processing and performance with respect to microstructure. Sufficient compositional contrast, with nano-scale resolution, between Ni and LSM with respect to YSZ was demonstrated, and automated procedures for image processing were developed, allowing for rapid production of reliable three-dimensional structural data. Techniques for calculating pertinent microstructural characteristics such as the phase tortuosity, phase connectivity, triple-phase boundary density (TPB), and electrochemically-active triple-phase boundary density (EA-TPB) were established.

This method was initially applied for proof of concept to the three-dimensional microstructure of a Ni – Y_2O_3-stabilized ZrO_2 (Ni-YSZ) anode active layer consisting of a standard composition of 50:50 weight % Ni:YSZ. The gas-phase tortuosity factor was found to be ≈ 2.0 and the volume-specific TPB length was found to be 4.28×10^6 m/cm^3. Analysis of the connectivity of the phases found that lack of connectivity in the Ni and pore phases resulted in a reduction of the EA-TPB density by ≈12%.

Subsequent reconstruction of a series of electrochemically characterized Ni-YSZ active layers with four different compositions varied between 40-70 weight % NiO was conducted. Calculations from the 3D reconstructions showed that the highest triple-phase boundary (TPB) density was at a Ni solids volume fraction of ≈0.42, which showed reasonable agreement with structural models for predicting TPB density. While the anode polarization resistance was minimized at the same composition where TPB density was maximized, implementation of electrochemical modeling showed that low EA-TPB density due to lack of connectivity and YSZ tortuosity both played relative roles in the resulting electrode polarization.

Application of the reconstruction procedure was additionally conducted on two different cathode systems. Firstly, the microstructures of three different $La_{0.6}Sr_{0.4}CoO_{3-\delta}$ (LSC) single-phase cathodes were reconstructed in order to determine the effect of surface area on the measured electrochemical impedance and to provide authentic microstructures for finite element electrochemical modeling. Secondly, the microstructures of a series of nine $La_{0.8}Sr_{0.2}MnO_3$ (LSM) - YSZ composite cathodes with composition varied between 30-70 weight % YSZ were reconstructed and examined in detail. In conjunction with electrochemical modeling and the performance of the sample with 50:50 weight % LSM:YSZ, the intrinsic linear-specific charge transfer resistivity of the LSM-YSZ-air triple-phase boundary was estimated to be ≈ 2.5 x 10^5 Ωcm at 800°C. The calculated TPB densities were compared with those estimated from a particle packing model showing excellent agreement, with the maximum TPB density depending heavily on the particle size ratio between LSM and YSZ. Structural analysis showed large levels of un-connected LSM particles and YSZ tortuosities as high as 6.5, features that, when included in electrochemical modeling, helped explain the large mismatch observed between the TPB densities and the measured polarization resistances.

Acknowledgments

First and foremost I would like to thank my advisor, Professor Scott Barnett, for accepting me into his research group and guiding me through my graduate research experience. His knowledge, competency, support, patience, and general likeability have made my experience at Northwestern the best that it could possibly be. His relationship as advisor, colleague, and friend is one that I cherish. Thank you also to the members of my dissertation committee, Prof. Peter Voorhees, Prof. Laurence Marks, and Dr. Dean Miller. Your expertise, guidance, and time are greatly appreciated.

I wish to thank my parents for providing me with a loving home and family and an education without which this dissertation would have never started. Thank you for being there and for pushing me to challenge myself in whatever ways possible. Thank you to my sister for being my role model, whose love and hard work are inspiring. Thank you to Lorrie for your love and patience. You truly make my life a better one. I wish to also thank all of my friends near and far who have made the past five years enjoyable and unforgettable ones. To Latham and Elina, thank you for always keeping my mind sharp.

I have worked with a great group of people over the years whose relationships have truly enriched my time at Northwestern. Thank you to the Barnett group members, past and present: Tammy Lai, Mae Kobsiriphat, Brian Madsen, Zhongliang Zhan, Yuanbo Lin, Blake Stevens, Scott Cronin, David Bierschenk, Megna Shah, and Jason Nicholas. Thank you also to Dr. Manoj Pillai and Dr. Ilwon Kim, whose guidance and collaboration at FCT have been very valuable. The work presented in this dissertation was aided greatly by a number of people at Northwestern University that I worked directly with in collaboration: Scott Cronin, Sherry Rukes, Ben Myers,

and Tom Hines. Your contributions are greatly appreciated and helped make this dissertation possible.

In addition to those at Northwestern, there were a number of collaborators that I worked with at other institutions. Thank you to Hsun-Yi Chen and Prof. Katsuyo Thornton at the University of Michigan, Prof. Stuart Adler at the University of Washington, John Hiller and Dr. Dean Miller at Argonne National Laboratory, Marcio Gameiro at Rutgers University, and Anh Duong and Prof. Daniel Mumm at the University of California-Irvine. Your collective guidance and expertise has been invaluable.

Lastly, thank you to the National Science Foundation Ceramics Program for providing the funding for this research, and to the Electron Microscopy Center at Argonne National Laboratory for providing their facilities under the support of the U.S. Department of Energy.

Table of Contents

List of Figures

List of Tables

CHAPTER ONE

Introduction

Chapter 1: Introduction

The drive toward increased energy efficiency and reduced air pollution has led to accelerated worldwide development of fuel cells. A fuel cell is an electrochemical energy conversion device that produces electricity and heat by combining a fuel and an oxidant. This is achieved by the integration of three main layers of material: two electrodes (the anode and cathode), and an electrolyte. Fuel is oxidized at the anode and oxygen is reduced at the cathode, while the electrolyte serves as an ionic conductor between the two electrodes. In addition to their theoretically high efficiency, fuel cells offer a compact distributed energy generation solution as well as a means of electricity generation with zero (in the case of pure hydrogen) to minimal (for hydrocarbon fuels) carbon dioxide and harmful greenhouse gas pollutants. This is especially pertinent regarding the current state of the world's energy consumption and CO_2 emissions, which calls for dramatic and comprehensive advancements in conversion and utilization of alternative energy sources.

There are many types of fuel cells which are differentiated by the type of electrolyte used. The selection of electrolyte in turn determines the operating temperature, the range of utilizable fuels, the charge carrier involved, and the catalyst materials employed in the electrodes. Among these types, solid oxide fuel cells (SOFCs) are being actively developed for clean and efficient distributed electrical generation from fuels such as coal, gasoline, and natural gas. Its electrochemistry is based on the use of a ceramic oxygen-ion conducting electrolyte. This solid ceramic structure prevents gas crossover from electrode to electrode, eases corrosion problems, and allows for flexible shape casting beyond the common plate-like construction typical of the other fuel cell types. SOFCs are the most sulfur-resistant, and are not poisoned by common

gases such as CO, allowing for their use in conjunction with next-generation coal-operated power plants.

The high operating temperature of SOFCs, commonly between 600-1000°C, allows for a number of advantages beyond fast kinetics. Firstly, the need for precious-metal catalysts such as platinum is eliminated, which reduces the overall material costs involved with fabrication. Secondly, the waste heat from the electrochemical reaction can be captured at this high temperature and utilized in co-generation to increase overall efficiencies up to 80-85 percent from a standard range of 50-60 percent. Thirdly, the high temperature allows for internal reforming of fuels. This reduces costs by eliminating the need for an external reformer added to the system and allows for the flexibility of operation on H_2, CO, CH_4, and higher hydrocarbons, reducing concerns regarding fuel availability, transport, and storage.

As the performance and cost of SOFCs have improved, the materials comprising them have become increasingly sophisticated, both in composition and microstructure. In particular, state-of-the-art fuel cell electrodes typically have a complex micro/nano-scale structure involving interconnected electronically and ionically conducting phases, gas-phase porosity, and catalytically active surfaces. Much is still not understood about the electrochemical reaction processes at the electrode-electrolyte interfaces. There are a number of potential rate-controlling steps related to bulk and surface processes that depend on the materials used and the microstructure of the electrode and interface.

As an example, composite electrodes such as Ni-YSZ (YSZ = 8 mol% Y_2O_3-stabilized ZrO_2) typically consist of three phases – an electronically-conducting solid (e.g., Ni), an ionically-conducting solid (e.g., YSZ), and a pore phase. Macrohomogeneous structural parameters desired include, at minimum, volume fractions, surface areas, and triple-phase

boundary (TPB) density. The importance of TPB density can be illustrated by considering the hydrogen oxidation reaction,

$$H_2 + O^{2-} \rightarrow H_2O + 2e^- , \qquad (1.1)$$

that occurs in an SOFC anode. The H_2 and H_2O exist in pores, the ions in the ionically-conducting phase, and the electrons in the electronically conducting phase. Thus, all three phases are involved in the reaction, such that the reaction is expected to occur primarily near triple-phase boundaries. It is also clear that each phase must be able to supply or remove the relevant reactants/products in equation 1.1 at the TPB. That is, there must be phase contiguity through the electrode to the surroundings, *e.g.,* from the electronically-conducting phase to the electrical contact. Thus, additional microstructural information required includes phase contiguity and tortuosity.

Determining this microstructure is a critical, yet usually missing, link between materials processing and electrode performance. Current methods of microstructural analysis, such as scanning electron microscopy, provide only two-dimensional anecdotes of the microstructure, and thus limited information about how regions are interconnected in three-dimensional space. This lack of experimental structural analysis has led to the development of numerous quantitative models to relate SOFC electrode microstructure to performance. These models often make use of porous electrode theory, which assumes the effect of microstructure can be embodied in macrohomogeneous properties such as surface area, three-phase boundary length, volume fraction of the various phases, and tortuosity of gas, ionic, and electronic transport paths. In the absence of a detailed 3D understanding of the microstructure, it can be difficult to justify the

assumptions of porous electrode theory rigorously. In addition, the relevant macrohomogeneous parameters can often be difficult to determine independently. For example, tortuosity is nearly impossible to measure from two-dimensional (2D) cross sections, since it relies on exactly how and where phases interconnect in three dimensions. While stereological methods can be used to estimate total three-phase boundary (TPB) length from 2D images, such estimates are only accurate for isotropic microstructures. More importantly, 2D images cannot differentiate which portions of a particular phase or TPB are connected to contiguous gaseous, ionic, and electronic transport paths. In many cases, such parameters must be estimated based on specific idealized geometric models, or remain adjustable parameters. Finally, under circumstances where porous electrode theory breaks down, the absence of 3D microstructural data makes it difficult to proceed. Although some workers have examined the role of local microstructure on performance, these models typically assume an idealized (hypothetical) 3D microstructure, rather than the actual structure in question.

It is clear that reconstruction and quantification of electrode microstructure is a critical link to understanding how a given electrode fabrication procedure yields a particular electrode performance. In order to measure 3D properties of electrode microstructure, this thesis introduces a serial-sectioning method using dual-beam focused ion beam - scanning electron microscopy (FIB-SEM) to make complete 3D reconstructions of solid oxide fuel cell electrodes. This allows for calculation of critical microstructural features, including the volume fractions and surface areas of specific phases, the levels of phase connectivity, and the triple-phase boundary and electrochemically-active triple-phase boundary lengths. The full development and analysis of this procedure is provided in Chapter 3. It is the goal of this thesis to use this microstructural information to address the large gap in SOFC research linking processing with

performance of both anodes and cathodes. Three-dimensional reconstructions of Ni-YSZ composite anodes were conducted and are presented in Chapters 5 & 6. Reconstructions of single phase LSC cathodes are provided in Chapter 4. Lastly, a series of LSM-YSZ composite cathode microstructures are reconstructed and analyzed in Chapters 7 & 8. In each case, the measured microstructures were compared with electrochemical testing in order to better understand the effects of microstructure on electrode polarization. The thesis is concluded by presentation of an array of possible research directions utilizing the achieved microstructures and the reconstruction procedure in general.

CHAPTER TWO

Background

Chapter 2: Background

2.1 Fuel Cell Introduction

2.1.1 Global Energy Needs and Energy Conversion

The first law of thermodynamics states that the total energy of a closed system is conserved. While energy can neither be created nor destroyed, it manifests and transforms itself by conversion from one form to another. Over the centuries, human civilization has made great strides in understanding and controlling the conversion of energy from its natural sources to forms that can be utilized to produce work and heat. Table 2.1 summarizes the different ways of converting various basic forms of energy from one to another, both by phenomenological means and by man-made devices.[1]

Amongst the vast array of possible energy conversions is the fuel cell, a device that is designed to directly convert chemical energy to electrical energy (and vice versa in the case of electrolysis cells). In almost all energy conversions, some energy is lost along the way to forms that can not be utilized. With that in mind, efficiency of conversion is usually maximized by taking the fewest steps as possible. In the case of fuel cells, direct conversion from stored chemical energy to electricity avoids Carnot efficiency losses associated with the more common transformation of chemical to thermal to mechanical (in the form of work) to electrical energy conducted in modern coal, gas, and oil power plants.

Table 2.1. Matrix of Energy Conversions.

from / to	**electro-magnetic**	**chemical**	**thermal**	**kinetic**	**electrical**	**nuclear**	**gravitational**
electro-magnetic		chemi-luminescence	thermal radiation	accelerating charge phosphor	electro-magnetic radiation electro-luminescence	gamma reactions nuclear bombs	
chemical	photo-synthesis photo-chemistry	chemical processing	boiling dissociation	dissociation by radiolysis	electrolysis	radiation catalysis ionization	
thermal	solar absorption	combustion	heat exchange	friction	resistance heating	fission fusion	
kinetic	radiometers	metabolism muscles	thermal expansion internal combustion	gears	electric motors electro-strictions	radioactivity nuclear bombs	falling objects
electrical	solar cells photo-electricity	fuel cells batteries	thermo-electricity thermionics	conventional generators		nuclear batteries	
nuclear	gama-neutron reactions						
graviational				rising objects			

In addition to their high efficiency, fuel cells offer a compact distributed energy generation solution as well as a means of electricity generation with zero (in the case of pure hydrogen) to minimal (for hydrocarbon fuels) carbon dioxide and harmful greenhouse gas pollutants. This is especially pertinent regarding the current state of the world's energy consumption and CO_2 emissions, which calls for dramatic and comprehensive advancements in conversion and utilization of alternative energy sources. Figure 2.1 shows the historical increase

in global energy consumption,[2] and Figure 2.2 shows the subsequent historical increases in CO_2 emissions following the industrial revolution and the discovery of fossil fuels.[3] The world population continues to grow, and the majority of those people live in developing countries that require increasingly more energy, so these trends are not expected to change in the near future. It can also be seen in Figure 2.3, a breakdown of U.S. energy sources and usage in 2006,[4] that not only are our energy sources dominated by coal, natural gas, and oil (non-hydro renewable energies make up less than 1 percent), but in addition, approximately 70% of the energy used to create electricity is wasted. Lastly, Figure 2.4 breaks down the CO_2 emissions for the U.S. in 2006, almost 20% of the total global emissions, which come completely from burning of fossil fuels.[5] Developing technologies that not only utilize renewable energy sources, but also work at higher efficiencies and with reduced emissions are vital to solving the world's energy problems, and fuel cells represent an important part of this larger effort.

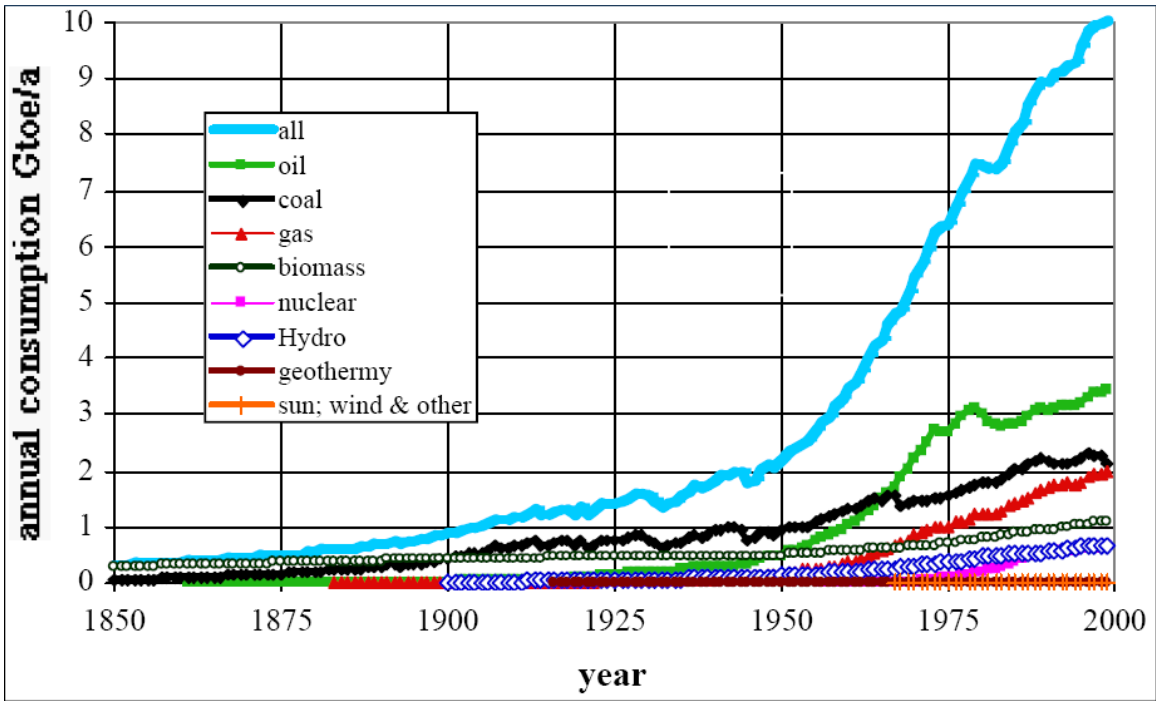

Figure 2.1. Global energy consumption in Gtoe per year.

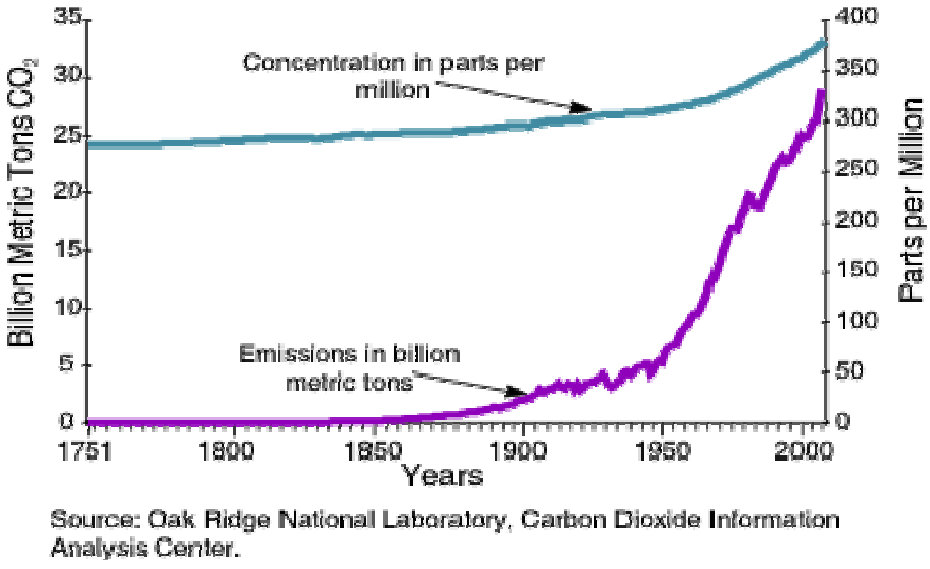

Figure 2.2. Global carbon dioxide emissions and atmospheric concentration from 1751-2004.

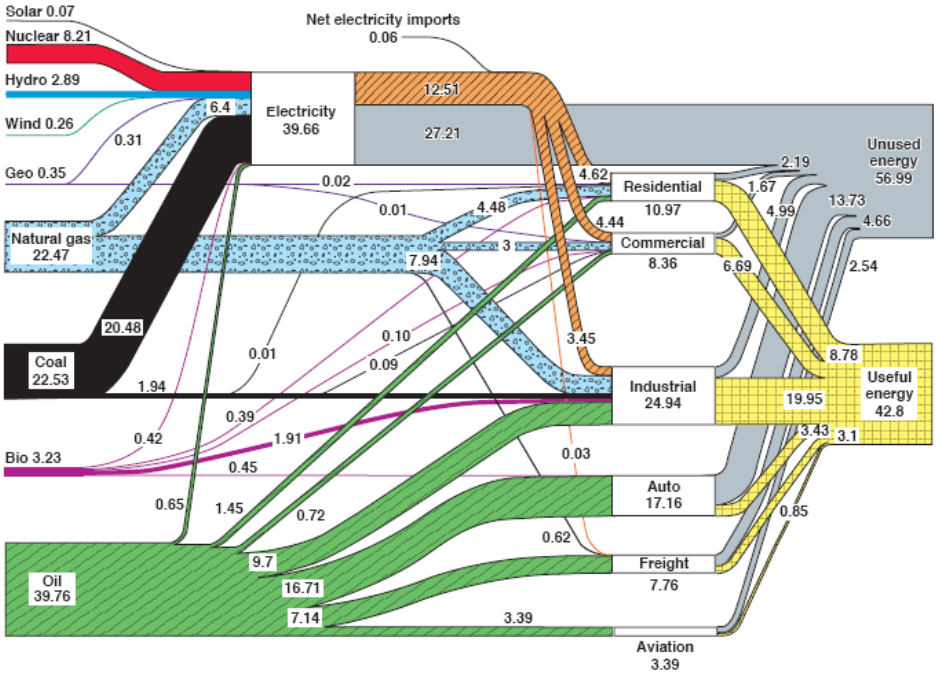

Figure 2.3. Estimated energy usage in the U.S. in 2006 with units in quadrillion Btus (quads).

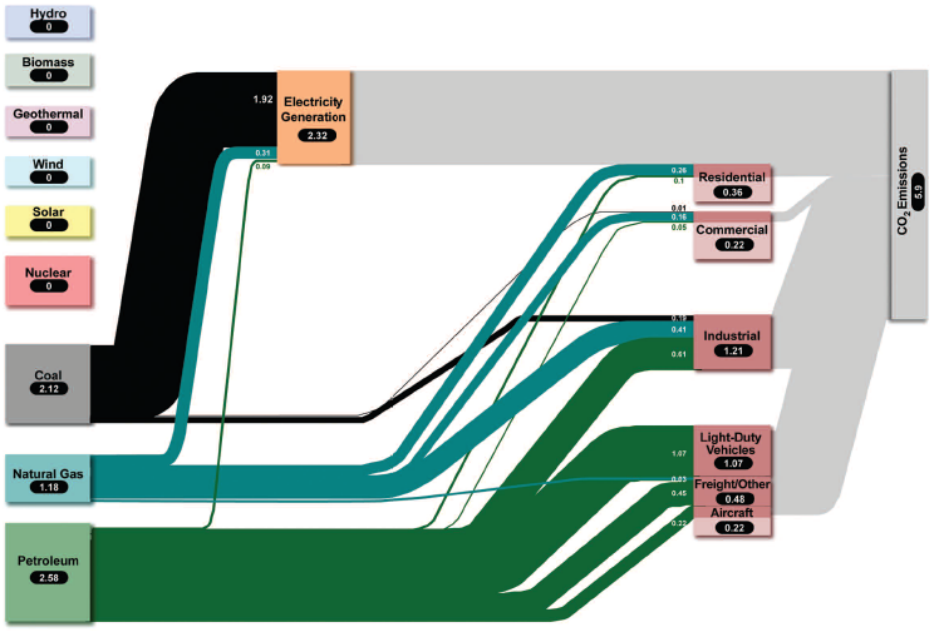

Figure 2.4. U.S. carbon dioxide emissions in 2006 from energy consumption (units in billions of metric tons CO_2)

2.1.2 Fuel Cell History

The first demonstration of the concept of a fuel cell can be traced back to 1839 when Sir William Grove immersed two platinum electrodes in a container of sulfuric acid and recorded the observed current and voltage.[6] Understanding of the underlying principles of a fuel cell was furthered in the late 1800's by Friedrich Ostwald, who sought to elucidate the various roles of the components of a fuel cell and successfully described the chemistry involved.[7] Despite this basic understanding, it wasn't until the mid 20th century that research into different types of fuel cells and the development of devices emerged. It was Baur and Preis in 1937 who first used a ceramic electrolyte,[8] building upon Nernst's discovery of solid-oxide electrolytes in 1899,[9] pioneering the field of solid oxide fuel cells.

2.1.3 Fuel Cell Types

A fuel cell is an electrochemical energy conversion device that produces electricity and heat by combining a fuel and an oxidant. This is achieved by the integration of 3 main layers of material: two electrodes (the anode and cathode), and an electrolyte. Fuel is oxidized at the anode and oxygen is reduced at the cathode, while the electrolyte serves as an ionic conductor between the two electrodes. An external circuit provides a path for DC electricity. This single unit cell can be operated in electrical series to build voltage (called a stack) by use of an interconnect, which connects the anode of one unit cell to the cathode of another.[10] A diagram of a single solid-oxide fuel cell (SOFC) is provided in Figure 2.5 to highlight these basic components and the representative electrochemical reaction that takes place.[11]

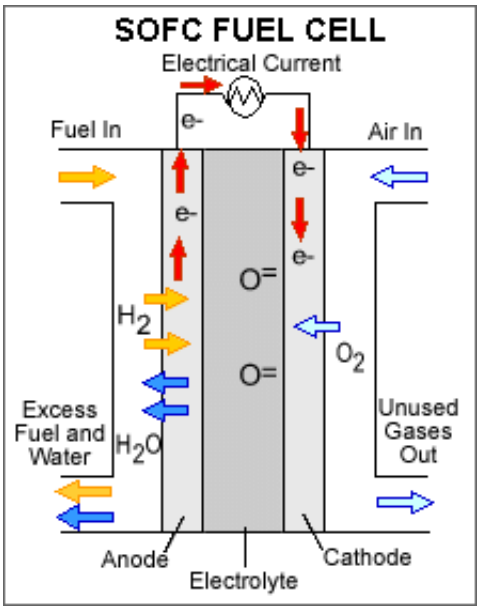

Figure 2.5. A diagram of a Solid Oxide Fuel Cell (SOFC) showing the electrochemical and structural components.

There are many types of fuel cells which are differentiated by the type of electrolyte used. The selection of electrolyte in turn determines the operating temperature, the range of utilizable fuels, the charge carrier involved, and the catalyst materials employed in the electrodes. A summary of these descriptors is provided in Table 2.2, where five main categories of fuel cells are described.[12] Polymer electrolyte membrane (PEM) fuel cells use a solid polymer as an electrolyte and are primarily used for transportation applications due to their fast start-up time and good power to weight ratio. However, PEM fuel cells are very sensitive to pollutants and require pure hydrogen as a fuel, limiting the storage options and flexibility of the total system. Direct methanol fuel cells fall within the PEM category and offer the advantage of liquid fuel storage. Alkaline fuel cells (AFC) use a potassium hydroxide solution in water as the electrolyte,

and were first widely used in the U.S. space program onboard spacecraft to produce both electricity and potable water. Commercialization has remained a challenge as cost and durability of AFC stacks remain a problem. Phosphoric acid fuel cells (PAFC) use a liquid phosphoric acid electrolyte. While this is a very mature technology, high cost from platinum catalysts remains a large barrier to widespread commercialization. Molten carbonate fuel cells (MCFC) offer many advantages over other types of fuel cells. Because of their high operating temperature, non noble metal catalysts can be used, and poisoning from carbon monoxide or dioxide does not occur. The main drawback, however, has been the durability of the cells due to their corrosive electrolyte. Solid oxide fuel cells (SOFC) are the final category of fuel cell and are the subject of this thesis. The following section goes into detail on the basics of SOFCs. A summary of the advantages, disadvantages, and possible commercial applications for the above described categories of fuel cells are listed in Table 2.3.[13]

Table 2.2. Summary of the major differences of the fuel cell types.

	Polymer Electrolyte (PEFC)	**Alkaline (AFC)**	**Phosphoric Acid (PAFC)**	**Molten Carbonate (MCFC)**	**Solid Oxide (SOFC)**
Electrolyte	Ion Exchange Membranes	Mobilized or Immobilized Potassium Hydroxide	Immobilized Liquid Phosphoric Acid	Immobilized Liquid Molten Carbonate	Ceramic
Operating Temperature	80ºC	65-220ºC	205ºC	650ºC	600-1000ºC
Charge Carrier	H^+	OH^-	H^+	$CO3^=$	$O^=$
External Reformer for CH_4	YES	YES	YES	NO	NO
Prime Cell Components	Carbon-based	Carbon-based	Graphite-based	Stainless-based	Ceramic
Catalyst	Platinum	Platinum	Platinum	Nickel	Perovskites

Table 2.3. A comparison of fuel cell technologies and their advantages, disadvantages, and possible commercial applications.

Comparison of Fuel Cell Technologies

Fuel Cell Type	Common Electrolyte	Operating Temperature	System Output	Electrical Efficiency	Applications	Advantages	Disadvantages
Polymer Electrolyte Membrane (PEM)*	Solid organic polymer poly-perfluorosulfonic acid	50 - 100°C 122 - 212°F	<1kW – 250kW	53-58% (transportation) 25-35% (stationary)	▪ Backup power ▪ Portable power ▪ Small distributed generation ▪ Transportation	▪ Solid electrolyte reduces corrosion & electrolyte management problems ▪ Low temperature ▪ Quick start-up	▪ Requires expensive catalysts ▪ High sensitivity to fuel impurities ▪ Waste heat temperature not suitable for combined heat and power (CHP)
Alkaline (AFC)	Aqueous solution of potassium hydroxide soaked in a matrix	90 - 100°C 194 - 212°F	10kW – 100kW	60%	▪ Military ▪ Space	▪ Cathode reaction faster in alkaline electrolyte, leads to higher performance	▪ Expensive removal of CO_2 from fuel and air streams required (CO_2 degrades the electrolyte)
Phosphoric Acid (PAFC)	Liquid phosphoric acid soaked in a matrix	150 - 200°C 302 - 392°F	50kW – 1MW (250kW module typical)	>40%	▪ Distributed generation	▪ Higher overall efficiency with CHP ▪ Increased tolerance to impurities in hydrogen	▪ Requires expensive platinum catalysts ▪ Low current and power ▪ Large size/weight
Molten Carbonate (MCFC)	Liquid solution of lithium, sodium, and/or potassium carbonates, soaked in a matrix	600 - 700°C 1112 - 1292°F	<1kW – 1MW (250kW module typical)	45-47%	▪ Electric utility ▪ Large distributed generation	▪ High efficiency ▪ Fuel flexibility ▪ Can use a variety of catalysts ▪ Suitable for CHP	▪ High temperature speeds corrosion and breakdown of cell components ▪ Complex electrolyte management ▪ Slow start-up
Solid Oxide (SOFC)	Yttria stabilized zirconia	600 - 1000°C 1202 - 1832°F	<1kW – 3MW	35-43%	▪ Auxiliary power ▪ Electric utility ▪ Large distributed generation	▪ High efficiency ▪ Fuel flexibility ▪ Can use a variety of catalysts ▪ Solid electrolyte reduces electrolyte management problems ▪ Suitable for CHP ▪ Hybrid/GT cycle	▪ High temperature enhances corrosion and breakdown of cell components ▪ Slow start-up ▪ Brittleness of ceramic electrolyte with thermal cycling

**Direct Methanol Fuel Cells (DMFC) are a subset of PEM typically used for small portable power applications with a size range of about a subwatt to 100W and operating at 60 - 90°C.*

2.1.4 Advantages of SOFCs

One of the most promising types of fuel cells is the solid oxide fuel cell (SOFC). Its electrochemistry is based on the use of a ceramic oxygen-ion conducting electrolyte. This solid ceramic structure prevents gas crossover from electrode to electrode, eases corrosion problems, and allows for flexible shape casting beyond the common plate-like construction typical of the other fuel cell types. SOFCs are the most sulfur-resistant, and are not poisoned by common gases such as CO, allowing for their use in conjunction with next-generation coal-operated power plants.

The high operating temperature of SOFCs, commonly between 600-1000°C, allows for a number of advantages beyond fast kinetics. Firstly, the need for precious-metal catalysts such as platinum is eliminated, which reduces the overall material costs involved with fabrication. Secondly, the waste heat from the electrochemical reaction can be captured at this high temperature and utilized in co-generation to increase overall efficiencies up to 80-85 percent from a standard range of 50-60 percent. Thirdly, the high temperature allows for internal reforming of fuels. This reduces costs by eliminating the need for an external reformer added to the system. Additionally, internal reforming allows for the flexibility of operation on H_2, CO, CH_4, and higher hydrocarbons, reducing concerns regarding fuel availability, transport, and storage.

In contrast, most of the engineering challenges regarding SOFCs derive from this high operating temperature. Large constraints on material selection exist, from thermal expansion matching, to electronic and ionic conductivities. Startup times are longer in order to reach these high temperatures, so SOFCs are less suited for the transportation industry and more ideally suited for long term, stationary power systems, as well as auxiliary power units for the aviation and automotive industries.[14, 15]

2.2 SOFC Electrochemistry

The most common electrochemical reaction that takes place in SOFCs is outlined below:

Anode: $H_2 + O^{2-} \rightarrow H_2O + 2e^-$ (2.1)

Cathode: $\frac{1}{2}O_2 + 2e^- \rightarrow O^{2-}$ (2.2)

Total: $H_2 + \frac{1}{2}O_2 \rightarrow H_2O$ (2.3)

The total chemical reaction produces only water. However, it is the separation of this into two electrochemical reactions that allows for free electrons to produce electricity.[16] The oxygen partial pressure gradient between the cathode and anode serves as the driving force for the oxygen anions (by oxygen vacancy diffusion in the electrolyte) and produces the resulting voltage and charge separation.

As mentioned before, one advantage of SOFCs is that they can be operated on a wide array of fuels, such as CO, higher hydrocarbons such as methane, propane, and octane, and even alcohols.[17-22] CO produces CO_2 as a waste product either as a direct reaction or through a shift reaction with water, which in turn creates H_2 as the fuel replacement. Hydrocarbons require a reforming reaction in order to be useful, and many SOFCs allow for this to occur internally, catalyzed within the cell electrode.[23-25] Some work, however, has shown that direct operation of SOFCs on dry hydrocarbon fuels is possible.[26, 27] Additionally, work has shown that adding a boundary layer to the anode can suppress carbon deposition by enhancing a steam reaction and by controlling the concentrations of the reactant gaseous species at the electrolyte interface, allowing for direct operation on carbon fuels such as methane.[28]

2.3 Materials and Requirements of SOFC Components

2.3.1 The Electrolyte

A fuel cell is usually classified by the type of electrolyte it uses, as it is the fundamental layer that determines the basic processes of the fuel cell. The following physical characteristics are required in an SOFC electrolyte:

(a) fully dense to prevent gas leakage between electrodes

(b) high oxygen ion conductivity and low electronic conductivity

(c) thin to reduce ohmic losses

(d) toughness to prevent cracking from thermal cycling

(e) chemically stable in reducing and oxidizing environments

Figure 2.6 shows the ionic conductivities of a number of electrolyte candidates for SOFCs.[29] The horizontal line shows a reasonable target resistivity of 0.1 Ωcm^2 for a 10 μm thick electrolyte, highlighting the temperatures at which this is achievable for different materials. The bulk of research focuses on two main categories of electrolytes: fluorite-structured (AO_2) and perovskite-structured (ABO_3). Figure 2.7 shows the crystal structure of each of these categories. Of the electrolyte candidates, yttria-stabilized zirconia (YSZ) and gadolinia-doped ceria (GDC) of the fluorite structure, and strontium, magnesium doped lanthanum gallate (LSGM) of the perovskite structure, are the most common and promising.

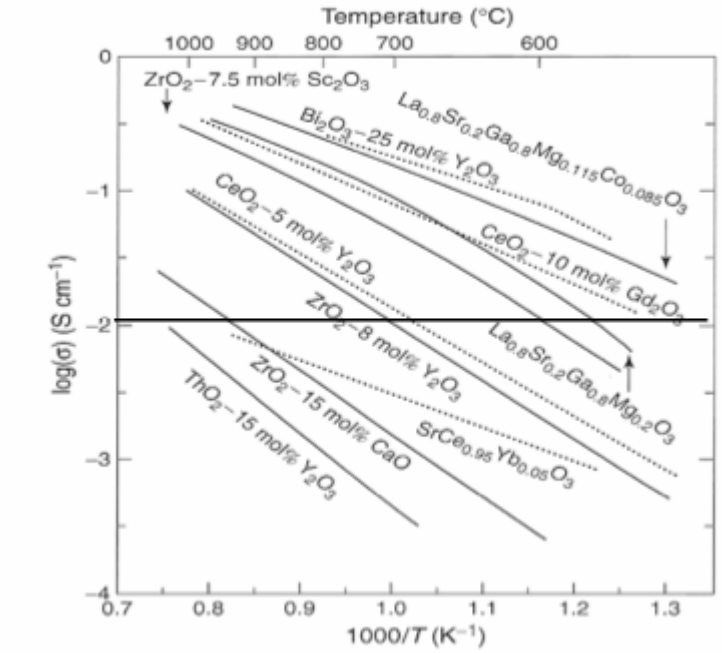

Figure 2.6. Conductivities of a number of electrolyte materials. The horizontal line shows a resistivity of 0.1 Ωcm^2 for a 10 μm thick electrolyte.

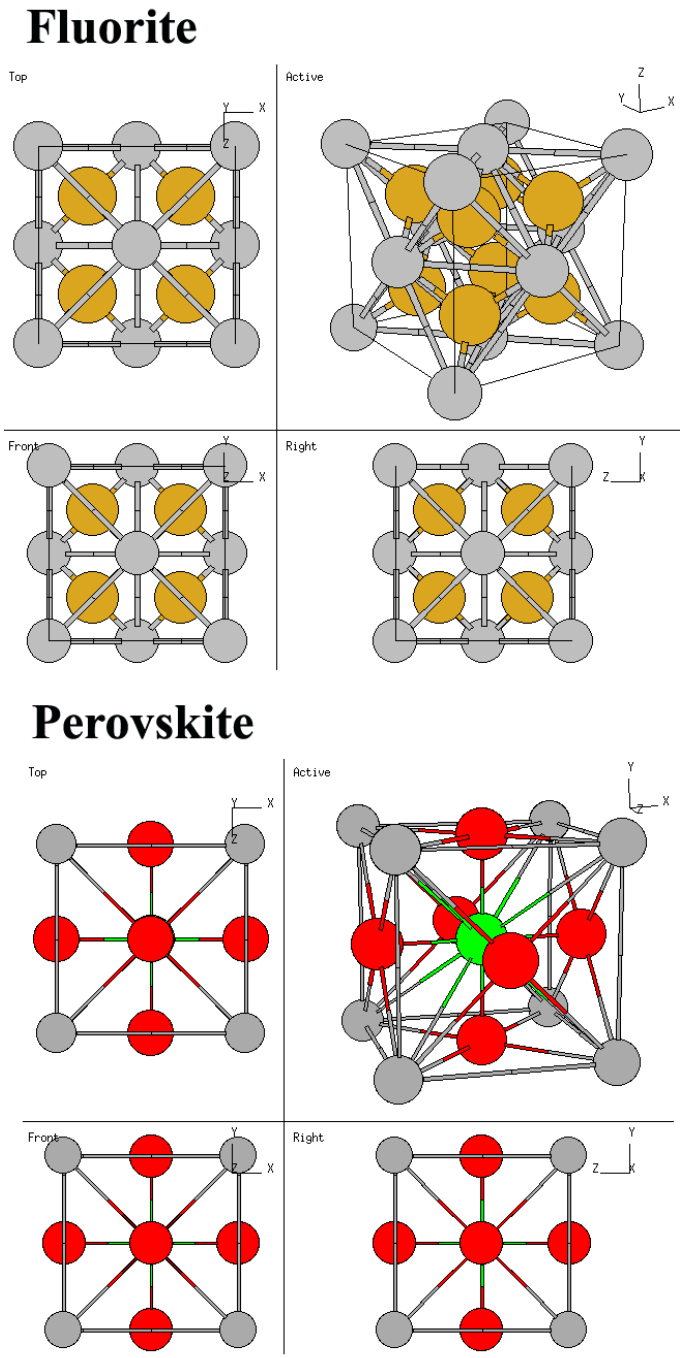

Figure 2.7. The fluorite and perovskite crystal structures. In the fluorite structure, the brown atoms are oxygen. In the perovskite structure the red atoms are oxygen and the A and B site atoms are the grey and green atoms (interchangeable).

2.3.1.1 Fluorite-Structured Electrolytes

Of all electrolytes, yttria-stabilized zirconia (YSZ) is the most common. Stabilized zirconia is ideal because it shows good ionic conductivity and stability in both oxidizing and reducing atmospheres. Doping zirconia stabilizes it in a cubic fluorite structure from room temperature up to its melting temperature. Doping by direct substitution of divalent or trivalent cations also increases its oxygen vacancy concentration by charge compensation.[30] Hence, oxygen vacancy diffusion is the mechanism for ionic transport and follows an Arrhenius dependency. YSZ reaches its maximum conductivity at a doping level of 8 mol% yttria. The Kroger-Vink notation for the stabilization with yttria is:[10]

$$Y_2O_3 \xrightarrow{ZrO_2} 2Y'_{Zr} + V_O^{\bullet\bullet} + 3O_O^x \qquad (2.4)$$

Yttrium does not provide the highest ionic conductivity of the possible dopants, which include the oxides of Yb, Sc, and Gd. Conductivity has been shown to be inversely proportional to the ionic radius of the dopant species.[31] This is due to the fact that oxide ion diffusion is affected by elastic strain energy, which effectively lowers the ion mobility, where all of these dopants have larger radii than Zr. As a result, Sc, which has the smallest radius amongst the dopant candidates (and best matched with Zr), shows the highest conductivity. However, yttria is most commonly used because of its availability and cost.[10] As shown in figure 2.6, YSZ achieves a suitable conductivity of 10 S/cm (with a 10 μm thick electrolyte) down to 700°C.

Processing conditions play a vital role in the final microstructure and grain morphology of YSZ, which affect the conductivity of the thin film. Many preparation methods such as die

pressing, screen-printing, dip-coating, centrifugal casting, RF magnetron sputtering, and spray pyrolysis have been studied and optimized, allowing for low cost deposition of a dense thin film electrolyte.[32-39] In the studies of this thesis, YSZ is the sole material used for the electrolytes.

Ceria doped with rare-earth oxides (Sm_2O_3 and Gd_2O_3) also has a cubic fluorite structure. In this case, Ce^{4+} is replaced with a trivalent ion, introducing oxygen vacancies within the structure to increase the conductivity.[40] Gadolinium doped ceria (GDC) has a very high ionic conductivity, allowing for operation at temperatures as low as 500ºC.[41] Its conductivity is approximately an order of magnitude great than that of YSZ, which is a function of the fact that Ce^{4+} has a larger ionic radius than Zr^{4+}, allowing for easier migration of oxygen anions within this more open structure.[16] Concerns exist, however, because at high temperatures in the fuel environment, Ce^{4+} can reduce to Ce^{3+}, producing a high electronic conductivity proportional to $P(O_2)^{-1/4}$ which serves to reduce the operating voltage and add losses to the cell.[16, 42]

2.3.1.2 Perovskite-Structured Electrolytes

Ion conducting perovskites have also been explored. Perovskites are easily tailored via doping on either the A or B cation sites, and a wide array of dopants and concentrations are tenable. The most common system is to dope lanthanum gallate with divalent Sr and Mg on the La and Mg sites (LSGM), respectively, to increase the oxygen vacancy concentration.[43-45] LSGM has shown high ionic conductivity (see Figure 6) and stability in reducing and oxidizing environments at temperature ranges of 700-1000ºC. However, reactivity with Ni and migration of La to form insulating compounds such as $SrLaGa_3O_7$ and $La_4Ga_2O_9$ emphasizes the need for

further exploration regarding the numerous requirements of material compatibility with potential electrodes.[16, 42]

2.3.2 The Anode

The anode is responsible for providing a site for the electrochemical oxidation of fuel. In order for this to take place, the anode must provide gaseous, electronic, and ionic transport to and from the electrolyte. It must also be catalytically active, and in the case of anode supported cells, must provide structural integrity. For these to occur simultaneously, the following physical characteristics are necessary:[23]

(a) connected porosity to allow for gas transport

(b) high electrical conductivity

(c) good thermal expansion match with the electrolyte

(d) stability in a reducing environment

(e) chemical compatibility with electrolyte and interconnect

To achieve these goals, two main categories of anode have emerged. One is a ceramic and metal composite, known as a cermet. The other is a purely ceramic anode that sometimes contains trace amounts of catalyst metals.

2.3.2.1 Ni-YSZ Cermet Anode

Cermet anodes meet the above requirements by combining two materials that can independently provide optimized solutions to the needs of the anode. Specifically, the metal provides the electronic conductivity and catalytic activity to oxidize the fuel and the ceramic provides the ionic transport pathway to the electrolyte. Extending this ionic pathway out from the electrolyte interface effectively increases the length of TPB within the electrode, a subject that will be discussed in further detail later. In addition to these fundamental properties, the metal and ceramic must be compatible and maintain all the structural needs outlined above.

The most common anode used is a nickel yttria-stabilized zirconia (YSZ) cermet. The reducing atmosphere of the anode allows for the use of metals, although these are limited to nickel, cobalt, and noble metals due to the need for stability in the more oxidizing fuel outlet conditions. Nickel is ideal because of its low cost and high electrochemical oxidation catalytic activity. Ni also shows a very low charge-transfer resistance at the triple-phase boundary which allows for a low activation polarization. Ni provides the electronic conductivity within the anode and a percolation threshold of ≈ 30 vol% exists under which disconnected Ni causes a dramatic drop in conductivity. This threshold, however, is dependent on microstructural properties such as the surface area of the YSZ support, the pore structure, and the particle size ratio, among others.[10, 46-48] For example, it has been shown that using a broader spectrum of sizes of Ni powder allows for closer packing and hence a higher conductivity at lower Ni concentrations. In addition, combination of fine and coarse YSZ has shown improved resistance over long times, as long as the amount of coarse YSZ is kept low.[49] It is important to note, however, that while these processing techniques might enhance the electrical conductivity, there can be trade-offs in

other features like the TPB density, such that the overall performance of the electrode may suffer.

The difference in the coefficients of thermal expansion of Ni (13.3 x 10^{-6} K^{-1}) and YSZ(10.5 x 10^{-6} K^{-1}) is a source of concern with regards to the stability of the anode-electrolyte layers over time and temperature cycling, but the addition of YSZ in the anode (to form the cermet) helps substantially.[10] Nickel coarsening and sintering is also a concern over time at such high temperatures, although the rigid YSZ structure aids in reducing this effect.[47, 50] It has been shown that a decrease in conductivity of 33% occurred in a Ni-YSZ cermet after 1000h of treatment in a dilute hydrogen atmosphere at 1000°C.[51]

The rate of coarsening and overall change in the Ni microstructure and conductivity is a function of a number of processing variables and the initial microstructure of the cermet. With that in mind, studies have shown that the amount of NiO and the type of YSZ powders used affect the microstructure of sintered, but pre-reduced NiO-YSZ composite anodes.[52] Studies have shown that commercial powders vary dramatically in size, and size distribution. In the case of NiO commercial powders, grain sizes varied from 0.5 to 14.7 μm,[53, 54] while studies of YSZ commercial powders found a three-fold difference in average surface areas.[55] Using coarsening treatments on the initial NiO and YSZ powders has been shown to have a dramatic effect on the overall performance of the electrode, and controlling the particle size distributions remains a key in processing studies.[56-58] Additionally, the type, size, and amount of pore former used have been shown to be important variables in controlling the pore microstructure.[59] All of these factors clearly accentuate the difficulty in understanding and controlling processing to achieve desired microstructures.

The logical next step to these studies is to determine optimal processing conditions for producing the lowest anode polarization, for which there has been an incredible amount of work conducted. However, these studies have been empirical due to the inability to fully quantify and understand the microstructures of these cermets. As a result, structures are described by their processing conditions: composition, particle size, porosity, method, etc. The best performance achieved for Ni-YSZ cermet-supported cells has been 1.8-1.9 Wcm^2.[60, 61] Additionally, it has been shown that a minimum overpotential is achieved at a Ni content of 40-45 weight %.[62, 63] The ratio of NiO/YSZ particle sizes also plays an important role in the overall performance of the electrode. Lee et al. determined that comparative particle sizes of Ni and YSZ were better than a large Ni/YSZ size ratio due to the enhanced connectivity and TPB density estimated from SEM micrographs, and Murakami et al. found that a ratio of 0.2 achieved the lowest activation polarization.[64, 65] The problem with these studies is that they make a determination while isolating one variable, when in reality all the variables are co-dependent, such that the optimal ratio will be a function of porosity, composition, particle sizes, and vice versa.

The microstructures of cermet electrodes are hard to control. Large microstructure changes can occur at high processing and operation temperatures and at reducing conditions. In addition, the porosity comes from the shrinkage that occurs from the reduction of NiO to Ni, so the pore structure is a direct function of the starting NiO structure. Having effective and repeatable processing methods is very important because low porosity, anisotropic mixing, and poor connectivity all contribute to reduced cell performance.

Sintering temperature and processing method play vital roles in determining an optimal microstructure.[53, 66] As a result, many unique processing techniques have been used to enhance the properties of the anode. In one case, with all variables kept constant, anodes made

by liquid condensation showed a dramatically better power density compared with those made by spray drying.[67] A relatively new sol-gel technique has also been demonstrated where a nitrate solution and then calcination is used to produce nano-size particles.[68] Standard powder processing from these combustion synthesis powders have produced cells that have shown improved performance.[69, 70] This technique can also be used in situ to stabilize and increase performance by creating a thin film of material on an already processed cermet.

Multilayer anodes, utilizing specific differences in microstructural requirements near and away from the electrolyte interface, have also shown improved performance.[71] These are based on a proposed two layer structure where the inner layer has a finer optimized microstructure and the outer structure is a coarser structure to help gas transport and contains higher amounts of Ni to improve the internal electrical resistance.[72] This technique of using an "active layer" adjacent to the electrolyte has become commonly adopted amongst most cermet processing.

Overall, little agreement in literature exists, and the many variables in processing and materials and the lack of proper microstructural study make understanding the connections of microstructure and performance difficult. Figure 2.8 shows an example of the large range of performance that has been reported in Ni-YSZ SOFCs, highlighting the sensitivity of the polarization to processing and microstructure.[53] In addition, gas flow rate, and content of oxygen, hydrogen, and steam at the electrodes all affect the experiments. Mogensen et al. have summarized these observations (see references listed 1-21 in [73]) and attempted to explain the discrepancies by placing blame on impurities and laboratory specific measurement and fabrication conditions.[73] It has been shown that impurities in NiO commercial powders, such as SiO_2 and Na_2O, at concentration levels of tens to hundreds of ppm, segregate to the anode-

electrolyte interface and form silicate glass phases containing, Na, Mn, Ti, Mg, K, and Al, that damage the electrolyte and the performance of the cell.[74, 75] This suggests that studies of microstructure and performance should not be compared between different laboratories and testing conditions, and emphasizes the difficulties that the research community faces.

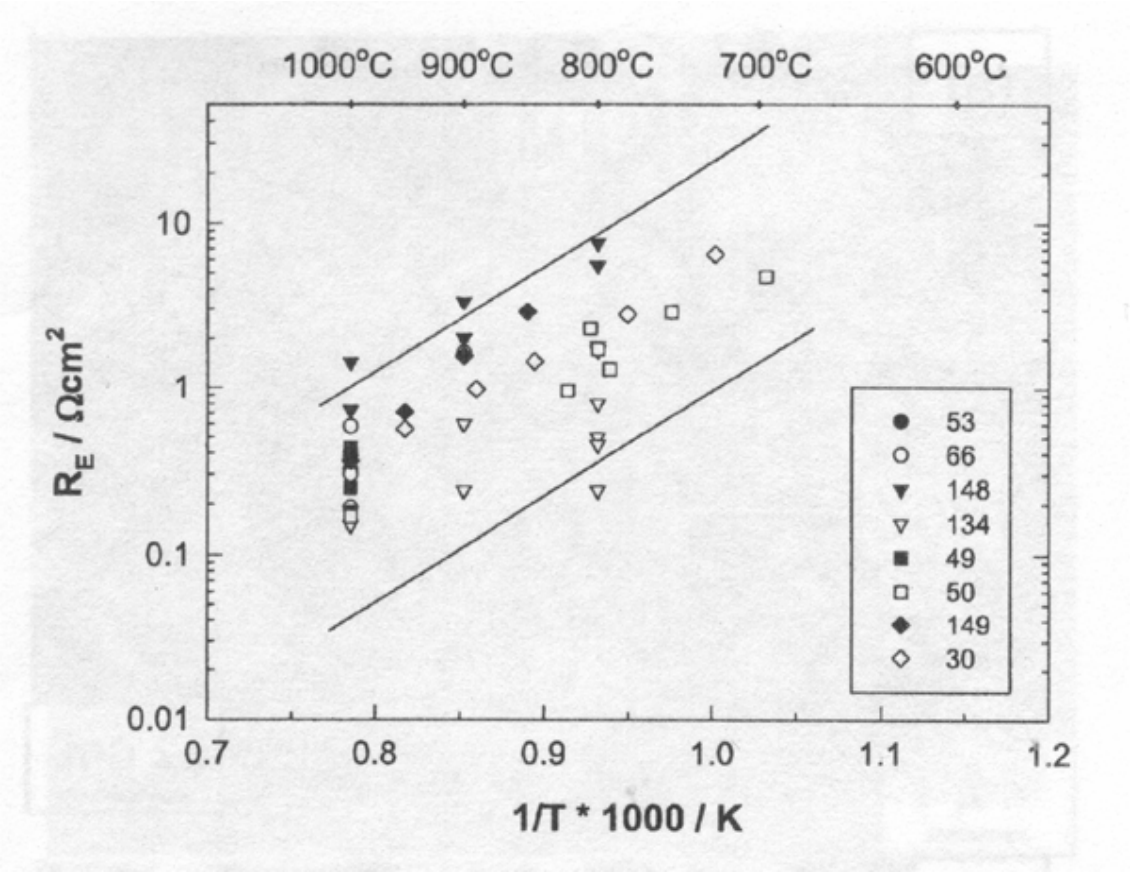

Figure 2.8. Literature values for various anode polarizations highlighting the large range of performance reported as processing, microstructure, and testing parameters vary. Resistances were measured by electrochemical impedance spectroscopy at open circuit voltage and under moist hydrogen. The numbers are the references as cited in Jiang and Chan.[53]

2.3.2.2 Other Cermet Anodes

One drawback of Ni is that the volume changes between Ni and NiO associated with redox cycling can cause mechanical failure in anodes with high Ni content. In addition, because Ni is a good catalyst for the cracking of methane and other hydrocarbons, it can cause coking (carbon deposition) within the anode when operating on CH_4 or CO[76]. Ni is also easily poisoned by sulfur, a contaminant in coal-based fuels. These limitations have spurred research into alternative anodes with different catalyst materials.[77]

As discussed in section 2.2, a large amount of research has been conducted focusing on the operation of SOFC anodes on hydrocarbon fuels. Studies have shown that coking can be reduced by additions of Mo or Au, and Co has been shown to increase cell performance in methane.[23] Other anodes use Ru, despite its higher cost, because it has a better sintering resistance and is a reforming catalyst.[42, 78]

Direct electrochemical oxidation of methane is achieved through use of mixed conducting rare-earth doped ceria anodes.[23] While degradation occurs from thermal expansion in reducing environments when Ce^{4+} goes to Ce^{3+}, the doping helps.[79] Cermets of Ni and samaria doped ceria (SDC) prepared by spray pyrolysis on an LSGM electrolyte have been demonstrated as an example of these alternative anodes.[80] In addition, Ni-SDC anodes with small amounts of Pd show good performance at low temperatures as well as catalytic activity towards partial oxidation of methane.[78] Other ceria-based cermets such as Cu-CeO_2-YSZ systems have shown effective direct hydrocarbon use,[26, 81, 82] implementing such unique processing techniques as impregnating a YSZ scaffold with a copper-ceria composite mixture.[83]

2.3.2.3 Ceramic Anodes

The purpose of using a ceramic anode is the same as that for non-Ni cermets: for better stability and direct use of methane and hydrocarbon fuels. Titanate-based oxides have shown good stability and n-type electronic conductivity in reducing atmospheres, such as yttria doped strontium titanate ($SrTiO_3$).[84, 85] Other perovskites have also shown good results as anodes, with doped lanthanum chromites receiving a lot of attention.[86] $La_{0.8}Sr_{0.2}Cr_{0.97}V_{0.03}O_3$ (LSCV)-YSZ has shown comparable electrochemical performance to Ni-YSZ after extended operation,[18, 87] and $La_{0.8}Sr_{0.2}Cr_{0.8}Mn_{0.2}O_3$-GDC composites have shown non-coking direct hydrocarbon use.[88] As discussed previously, Ru is an excellent catalyst for methane steam reforming, although it is very expensive. It has been shown however that small amounts of Ru can be implemented in perovskites such as $La_{1-x}Sr_xCr_{1-y}Ru_yO_3$.[89] Additionally, precipitation of Ru from perovskite anodes to nucleate nanometer scale particles as electrocatalysts has been shown as an effective processing method.[90] Other perovskites explored are $(La,Sr)(Ti,Ce)O_3$ by [91] and $Nd(Cr_{1-x}Mg_x)O_3$ by [92].

2.3.3 The Cathode

The cathode is responsible for providing a site for the electrochemical reduction of oxygen. In order for this to take place, the cathode must provide gaseous, electronic, and ionic transport to and from the electrolyte and must also be catalytically active, while maintaining stability with the other cell components. For these to occur simultaneously, the following physical characteristics are necessary:[93]

(a) connected porosity to allow for gas transport

(b) high electrical conductivity

(c) good thermal expansion match with the electrolyte

(d) stability in a oxidizing environment

(e) chemical compatibility with electrolyte and interconnect

To achieve these goals, two main categories of cathode have emerged. In one case, a two-phase composite is used, much like the Ni-YSZ system, where the electronic and ionic pathways are isolated in order to maximize their conductivities. Strontium-doped lanthanum manganite (LSM) represents the most common electronically conducting material used in composite cathodes. In the second case, a mixed ionic-electronic conductor (MIEC) is used as a single-phase cathode. Strontium-doped lanthanum cobaltite (LSC) is the most common MIEC cathode.

2.3.3.1 LSM-YSZ Composite Cathodes

The most common cathode material used today is strontium doped lanthanum manganite, $La_{1-x}Sr_xMnO_{3-\delta}$ (LSM). Lanthanum manganite is a p-type conductor, and doping the lanthanum site with divalent cations increases its conductivity via the small polaron mechanism by producing more Mn^{4+} atoms:

$$SrO + \tfrac{1}{4}O_2(g) + La_{La}^{x} \xrightarrow{LaMnO_3} Sr_{La}^{'} + (Mn_{Mn^{3+}}^{4+})^{\bullet} + \tfrac{1}{2}La_2O_3 \qquad (2.5)$$

As a result, the conductivity of LSM follows an Arrhenius dependency and is greater than 10 Scm^{-1} at 700°C.[94] Much of the properties of LSM, including the CTE and electronic and ionic conductivity, depend on the stoichiometry of the La and O and on the doping levels of Sr. If the stoichiometry is oxygen deficient, the electronic conductivity is a function of the mean Mn valence, and hence increases with increasing Sr content.[Mizusaki SSI 132 2000] In contrast, a La deficient stoichiometry shows lower electronic conductivity.[95] The most common doping scheme used is that of $La_{0.8}Sr_{0.2}MnO_{3-\delta}$, which has a TEC of 11.3 x 10^{-6} K^{-1}, similar to that of YSZ.[94]

While LSM has a high electronic conductivity, its ionic conductivity is very low. Measurements of the oxygen diffusion coefficient showed values within 10^{-11} to 10^{-13} cm^2s^{-1}, depending on the doping levels, which is much less than MIEC values.[96, 97] Additional studies using oxygen isotopes have found minimal concentration gradients, and hence slow diffusion in LSM.[98] Because of the ionic transport limitations of LSM, the most common processing of the cathode is as a composite of LSM-YSZ.

Lanthanum deficient, non-stoichiometric processing is favorable due to detrimental second phase formation of $La(OH)_3$ when lanthanum is in excess and because reaction with YSZ at 1200ºC can produce $La_2Zr_2O_7$ which significantly reduces cell performance.[99] However, it has been shown that A-site non-stoichiometry can increase the sinterability of LSM in composite cathodes, although this effect is reduced when the cathode is placed under polarization.[100] Processing temperatures are also kept below 1400ºC in order to minimize manganese migration.[10, 101]

Cathodes are commonly made from standard powder processing routes. Powders are made by solid state reaction or nitrate solution calcinations to produce nano-particles.

Techniques include (for planar cells) screen printing, tape casting, plasma spraying, and spin coating, among others, all followed by sintering.[102-106] Using a nitrate solution to impregnate pre-fabricated YSZ scaffolds has become a more popular method for introducing nano-sized LSM into the composite.[107, 108] Additional impregnation with GDC to produce a thin film on LSM has shown improved performance.[109, 110] Because the electrical conductivity of these LSM-YSZ composites is ≈10 times less than that of pure LSM, an LSM current collection layer is often fabricated on top of the composite layer to aid in reducing the electrical resistivity.[111, 112] Additionally, it has been observed that a break-in time is needed for LSM cathodes, requiring up to 150 hours of operation to reach an equilibrium polarization.[105, 113]

With the development of low resistance thin film electrolytes, the dominant polarization in planar SOFCs at temperatures of 600-850°C is due to the cathode, as the inherent electrochemical activity of oxygen reduction is less than that of the oxidation of the fuel at the anode.[114, 115] As a result, a substantial amount of work has concentrated on optimizing the cathode. As with the anode, most of this work has relied on empirical studies focusing on processing-performance relationships due to the lack of adequate means for quantitative microstructural analysis. As discussed previously, a composite is used to increase the TPB length away from the electrolyte interface and to reduce the sintering of LSM.[116, 117]

As expected, electrode thickness, particle size, and sintering temperature are all important factors in achieving microstructures that produce optimal performance. A composition containing 40-50 weight % YSZ has been shown to maximize performance.[118, 119] Sintering the cathode at 1100°C was determined to be optimal in screen-printed electrodes because it strikes a balance between high interfacial resistance from incomplete inter-particle contact at low

temperatures and loss of TPB from coarsening at high temperatures.[116] Sintering at lower temperatures allows for a less dense, finer microstructure which has a decreased polarization resistance.[120] A series of electrodes made with a range of staring LSM particle size supported this result, showing that electrodes with the smallest particle sizes showed the best initial performance, but also the greatest degradation in polarization as the smaller particles were more prone to sintering.[121, 122] The active thickness of an LSM-YSZ composite cathode was shown to be around 20μm, so processing of thick film cathodes is not necessary, although this active thickness will vary depending on microstructural factors.[123] Additional studies of screen printed LSM-YSZ showed optimized performance when using ethyl cellulose as a binder, a 120 mesh size, and sintering conditions of 1200°C for 2 hours.[113] Overall, it is desirable to have small grain, highly connected microstructure, as long as it is stable at operating temperatures.

2.3.3.2 LSC Mixed Electronic-Ionic Conducting Cathodes

The most common mixed electronic-ionic conductor studied for SOFC cathodes is strontium doped lanthanum cobaltite, $La_{1-x}Sr_xCoO_{3-\delta}$ (LSC). Doping lanthanum cobaltite with lower valence cations produces higher ionic conductivities than lanthanum manganite under the same conditions. The overall kinetics of LSC increase with increasing amounts of the dopant Sr.[124] Because of the mixed-conductor quality of LSC, it is commonly processed as a single-phase cathode. This allows the electrochemical processes and charge-transfer reactions to be extended to the two-dimensional surface of the electrode, opposed to the one-dimensional TPBs of composite electrodes like LSM-YSZ. The importance of the microstructure of MIEC

electrodes will be discussed later. Compared to LSM, lanthanum cobaltite decomposes at higher oxygen partial pressures, has a higher thermal expansion coefficient (larger difference with YSZ), and is more reactive with YSZ. As a result, work on LSC has focused on GDC and SDC electrolyte cells, and in some cases it has been used as part of an LSC-GDC composite. Doping on the B site of LSC with Fe to produce $La_{0.6}Sr_{0.4}Co_{0.2}Fe_{0.8}$ (LSCF), for example, has shown promise in fighting the reducing nature of LSC and has aided in reducing the CTE to match that of GDC.[101, 125, 126]

2.3.3.3 Other Cathodes

Work is not limited solely to LSM-YSZ cathodes. Designing two-phase composites allows for the optimization of each material separately, and much work has been done using GDC composite cathodes due to its higher ionic conductivity than YSZ. Tests of LSM-GDC, LSCF-GDC, and LSCF-GDC-Ag have shown lower interfacial resistance and polarization resistances as low as .01 Ωcm^2 at 750ºC.[117, 125, 126]

Different doping schemes among the A and B elements of perovskites have also led to a diverse array of research. Notably successful among these for reduced-temperature SOFCs are $Ba_{0.5}Sr_{0.5}Co_{0.8}Fe_{0.2}O_{3-\delta}$ (BSCF), $Nd_{0.7}Sr_{0.3}Fe_{0.2}Co_{0.8}O_3$ (NSCF), and $La_{0.8}Sr_{0.2}FeO_{3-\delta}$ (LSF).[42, 127] Other work has focused on replacing the LSM in the composite with MIEC materials with higher ionic conductivity such as LSCF and SSC in order to reduce interfacial polarization resistances.[128] These materials are commonly matched with different electrolyte materials such as GDC and SDC, respectively. A summary of the CTE, electronic, and ionic conductivities of the most common cathode perovskite materials is provided in Table 2.4.[129]

Cathodes commonly will be deposited with an initial thin interlayer that has ideal small microstructure for the oxidation reduction reaction to take place, with a bulk cathode layer deposited on top with larger porosity and grain structure for better gas transport and electronic conductivity, much like what is done with Ni-YSZ anodes. Exotic multi-layer cathodes are being developed as well that grade composite ratios and doping concentrations normal to the electrolyte interface in order to maximize conductivity and stability in their desired regions.[130]

Table 2.4. The thermal expansion coefficients (from 30-1000°C), and electronic (σ) and ionic (σ_o) conductivities of various perovskite-type oxide cathode material candidates at 800°C in air. The table is taken from Ullmann et al.[129]

Composition	TEC (10^{-6} K^{-1})	log σ (S/cm)	σ_o (S/cm)	E_a (σ_o) (eV)
$Sr_{0.9}Ce_{0.1}CoO_{3-x}$	21.5	2.47	0.133	0.82
$Sr_{0.9}Ce_{0.1}FeO_{3-x}$	20.2	1.46	0.064	0.87
$Sr_{0.85}Ce_{0.15}Fe_{0.8}Co_{0.2}O_{3-x}$	18.5	1.59	0.016	1.00
$Sr_{0.9}Ce_{0.1}Fe_{0.8}Ni_{0.2}O_{3-x}$	18.9	1.94	0.04	
$La_{0.3}Sr_{0.7}CoO_{3-x}$	25.0	2.96	0.76	
$La_{0.5}Sr_{0.5}CoO_{3-x}$	22.3	3.13	0.093	
$La_{0.6}Sr_{0.4}CoO_{3-x}$	20.5	3.2	0.22 [1]	
$La_{0.65}Sr_{0.3}Fe_{0.8}Co_{0.2}O_{3-x}$	14.9	2.20	4×10^{-3}	0.85
$La_{0.6}Sr_{0.4}FeO_{3-x}$	16.3 [22]	2.11	5.6×10^{-3}	0.75
$La_{0.6}Sr_{0.4}Fe_{0.8}Co_{0.2}O_3$	17.5	2.48	8×10^{-3}	1.32
$La_{0.6}Sr_{0.4}Fe_{0.5}Co_{0.5}O_3$	(20.3) [19]	2.69		
$La_{0.6}Sr_{0.4}Fe_{0.2}Co_{0.8}O_3$	(21.4) [19]	2.43 [23]	0.058	
$La_{0.8}Sr_{0.2}Co_{0.1}Fe_{0.9}O_{3-x}$	13.9	1.50	2.2×10^{-3}	1.33
$La_{0.8}Sr_{0.2}Co_{0.2}Fe_{0.8}O_{3-x}$	14.8	1.94	2.3×10^{-3}	1.34
$La_{0.8}Sr_{0.2}Co_{0.8}Fe_{0.2}O_{3-x}$	(19.3) [19]	3.00 [10]	4×10^{-2} [1]	
$La_{0.8}Sr_{0.2}Co_{0.5}Fe_{0.5}O_{3-x}$	(17.6) [19]	2.55		
$Pr_{0.8}Sr_{0.2}Fe_{0.8}Co_{0.2}O_{3-x}$	12.8	1.88	1.54×10^{-3}	1.58
$Pr_{0.8}Sr_{0.2}Mn_{0.8}Co_{0.2}O_{3-x}$	10.9	1.92	3×10^{-5}	0.87
$Pr_{0.65}Sr_{0.3}MnO_{3-x}$	11.6	2.32	3.4×10^{-4}	1.19
$Pr_{0.7}Sr_{0.3}Mn_{0.8}Co_{0.2}O_{3-x}$	11.1	2.3	4.4×10^{-5}	0.81
$Pr_{0.75}Sr_{0.2}Mn_{0.8}Co_{0.2}O_{3-x}$	10.8	1.98	1.1×10^{-4}	
$La_{0.65}Sr_{0.3}MnO_{3-x}$	12.3	2.01	1.7×10^{-4}	
$La_{0.75}Sr_{0.2}Mn_{0.8}Co_{0.2}O_{3-x}$	9.5	1.9	3.1×10^{-5}	
$La_{0.9}Sr_{0.1}Ga_{0.8}Mg_{0.2}O_{2.85}$	11.6	−1.00	0.10	0.73
$La_{0.9}Sr_{0.1}(Ga_{0.9}Co_{0.1})_{0.8}Mg_{0.2}O_{3-x}$	13.0	−1.02	0.095	0.71
$La_{0.8}Sr_{0.2}Ga_{0.8}Mg_{0.2}O_{3-x}$	11.4	−1.00	0.10	0.73

[a] Values in parentheses are interpolated values.

2.4 SOFC Thermodynamics

2.4.1 Thermodynamic Principles

Energy that is available for conversion into usable work is called Gibbs free energy, which differs from the total energy by the amount of energy lost in the form of entropy. Therefore, the maximum electrical work done by a fuel cell is equal to the change in the Gibbs free energy of the electrochemical reaction (at constant temperature and pressure):

$$W_{el} = \Delta G = - n \cdot F \cdot E \tag{2.6}$$

where n is the total number of electrons transferred (mol), F is Faraday's constant (96487 Coul/g-mole electron), and E is the theoretical ideal electrical potential of the fuel cell. The standard change in Gibbs free energy, defined as:

$$\Delta G^\circ = - n \cdot F \cdot E^\circ \tag{2.7}$$

where the reaction is in standard state conditions (298K and 1 atm), has been calculated for an immense number of electrochemical reactions and is easily found in tables listed on the internet. The Gibbs free energy change at non-standard conditions can be calculated from the following equation:

$$\Delta G = \Delta G^\circ + RT * \ln\left(\frac{[C]^c [D]^d}{[A]^a [B]^b}\right) \tag{2.8}$$

for the general cell reaction:

$$aA + bB \rightarrow cC + dD \tag{2.9}$$

where R is the universal gas constant. Substituting in equations (2.6) and (2.7) and the electrochemical reaction (2.3) into (2.8) yields:

$$E = E^{\circ} + \frac{RT}{4F} \ln\left(\frac{p_{O_2}^{c} \, p_{H_2}^{a\ 2}}{p_{H_2O}^{a\ 2}} \right) \tag{2.10}$$

which is known as the Nernst equation and represents the ideal potential of a solid oxide fuel cell operating with hydrogen at the anode and oxygen at the cathode. At standard conditions, the ideal standard potential is 1.18 volts with gaseous water product (which is reasonable considering the operating temperatures of an SOFC).[12]

2.4.2 SOFC Efficiency

The theoretical efficiency of a fuel cell, operating reversibly, can be described by the usable energy that can be converted to work, the Gibbs free energy change, divided by the total stored chemical energy released in the electrochemical reaction, the change in enthalpy:

$$\eta = \frac{\Delta G}{\Delta H} \tag{2.11}$$

Under standard conditions of 298K and 1 atmosphere, the change in enthalpy for the reaction of hydrogen and oxygen to liquid water is 285.8 kJ/mole, and the change in Gibbs free energy is 237.1 kJ/mole. As a result, the maximum efficiency of a SOFC at standard conditions and operating reversibly is given by:[12]

$$\eta_{ideal} = \frac{237.1}{285.8} = 0.83 \tag{2.12}$$

In reality, fuel cells are not run at the ideal cell voltage, as there are a number of losses within the cell that contribute to reduced operating voltage. As the current is increased, the voltage decreases as a function of these internal losses. This subject is discussed in section 2.5. As a result, there are additional efficiency losses related to the operating voltage with respect to the ideal reversible voltage:

$$\eta = \frac{(0.83)(V_{actual})}{(V_{ideal})} \tag{2.13}$$

Hence, the maximum efficiency of an ideal SOFC operating at voltage V_{cell} at standard conditions is:

$$\eta = \frac{(0.83)(V_{actual})}{(1.18)} = 0.70 * (V_{actual}) \quad (2.14)$$

2.5 SOFC Operation and Performance

2.5.1 Operational Losses

Polarization, or overpotential, describes a voltage loss within the cell. This can come from a number of sources and helps define the quality and efficiency of the cell as a whole. The theoretical voltage of a cell is described by the Nernst potential (equation 2.10), which is derived from the thermodynamic free energy change involved in the electrochemical oxidation of hydrogen, and is a function of the respective gas partial pressures and temperature.

Polarizations are subtracted from this Nernst potential to give the real operating potential of a cell, all of which are functions of the current density. The primary polarizations are a) ohmic; b) concentration; and c) activation. Figure 7 shows a standard voltage vs. current plot for an SOFC with the respective polarization regions outlined.[12]

2.5.2 Ohmic Polarization

Ohmic polarization comes directly from resistive losses within the cell described by Ohms Law:

$$\eta = (\rho_e l_e + \rho_c l_c + \rho_a l_a + R_{contact})i \quad (2.15)$$

where ρ is the electrical resistivity of the electrolyte, cathode, and anode. Because the conductivity of the electrolyte is orders of magnitude lower than those of the electrodes, most of the ohmic loss generally comes from the electrolyte, which is why thin electrolytes are ideal.

2.5.3 Concentration Polarization

Concentration polarization is caused by the limitations of gaseous transport and contributes significantly to the overall polarization when current densities are high. The overall cell reaction in equilibrium must provide enough reactants and remove enough products such that a steady state is reached and a concentration gradient is minimized. If one of these processes is slowed down, a concentration polarization is produced. This is generally a function of binary diffusion and electrode microstructure, which can be further described by volume % of porosity and pore tortuosity. More complicated mechanisms such as adsorption/desorption and surface diffusion are considered negligible. In the anode, binary diffusion is described by H_2 and H_2O, and in the cathode it is described by O_2 and N_2. Because the binary diffusivity of H_2-H_2O is much greater than O_2-N_2 and because the partial pressure of H_2 is much greater than that of O_2, the cathode concentration polarization is usually greater than that of the anode. An exception to this can occur, however, in anode supported cells (due to the thickness dominance) and when high fuel utilization is attempted, such that the H_2 partial pressure is quite low at the anode/electrolyte interface. The cathode polarization is described by equation (2.16), derived from Fick's First Law, and is a function of current density.[61]

$$\eta_{conc}^{c} = -\frac{RT}{4F}\ln\left(1-\frac{i}{i_{cs}}\right) \tag{2.16}$$

i_{cs} is the cathode-limiting current density, the current density at which the oxygen is starved at the electrolyte interface, and corresponds to the maximum potential current of the cell. i_{cs} has the following form[61]

$$i_{cs} = \frac{4Fp_{O_2}^{c}D_{c(eff)}}{\left(\frac{p-p_{O_2}^{c}}{p}\right)RTl_c} \tag{2.17}$$

where $D_{c(eff)}$ is a function of the binary diffusivity, vol% porosity, and tortuosity, and l_c is the cathode thickness.

2.5.4 Activation Polarization

Activation polarization is a function of the electrochemical reaction kinetics and is best described as an activation energy for the charge transfer reaction. It is a function of a number of mechanisms involved in this multi-step process, often with parallel pathways. The complicated nature of this reaction process has made it difficult for scientists to define a rate-limiting step and a definitive pathway. There are a number of potential rate-controlling steps related to bulk and surface processes that depend on the materials used and the microstructure of the electrode and interface. A diagram illustrating these pathways is provided in Figure 2.9.[124] Current research has focused on reducing the activation polarization in cathodes because it has been

shown that this is the primary contributor to the area specific resistance now that ultra-thin electrolytes have been developed. As a result, most of the following studies and equations will focus on the cathode. Experimental studies of electrochemical reaction pathways and kinetics are discussed in section 2.6.3.

The Butler-Volmer equation gives a quantitative relationship between current density and the activation polarization, and is of the form[14]

$$i = i_o^c \left\{ \exp\left[\frac{\beta z F \eta_{act}^c}{RT} \right] - \exp\left[-\frac{(1-\beta) z F \eta_{act}^c}{RT} \right] \right\} \tag{2.18}$$

where i_o^c is known as the exchange current density and β is a positive constant less than one. While η_{act}^c can not be determined from i, high and low-current limits simplify the equation such that at low currents

$$\eta_{act}^c \approx \frac{RT}{zFi_o^c} i \tag{2.19}$$

where $\frac{RT}{zFi_o^c}$ is defined as the charge transfer resistance R_{ct}^c, and at high currents

$$\eta_{act}^c \approx \frac{RT}{\beta zF} \ln i_o^c - \frac{RT}{\beta zF} \ln i \tag{2.20}$$

which is known as the Tafel equation. The exchange current density i_o^c is a function of the triple-phase boundary density, oxygen vacancy concentration and mobility, electron concentration, and temperature.

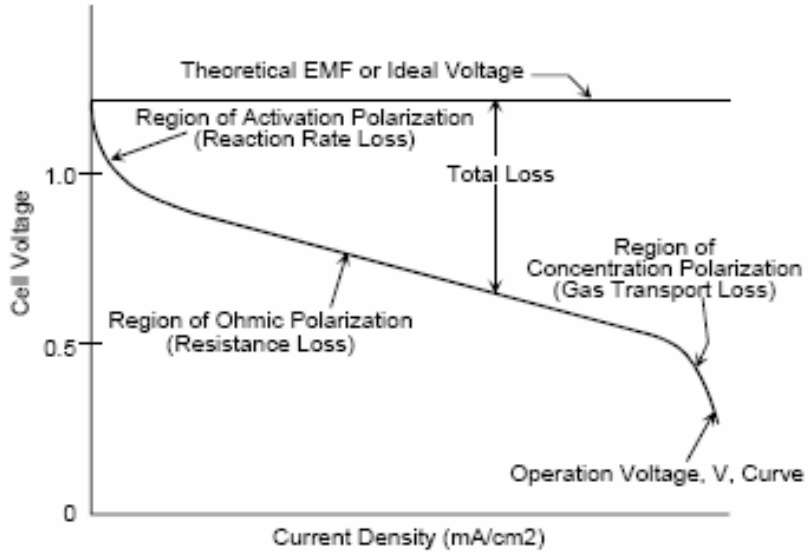

Figure 2.9. Voltage vs. Current plot for an SOFC showing the respective polarization regions.

2.6 The Importance of Microstructure

As discussed previously, electrodes materials can be either electronically conducting or mixed electronic-ionic conductors (MIEC). Electrodes can also be single phase or two-phase composites. For single-phase electronically conducting electrodes, it is commonly understood that the charge transfer reaction takes place at the triple-phase boundary (TPB), the site where the electronic conductor, electrolyte, and gas meet, such that the electrode kinetics scale with the

TPB contact area.[98, 123, 131, 132] A strategy to increase cathode reactivity has been to produce two-phase composite electrodes consisting of an electronically conductive material mixed with an ionically conductive material, such as the Ni-YSZ composites described in section 2.3.2.1, so that the number of TPB sites is effectively increased. Another strategy to increase cathode reactivity is to use an MIEC material such that the reaction area is not just contained to the TPB sites, but is expanded to the entire surface of the cathode. An illustration of these approaches is provided in Figure 2.10, where the reaction area for each tactic is highlighted in red.[124] The advantage of a two-phase electrode over an MIEC electrode is that the transport properties of the two materials can be optimized separately, which allows for easier material selection and better overall performance.[133]

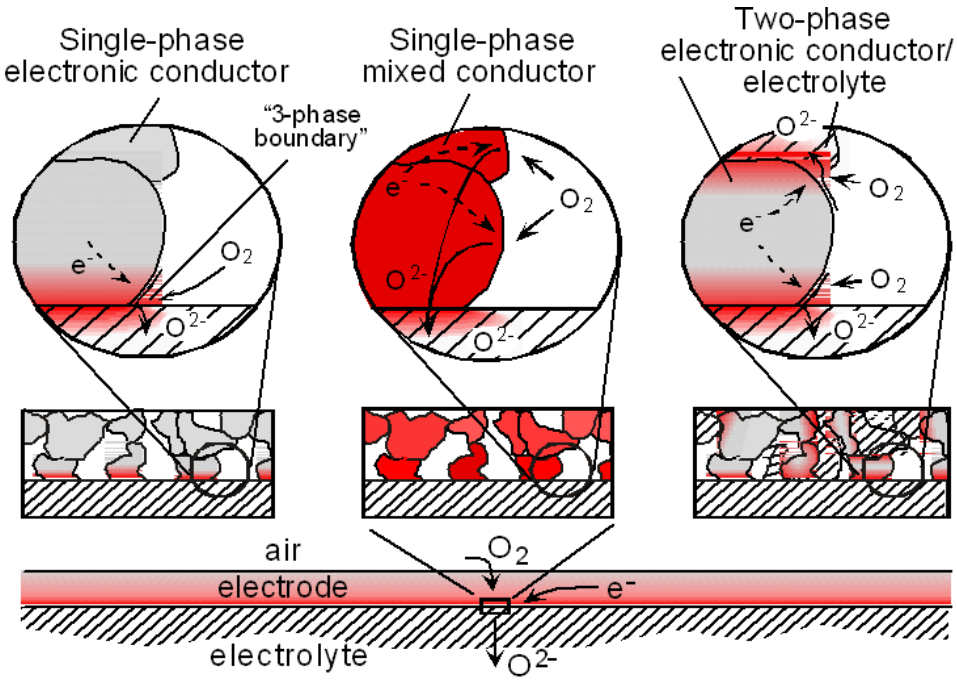

Figure 2.10. Illustration of the effective increase in reaction area by implementation of a mixed conducting or two-phase electrode. Adapted from [124].

In each case described above, the morphology and extent of the reaction zone, highlighted in red in Figure 2.10, depends on the microstructure of the electrode. Therefore, understanding the effectiveness of these strategies and the overall reaction process that takes place relies heavily on our ability to measure and quantify the microstructure. With regards to the losses experienced within the electrode, the concentration polarization depends on pore structure and morphology. The activation polarization depends on the connectivity and tortuosity of the phases, the TPB density, and the surface areas, amongst others.

The following discussion first focuses on the triple-phase boundary and the study of the reaction kinetics involved with activation polarization, both theoretically and experimentally. Because the reaction kinetics are inherently tied to the microstructure of the electrode, this discussion is followed by a summary of the limited experimental work conducted that has focused on electrode microstructure. This lack of structural analysis is due to the absence of a means for quantitative three-dimensional structural analysis. As a result of this inability, experimental studies of the influence of the TPB through the controlled processing of patterned electrodes were conducted and are also discussed. Additionally, the lack of experimental structural analysis has led to a wide array of microstructural modeling, which is summarized as a conclusion to this section.

2.6.1 The Triple Phase Boundary (TPB)

The TPB is characterized by a line and has a line density of the form cm/cm^3, which corresponds to the length of lined associated with a certain volume of electrode. A detailed understanding of the relation between TPB density and electrode polarization has yet to be

developed due to the complicated nature of the electrochemical reaction pathways and due to the fact that accurate TPB density measurements in composite electrodes have not been recorded beyond estimations from 2D images. It has been shown, at the least, that engineering of a two-phase electrode has reduced overall polarization resistance by a general increasing of the TPB line length.[123, 134, 135] These empirical observations have resulted in a loose definition of R_{ct}, such that the TPB charge transfer resistivity is defined as ρ_{ct} in the equation[136]

$$R_{ct} = \frac{\rho_{ct}}{l_{TPB}} \tag{2.21}$$

which defines ρ_{ct} as a material property independent of microstructure. We will see, however, as discussed in the following sections, that this definition is difficult to support experimentally, and generally only applies to patterned single-phase electronic conducting electrodes. It is important to note that this scaling of polarization with the inverse of the TPB length can be described by co-limitation with adsorption and surface diffusion, assuming the utilization length is small compared to the particle size. Additionally, limiting mechanisms that scale with geometric factors that are strongly correlated to TPB length can be confused as being dependent on the TPB length. Clearly this accentuates the difficulty in understanding electrochemical reaction chemistry and kinetics.

2.6.2 Theoretical Electrode Reaction Kinetics

2.6.2.1 Oxygen Reduction at the Cathode

The possible reaction pathways for the reduction of oxygen gas at the cathode are summarized below. It is important to emphasize that these represent only a generic sequence of plausible reaction steps, and have not been proven with a degree of certainty.[94]

i) oxygen molecule adsorption and dissociation into oxygen atoms at the cathode surface
ii) surface diffusion of adsorbed oxygen
iii) incorporation and subsequent bulk diffusion of oxygen inside the oxide lattice
iv) incorporation of adsorbed oxygen in the O_2/cathode/electrolyte three-phase boundary
v) transport of oxide ions in the solid electrolyte

Steps (i), (iii), or (iv) are where charge transfer occurs. A schematic summary of these reaction steps is provided in Figure 2.11.[124] The main difference between composite and MIEC electrodes is that (iii) can occur at a higher rate than (iv) for MIEC electrodes, depending on the structure and material properties of the cathode.

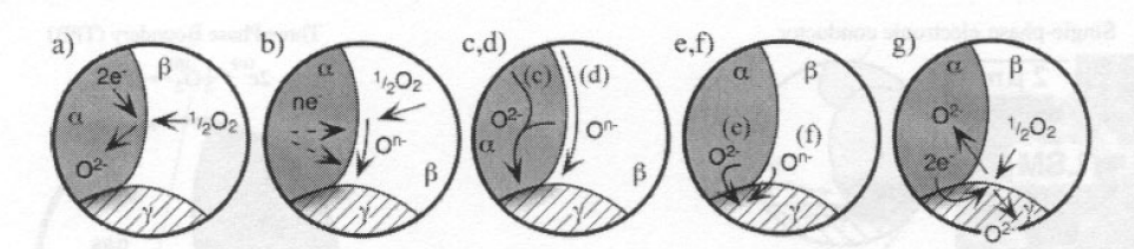

Figure 2.11. Some mechanisms thought to govern oxygen reduction in SOFC cathodes. Phases α, β, and γ refer to the electronic phase, gas phase, and ionic phase, respectively: (a) Incorporation of oxygen into the bulk of the electronic phase (if mixed conducting); (b) adsorption and/or partial reduction of oxygen on the surface of the electronic phase; (c) bulk or (d) surface transport of O^{2-} or O^{n-}, respectively, to the α/γ interface; (e) electrochemical charge transfer of O^{2-} or (f) combinations of O^{n-} and e^-, respectively, across the α/γ interface, and (g) rates of one or more of these mechanisms wherein the electrolyte itself is active for generation and transport of electroactive oxygen species. Copied from Adler.[124]

2.6.2.2 Fuel Oxidation at the Anode

The possible reaction pathways for the oxidation of fuel at the anode are summarized below. Once again, it is important to emphasize that these represent only a generic sequence of plausible reaction steps, and have not been proven with a degree of certainty.[137]

i) adsorption of H_2 on the surface of YSZ or Ni

ii) surface diffusion of adsorbed H_2 to the TPB

iii) electrochemical charge transfer reaction at the TPB

The main difference between the anode and cathode reaction pathways is that Ni can not conduct oxygen anions, so the reaction is restricted to the TPB (although the reaction area can be considered to include the surface area near the TPB where surface adsorption and diffusion occurs).

2.6.3 Experimental Studies of Reaction Kinetics

Both the anode and cathode reaction pathways are complicated and difficult to explain. A large effort has been conducted to experimentally ascertain which reaction step(s) is (are) rate limiting. The difficulty in this goal is that reaction pathways are often occurring in parallel and are co-limiting, and that the morphology of the microstructure can dictate which step will be dominant, such that electrodes can express different electrochemical behavior despite using the same materials and processing variables. A summary of the experimental studies of electrode reaction kinetics is provided below.

2.6.3.1 Oxygen Reduction on MIEC Cathodes

Most of the experimental work on MIEC electrodes has focused on strontium doped lanthanum cobaltites.[138] From this work a number of conclusions have been made regarding the nature of the electrochemical reactions on MIEC electrodes.[124] Firstly, MIEC materials allow for bulk transport of oxygen reduced on the surface, effectively extending further from the electrolyte the surface area on which reduction can occur and expanding the active area of the

electrolyte from just the TPB sites to include the electrode/electrolyte interface. Secondly, when there is significant bulk transport, a measurable capacitance occurs that is attributable to reactive intermediates that can reside in both the surface and bulk reactions. Thirdly, MIEC electrodes are co-limited by transport and molecular dissociation. This balance is struck by extending the limit at which the electrode is active further from or closer to the electrolyte interface. This variable δ represents the characteristic distance related to solid-state diffusion and oxygen surface exchange, and is interpreted as the distance the reaction zone extends beyond the TPB. Figure 2.12 shows a qualitative schematic diagram of the influence of δ and how it depends on the relative rate of bulk diffusion.[96] In case (a.) the cathode is limited by surface exchange, while in case (b.) it is limited by bulk diffusion. The value for δ can be anywhere from .4 to 20μm, depending on the structure and testing conditions, but usually is between 3-5μm.[124] Fourthly, the overall cathode polarization is sensitive to the electrode/electrolyte interface and the materials selected.[139] Lastly, while it has been established that bulk transport plays an important role in MIEC polarization, the level to which it contributes has only been evaluated in extreme cases where it is the dominant path (manipulated either by unique patterned structures or through high bulk diffusivity materials). Understanding the role of bulk transport in regular porous electrode structures remains a key. In conclusion, it is clear that the microstructural characteristics of electrode-electrolyte interfacial area, electrode surface area, and solid-phase tortuosity all play a large role in MIEC electrode performance and determining the limiting electrochemical reaction pathways.

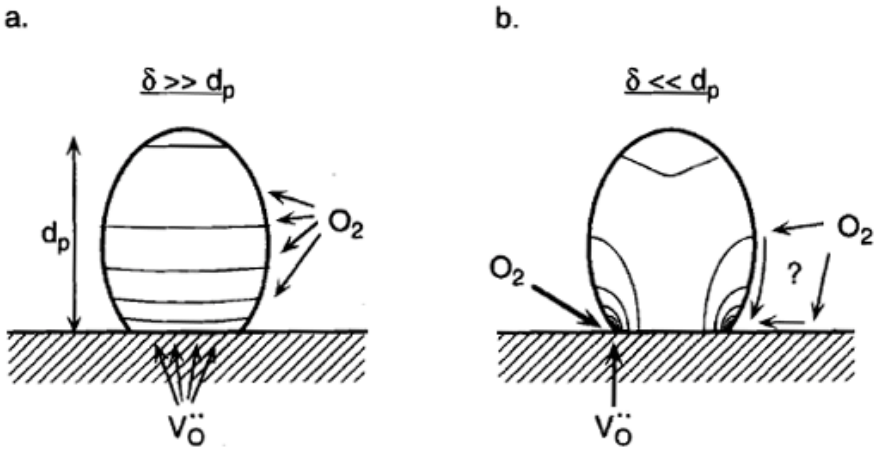

Figure 2.12. Qualitative sketch of the expected vacancy concentration profile in a mixed conducting electrode particle in contact with the electrolyte as a function of the penetration depth, δ. (a.) When δ is much larger than the average particle size, the reaction occurs over the entire particle. (b.) At small δ, the reaction is restricted to the three-phase boundary, where other more localized or concerted processes (marked as "?") may dominate. Copied from Adler et al.[96]

2.6.3.2 Oxygen Reduction on LSM-Based Cathodes

There has been little consensus regarding the electrochemical reduction of oxygen in LSM and LSM-YSZ composite electrodes and measurements done with electrochemical impedance spectroscopy (EIS) have shown inconsistent results. This is mostly a function of the complexity of the structures involved and the reaction mechanism itself. For example, if the limiting pathway is determined to be surface related, then the subsequent surface structure of the electrode being tested becomes important. The same is true with reactions at the triple-phase

boundary, or bulk processes. Because most of the work conducted does not measure these microstructural features, it is expected that there would be difficulty in discerning what reaction steps are associated with specific EIS arcs and what resistivity is associated with each step. Despite this, a large amount of work has focused on the electrochemical reaction mechanisms in composite LSM-YSZ electrodes.[98, 99, 103, 118, 140-145] A summary of the processes found to affect the impedance of LSM-YSZ composite cathodes is provided in Table 2.5, where the numbered references are those listed in Jorgensen and Mogensen (2001).[143] This table highlights the wide range of impedance responses observed that depend on temperature and oxygen partial pressure and can only be associated with certain physical and electrochemical characteristics without much conclusion.

Table 2.5. Overview of the processes found to affect the impedance of LSM/YSZ composite cathodes. Table is taken from Jorgensen and Mogensen and numbered references of data found in literature refer to those listed in their paper.[143] f_{max} = summit frequency, T_s = sintering temperature, T_m = measurement temperature, E_a = activiation energy, and LCM = $(La,Ca)MnO_3$.

Arc	f_{max} (Hz)	E_a (eV)	x in $(p_{O_2}^{-x})$	Characteristics	Process
A	~ 10^4 (this work) ~ 5×10^3 [27]	1[27]	0[27]	These arcs depend strongly on microstructure. The two arcs may have similar f_{max} and are therefore not always separable. Increases with increasing composite thickness.[9]	Transport/transfer of oxygen intermediates/oxide ions between LSM and YSZ and through the YSZ of the composite.
B	10^2-5 $\times$ 10^3 (this work)				
C	$f_{max} = f(T_s, T_m)$, $0.1 < f_{max} < 10^4$	2[9]	0.5[15,51] (LCM)	Summit frequency decreases with increasing sintering temperature (Fig. 7).	Reflects competitive elementary processes in the overall oxygen reaction mechanism. The processes are assumed to be dissociative adsorption, transfer of species at TPB and surface diffusion.
	Example (this work): T_s = 1300°C T_m = 1000°C 5 < f_{max} < 30 T_m = 850°C 0.5 < f_{max} < 20	1.8-1.9[15] 1.5-1.6[27]	0.3[8] 0.14-0.3[27]	The magnitude of this arc is strongly related to the length of TPB and decreases with increasing composite thickness[9] Magnitude changes with current passage (activation) (Fig. 8), assumed to be related to segregates at the TPB.	
D	5-10 (this work), 2[27] 1.4[51] (LCM), 5[52]	0 (this work)	0.6-0.8[27] 1[51,52] (LCM)	Magnitude increases with increasing cathodic overvoltage (Fig. 9). Independent of measurement temperature (Fig. 6). Most pronounced for electrodes with high $f_{max,C}$ (*eg.* electrodes sintered at 1100°C or below).	Gas diffusion in a stagnant gas layer above the electrode structure.
E	~0.03-0.4 (this work)	-	-	Inductive are, possibly related to electrode activation. More than one process may be present.	Assumed to be related to segregates at the TPB

The easiest remedy to the lack of quantification of composite microstructure is to use patterned electrodes that have a defined structure. This allows for the isolation and quantification of specific structural features such as TPB density, LSM surface area, and LSM-electrolyte interfacial area. A number of studies have focused on these patterned electrodes, usually prepared by pulsed laser deposition and photolithography.[146-151] Generally, these results have shown that the dominant mechanism depends on the temperature, oxygen partial pressure, and applied overpotential. Radhakrishnan et al. showed an inverse linear relationship between the charge-transfer resistance and the TPB length, calculating a charge-transfer resistivity of 1.26×10^5 Ωcm at 800°C and in air. Two studies using microelectrodes have also shown that current constriction in the electrolyte at the TPB also adds a resistance to the electrode.[152, 153] One limitation to these microelectrode studies is that they artificially reduce the bulk path length, so it has been observed at intermediate to high temperatures that bulk diffusion is the dominant pathway, a result that is hard to compare with normal composite structures.[146, 147]

From this range of work a number of broad conclusions can be made regarding oxygen reduction on LSM. Firstly, at low overpotential the reduction is mediated by a surface mechanism. This makes sense in that the oxygen is fully stoichiometric at low overpotential and hence displays poor bulk diffusion. Much like the Ni-YSZ composite system, the LSM-YSZ electrode in this case is expected to be limited by the steps (ii) and (iv) as listed in section 2.6.1.1. However, the range of this surface reaction from the TPB remains undetermined, although studies have shown in certain conditions that it is less than 1 μm.[98, 154] As a result, the subsequent polarization dependence on the TPB density is a function of the microstructure and the LSM grain size. Secondly, at high overpotentials the LSM becomes reduced enough to

elicit bulk diffusion behavior. The level to which this contributes to the overall polarization has not been quantified. Lastly, observations of irreversible behavior, the sensitivity of LSM to processing and operating history, and the impact of impurities and the formation of insulating phases at the solid-solid interfaces emphasize the extreme difficulty in determining a clear understanding of oxygen reduction on LSM. Additionally, while the use of patterned electrodes allows for the isolation of specific structural variables, the comparison of results with composite electrodes with substantially more complicated structures remains suspect.

2.6.3.3 Fuel Oxidation on Ni-Based Anodes

In many ways the steps of the anode fuel oxidation reaction are similar to that of the cathode, and much of the research is conducted in a similar manner through the use of EIS and patterned electrodes. However, with respect to Ni as the catalyst, it is expected that studies will be less convoluted due to the lack of a bulk transport pathway. As a result, the surface and TPB structure play an especially important role in elucidating the exact mechanisms involved.

An incredible amount of research has been conducted attempting to define the exact electrochemical pathway of the oxidation of hydrogen in Ni-YSZ systems.[155-161] The importance of these studies is that if a rate-limiting mechanism can be identified, its dependence on the electrode structure can be determined and resulting optimized structures can be manufactured. Unfortunately there has been little agreement on the reaction pathways and kinetics and a number of mechanistic theories have been presented that identify the rate-limiting steps as charge-transfer [155, 160, 162, 163], surface diffusion [155, 164, 165], adsorption and desorption [165, 166], and sintering reactions and impurities [75, 160, 167], among others.

Figure 2.13 shows two different mechanistic pathways that have been proposed.[168] In case (a), supported by work of Holtappels et al. [163] and Mogensen et al. [165], interstitial hydrogen in Ni and surface hydroxyl formation play an important role. In case (b), supported by work of Jiang et al. [155, 169], all the reactions are confined to the surfaces of Ni and YSZ. In either case, the reaction kinetics are restricted to where the gas, Ni, and YSZ phases meet at the TPB, which emphasizes the importance of optimizing the TPB density in Ni-YSZ anodes.

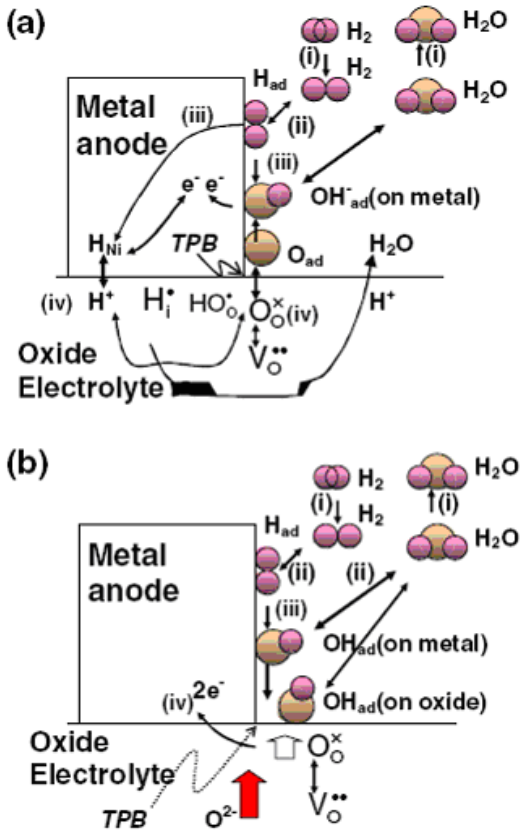

Figure 2.13. Schematic diagram of possible reaction processes for H_2 oxidation around the H_2-H_2O/anode/electrolyte interfaces. (a) Proposed by Holtappels et al. [163] and Mogensen et al.[165] (b) Proposed by Jiang et al.[155, 169] Figure copied from Horita et al.[168]

It is unrealistic to expect a unified reaction mechanism, as the current and potential distribution within 3D porous structures and the available reaction area depend on the complicated, often unrepeatable microstructure. As with the LSM-YSZ cathode system, co-limitation between different mechanisms is likely, as the electrode will adjust to reach equilibrium between these mechanisms by extending or shortening the active thickness. Studies have shown that this active thickness is on the order of approximately 10 microns, although it is obvious that this depends on the testing conditions and the microstructure.[22, 160]

Work on Ni-patterned anodes has also been conducted to analyze the relationship between TPB length and electrochemical performance.[164, 166, 167, 170, 171] Time-dependent resistive components were analyzed with EIS, but identifying which reaction mechanisms they corresponded to remained difficult. As was the theme with the cermet structures, data from different groups is scattered due to different designs and testing systems. Figure 2.14 shows a plot of the various TPB line-specific resistances (LSR) found in literature which differ as much as two orders of magnitude at comparative temperatures. Bieberle et al., who used the largest range of TPB lengths, found that the relationship between TPB length and the overall electrode polarization was described by

$$R_p = \frac{\beta}{l_{tpb}^{\ \alpha}} \tag{2.22}$$

where $\alpha = 0.80 \pm 0.04$ and $\beta = 336.5 \pm 86.7\ \Omega m$ at OCV (it is dependent on the overpotential).[170] It is interesting to note that they achieved a non-linear result for α, when it is generally assumed to be a linear relationship as shown in equation 2.21. This suggests that there is perhaps a

mechanism that does not depend on the TPB that is playing a role in the polarization of these patterned electrodes. The linear specific resistance for the Ni-YSZ-H_2 system is then ≈ 3.4 x 10^4 Ωcm at 700°C, compared to the reported values of the LSM-YSZ-air system of ≈ 1.2 x 10^5 Ωcm at 800°C, which corroborates the higher electrochemical catalytic activity that is seen in anodes and thus higher resistances in cathodes in general. As with the cathode patterned electrodes, it is important to note that due to the flat-plate Ni-pattern design, microstructural effects were eliminated, and so direct comparison with Ni-YSZ cermet anodes is arguably void.

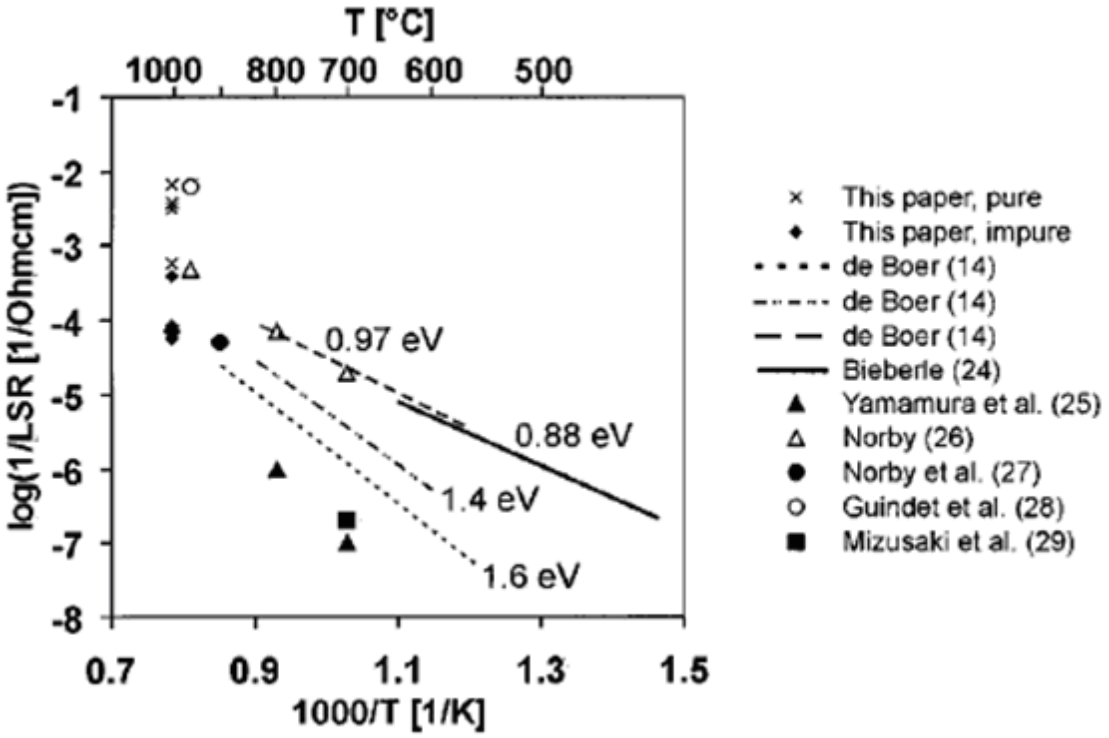

Figure 2.14. Summary of R_{tpb} (LSR) data from literature for Ni-YSZ showing the large range of experimental values. Numbered references are those found in Hansen et al. Figure copied from Hansen et al.[167]

2.6.4 Experimental Studies of SOFC Electrode Microstructure

As has been emphasized in previous sections of this thesis, the microstructure, as described in three dimensions, plays a vital role in understanding the relationship between processing and performance. Quantitative analysis of microstructural features pertinent to electrochemical reaction mechanisms such as the surface area densities, the tortuosity and connectivity of each phase, and the TPB density, which manifest themselves in three-dimensions, remains a key area of research on which future studies must focus. This is especially important for composite electrodes whose complex structure extends beyond the plane of the electrolyte interface. Despite this significance, only a few studies have attempted to quantify the three-dimensional microstructure. This is due to the fact that, until recently, methods of microscopy that provide the ability to image in three-dimensions at high resolution and with sufficient compositional contrast have not existed. The following represent the few efforts that have analyzed SOFC electrode microstructure in detail.

2.6.4.1 Interfacial Studies

The simplest of these, which only evaluate the two-dimensional structure of the electrode/electrolyte interface, consist of studies focusing on single-phase electrodes. In these cases, the electrode is removed from the electrolyte and the fingerprint of the electrode contact area on the electrolyte is subsequently identified. From this, the contact area and TPB length on the surface can be extracted. This has been done a few times for LSM electrodes.[123, 140, 154] Another study with an electrode of Ca-doped lanthanum manganite used a cross-section of the electrode/electrolyte interface to estimate the contact area and TPB density.[135] These studies

do not go as far as to quantify the structure of the electrode itself, such as the surface area and phase connectivity.

Other studies of the interface have used focused ion beam (FIB) thinning and liftout to prepare TEM samples that subsequently analyzed the nanoscale microstructure. In each case the degradation of the electrode by formation of insulating phases at the solid-solid interfaces was analyzed at high resolution.[172, 173] While these studies do not fully quantify three-dimensional properties of the full electrode microstructure, they represent an important step in studying the specific structure at TPB sites and how this affects the reaction kinetics.

2.6.4.2 Stereological Methods

Stereology is a method of estimating the properties of something in three-dimensions from only information given in two-dimensions. Specifically, it allows for the estimation of volume percentages, surface areas, and TPB densities from single 2D micrographs. An analysis of the methods and accuracy of stereology is provided in section 3.5.

There have been a few studies that use stereology to analyze the three-dimensional structure of SOFC electrodes. Lee et al. in a series of papers used the line-intercept method of stereology to estimate the size and distribution, contiguity, and interfacial area of each phase in a Ni-YSZ composite anode.[63, 174, 175] They were able to identify each phase by combining three sets of images where in each case one phase was identifiable. They used an optical microscope to get Ni compositional contrast, an SEM to identify the epoxy-filled porosity, and again an SEM to identify the YSZ after etching away the Ni with acid. These were then combined to provide one segmented image – an image that has one uniform color assigned to

each phase. Overall the resolution of the image was fairly poor because of the use of an optical microscope, and there was some blurring at the phase boundaries.

Once the segmented image was obtained, the line intercept method was used to count contact points of grains, although it is unclear as to how boundaries between grains of the same material were identified. The contact point information was then combined with nearest neighbor particle packing theory equations extrapolated from a two-phase system to that of a three-phase system. Overall this method is fairly inaccurate and relies on a highly simplistic model that does not correspond to real anode structures. They were able to show that contiguity between phases was dependent on the volume % of that phase, which would be expected, but the contiguity values were given as a fraction of the nearest neighbors that were the same material, which can not be extrapolated to anything of physical meaning. Additionally, a further study where the porosity was filled with a highly conductive material and the conductivity was measured using EIS to determine the connectivity of the pore phase showed that the experimental connectivity was much less than that estimated from the image analysis method, emphasizing in their own study the inaccuracy of the method.[175]

Another study by Zhao et al. varied the composition of LSM-YSZ cathode interlayers between 25-60 weight % LSM and used stereology to calculate structural features.[176] A Cameca SX 50 electron microprobe was used to get color coded micrographs with clear contrast between the LSM, YSZ, and porosity. Using stereological techniques on single micrographs, they calculated volume fractions and TPB densities for each sample. The TPB density ranged from 1.8-6.5 x 10^3 cm^{-1}. This corresponds to a line density per area of electrode, and because the thicknesses of the electrode were not published, it is unclear what the subsequent TPB volume densities would be. Using the Tanner-Fung-Virkar (TFV) model described later in section

2.6.5.2, Zhao et al. back-calculated the linear charge transfer resistance for the LSM-YSZ-air TPB to be ≈ $1.0*10^5$ Ωcm at 800˚C, which agrees well with the value of 1.26×10^5 Ωcm estimated from patterned LSM cathodes.[146]

2.6.4.3 Full 3D Reconstructions

As discussed in further detail in section 2.7, a dual-beam FIB-SEM serial-sectioning technique, a new method of microscopy for creating a fully continuous 3D set of data, was developed and used by the author of this thesis to reconstruct the microstructure of SOFC anodes and cathodes. The work conducted is presented in this thesis, part of which has been published in peer-reviewed journals and in conference proceedings.[177-181]

During the period of time that the research in this thesis was being conducted, two papers known to the author were published that conducted a full 3D reconstruction of electrode microstructure. Gostovic et al. reconstructed a set of LSCF single-phase cathodes sintered at different temperatures using the FIB-SEM serial-sectioning method.[182] In addition to the volume percentages and surface areas, the tortuosity of the pore phase was calculated using a center of mass feature in the Amira 3D imaging software package. While this calculation does qualitatively describe the tortuosity, it does not correspond to the actual gas diffusion limitations associated with pore tortuosity. The volumes of LSCF analyzed were between 227-439 μm^3, which are questionably too small to obtain good statistics, depending on the feature size of the LSCF. The X-Y resolution taken with the SEM was 3 nm and the FIB slice resolution in the Z direction was 20 nm. Unfortunately there appeared to be substantial variation and error in the volume % calculation, which is the simplest calculation and is a direct function of the

segmentation of the SEM images. They report that the porosity increases with increasing sintering temperature, which is contradictory to the physics of sintering. They explain this by claiming large variations exist depending on what X-Y resolution is used. Although artifacts can be seen in surface area calculations from the use of non-cubic voxels (where the X-Y resolution does not match the Z resolution), the volume percentage should not be greatly affected by changes in resolution, as long as it does not approach the feature size. By decreasing the resolution by a factor of 2, it was reported that the porosity changed by as much as 6%, which should not occur. From the images collected it appears that the porosity was under-estimated during the segmentation process due to misidentification of solid material observed through pores that did not exist at the plane of interest, which could explain the large standard deviation seen in the calculations.

Izzo et al. also published a 3D reconstruction of a Ni-YSZ composite anode from a tubular SOFC using high-resolution (42.7 nm) x-ray tomography.[183] While they were unable to obtain contrast between the Ni and YSZ phases, they did reconstruct the entire pore structure. The tortuosity of the pores was calculated by solving Laplace's equation, and the results showed isotropic pore structure with values around 3. The Lattice-Boltzman Method (LBM) was implemented to model the mass transport within the pore phase, demonstrating an important step in using real microstructures to model electrode kinetics.

While this work represents an important step in the proliferation of the use of FIB-SEM and X-ray nanotomography, there clearly is much improvement that still needs to be made. Overall there is a large gap in SOFC research where 3D microstructural analysis exists, and it is the purpose of this thesis to serve as a starting point for the greater effort to fill this gap.

2.6.5 Modeling of Microstructure

The lack of an experimental method of measuring three-dimensional microstructure has lead to a wide array of modeling that analyzes both the processing-microstructure relationships and microstructure-performance relationships. These are summarized below.

2.6.5.1 Processing-Microstructure Relationships

Most structural models are based on the random packing of spherical particles. A geometric model of composite electrodes using this method was developed by Deng and Petric based on primary microstructural characteristics.[184] Solid grains were assumed to be the same size and particle packing was evaluated based on the degree of necking between grains. The TPB density was calculated as

$$L_{3pb} = \frac{72\alpha[D_p - (D_p + D_s)V_p]V_p}{D_s^2 D_p^2 (1-\sqrt{1-\alpha^2})} \tag{2.23}$$

where D_p and D_s are the pore and solid grain diameters, V_p is the vol% porosity, and αD_s is a measure of the neck contact diameter between solid grains, where $\alpha < 1$. Analysis of this equation concluded that a small solid grain size is ideal for maximizing the TPB line density. Pore size and vol% porosity prove a more complicated dependence, but in conclusion, a small pore size and higher porosity (30% is satisfactory) show the best TPB density. Sintering temperature experiments on LSM-YSZ found that lower sintering temperatures, which produced

lower density and smaller grains, showed improved performance, which is in agreement with the geometric modeling.[185]

Sunde determined separately, using a model based on coordination theory of the random packing of spherical particles,[186-188] that the TPB volume density is defined as follows[189, 190]

$$L_{tpb} = 2\pi r n n_{io} n_{el} \frac{Z_{io} Z_{el}}{Z} p_{io} p_{el} \sin\tfrac{\theta}{2} \tag{2.24}$$

where r is the radius of the smaller particle, θ is the contact angle between electronic and ionic particles, $n_{(io,el)}$ is the number of particles per unit volume (fraction ionic, electronic), $Z_{(io,el)}$ are the respective coordination numbers, and $p_{(io,el)}$ are the respective probabilities that the phase is contiguous with the current collector and electrolyte. While this model more accurately accounts for grain size differences between solid phases and particle connectivity, the Deng and Petric model is based more practically on controllable processing parameters instead of other 3D microstructural properties.

A model by Janardhanan et al. combines the two methods presented above, where particle coordination number theory is used in conjunction with the overlap of spheres, which in this case, opposed to Deng and Petric, allows for particles of different size. The resulting TPB volume density was given as

$$L_{TPB/V} = \frac{\varphi(1-\varphi)(1+M) Z_{i-e} 2\pi a}{(4/3)\pi(r_1^3 + M r_2^3) - (1-\psi)(1+M) V_1} \tag{2.25}$$

where φ is the porosity fraction, M is the product of the ratios of volume fraction and particle radii of the two phases (equal to the ratio between the number of particles of each), r_x is the radius for phase x, $Z_{i\text{-}e}$ is the coordination number between the ionic and electronic phases, ψ is the fractional overlap of particles, V_1 is the average volume loss from the overlap, and a is the radius of the circle of overlap between particles.

These types of models are quite powerful in their descriptions of solid-solid interactions in composite structures, however they tend to neglect the structure and effect of porosity, and the resulting connectivity information they give does not match well with real structures. Many of them are based on the probability that a particle is part of a contiguous phase, given by

$$p_i = \left\{1 - \left[(4.236 - Z_{i-i})/2.472\right]^{2.5}\right\}^{0.4} \tag{2.26}$$

where $Z_{i\text{-}i}$ is the coordination number between two like particles.[187, 191] Zhu et al. use this percolation theory to describe their own TPB volume density given by

$$L_{TPB/V} = 2\pi r_c n^* n_{el} n_{io} p_{el} p_{io} Z_{el} Z_{io} / Z \tag{2.27}$$

where r_c is the overlap neck radius, n_x is the number fraction of particles of type x, Z_x is the average coordination number for phase x, and n* is given by

$$n^* = (1-\varepsilon)/\left\{\tfrac{4}{3}\pi r_{el}^3\left[n_{el} + (1-n_{el})P^3\right]\right\} \tag{2.28}$$

where ε is the porosity.

Unfortunately, despite the fact that each of the Zhu et al. and Janardhanan et al. models are based on the same particle packing premise, their predictions of the TPB density often give contradictory information. An example of this is provided in Figure 2.15, where the TPB density as a function of the volume fraction of ionic conductor is given for a number of particle size ratios. For ratios of electronic to ionic particle radii of greater than one, Zhu et al. predicts a shift in the TPB maximum towards an electronic-phase rich composition, while Janardhanan et al. shows a shift of the TPB maximum towards an ionic-phase rich composition. This highlights the difficulty faced in trying to predict the microstructure of real electrodes from simplified models such as those presented above, where there is still difficulty in obtaining agreement.

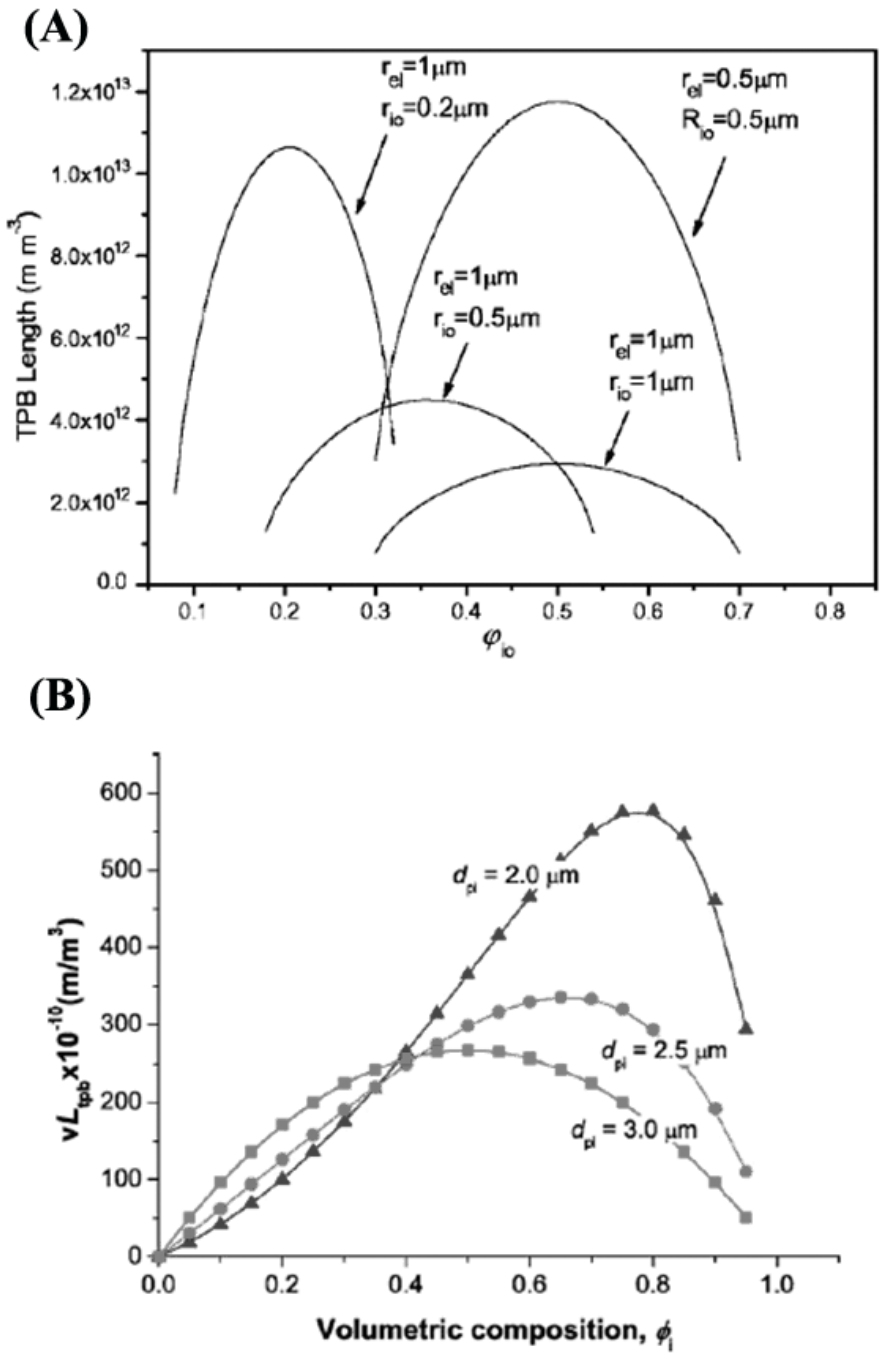

Figure 2.15. TPB density as a function of YSZ composition from structural models by **(A)** Zhu et al.[191] and **(B)** Janardhanan et al.[192]

2.6.5.2 Microstructure-Performance Relationships

There are three main types of models of electrochemical performance in SOFC electrodes. Each type represents a different level of structural and electrochemical analysis as illustrated in Figure 2.16.[193] For the most basic level (Figure 2.16A), the electrode is treated as a homogeneous continuum, where structural characteristics are taken by their macroscopic averages and electronic and ionic flows through the electrode are treated as contiguous and increasing and decreasing, respectively, as they move away from the electrolyte through the electroactive layer. Many examples of this model have been implemented, including both composite and MIEC electrodes.[96, 138, 194-196] The next level of analysis, as illustrated in Figure 2.16B, uses the random packing of spheres, also known as the Monte Carlo model, to simulate electrode polarizations by effectively treating each electronic and ionic particle as a resistive element existing within a series of percolated pathways.[197-207] In these models gas transport is ignored and the electrochemical reaction occurs at active three-phase boundaries. This type of model is very popular because it can implement specific microstructural features as discussed in the previous section. Lastly, as illustrated in Figure 2.16C, finite element modeling (FEM), finite difference calculations, or discrete boundary value equations are solved to calculate current density or chemical potential distributions within defined microscale structures in order to measure electrode polarizations (also known as Thin Film models).[72, 134, 136, 208-211] For further discussion and summary, the reader is directed towards a number of reviews that have been published on the subject.[189, 193, 212] An example of each of these types of models is provided below.

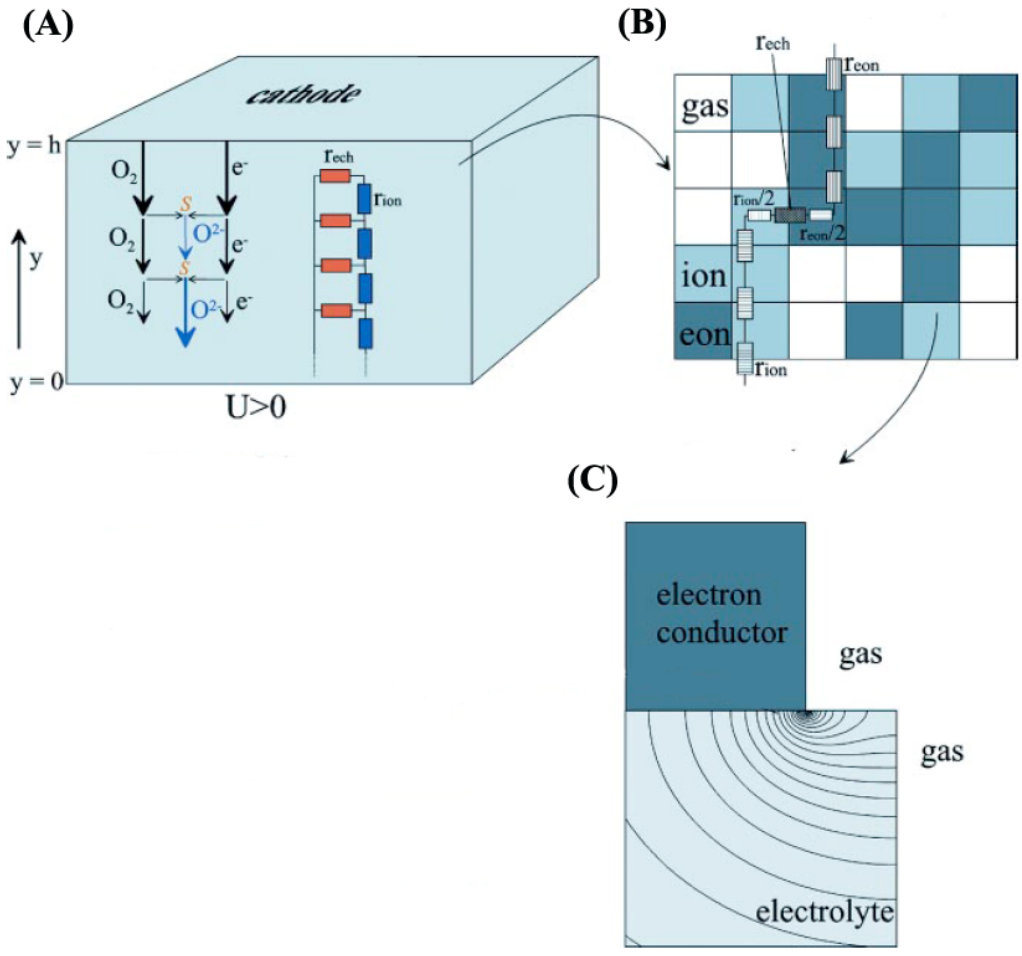

Figure 2.16. Sketch illustrating the three levels used in SOFC cathode simulations. **(A)** The electrode is treated as a homogeneous continuum and transport is modeled as one-dimensional differential equations. **(B)** The electrode is treated as a random array of particles that each correspond to a resistive element in a percolated pathway. **(C)** The current density or chemical potential distributions are calculated within a defined microscale structure in order to measure electrode polarization. Figure copied and modified from Fleig.[193]

Extensive impedance studies of single-phase MIEC cathodes have been conducted by Adler who, along with Lane and Steele, developed the ALS model for oxygen reduction.[96] In conjunction with porous electrode theory, the model describes the electrode as a super-position of two continua, which can be described by bulk statistics, reducing the solution to a system of one-dimensional differential equations, as displayed in Figure 2.17. The state equations are based on one variable, the vacancy concentration. Agreement of experimental impedance with their model suggests that the cathode kinetics are dominated by solid-state diffusion and surface exchange. Electrode kinetics improve with increasing vacancy concentration and diffusivity, surface area, and connectivity, as long as there is sufficient ionic conductivity. Hence, microstructure plays an important role in the overall reaction rate.

Chen et al. developed a model based on the random packing of spheres of two different materials. The rate limiting steps were assumed to be only surface diffusion and oxygen ion transfer into YSZ at the TPB. The model also assumed that interfacial reactions and concentration polarizations were negligible. An illustration of the setup of the model is provided in Figure 2.18. The effective resistivity of each phase as a function of the microstructure was determined to be

$$\rho^{eff} = \frac{\rho^{o}}{(1-\varepsilon)\phi p} \tag{2.29}$$

where ρ° is the resistivity of the pure material, ε is the porosity, Φ is the volume fraction, and p is the probability that the particle is contiguous with the electrolyte and current collector, which can be calculated from the respective correlation numbers.[190] It was found, in analogy to Ni-YSZ

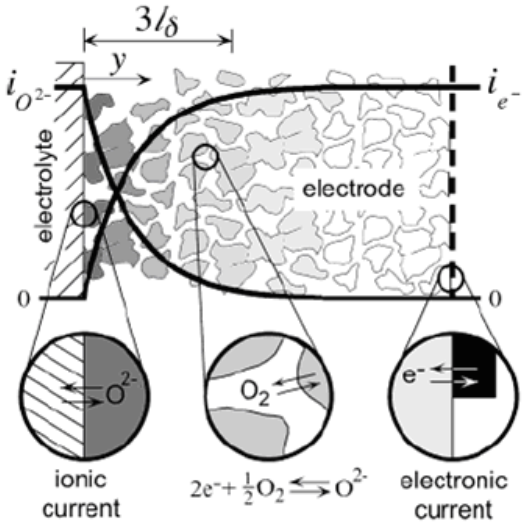

Figure 2.17. Macrohomogeneous model of porous mixed conducting electrodes. Oxygen reduction occurs within the porous electrode where electronic current is converted to ionic current. l_δ is the distance within which most of the oxidation reaction occurs. Figure copied from Adler.[124]

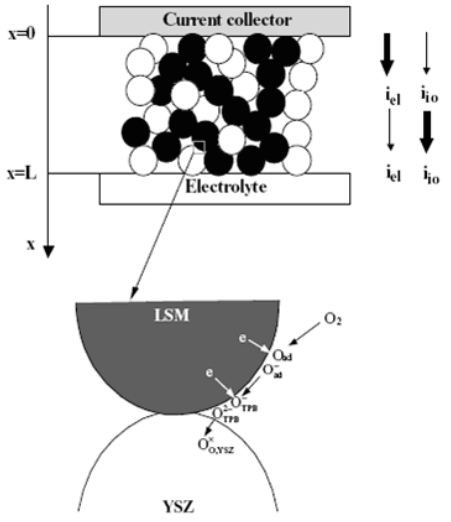

Figure 2.18. A schematic diagram of an LSM/YSZ composite cathode showing the random array of ionic and electronic particles and the assumed electrochemical reaction processes at the three-phase boundary. Figure copied from Chen et al.[190]

studies [53, 66], that smaller particle size increased TPB density and correspondingly cell performance, and that the larger the YSZ/LSM particle size ratio, the higher the content of YSZ was necessary for optimum resistivity. Results were consistent with the trends shown in Figures 2.21 & 2.22 calculated using the Tanner-Fung-Virkar thin film model discussed in the next section. The Chen et al. model also showed that the minimum polarization resistance does not occur at the volume fraction with maximum TPB density. Figure 2.19 shows both the TPB density and the polarization resistance for three different particle size combinations, showing that the minimum polarization in each case occurs at a higher YSZ content than where the maximum TPB density occurs, suggesting that the electrode is partially limited by oxygen ion diffusion within the YSZ.

Tanner, Fung, and Virkar developed a model (TFV) of composite electrodes where the structure of the electrode was mimicked by extending the electrolyte phase into the electrode through a series of uniform columns. Additionally, the catalytically active electronic particles which would be distributed on the surface of the electrolyte columns are assumed to be equivalent to a continuous thin charge-transfer layer. This set-up is illustrated in Figure 2.20. In this model, the one-dimensional (laterally averaged) chemical potential of oxygen vacancies, which was shown to be negligibly equivalent to the two-dimensional model, is calculated to determine the overall electrode polarization.

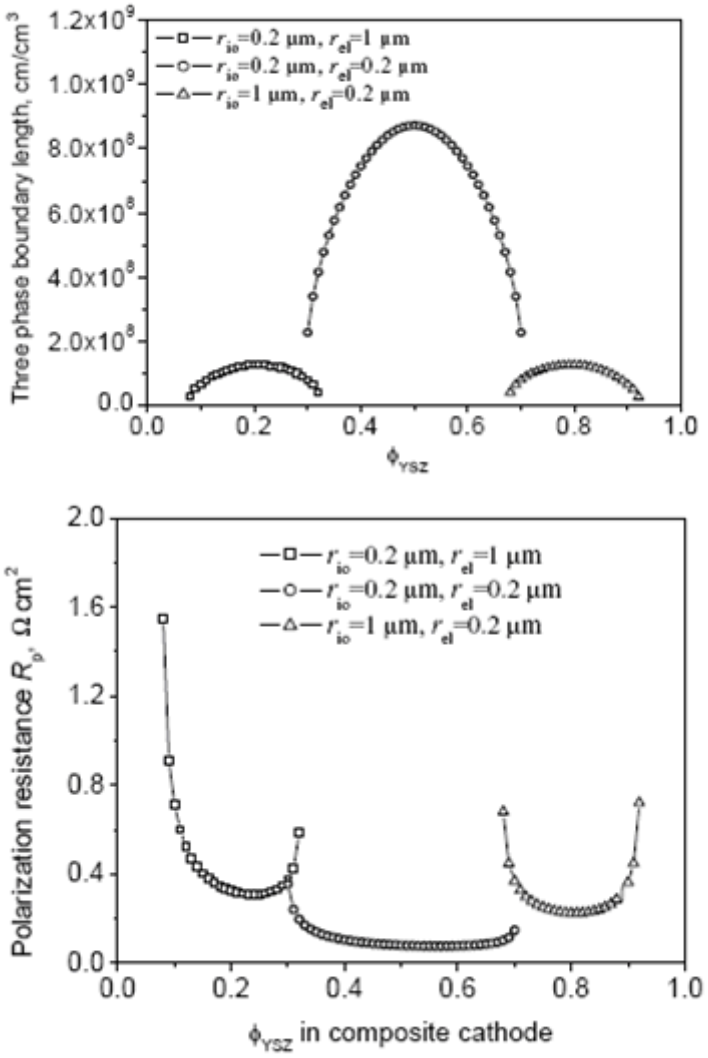

Figure 2.19. TPB density and polarization resistance as a function of YSZ volume percentage (solids only) from the Chen et al. model for three different particle size ratios. Figures copied and combined from Chen et al.[190]

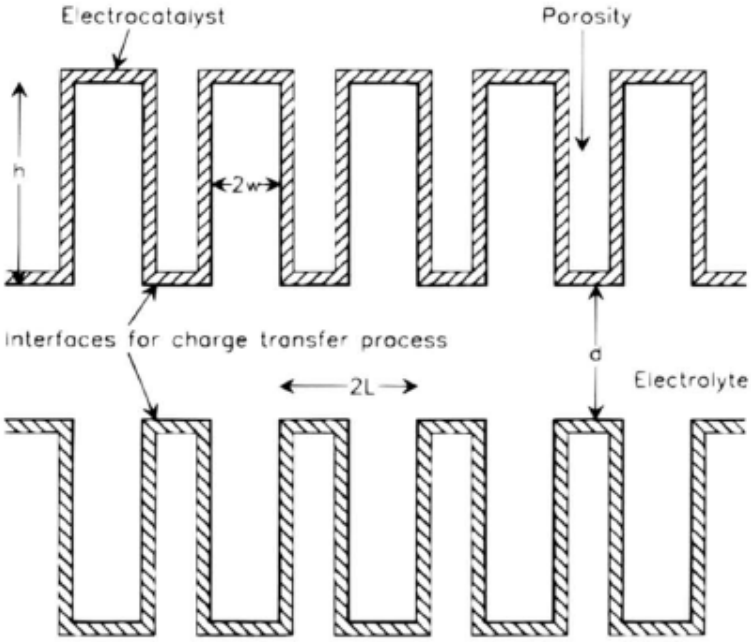

Figure 2.20. Schematic diagram of the TFV model electrode and the distribution of the electrochemical active area to the surface of the electrolyte. Figure copied from Tanner et al.[136]

Using the low current density limit established in equation (2.19), and assuming negligible concentration polarization, an expression for the effective charge transfer resistance (the resistance as a result of the two-phase structure where the electrolyte extends into the electrode) can be estimated as

$$R_{ct(eff)} \approx \sqrt{\frac{R_{ct} d \rho_i}{(1 - V_V)}} \tag{2.30}$$

where d is the grain size and ρ_i is the ionic resistivity of the ionic conductor respectively, R_{ct} is

the intrinsic surface charge transfer resistance, and V_v is the porosity.[136] This equation shows that decreasing the grain size, ionic resistivity, and porosity will serve to decrease the effective charge transfer resistance. It is also important to note that with standard values such as vol% 25, grain size 1 micron, ionic resistivity 50 Ωcm (~for YSZ), and charge transfer resistance ~2 Ωcm^2, the effective resistance is reduced by a factor of ~17 due to the two-phase structure.[14] Figure 2.21 shows the effect of electrode thickness on $R_{ct(eff)}$ for different values of R_{ct}. Figure 2.22 shows that finer microstructures result in lower effective resistances and allow for thinner electrodes.[136] The thickness of the electrode that is active, i.e. the distance from the interface that contributes to the overall reaction, is also estimated as[14]

$$\lambda \approx \sqrt{\frac{R_{ct} d (1 - V_v)}{\rho_i}} . \qquad (2.31)$$

Using the same values as above, a standard critical thickness is ~17 μm. Electrodes thicker than this will have the same activation polarization but will run the risk of developing an appreciable concentration polarization.

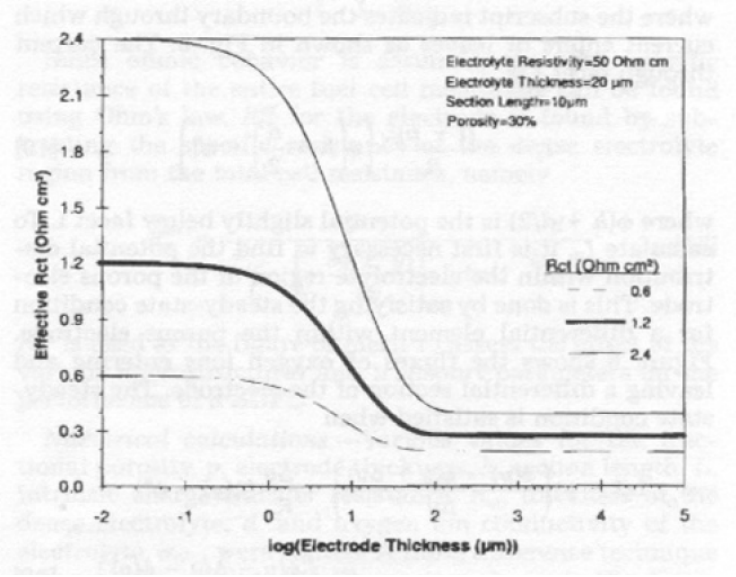

Figure 2.21. A plot of R_{ct}^{eff} as a function of electrode thickness from the TFV model. Figure copied from Tanner et al.[136]

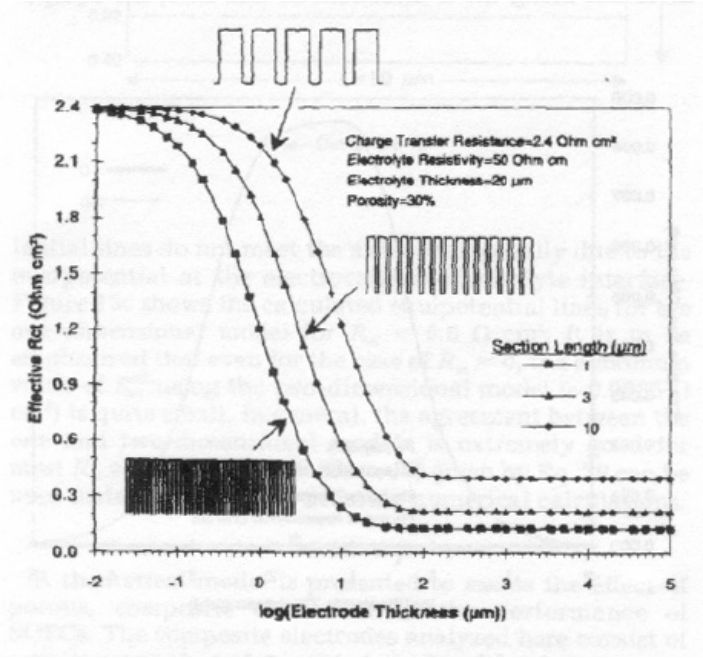

Figure 2.22. A plot of R_{ct}^{eff} as a function of electrode thickness for section lengths of 1, 3, and 10 µm as calculated from the TFV model. Figure copied from Tanner et al.[136]

Sunde reviewed the ability of the different model systems (thin-film, random packing/Monte Carlo, porous electrode) to account for a series of experimental observations. These experimentally observed phenomena are summarized below, taken directly from Sunde [189]:

I. an apparently completely disordered structure, made up of particles of the electrode and electrolyte material uniform in extension and mixed at random

II. a porosity often in the order of 30% (with some variations)

III. an abrupt increase in conductivity with volume fraction Φ of the electrode material at a certain critical fraction Φ_c

IV. a decrease in Φ_c with increasing ratio between electrolyte-particle radius a_{el} and electrode-particle radius a_{ed}

V. a more or less abrupt decrease in conductivity with coarsening of the electrode particles

VI. a relatively broad minimum in polarization resistance at intermediate Φ. For $a_{ed}/a_{el} = 1$ the minimum often occurs around $\Phi = 0.4\text{-}0.5$

VII. a (strong) dependence of the minimum polarization resistance of a_{ed}/a_{el}

VIII. an increase in Φ at which the polarization resistance is minimum with decreasing a_{el}/a_{ed}

IX. structure-dependent impedance spectra. Also, in some cases impedance spectra change shape as a function of temperature: the higher the temperature, the more features become apparent in the spectra

X. a marked thickness dependence of the polarization resistance at intermediate Φ; the larger the thickness the lower the polarization resistance, reaching an asymptotic limit at large thickness

XI. at high values of Φ, the polarization resistance is thickness-independent

The ability of each model to describe the experimental phenomena listed above is summarized in Figure 2.23.[189] While the Monte Carlo and porous electrode models were in agreement with most observations, none of the models could accurately predict the dependence of the minimum polarization as a function of particle size ratio. This emphasizes that much work is still needed in determining microstructural properties as a result of precursor particle size, as illustrated previously in section 2.6.5.1. In conclusion, while models can serve to describe a lot of observed electrode behavior, they are inherently based on simplified structures, and hence, are limited in their ability to mimic real electrode structures. The experimental reconstruction and insertion of real electrode structures into electrochemical models can prove invaluable in understanding the nanoscale reaction kinetics and the resulting macroscale electrode polarization.

Experimental observations	Thin film	Monte carlo	Porous electrode
I		√	√
II		√	√
III		√	√
IV		√	√
V		√	√
VI		√	√
VII			
VIII		√	√
IX		√	
X	√	√	√
XI	(√)	√	

Figure 2.23. Comparison of models of composite electrodes for SOFC. Theoretical predictions in agreement with experimental observations are indicated by a √ symbol. Copied from Sunde.[189]

2.7 3D Microscopy

Over the past decade great strides have been made in the field of 3D microscopy. Tomographic methods using a number of different instruments and techniques have developed for different size-scales and material systems.[213, 214] These techniques and their respective resolutions and volumes of reconstruction are provided in Figure 2.24.[215] As further advancements are made, it is expected that the resolutions of some of these techniques will continue to improve.

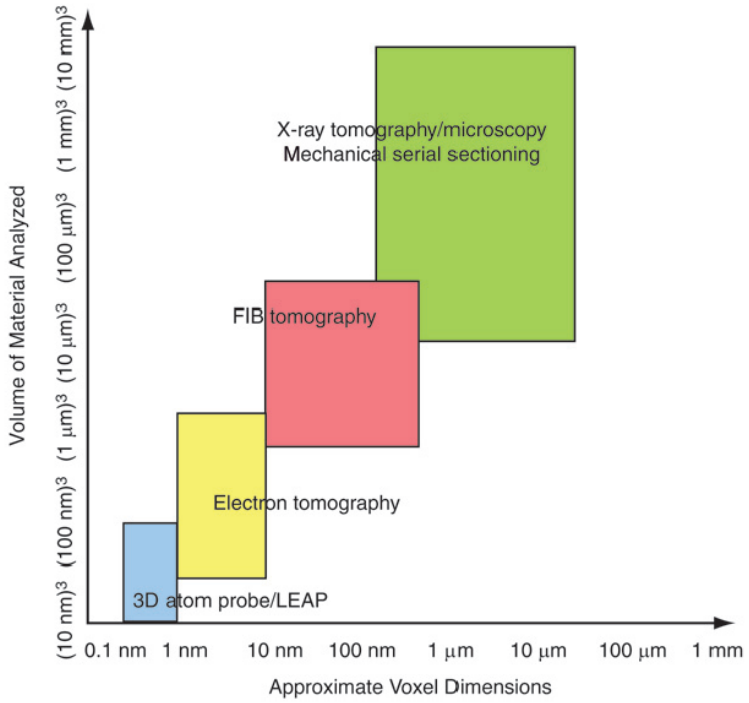

Figure 2.24. Graphical representation of the resolution and typical volume analyzed per experiment for modern tomographic characterization methods. The focused ion beam (FIB) and FIB-scanning electron microscopy (FIB-SEM) tomography experiments cover a critical length-scale gap and are ideally suited for 3D characterization of submicron- and micron-sized microstructural features. LEAP is local electrode atom probe tomography. Copied from Uchic et al.[215]

Mechanical serial sectioning is an established low-resolution destructive method for obtaining three-dimensional microstructural information. Much work has been done studying the coarsening of two-phase mixtures and the reader is directed towards a number of papers on this work and the general procedure.[216-219] X-ray tomography is a non-destructive low-resolution method for 3D analysis.[220] In this case, an x-ray beam is focused on the sample

which is rotated through a range of angles. The subsequent x-rays that transmit through the sample are collected as projected 2D images and the full reconstruction is achieved by combining all projections through the use of computerized software. Recent advancements in the technique have greatly improved the resolution down to less than 50nm in some cases, competitive with FIB serial-sectioning.[183, 221]

Electron tomography and atom probe methods both achieve nanometer resolution three-dimensional information. In electron tomography, a TEM sample is rotated through a single-axis tilt series and the direct back-projected bright-field images are reconstructed using software, much like that done with x-ray tomography. This method is limited in volume because a thin enough sample (hundreds of nm) is needed in order to get electron transmission. Different techniques for computing microstructures from electron tomography tilt-series images are summarized by Midgley and Weyland.[222]

Atom probes achieve even higher resolutions than electron tomography, as the approximate atomic-scale structure is achieved.[223, 224] In this method, the material being observed must first be prepared into a thin-tip geometry with a diameter usually on the order of 100 nm. A large electric field applied to the tip then induces field-evaporation of atoms. A detector records the position and time-of-flight of the atoms and the atomic structure of the original tip can subsequently be recreated.

FIB serial-sectioning is a new method rapidly developed over the past 5 years for obtaining micron- and submicron-resolution 3D reconstructions. Examples have been published of the use of this technique on alloys, ceramics, and semiconductors, among others.[225-229] The typical geometry of the FIB slicing and subsequent image collection is shown in Figure 2.25.[226] In this setup the ion beam is used to polish a face of material and successively mill

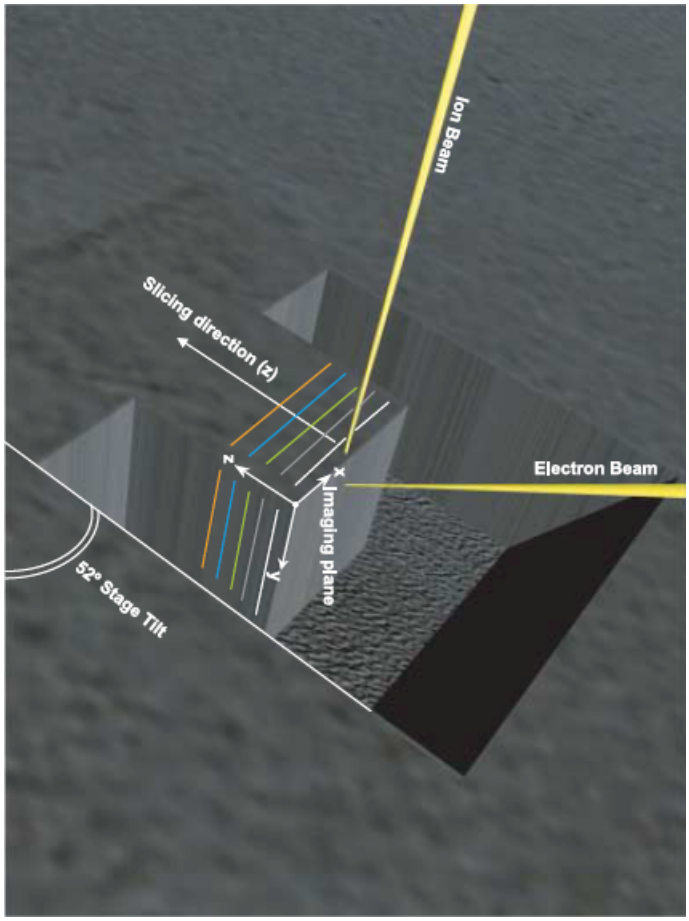

Figure 2.25. Schematic illustration of a sample cube and geometrical relationships of the imaging plane with electron and ion beams. Copied and modified from Holzer et al.[226]

away thin slices. Between each slice, an image of the face is collected, such that a series of images is collected over the volume of material that is removed. The type of image collected determines the complexity of the process. In single-beam FIB tomography, the sample is rotated and/or tilted between each slice in order to align the ion-beam normal to the face such that an ion image is collected. A dual-beam FIB-SEM is used to collect standard SEM images, a procedure that does not involve any movement of the sample between slices. A FIB-SEM can also be used with an electron backscatter detector (EBSD), often to resolve polycrystalline structures.[230, 231] In this case, the sample must be rotated between slices in order to align the face to the electron beam. EDS x-ray mapping is usually not used because of the low spatial and depth resolution and the time required for image collection. In all of these cases, any movement of the sample stage requires an in-situ realignment to ensure uniform slicing. The EBSD method requires longer collection times to obtain images, where the total collection time for a series of 100 images may take as long as 24 hours. This is compared to the 2-3 hours needed when using normal SEM imaging, depending on the ion beam current and image scanning parameters.

The resolutions achievable in FIB-SEM tomography are ideal for the micron and sub-micron scale of SOFC electrode microstructures. Figure 2.26 shows the tradeoff between the ion- and electron-beam resolutions and the volume of material analyzed, with respect to the feature size of the microstructure.[226] There are trade-offs, however, in that as the beam current is reduced, the time needed to mill away the material increases. In general, it is assumed that the resolution must be at least 10 times that of the feature size in order to achieve good microstructural representation of surface features. Holzer et al. shows that resolutions as low as 6 nm in the X-Y plane and 16 nm in the Z-plane (ion slicing) are achievable.

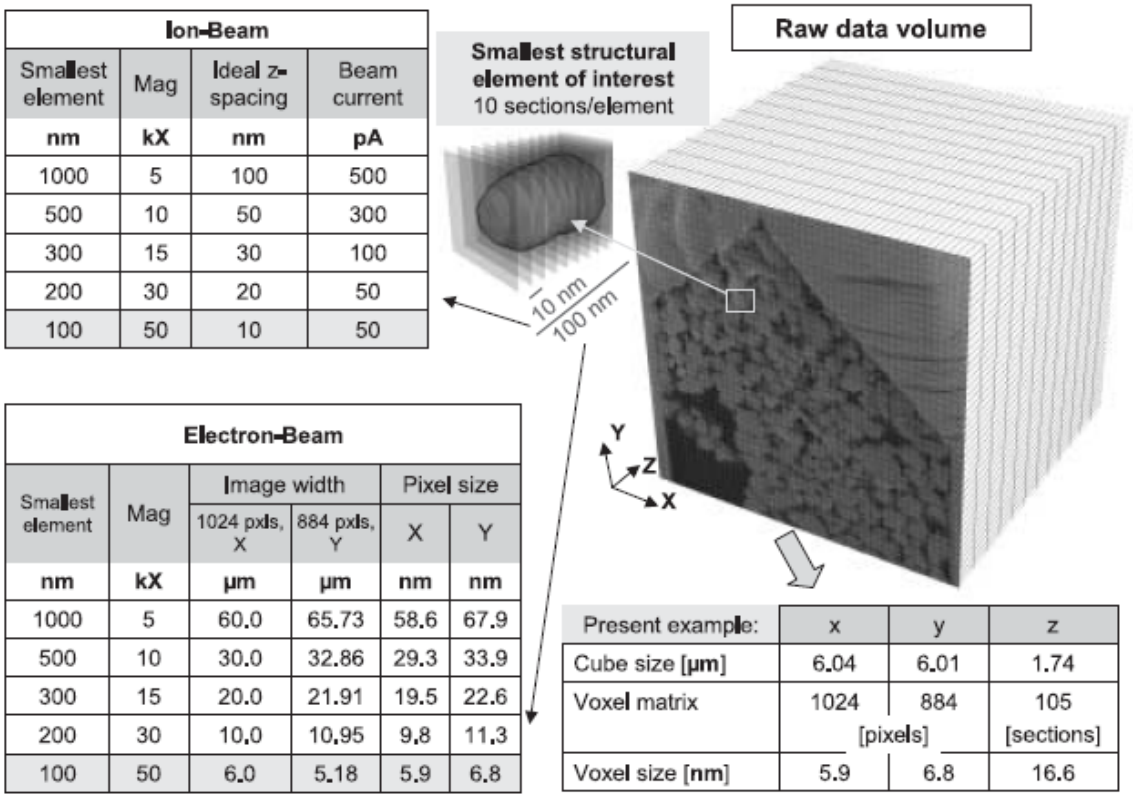

Figure 2.26. Empirical relationship between structural dimensions (i.e. fineness of microstructure) and the corresponding optimal settings for the ion and electron beams. The example highlighted in grey illustrates optimal settings for the 3D reconstruction of 100-nm-sized particles, which would require erosion of slices as thin as 10 nm. Voxel dimensions at the highest resolution that can be achieved at present are shown in the table at the bottom right. The voxel geometry in the raw data is distorted because the z-spacing (16.6 nm) is approximately three times larger than the corresponding pixel resolution (5.9 x 6.8 nm). Copied from Holzer et al.[226]

Vital to the accurate reconstruction of composite structures is the presence of a sufficient contrast mechanism in the imaging. This is the main reason for using the different detectors described above. For example, an EBSD detector is used when reconstructing grain structure. Fundamentally the methodology is the same regardless of the type of detector, with the exception of stage movement. In each case, achieving an image with sufficient contrast to identify desired phases is the ultimate goal.

While optical microscopy can achieve contrast between Ni and ceramics, the best resolution achievable is 200 nm, which is too low for typical microstructures, and combined FIB and optical microscopes do not exist. Thyden et al. have demonstrated a contrast mechanism for the Ni-YSZ anode composite with standard SEM detectors.[232] A field emission SEM is used because it allows for low accelerating voltage with sufficient signal intensity and resolution. They show that the backscatter coefficient is a function of the accelerating voltage when below 5kV, as illustrated in Figure 2.27.[232] They then use a lateral secondary electron (SE) detector to get enough signal of SE2 electrons which are a direct function of the backscatter coefficient. They also showed that use of an inlens detector to collect SE1 electrons, which are sensitive to positive charging in un-percolated Ni, gives contrast between percolated and un-percolated Ni, an additional piece of structural information that is vital to understanding the electrochemical activity of the anode. An illustration of the percolated-Ni contrast mechanism is shown in Figure 2.28, where the SE coefficient for un-percolated Ni must be less than 1 in order to have charge balance such that the emitted electrons equals the number of incident beam electrons.[232] Percolated Ni at those low accelerating voltages has an SE coefficient greater than 1. Work presented in this thesis and previously published has also shown that excellent contrast between Ni and YSZ can be achieved and enhanced by collecting SEM images during simultaneous FIB

milling, a feature that is only available on Zeiss dual-beam instruments that bypass the use of large magnetic fields near the sample.[177, 180] The details of this mechanism are discussed in section 3.2.3.

After a series of images are collected, large amounts of image processing and post-microscopy work are involved.[230, 231, 233] The details of this processing for the work conducted in this thesis are presented in section 3.3. The reconstructions achieved can be gleaned for any amount of macroscopic information, including particle size distributions, tortuosities, surface areas, TPB densities, etc.[180, 234] The reconstruction can also be used for finite element modeling, although an immense amount of image and data processing are needed to make this happen.[233]

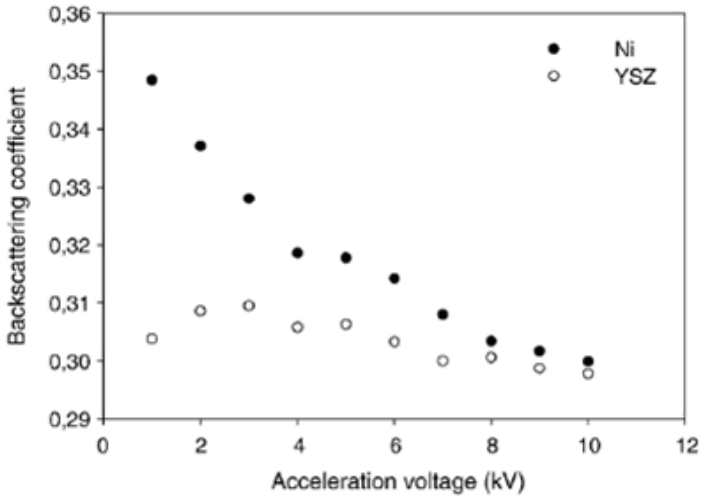

Figure 2.27. Illustration of the results from Monte Carlo calculations of backscatter coefficients for Ni and YSZ as a function of acceleration voltage. Copied from Thyden et al.[232]

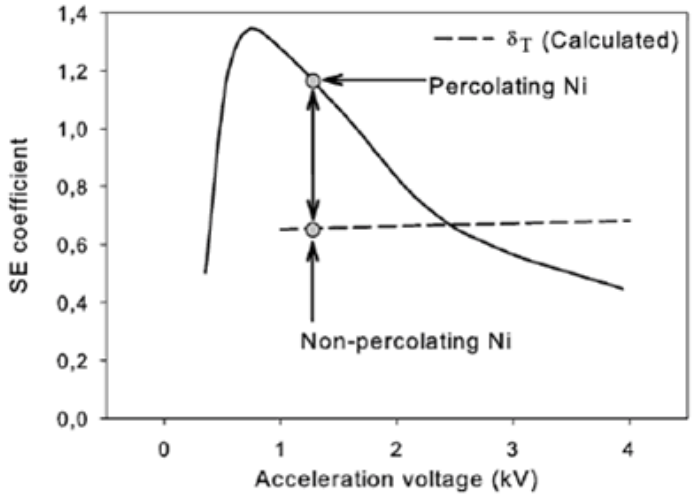

Figure 2.28. Secondary electron coefficient for Ni as a function of acceleration voltage. The schematic drawing illustrates the contrast mechanism for identifying percolated Ni particles. Copied from Thyden et al.[232]

CHAPTER THREE

FIB-SEM Serial-Sectioning Procedure

Chapter 3: FIB-SEM Serial-Sectioning Procedure

3.1 Introduction

The following represents a thorough synopsis of the methods and procedures involved in the fabrication, testing, reconstruction, and microstructural measurement of solid oxide fuel cell electrodes. A large amount of work has been conducted to ensure the reconstruction data is correct and errors are minimized, and a large amount of work goes into achieving these reconstructions.

3.2 Cell Fabrication

Each fuel cell studied in this thesis was fabricated using common powder processing techniques. Because each experiment involved different fuel cell designs, materials, and processing techniques, the reader is referred to the experimental procedure section of each chapter in order to reduce confusion.

3.3 Electrochemical Testing

The fuel cells in this thesis were electrochemically characterized using a Zahner IM6 electrochemical testing station. Impedance measurements were taken over a range of frequency between 100 mHz - 1 MHz at OCV. In each case two wires were attached to each electrode (4 wires total) such that the voltage and current response were measured on independent circuits. Collection of current versus voltage data (IV plots) was conducted in the same manner. For cells that had both an anode and cathode the cell was sealed to the end of a ceramic tube using silver

paste to isolate the two electrode gas environments. For symmetric cathode-electrolyte-cathode cells, the cell was simply placed in a furnace in air. The temperature during the testing was recorded by a thermocouple placed within a centimeter of the cell in the tube furnace. Gas flow was 50 sccm humidified hydrogen for anode testing, and ambient air for cathode testing, unless otherwise stated.

3.4 Microscopy

3.4.1 Procedure Overview

The first step in 3D microstructure reconstruction is to obtain volumetric information that can be interrogated to provide 3D information. The advent of dual-beam focused ion beam – scanning electron microscopy (FIB-SEM) has greatly facilitated this process by providing high-quality volumetric data. The configuration, illustrated schematically in Figure 3.1, allows simultaneous collection of a series of 2D cross-sectional SEM images as the specimen is sectioned by the FIB along the third axis. The fuel cell was first cut and polished, leaving a cross-sectional surface with the electrodes and electrolyte exposed. The focused ion beam (FIB) was then used to mill a rectangular trench into this surface in the vicinity of the electrode/electrolyte interface, as shown in Figure 3.1 for the case of a Ni-YSZ/YSZ interface. The electron beam was used to image one of the trench side walls at an angle of 36° from normal to the side wall. As the FIB "shaves" away material from this surface, tilt-corrected SEM images can be acquired, with scan- and frame-grab rates synchronized with milling rate for high quality imaging. In this manner, a series of 2D images can be obtained. A few typical 2D images from a Ni-YSZ anode are shown in Figure 3.2. The spacing between consecutive images, calculated

from the fixed FIB milling rate and the milling time per image, is usually 40-50 nm, depending on the sample and microstructure. The details of this entire procedure are provided below.

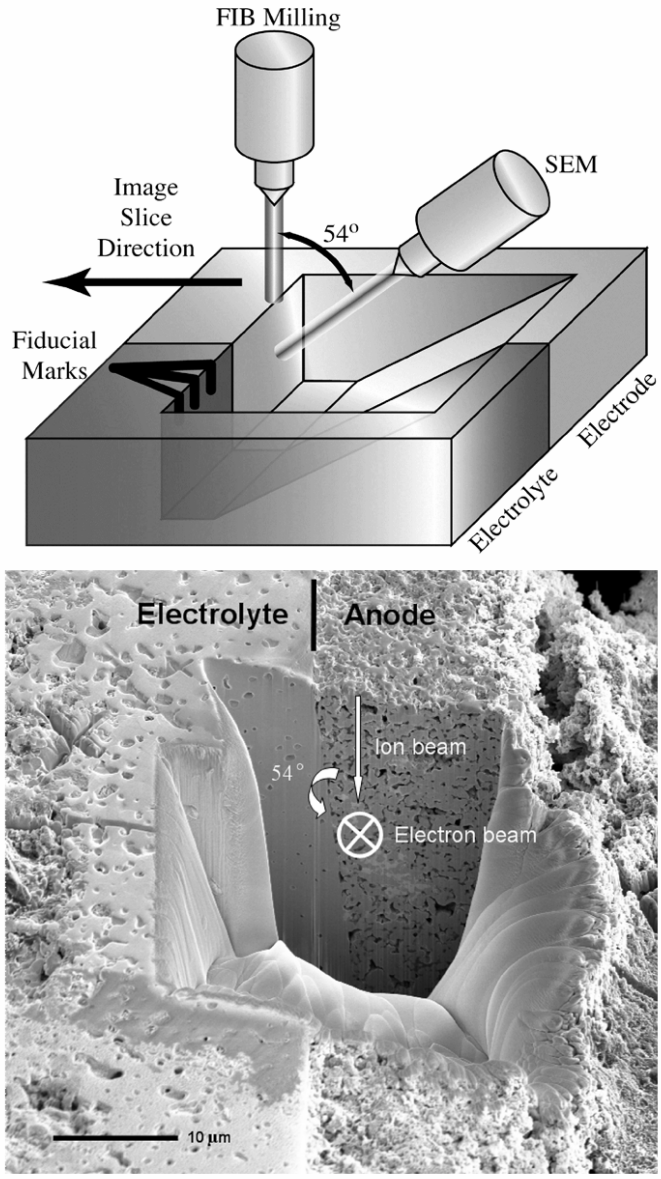

Figure 3.1. A schematic drawing showing the FIB-SEM geometry and a low magnification SEM image of a FIB-etched region at the anode/electrolyte interface of a SOFC.

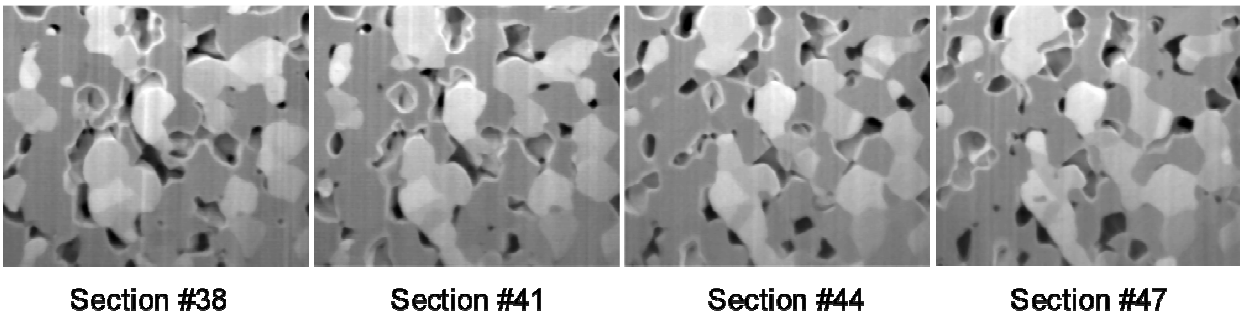

Figure 3.2. Four representative SEM image sections of a Ni-YSZ anode each separated by ≈130 nm, illustrating the change in the microstructure with depth along the milling direction.

3.4.2 FIB-SEM Instruments Used

Three different dual-beam FIB-SEM instruments were used throughout this thesis: a Zeiss 1540XB at Argonne National Laboratory, a Zeiss 1540ESB at University of California-Irvine, and an FEI Helios NanoLab at Northwestern University. The Zeiss instruments are designed with an angle of 54° between the ion and electron beams, while the FEI instrument is designed with an angle of 52°. The fundamental difference between the two types of instrument is in the electron beam lens design. Zeiss does not use a high magnetic field near the sample stage, enabling the instrument to have true simultaneous ion and electron beam use. This is a function of their patented electron column of which the details are unknown to the author. This simultaneous milling and imaging is vital to achieving excellent compositional contrast between Ni and YSZ, as discussed in section 3.2.3. The FEI instrument allows for simultaneous beam use in their "spy" mode, although poor compositional contrast is observed and the exact details of whether or not the beams are cycled or truly simultaneous is unknown.

3.4.3 Sample Preparation

After electrochemical testing, samples were cross-sectioned and broken into small pieces. In some cases, when noted, the porous phase of the samples was filled with a commercial epoxy. The procedure for this is as follows. Buehler Epo-thin resin and hardener were mixed together at ≈ 40°C. The sample was placed in a small mechanical pump vacuum box and the mixed epoxy was sucked through a hose and filled a small cup in which the sample was placed. Rapid cycling of the vacuum off and on was conducted in order to aid the elimination of bubbles. The sample was then cured in a controlled oven at ≈ 40°C for 24 hours.

Samples were polished using SiC polishing papers on a motorized wheel down to a finish of ≈ 1 micron. They were then attached to an SEM stub using a conductive Ag paint or Electrodag502 carbon paste from Ted Pella such that the cross-section revealing the electrode-electrolyte interface was facing straight up, normal to the face of the stub. They were then coated with conducting material (usually Au/Pd) in a sputter coater to reduce any charging. In some cases the LSC samples were placed with the electrolyte parallel to the stub face, such that the top cathode surface faced straight up, and were not coated due to the sufficient electronic conductivity of the MIEC cathode.

All cells in this thesis initially had a large trench cut in order to clear space to image a face of material that is viewable with the SEM beam. This was first done in bulk with a high current ion beam that also causes structural damage and large amounts of re-deposited material at the trench edges. This edge material and damage was then removed with subsequent steps of reduced current ion beam milling. For example, with the FEI instrument, initially a 2.8 nA ion beam current at 30kV was used to mill a 14 x 10 μm box ≈ 10-15 microns deep (this takes about

30 minutes). A 0.92 nA ion beam was then used to clean the trench walls and a 0.46 nA beam was used to polish (the beam mills forward in one movement) the face of interest before slicing. The current used for the slicing or polishing of the face was .0928 nA. The trench dimensions were chosen to be able to see at least 10 microns of material in the Y direction (up and down) and wide enough that re-deposition of milled material on the side walls did not interfere with at least 10 microns of viewable material in the X direction (left and right). Fiducial marks were placed on top surface of the sample to aid in the alignment of the images. Figure 3.3a shows a zoomed out view of a milled region highlighting the electrolyte and electrode layers, while Figure 3.3b is a zoomed in view of the same region showing the trench and re-deposition on the side walls that occured after the series of slices were conducted. The fiducial X marks milled on the top surface of the electrolyte are also visible. In some cases a layer of platinum approximately 1 micron thick was deposited on the top surface where the milling occured in order to help reduce “curtaining” and other uneven milling effects due to top surface roughness.

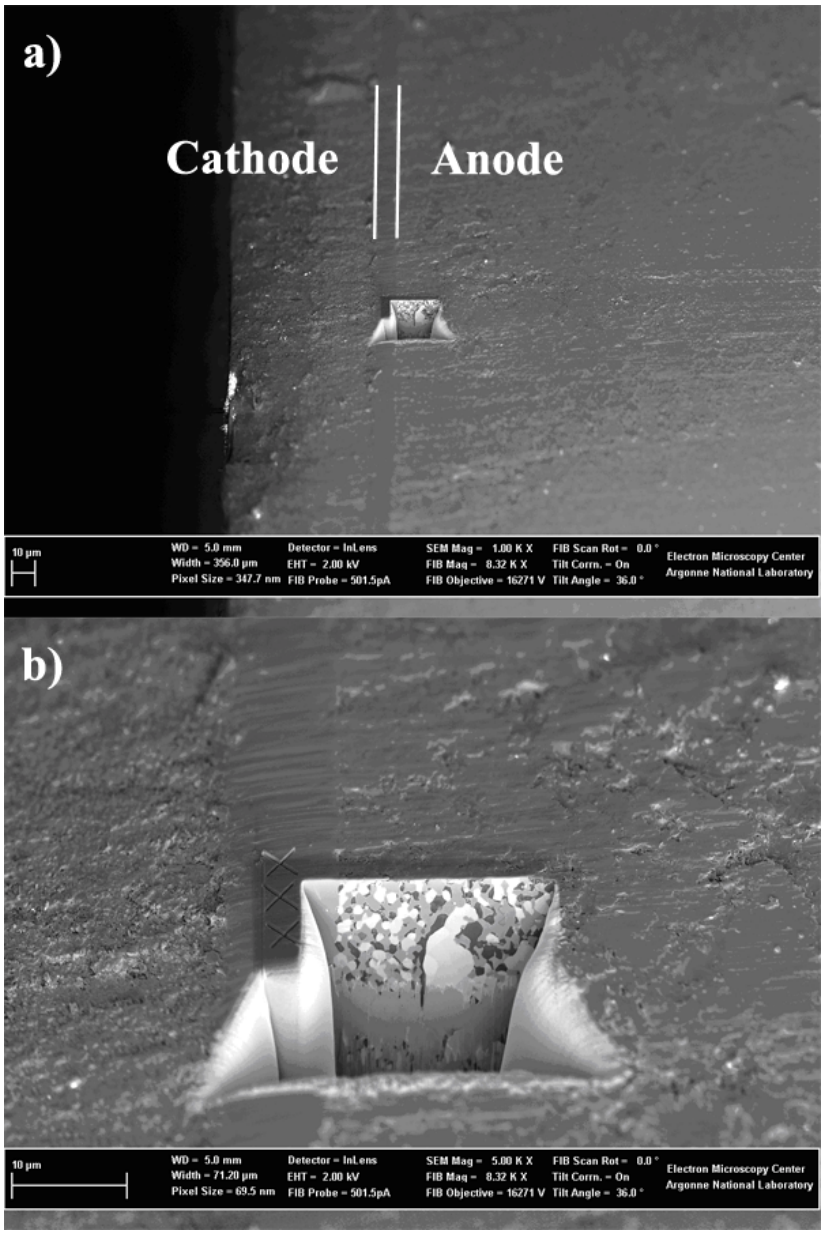

Figure 3.3. Micrographs of a Ni-YSZ anode region milled for reconstruction purposes. (a) A zoomed-out view highlighting the polished cross-sectional surface and the cathode, electrolyte, and anode support layers. (b) A zoomed-in view of the same sample region as that in (a) highlighting the viewable polished anode surface and the redeposition that occurs on the sides of the trench during milling.

3.4.4 Achieving Compositional Contrast

As mentioned in section 2.7, achieving sufficient and unambiguous compositional contrast is extremely important for obtaining easy and accurate reconstructions. Energy dispersive x-ray spectroscopy (EDS) can identify material contrasts, but collection times are extremely slow and the resolution is limited by the interaction volume of the incident electrons. Additionally, EDS will not image the porosity accurately, as it will identify material that is visible within pores. Figure 3.4 demonstrates this, showing identification of Ni in red, YSZ in blue, and the porosity barely identifiable.

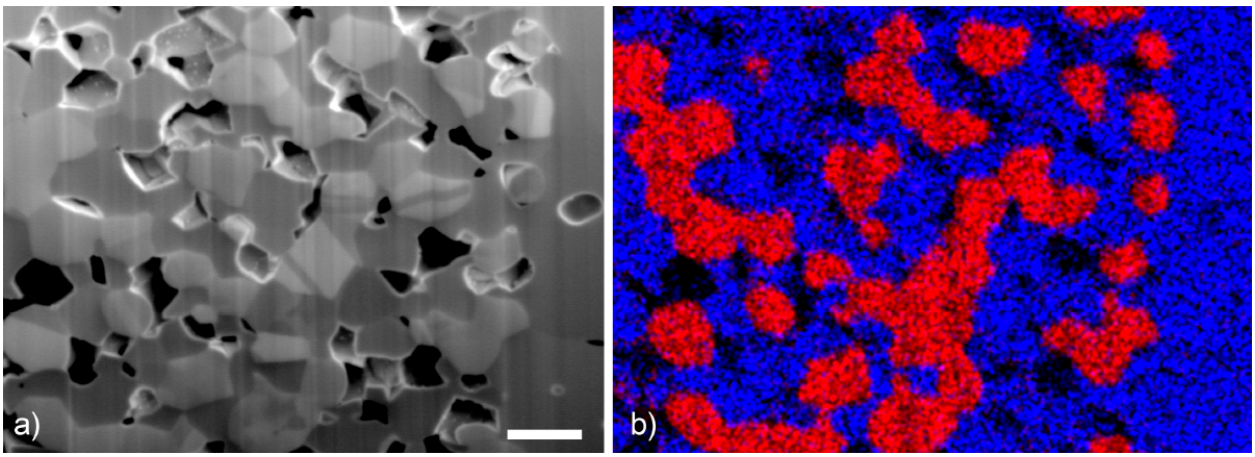

Figure 3.4. (a) SEM image showing the Ni phase as lighter contrast and YSZ as darker contrast. Collected with 2 keV electron-beam energy and ≈1.4 nA beam current with simultaneous ion-beam operation at 30 kV and 280 pA current. (b) An EDS map of the same sample showing Ni in red and Zr in blue. Images collected by Ben Myers using the FEI Helios at Northwestern University.

For the Ni-YSZ system, backscatter contrast is generally insufficient due to the convergence of the backscatter coefficients as a result of the 36° sample tilt and the subsequent reduction of the signal to noise ratio. However, as previously described by Thyden et al.[232], low energy electron beams will positively charge insulating and/or electrically isolated materials. We have observed that this charging mechanism is enhanced by simultaneous bombardment of ions (parallel to the surface), possible with the use of a dual-beam FIB-SEM, which also induces a positive charge in insulating materials. An example of the charge-contrast exhibited during simultaneous electron beam imaging and ion milling is shown in Figure 1a using the FEI instrument at Northwestern University. In this case the YSZ positively charges and appears darker than the lighter grey Ni grains. Figure 3.5 shows the effect of turning on the ion beam while collecting SEM images for the Zeiss instrument at Argonne. As can be clearly seen, the contrast is barely visible with the ion beam off, while the second image shows the induced charging caused when the ion beam is on. Frame-averaging is used in both cases in order to reduce interference caused by emission of secondary electrons from the ion beam bombardment. As discussed previously, it is unclear as to why the Zeiss instrument shows better contrast than the FEI instrument, although it is postulated that it is due to the absence of magnetic lenses near the sample and the better SEM column with the Zeiss instrument.

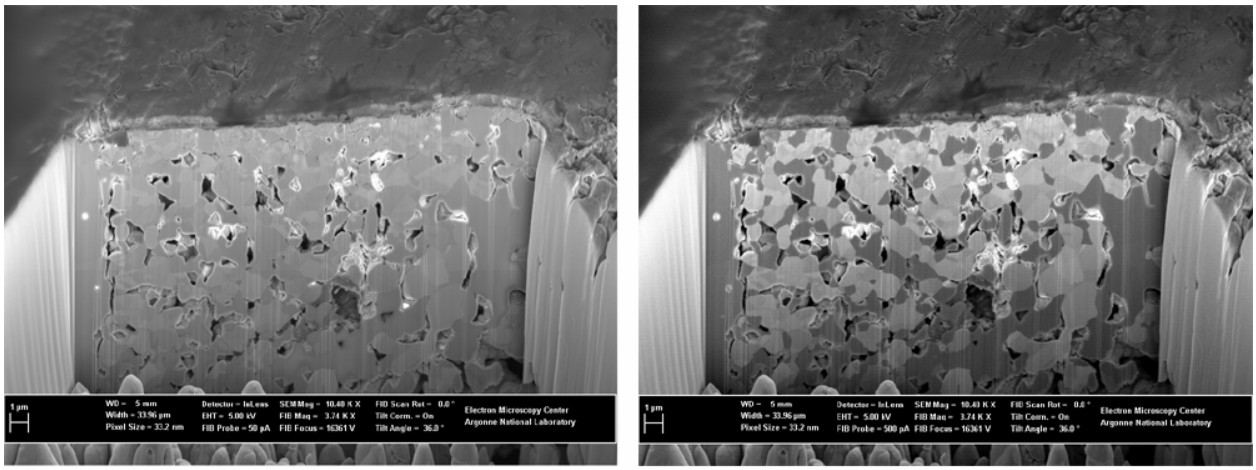

Figure 3.5. Two micrographs of the same Ni-YSZ surface. In the first image the ion beam is turned off and contrast between Ni and YSZ is faint. In the second image the surface is simultaneously polished with ions and clear contrast is observed between the Ni (light grey) and YSZ (dark grey).

Further analysis of this contrast mechanism was conducted in collaboration with Ben Myers in the Electron Probe Instrumentation Center (EPIC) at Northwestern University. While low energy incident electrons have been shown to produce positive charging, higher energy electron beams can contrastingly produce negative charging. Figure 3.6b shows an example of this, where the YSZ phase shows up as bright contrast as a result of the negative charge balance. If the charging is not strong from the electron beam, the contrast can be inverted by use of the ion beam to overwhelm the negative charge, resulting in a positive net charge, as shown in Figure 3.6a. Hence, the charge contrast observed by simultaneous ion bombardment is enhanced by choosing a low energy electron beam, and vice versa.

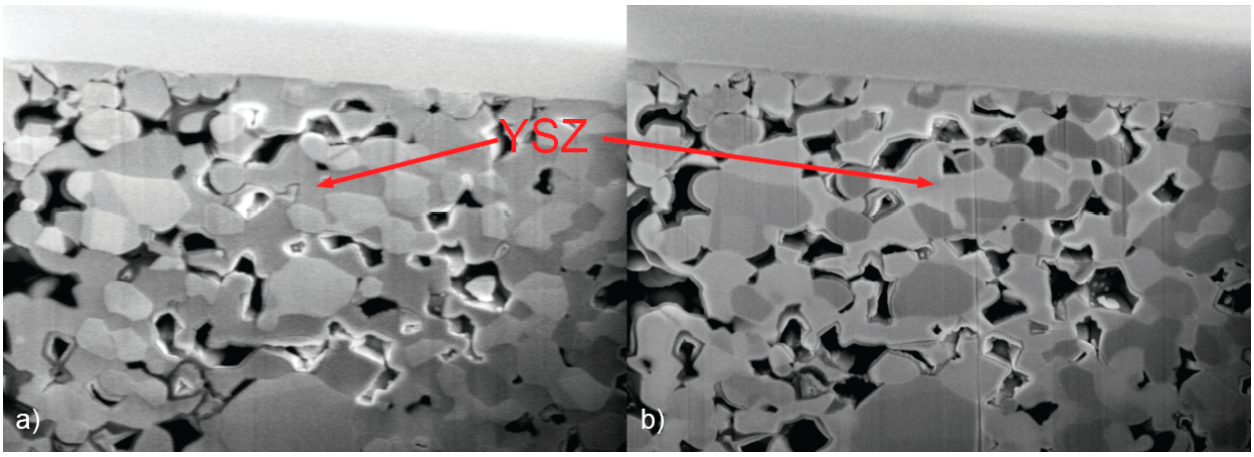

Figure 3.6. Micrographs collected using a 5keV electron energy. (a) Image taken with simultaneous ion bombardment. (b) Contrast inversion observed when the ion beam is turned off. Images collected by Ben Myers using the FEI Helios at Northwestern University.

It is also observed that ion bombardment (parallel to the surface being observed) can provide a contrast mechanism based on the connectivity of conductive phases. Similar to the work reported by Thyden et al., we show in Figure 3.7a that isolated Ni particles will charge positively under low energy electron beams. However, ion bombardment appears to negate this passive voltage contrast, as shown in Figure 3.7b. Hence, images collected during simultaneous electron- and ion-beam bombardment result in material contrast independent of connectivity. It is possible that this insensitivity to Ni connectivity is a time dependent work function mechanism, where the ion beam is serving to charge the surface only (affecting the work function differently for Ni and YSZ) and the effects are being observed rapidly enough with the electron beam that neutralization of the developed charge due to grounding of the percolated Ni

has not yet taken place. Certainly, further analysis of these unique contrast observations would be beneficial. Combination of these two types of images allows for the identification of isolated Ni particles with respect to the rest of the Ni phase, however the automatic collection of these two types of images would be difficult and greatly complicate the reconstruction procedure.

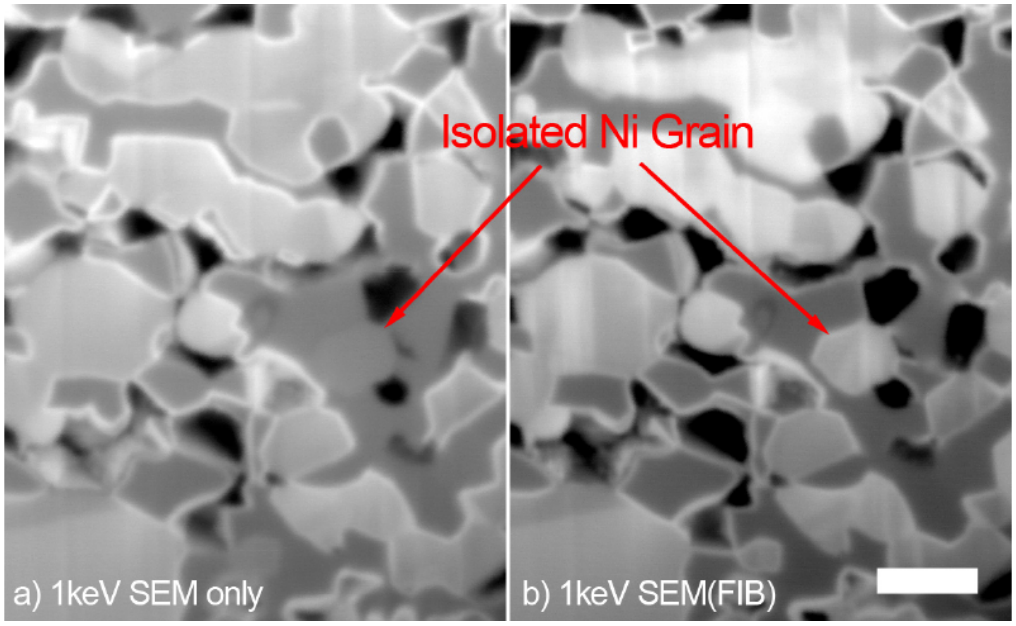

Figure 3.7. Micrographs collected using a 1 keV electron energy. (a) Positive charging of insulating YSZ and isolated Ni particles due to passive voltage contrast. (b) Ion-induced charge contrast showing isolated Ni particles with the same contrast as connected Ni. Images collected by Ben Myers using the FEI Helios at Northwestern University.

Filling the pores with an epoxy has also provided a number of advantages in achieving high quality images. Epoxy impregnation allows the focused ion beam to produce nearly planar

sectional surfaces for imaging without the contrast variations associated with charging of the pore edges, and signal emitted from within the pores, that previously made accurate segmentation and reconstruction of three-dimensional (3D) volumetric data sets difficult. Figure 3.8 shows an example of this, where significant charging and phase boundary blurring in the open pores is visible, compared to the clear and unambiguous compositional contrast in the epoxy-filled sample. Although the mechanism is unknown, it also appears that the epoxy may aid in accentuating the contrast between solid phases. It is possible that this is due to the fact that the epoxy stays black under most imaging conditions, which allows for the digital contrast and brightness to be increased and optimized for the two solid phases without regard to the porosity.

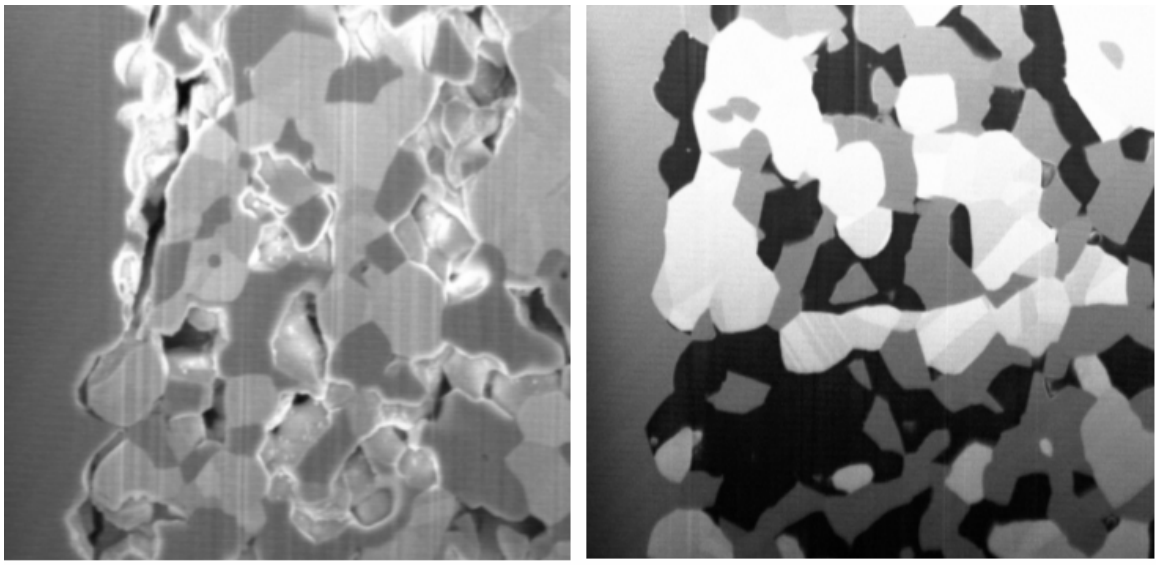

Figure 3.8. Two micrographs from the same Ni-YSZ anode sample. In one case the open porosity charges significantly and is hard to distinguish, while in the second case the porosity is impregnated with an epoxy, appearing black in the image.

Achieving contrast between LSM and YSZ has proven to be a more difficult task than the Ni-YSZ system. Several attempts were made with different microscopes and SEM imaging conditions in an attempt to obtain adequate image contrast between the LSM and YSZ phases in LSM-YSZ cathodes. These attempts were mostly unsuccessful. In some cases, good contrast was obtained in FIB images, but this is not useful because sectioning with FIB imaging would require that the sample be moved between milling and imaging steps. Recently, good contrast was achieved using a Zeiss Crossbeam 1540EsB system equipped with an in-lens energy-selective backscatter (EsB) detector. The relatively weak SEM image contrast between LSM and YSZ was addressed by using low electron beam energy and an energy-selective (biased) in-lens backscattered electron detector. Although backscattering yields are generally insensitive to electron beam energy above 5keV, they are often found to have a significant dependence below this, as has been observed with the Ni-YSZ system. The beam energy was thus an important variable for maximizing contrast between phases with similar atomic mass. Electron beam energies below 2keV were utilized in taking the present images. The low energies had the additional advantage that the interaction volume was significantly reduced, with attendant improvements in the spatial resolution. The biasing of the backscattered electron detector also significantly improved the chemical differentiation of phases by rejecting secondary electrons that did not show a strong correlation between atomic mass and electron counts at the detector. A typical 2D image from a screen-printed LSM-YSZ cathode is shown in Figure 3.9. The contrast obtained is sufficiently good to allow for LSM-YSZ 3D reconstruction.

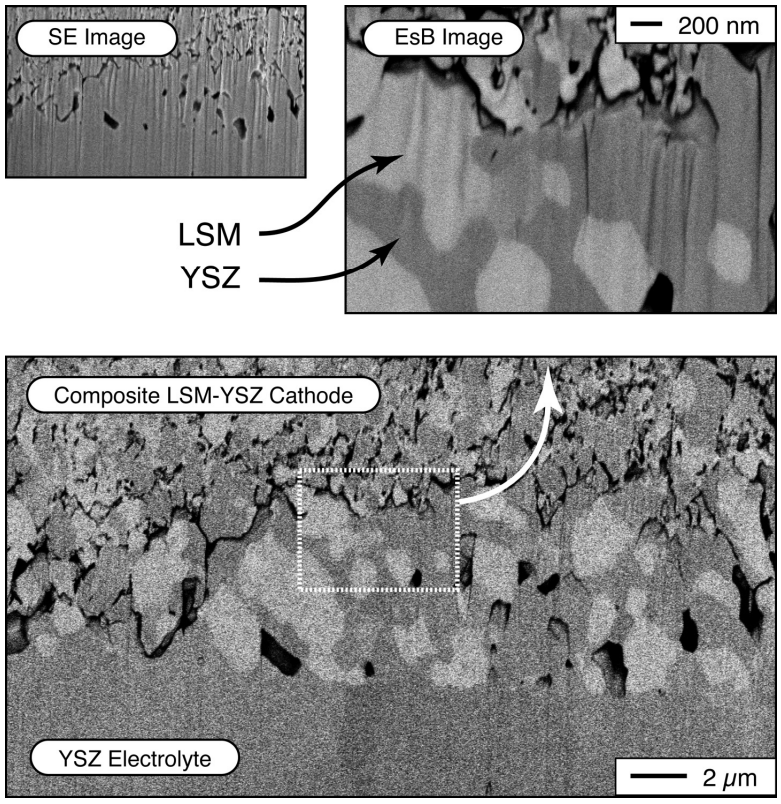

Figure 3.9. Example of a 2D image of a LSM-YSZ cathode showing good contrast between the phases. Also shown at the upper left is a secondary electron image where the lack of contrast is evident.

3.4.5 Image Collection Parameters

Images are collected with a "tilt-correction" turned on. This effectively stretches the images in the Y direction (up and down) by a factor of cos(90–α) where α is the angle between the electron and ion beams. This accounts for the fact that the SEM electron beam is viewing the face of interest at a specific angle other than normal. Additionally, the images are collected with

"auto-focus" turned on, such that the face of interest remains in focus as it is milled away and moves further from the focal point in the Z direction (the direction normal to the face of interest).

The specific e-beam parameters such as the energy, current, zoom (resolution), dwell time, etc. depend on the sample and the instrument being used. Usually, as discussed in section 3.4.4, a 2 kV e-beam energy was used, unless otherwise noted.

For the FEI instrument, the auto-slice-and-view mode was usually utilized, which automatically cut slices of specific thickness, pausing the i-beam between slices and collecting an SEM micrograph. This method is good for single phase electrodes where no solid-phase contrast mechanism is needed. Images were collected with pixel dimensions of 1024x884 striking a balance between collection time and total instrument time. As mentioned previously, an ion-beam current of .0928nA at 30kV was used to mill the electrode.

For the Zeiss instrument at Argonne, the following parameters were used, unless otherwise noted. A scan speed of 2, cycle time of 8.8, zoom factor of 2, and number of frames averaged of 40 were used in order to best eliminate any interference observed in the signal from the simultaneous operation of the ion beam. In this setup, the electrode was milled continuously and images were captured in real time at time intervals calculated based on the rate of milling. A zoom of 14kX resulted in 24.8 nm image resolution. An ion-beam current of 501.5 pA at 30kV was used for the fine milling.

In either case, a goal of about 30-60 seconds per slice is maintained in order to keep a total collection time of approximately 3 hours for a 10x10x10 micron volume. The exact mill times, image dwell times, etc., as discussed above, depends on the instrument and sample.

3.5 Image Processing

3.5.1 Alignment

Once a series of images is collected, a FFT-based algorithm is subsequently implemented to verify the alignment of the images. In this procedure, the fiducial marks placed on the top surface of the sample (and which should appear in the images) are used for a reference point for aligning, but in general, any distinctive feature on the top surface that does not get milled away can be just as, if not more effective in cases. The Medical Image Processing, Analysis, and Visualization (MIPAV) freeware package was used for this procedure. Two degrees of freedom were selected (the X and Y directions) and a region of interest (ROI) was selected to include the fiducial marks, such that only the ROIs between two images are used for the alignment algorithm. When the alignment adjustment is determined, the entire image is shifted automatically.

3.5.2 Cropping

Once the bulk images are aligned, the entire series of images is inspected to determine the maximum volume of material that can be analyzed. This depends on factors such as the influence of shadowing from side walls as well the quality of contrast in the images, especially early in the image series when focus and contrast adjustments are possibly still being made. Once it is determined where the series of images should be cropped in the X, Y, and Z directions, a program written in the Interactive Data Language (IDL) platform is used to conduct the cropping.

During this cropping procedure, an additional shift of the images is needed. This is due to the fact that as you mill back in the Z direction, because the face is being viewed at an angle other than normal, the face image (not the surface and rest of the sample) will shift up by a constant value. This shift is calculated to be equal to ztan(90-α) where z is the thickness of each slice and α is the angle between the electron and ion beams.

3.5.3 Filtering

Digital filtering of the images is conducted in order to enhance the contrast and reduce artifacts and shadowing that occurs. The amount of filtering conducted and the success of the filters depends strongly on the original image quality. Often, shadowing occurs from the top of the images to the bottom due to the angle of the electron beam and due to the walls of the trench that can deter secondary electron collection. This shadowing can prevent accurate segmentation when thresholding the entire image at a constant value. All of the filtering in this thesis was conducted in Adobe Photoshop using the "batch" feature to automate the procedure for the entire set of images. The number and sequence of filters used depends strongly on the original image quality. Each set of images tends to have a unique filtering procedure determined by manual experimentation. The following is a list of the filters used and the effect they have on the image.

Filters used and their effect:

Dust and Scratch or Despeckle – These eliminate pixels that are surrounded by pixels of a

different greyscale beyond a certain threshold, such that artifacts such as "dust" or "scratches" are removed. This helps to improve the uniformity of the greyscale level of the phases.

Autolevel – This takes the darkest and lightest pixels in the image and stretches them to be the minimum and maximum values of 0 and 255, respectively. All other greyscales are linearly extrapolated to the amount of stretching that occurred. This helps increase the contrast in the image.

Autolevel Dark and Autolevel Bright – This automatically levels the background of the image, depending on whether the background is a bright color or dark color, respectively. This is similar to the high pass filter, where variations in the brightness of the background can be eliminated.

High Pass – This takes a Fourier transform of the image and eliminates large wavelength trends. This helps to eliminate shadowing that occurs over the breadth of the image.

3.5.4 Segmentation

Segmentation is the process of converting the images to images where each phase is assigned a specific greyscale color. For example, in the case of the Ni-YSZ-pore anode, the Ni phase will be assigned the greyscale value of 255 (white), YSZ will be assigned 127 (grey), and the porosity will be assigned 0 (black). Figure 3.10 shows an example of this, where the filtered image and subsequently segmented image are displayed next to each other. The quality of the images and the effectiveness of the filtering procedures dictate whether or not the image series

can be automatically segmented or whether some hand-segmentation must occur. In either case, the segmentation itself is conducted by thresholding the set of images at two greyscale values.

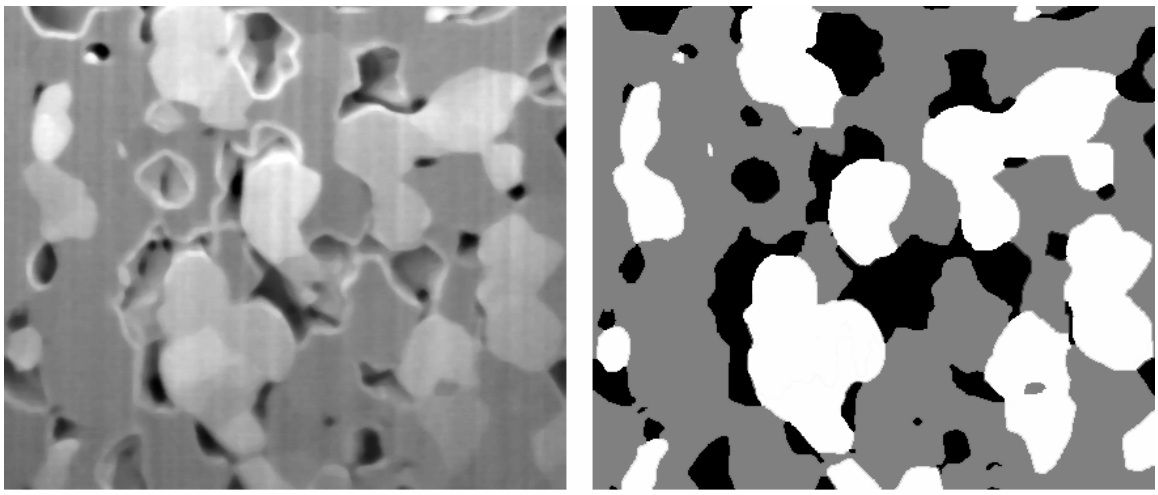

Figure 3.10. Filtered and segmented images of a Ni-YSZ anode showing the assignment of each phase to a specific greyscale color in the segmented image (Ni is white, YSZ is grey, and LSM is black).

When hand segmenting is needed, the phases must be identified by using the "magic wand" feature in Photoshop or by tracing the phase boundaries with the "pencil" feature. This procedure usually takes about 5 minutes per image, which if there is a set of 200 images, takes 17 hours. Overall this means that the hand segmentation of a set of images usually takes a week of extremely tedious labor to conduct. Obviously, there is great desire to be able to do the segmentation automatically. If the image quality is good enough, the images can be directly

thresholded after the filtering procedure. All the LSM-YSZ reconstructions presented in this thesis were automatically segmented.

In either case, after the filtering and/or the hand-identification of the phases, the next step of thresholding at two greyscale values is conducted automatically using an in-house program written in IDL. Thresholding at two values leaves a thin (usually 1-2 pixels wide) layer of grey pixels between white and black phases. This false layer is also removed using an in-house program in IDL that identifies grey voxels that are less than 2 voxels wide and reside between a black and grey phase, so as not to affect the normal grey phase.

The data set after segmentation and removal of the grey layer typically contains a number of single-voxel errors that can create significant artifacts in subsequent analysis, *e.g.,* apparent single-voxel-sized particles. Thus, it was found necessary to carry out an initial image filtering step to smooth the phase boundaries and eliminate single voxel errors. Segmented images were filtered according to the following procedure.

The original anode volume is defined by a three-dimensional matrix $U_1(x,y,z)$ with dimensions $m_x = 370$ and $m_y = 430$ (pixel dimensions of a single image), and $m_z = 82$ (# of images – into the plane). Each voxel is assigned a label M (for Ni metal), C (for YSZ ceramic), or P (for pore). From U_1 we create a new three-dimensional data set U_2, which is a smoothed version of U_1. To set the value of $U_2(x,y,z)$, voxels in U_1 a distance of 1 voxel around (x,y,z), *i.e.,* the voxels $(x \pm 1, y \pm 1, z \pm 1)$ are examined. $U_2(x,y,z)$ values are then set to either M, C, or P depending on which label occurs most often in these surrounding 26 voxels in U_1. In the case that there is a tie, *i.e.*, the largest value is attained by more than one of the labels M, C, or P, we randomly pick a value for $U_2(x,y,z)$ among those that are tied. This procedure is applied for all

values of (x,y,z), fully defining U_2. The same procedure can be repeated on U_2 to get U_3, and so on.

The number of post-filtering steps (also called "dust and scratch" steps) conducted, as described above, depends on the sample and the segmented images. Filtering should minimize errors in volume and triple-phase boundary measurements due to minor segmentation error, but should not significantly alter the structure. In the case of the Ni-YSZ anode described in Chapter 5, the following analysis was conducted. Figure 3.11 shows an example of the effect of different numbers of filtering steps on a typical image region. Too many filtering steps (*e.g.,* 10 times) leads to the disconnection of two white and black phases and reduces dramatically the existence of a white "peninsula." In general, the continued filtering of the images reduces high-curvature surface areas, effectively shrinking the Ni and pore phases. The effect of these dust and scratch removal steps on the TPB density is shown in Figure 3.12, where part a) shows the results for the Ni-YSZ anode, and part b) shows the results for the 55:45 LSM:YSZ sample discussed in Chapter 8. As can be seen, there are two basic regimes in the curves. For the first and second filtering steps, there is a steeper drop in the TPB density, after which, a continual and less steep decline in TPB density is observed with repeated filtering steps. This shows that small voxel errors, as displayed later in Figure 5.4, and interfaces with extreme curvature are initially removed in the first two filtering steps in this first regime. After this, the microstructure has reached its smoothed correct form, at which point subsequent filtering steps serve to only shrink the phases and their interfacial areas. As a result, it was determined that for the samples analyzed in this thesis, the segmented images should be filtered 2 times in order to strike a balance between removing small voxel errors and preventing microstructural changes. It is important to note, as displayed in Figure 3.12c for the series of cathode compositions studied in

Chapter 8, that although the magnitudes of the TPB densities are sensitive to the filtering steps, the changes as a result of the filtering are equal for each sample analyzed, such that the differences between TPB densities between samples stays consistent. This emphasizes the fact that as long as consistency is maintained in the filtering and image processing procedures, errors are minimized when comparing values for different samples.

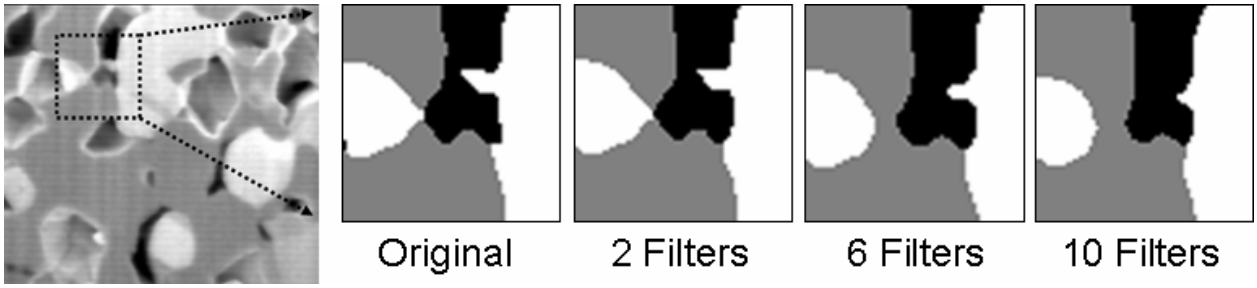

Figure 3.11. Representative anode microstructure (Ni is white, YSZ is grey, and porosity is black) showing changes resulting from increasing numbers of filtering steps.

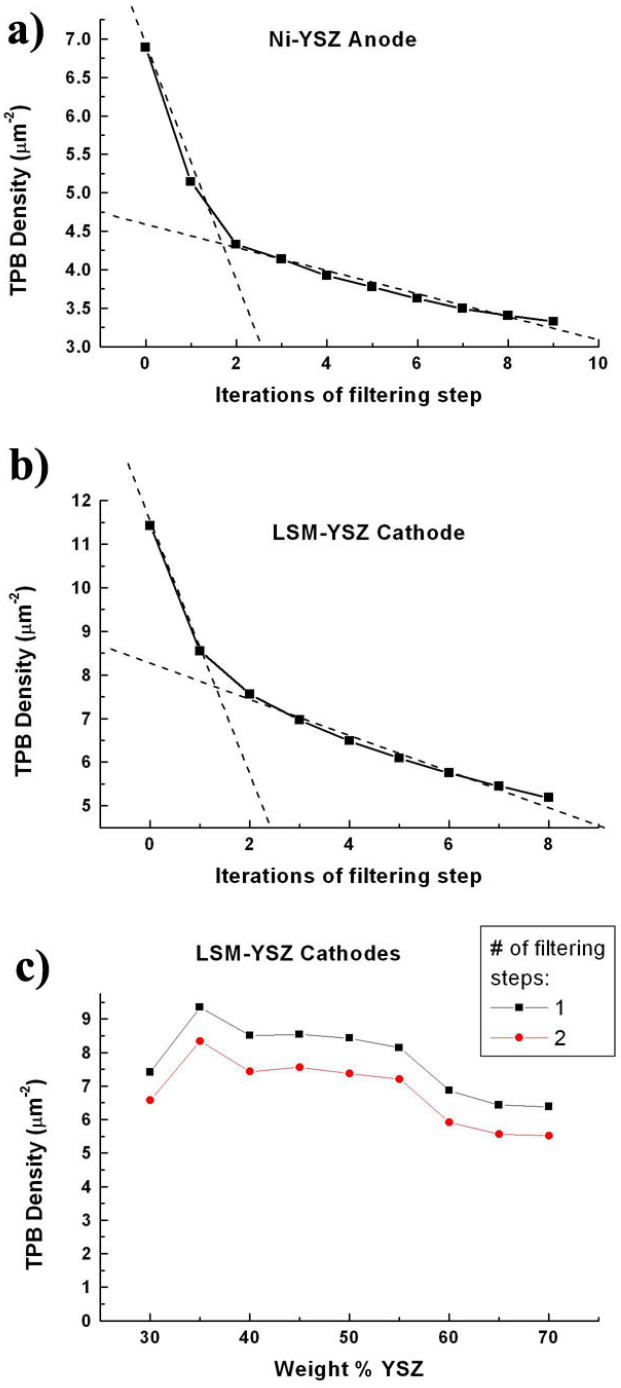

Figure 3.12. Analysis of the effect of the filtering steps on the TPB density for a) Ni-YSZ and b) LSM-YSZ electrode structures. c) The TPB densities for each cathode composition studied in Chapter 8 after 1 and 2 filtering steps.

3.6 Calculations

Once the final set of segmented images is achieved, any number of calculations can be conducted with regards to relevant features of the microstructure. These calculations are summarized below. In each case, the phases are identified by their assigned greyscale value.

3.6.1 Volume Percentages

Volume percentages are calculated by counting the total number of voxels of a specific phase and dividing it by the total number of voxels in the analyzed volume.

3.6.2 Surface Areas

The calculation of surface area density relies heavily on the reconstruction procedure and any surface or bulk smoothing that is done using IDL. The common procedure for calculating the surface area is to take the bulk voxel data and mesh the surface of whichever phase you are measuring using the MESH_SURFACE command in IDL. This describes the surface of the phase by hundreds of thousands of connected triangles or polygons, depending on what is requested, and their respective vertices. The resolution of these vertices is better than the voxel resolution, so the zig zag edge of a series of voxels heading in a diagonal direction tends to be still visible when the surface is meshed. This is called the “wedding cake” effect. This effect is even more apparent when the voxels are not cubic, i.e. the Z resolution is different than the X and Y resolution.

This affect was analyzed for the case of the Ni-YSZ sample discussed in Chapter 5. Due to the different resolutions in different directions – 10 nm in the image plane and 50 nm between images – in the 3D data sets, the desired approximately cube-shaped voxels were obtained by reducing the resolution to 41.7 nm in the images. This loss of resolution was not a serious problem for the present anode, which was typical of state-of-the-art SOFC anodes, where the feature sizes ranged from ~ 200 nm to 1 μm. In one case, we adjusted the image resolution to check for potential errors. We calculated the total interfacial areas on 2D images with the original resolution (13.9 nm) and with the reduced resolution (41.7 nm) that was normally used to obtain nearly cube-shaped voxels. The reduction in the interfacial areas in the 2D images due to resolution reduction was found to be ≈ 5% on the average, providing an estimate for the errors in the surface area associated with the resolution used.

An effective method for eliminating the wedding cake effect, in addition to adjusting for cubic voxels, is to use a mesh smoothing function in IDL. This treats each of the vertices as if there was a spring between it and its neighbor vertices. This is different from bulk smoothing, where each voxel is taken to be the average value of its neighbor voxels. One can image then, depending on the strength of the spring and the distance between neighbors, that large "bumps" or edges in the surface will tend to constrict towards the more planar surface structure.

The effectiveness of this smoothing strategy was analyzed for the LSM-YSZ sample discussed in Chapter 7, with X-Y resolution of 40.8 nm and Z resolution of 53.3 (nearly cubic voxels). The surface smoothing variables are expressed as [i, δ], where i is the number of iterations the surface smoothing is conducted and δ is the metaphorical "strength" of the springs. Table 3.1 shows the surface area densities for the YSZ, LSM, and Pore phases for different iterations of the smoothing procedure. Figure 3.13 shows a zoomed in view of the YSZ surface

for each of the smoothing procedures listed in Table 3.1, as visual reference. The difference between no smoothing and the [2, 0.5] surface smoothing is substantial. It can be seen that the roughness and faint wedding cake effect are greatly dampened. An additional smoothing to [4, 0.5] has less of an effect on the surface areas, but visually it can be seen that some roughness on the surface is removed. Further smoothing to [6, 0.5] appears to only shrink the YSZ phase, while the surface roughness looks the same as that with [4, 0.5]. As a result, it was concluded that a surface smoothing of [4, 0.5] was ideal for these samples because it sufficiently smoothed the surface roughness without changing the microstructure. In contrast, the [3,3,3] bulk smoothing, the smallest possible smoothing where the nearest first neighbor in the x, y, and z directions is used to average, has as large an effect as [6, 0.5] surface smoothing and can eliminate peninsulas and thin regions of structure. In conclusion, the level of surface smoothing used is somewhat subjective, but it is important that whatever method is chosen must be used with all samples to maintain consistency, and must not affect the overall microstructure.

Table 3.1. Surface area densities measured for an LSM-YSZ porous microstructure as a function of the smoothing technique used on the original set of segmented images.

	YSZ (μm^{-1})	LSM (μm^{-1})	Pore (μm^{-1})
None	3.636	2.116	4.477
[2, 0.5] surface	3.240	1.897	4.035
[4, 0.5] surface	3.118	1.825	3.918
[6, 0.5] surface	3.033	1.775	3.840
[3,3,3] bulk	3.033	1.783	3.867

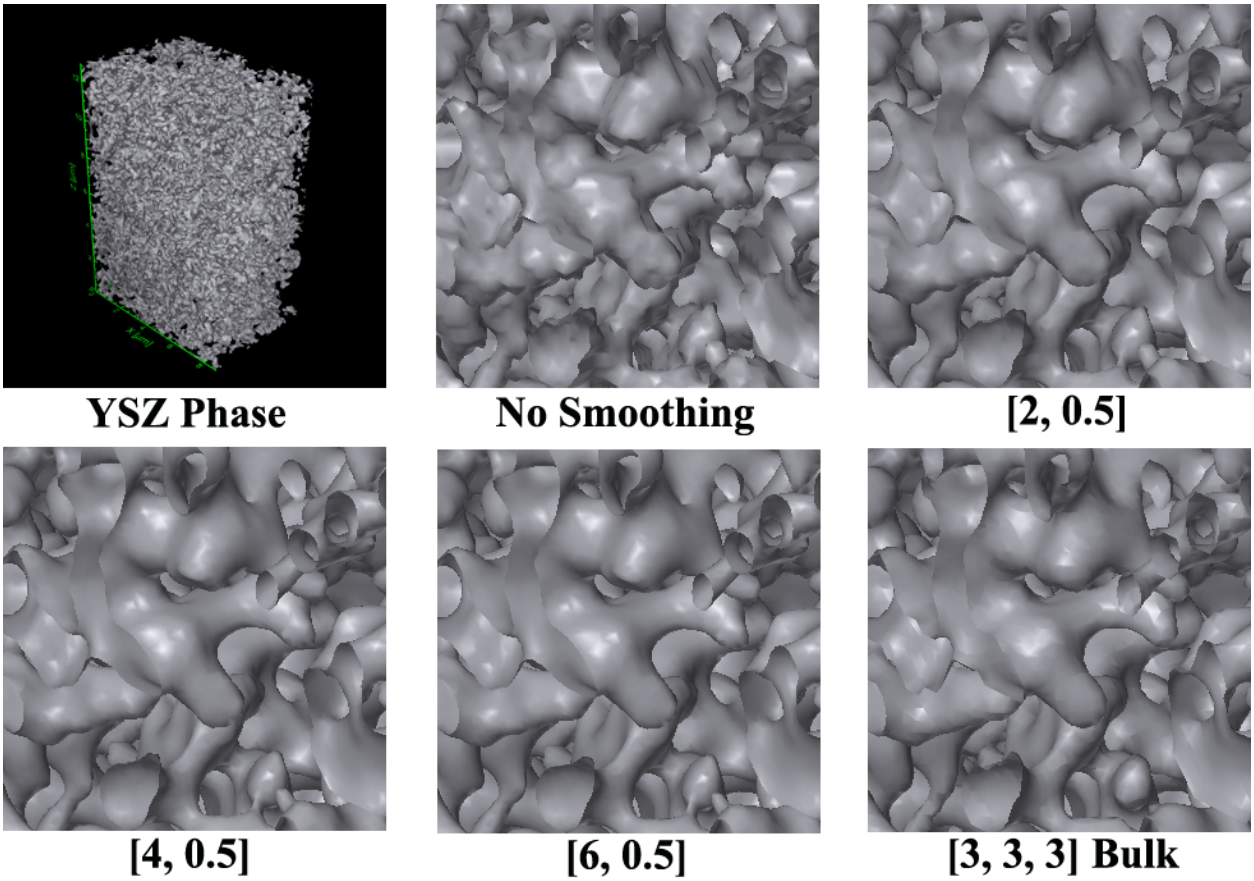

Figure 3.13. The YSZ phase from the LSM-YSZ sample discussed in Chapter 7 showing the surface as a function of different smoothing iterations and techniques.

3.6.3 Triple-Phase Boundary (TPB) Density

The triple-phase boundary density was calculated by identifying the voxel edges that simultaneously touch voxels of three different phases. It is important to note that this method measures line length by adding only orthogonal components, such that the overall length measured should be larger than the set of real, randomly angled diagonal line segments. For example, if a TPB happens to run at a 45° angle in the X-Y plane, the length measured by adding the X and Y orthogonal vectors will be greater by a factor of square root 2. Hence, the correction factor is simply the sum of the orthogonal segment lengths divided by the direct line length. The total overestimate can be accounted for by finding the average value for this correction factor over all angles in 3D space. This is accomplished by integrating this correction factor over the surface (S) of a sphere (a method in polar coordinates to ensure every angle is counted only once), and dividing this integral by the surface area of the sphere (to find the average value). The integral is first set up in Cartesian coordinates shown in equation (3.1).

$$\frac{\int_S \frac{(X+Y+Z)}{\sqrt{X^2+Y^2+Z^2}}\,dS}{\int_S dS} \tag{3.1}$$

Converting to Polar coordinates and defining the sphere surface as (p = 1) in the octant of space where X, Y, and Z are all positive (θ and φ go from 0 to π/2) gives equation (3.2), evaluated as ≈1.455.

$$\frac{\int_0^{\frac{\pi}{2}}\int_0^{\frac{\pi}{2}}(\sin\varphi\cos\theta+\sin\varphi\sin\theta+\cos\varphi)(\sin\theta)(\rho^2)d\theta d\varphi}{\int_0^{\frac{\pi}{2}}\int_0^{\frac{\pi}{2}}(\sin\theta)(\rho^2)d\theta d\varphi}=\frac{\frac{\pi}{4}+\frac{3}{2}}{\frac{\pi}{2}}\approx 1.455 \qquad (3.2)$$

Hence, the measured triple-phase boundary density should be divided by 1.455 to achieve the most accurate value.

3.6.4 Tortuosity

The tortuosity calculations are done in collaboration with Professor Katsuyo Thornton and graduate student Hsun-Yi Chen at the University of Michigan. As a first attempt at evaluating gas-phase tortuosity, we assumed that transport within the pore subdomains is described by Laplace's equation,

$$\frac{\partial u}{\partial t}=0=\nabla^2 u\,, \qquad (3.3)$$

where u is the concentration, such that solving this steady state diffusion equation allows for calculation of the flux. Recent flux-based Monte Carlo simulations in porous media suggests that such an approach should be generally valid for both molecular and Knudsen diffusion, provided that the porosity is higher than ~10%.[235] Figure 3.14 schematically illustrates the calculation procedure. We first converted the 3D reconstructed volume of the gas pores, as shown in Figure 3.14 for the Ni-YSZ sample discussed in Chapter 5, into a finite-element mesh.

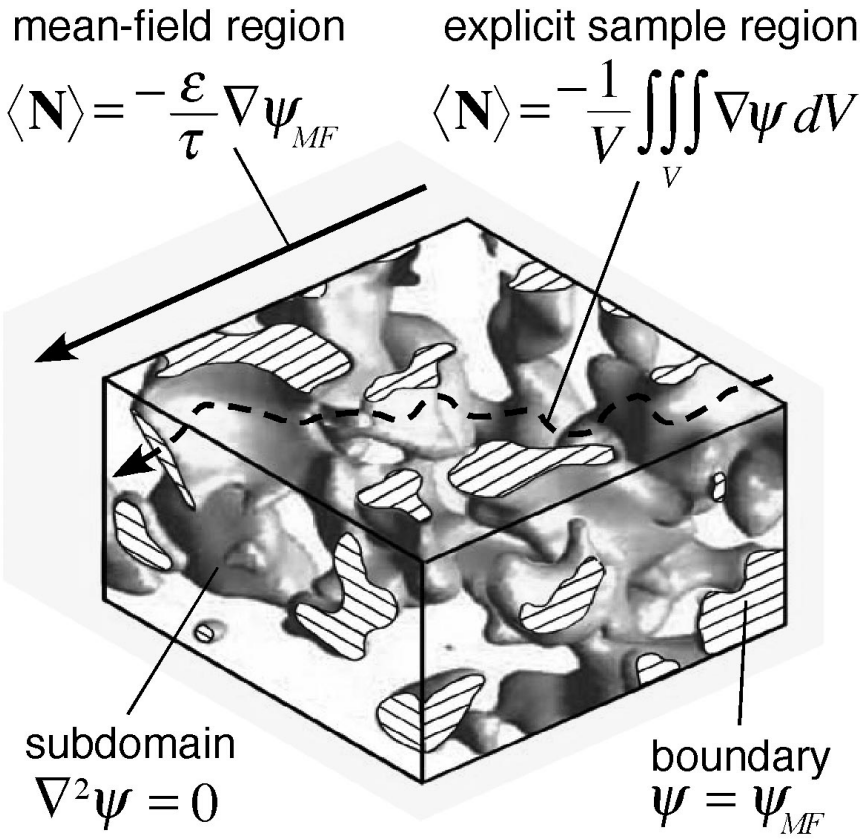

Figure 3.14. Procedure for calculating tortuosity on a finite sample volume. The pore subdomain was converted into a finite-element mesh. The flux is given by $-\nabla\psi$, where ψ is the solution to Laplace's equation $(\nabla^2\psi = 0)$ with no-flux boundary conditions on the pore-solid interfaces. The boundary conditions on the sample boundaries were given as follows. For tortuosity along the x_i-direction, the boundary conditions at the sample boundaries at $x_i = 0$ and $x_i = L_i$, where L_i is the sample size along x_i, were given by $\psi = C$ and $\psi = 0$, respectively. To reduce effects of disconnected pore sub-domains caused by the limited sample size, we imposed $\psi = \psi_{MF}$ on the other sample boundaries, where $\psi_{MF} = C(1 - x_i / L_i)$ is the mean field solution to Laplace's equation in the absence of the microstructure.

In practice, the no-flux boundary condition at the pore-solid interface was replaced by setting the diffusivity in the solid to be much smaller than that in the pore and solving $\nabla \cdot (D(x)\nabla \psi) = 0$ instead, where $D(x)$ is the position dependent diffusivity and $-\nabla \psi$ is the flux. The test results using artificial microstructures showed that using a factor of 100 between the two diffusivities ensured that the results were not altered by this approximation.

The boundary conditions for the walls of the volume were set accordingly to the illustration in Figure 3.14. The front and back wall normal to the direction of calculation were set to have concentrations of 0 and 100 respectively. While the boundary conditions for the sidewalls were set to have a concentration as given by the mean field solution ($u=100-100\ x_i/L_i$), where x_i is the distance from the face with concentration 0, and L_i is the total length of the volume in the calculated direction. The reason to use the mean field boundary condition, in comparison to a no flux boundary, is to avoid the effects caused by the pore volumes that are isolated on the boundary due to sampling of the microstructure. The effect of these isolated boundary pores is expected to be small for large sample volumes, but should become substantial as the sample volume approaches the size scale of the porosity. Figure 3.15 shows the size effect observed when the mean field boundary condition is not used, compared to when it is implemented, clearly showing that the mean field boundary condition aids in providing consistent results irrespective of the sample volume.

We initially used FEMLAB, commercial software from Comsol, Inc., to obtain ψ, but further calculations were conducted in the same manner using the finite-difference method within an in-house program written in FORTRAN. The tortuosity was then recovered by

equating the macrohomogeneously-defined flux to the volume-average flux within the sample volume:

$$-\frac{\varepsilon}{\tau}\nabla\psi_{MF} = -\frac{1}{V}\iiint_{V}\nabla\psi dV\,, \tag{3.4}$$

where V is the sample volume, ε is the porosity, and τ is the tortuosity. This procedure was performed for the three primary axes, $x_i = x, y, z$, of the sample volume to determine the isotropy of the tortuosity factor.

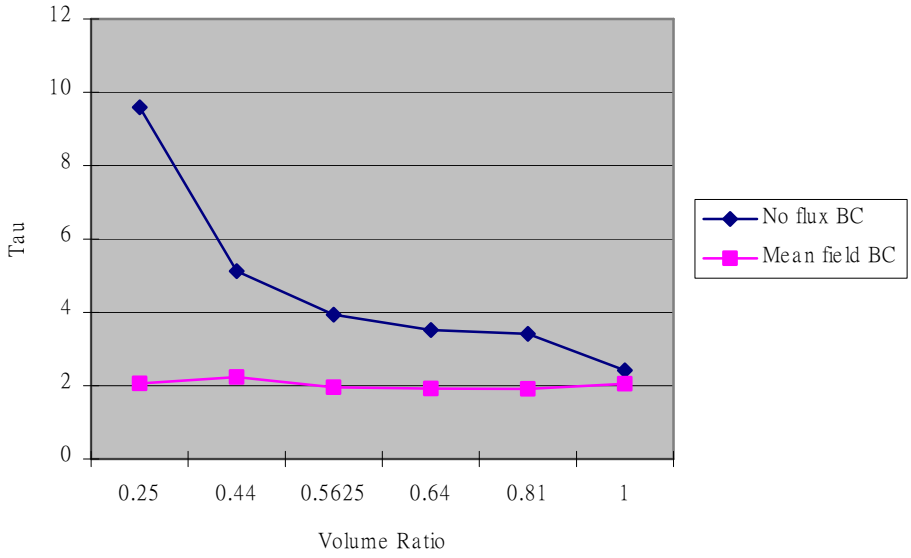

Figure 3.15. Tortuosity results with respect to different volume ratios for the no flux, and mean field boundary conditions, highlighting the size effect that occurs when the mean field boundary condition is not implemented. The data is for the Ni-YSZ anode discussed in Chapter 5, calculated by Hsun-Yi Chen.

3.6.5 Phase Connectivity

The connectivity calculations were done in collaboration with Dr. Marcio Gameiro from Rutgers University. Methods for extracting phase contiguity data from 3D images have been developed previously, but not applied to fuel cells.[236-238]

Here we use the term "network" to describe a fully-contiguous and separate subset of a phase. This step of the algorithm starts with a corrected three-dimensional image $U_3(x,y,z)$, as described in section 3.5.4, where each voxel is assigned a label M, C, or P, for metal, ceramic, and pore, respectively. Each voxel is assigned a second label that says whether the corresponding cube is an interior or a boundary cube, with respect to the outer surface of the volume analyzed. If it is a boundary cube, this label also specifies to which of the boundaries the cube belongs (top, bottom, left, right, front, or back). The voxels are then converted to a 3D graph where each voxel represents a point in space. Points are connected on the graph if their neighbors have the same label, such that contiguous networks of a single phase become interconnected by a network of lines. These separate graphs are then identified and their corresponding voxels in $U_3(x,y,z)$ are given a label associating them with a specific network. In addition, each network is analyzed to determine if any of the voxels contain boundary labels. If none are found, the network is "isolated." If the network includes one and only one boundary label, the contiguous network is labeled "dead-end" (it enters the volume analyzed and dead-ends within). If the network intersects more than one boundary, i.e., it enters and exits the volume analyzed, it is labeled "across" and is considered contiguous throughout the electrode.

After the interconnectivity of each of the Ni, YSZ, and pore phases is obtained, the calculation of the "active" triple-phase boundary density, *i.e.,* the portion of TPB length that is

connected to contiguous ionic, electronic, and gaseous transport paths, can be conducted. In this manner, a similar procedure is applied to the edges of the voxels to identify whether they are TPB components and whether they are touching contiguous networks of each phase. Each edge is labeled a TPB component if the four voxels it touches include all three M, C, and P labels. In addition, these voxels are already labeled, as described above, as to whether they are part of an isolated, dead-end, or across network. The TPB component is then labeled "inactive" if it lies on any isolated network, "unknown" if it lies on any dead-end network (and no isolated networks), or "active" if it lies on across (completely contiguous) networks for each Ni, YSZ, and pore phase.

3.7 Comparison to Stereology

3.7.1 Stereology Limitations

Accurate segmentation and 3D reconstruction of SOFC electrodes requires a significant effort. Thus, it is useful to know when simpler measures such as stereology can be used and the errors associated with these methods. While stereological methods can be used to estimate quantities such as volume fractions, interface areas, and total three-phase boundary (TPB) length from 2D images[176], it is not clear how accurate such methods are, especially if microstructures are non-isotropic. Furthermore, 2D images cannot differentiate which portions of a particular phase or TPB are connected to contiguous gaseous, ionic, and electronic transport paths. Similarly, tortuosity is nearly impossible to measure from two-dimensional (2D) cross sections, since it relies on exactly how and where phases interconnect in three dimensions. These limitations of 2D characterization methods make it important to apply three-dimensional (3D)

reconstruction methods to SOFC electrodes in order to calculate the relevant 3D microstructural properties that describe the electrode electrochemical activity. However, in some cases, stereology provides great benefits due to its relatively fast estimation of simple parameters and its ability to use easily collected 2D images. The following is a discussion of the methods of stereology and the accuracy achieved for simple calculations of volume percentage, surface area, and triple-phase boundary density.

3.7.2 Stereology Methods

All stereological calculations are conducted by placing an overlay on top of a 2D image.[239] Reapplication of the overlay on one image, and/or application of the overlay on a number of images, gives better statistics and more accurate results. The overlays for each calculation are shown in Figure 3.16, placed on top of an already segmented image in order to accentuate the phases. In normal practice, the image used would be a filtered image that had not been segmented.

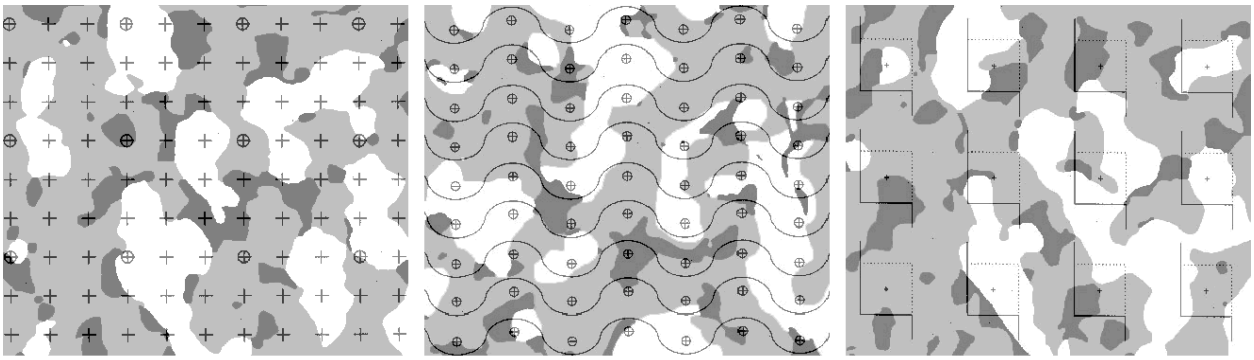

Figure 3.16. Overlays for the respective microstructural calculations using stereology.

For the calculation of volume fractions, shown in Figure 3.16, the number of points or crosses that fall on each specific phase are counted and then divided by the total number of points, given as $V_{given\ phase} = P_{given\ phase}/P_{total}$.

For the calculation of surface area density, shown in Figure 3.16, the total number of intersections between the overlayed lines and the boundary of a specific phase are counted. The surface area density is then calculated as

$$Sv \approx \frac{2\Sigma I}{(l/p) * \Sigma P} \tag{3.5}$$

where ΣI = the total number of line intersection points, ΣP = the total number of grid points hitting the reference space (in the case of the overlay shown, this equals 63), and (*l*/*p*) = the length of the test line per grid point. This line is shown below in Figure 3.17 with its respective grid point. The length of this line is calculated to be ≈ 4/3 its width, based on its elliptical shape.

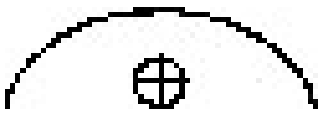

Figure 3.17. Line overlay with grid point for the calculation of surface area density by stereology.

The triple-phase boundary density is calculated, shown in Figure 3.16, by counting the total number of points within the framed boxes where the three phases meet. The TPB density is then given as

$$Lv = \frac{2 * \Sigma Q}{A_f * \Sigma P} \tag{3.6}$$

where A_f = the area of the frame, ΣQ = the total number of TPB sites counted in the frames, and ΣP = the total number of frames overlayed on the image (this equals 12 for the overlay shown in Figure 3.16).

3.7.3 Accuracy of Stereology

Stereology of 2D images provides limited structural data (not including phase tortuosity and interconnectivity, for example) with less image processing than 3D reconstruction. To assess the accuracy of stereological methods, we applied standard stereological techniques to the complete set of Ni-YSZ images discussed in Chapter 5 to calculate volume percentages, surface areas, and triple-phase boundary density, and compared them with the 3D reconstruction values (Table 3.2). The errors listed are the percentage difference between the two methods used. It can be seen that there are inherent inaccuracies in stereological calculations; one possible source of error is an anisotropic microstructure. The error is large for the TPB density calculation, which confirms that 3D reconstruction should be conducted to obtain the best TPB data.

Table 3.2. Macrohomogeneous microstructural parameters for a Ni-YSZ cermet anode using 2D stereology and 3D reconstruction, and the percentage difference between the two methods.

	Volume %			Surface Area (μm^{-1})			TPB (10^6 m/cm^3)
	Pore	Ni	YSZ	Pore	Ni	YSZ	
2D Stereology	0.217	0.260	0.523	2.30	1.50	2.71	3.51
3D Analysis	0.195	0.259	0.546	2.4	1.6	3.0	4.28
Average Error	11.3%	0.4%	4.2%	5.0%	6.2%	9.7%	18.0%

One advantage of a full 3D data set is that the large amount of data obtained provides good statistics, especially compared to single 2D images often used to characterize SOFC electrodes. To illustrate this, we did the stereological analysis with different numbers of images from 1 to the full 80-image data set. Figure 3.18 shows the relative standard deviation of the microstructural quantities versus number of images analyzed. The TPB density had the highest standard deviation. In order to obtain a ≤5% relative standard deviation for any of the quantities, it was sufficient to analyze ≈16 images, each with an area of 31.1 μm^2, *i.e.,* a total image area of 498 μm^2. This is much less than the number of images required for the 3D reconstruction, as dictated by the standard rule of thumb of 10 images per feature length (≈1 μm for the present anode) needed to obtain the appropriate resolution in the slicing direction.[226] It can be concluded that it is sufficient to expedite the calculations of volume percentages and surface areas by skipping the segmentation procedure and conducting stereological calculations as long

as an error range of ±6% is acceptable. Only estimates within ±15% of the TPB density can be achieved with stereology.

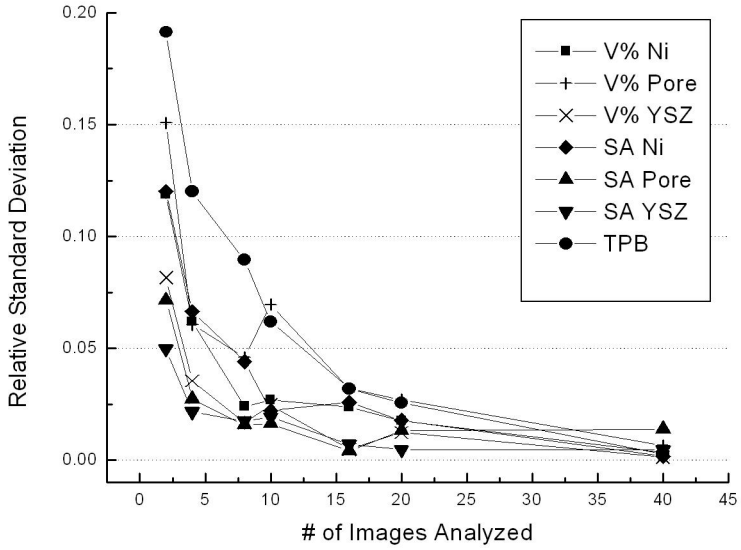

Figure 3.18. Relative standard deviations of the stereological calculations for volumes, surface areas, and TPB, as a function of the number of images used out of a total sample volume of 80 images.

3.8 Data Confidence

3.8.1 Representative Volumes

Obtaining reconstructions of volumes that are representative of the macroscopic qualities of an electrode is essential for acquiring reliable data. This is in part a function of the quality of processing, as highly anisotropic structures would be difficult to measure. However, assuming

reasonable limits of consistent processing, the question remains as to what volume of material can be considered representative of the electrode with sufficiently low errors.

The easiest and best way to analyze the effect of the sample volume on the calculations made is to take a large volume of material and subsequently measure microstructural features for a series of smaller volumes. This study was conducted for the LSM-YSZ sample with starting weight ratio of 35:65 LSM:YSZ, as discussed in Chapter 8, due to its large volume of reconstruction allowing for a large range of volumes to analyze. Figure 3.19 shows the volume % and surface area density calculations for different volumes of this sample. For each calculation, a cube approximately one tenth the size of the total volume was chosen from each of the 8 corners of the sample space. Each of these 8 cubes was then expanded in volume approximately 10 times until they all constituted the entire volume. Each chart includes a line plot for each set of expansions from the corners. In this manner, the consistency of the calculations and the magnitude of error as a function of the sample volume are analyzed.

Figure 3.19 shows that the volume percentage is more sensitive to the sample volume compared to the surface area density, where most of the surface area calculations fall within a range of ±2% error, compared to ±5% for the volume percentages. Figure 3.20 shows the TPB calculations as a function of sample volume, where a volume of 500 μm^3 or greater gives a less than ±2% error, a similar result to the sensitivity of the surface area density to sample volume. These results are comparative to those which are discussed in section 3.8.2. Overall, it appears that a volume of at least 500 μm^3 (≈ 37% of the total sample volume) is required to have good confidence in the calculations made. The minimum volume required is a function of the feature size of the microstructure. The larger the feature size, the larger the volume required in order to be representative of the microstructure. Holzer et al. gave a general rule of thumb requiring at

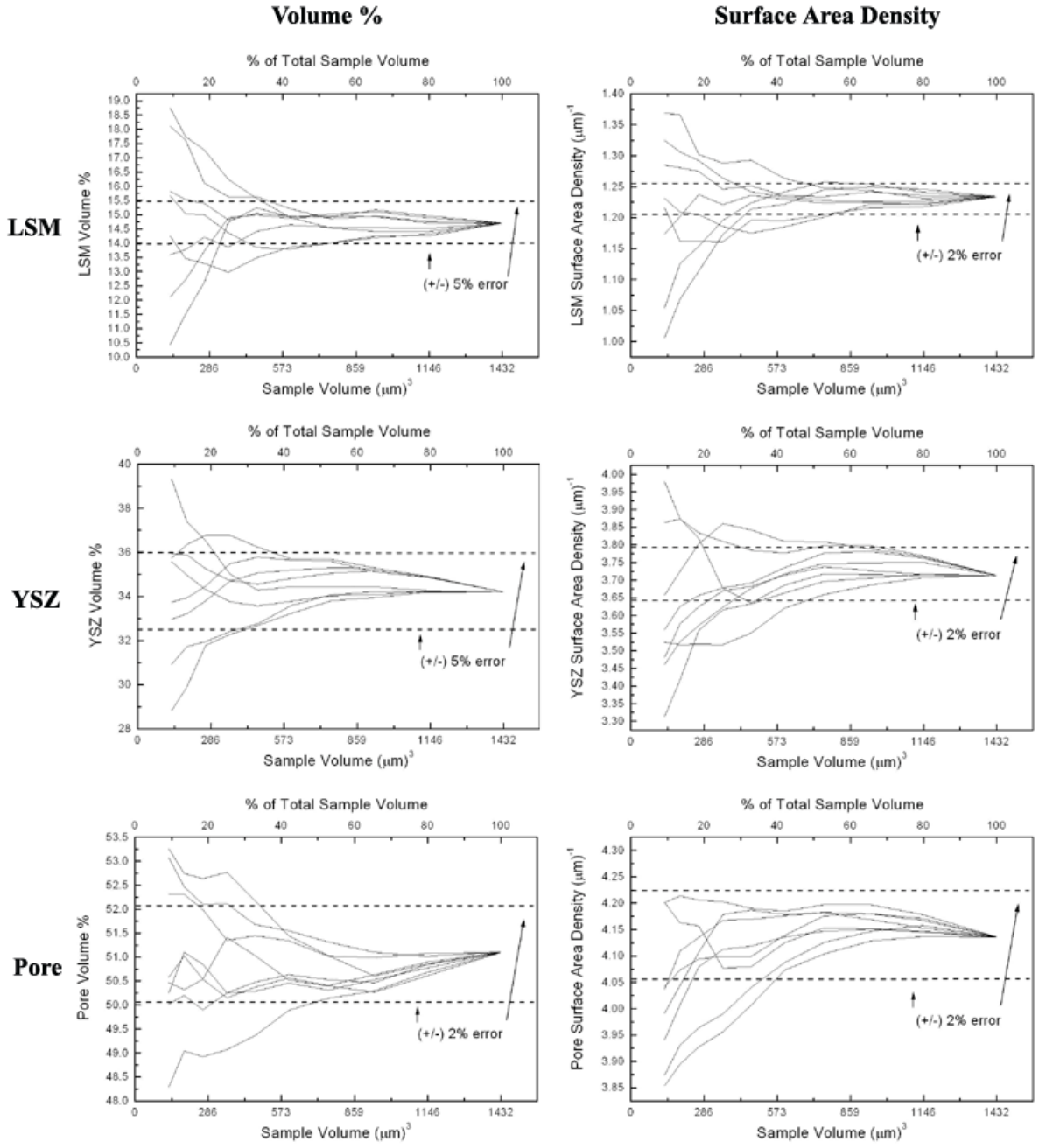

Figure 3.19. Volume % and surface area density calculations for the YSZ, LSM, and pore phases where 8 small cubes taken at each corner of the sample space were sequentially expanded up to the full volume.

least 10 times the length of the feature size per sample dimension.[226] The feature size of the microstructure can be estimated by multiplying the ratio of the phase volume to the surface area density by a factor of 5 (the factor is 4 for straight tubes and 6 for spheres). For the LSM-YSZ sample analyzed in this section, the estimated feature size is 0.65 μm for LSM and 0.41 μm for YSZ. Taking the largest feature size and using the 'times 10' rule, a volume of at least 275 μm^3 is required. This appears to underestimate the volume needed based on the analysis in Figures 3.19 and 3.20, which show that approximately twice that volume is necessary. It is important to note that based on this study, the volumes acquired in this thesis are sufficient to achieve at least better than 5% error.

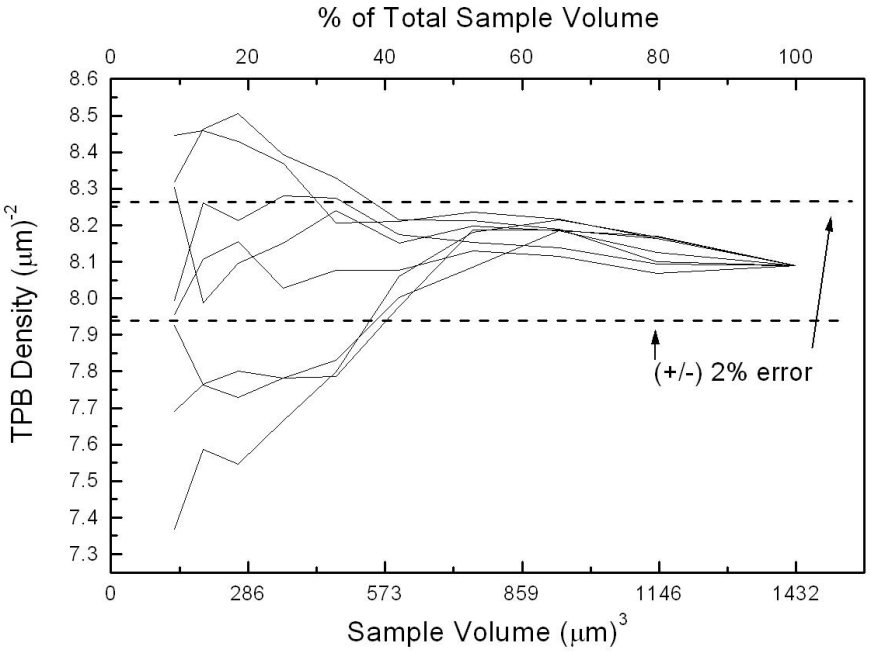

Figure 3.20. TPB calculations for 8 small cubes taken at each corner of the sample space that were sequentially expanded up to the full volume.

3.8.2 Calculation Errors and Sensitivities to Segmentation

An important potential source of error in the above structural quantities is the identification of phase boundaries (segmentation) in the 2D images. To test the magnitude of the errors, the images were segmented again with pore boundaries moved over a reasonable range of positions, typically 2-4 pixels, such that the inside and outside edge of each uncertain boundary was used, as shown in Figure 3.21. The resulting error ranges are summarized in Table 3.3. Note that the pore-YSZ boundaries were particularly broad due to apparent charging effects (image farthest left in Figure 3.21), producing a relatively large error range in the pore volume and surface area, while the Ni remained mostly unaffected. Table 3.3 illustrates that the segmentation uncertainty had a large influence on the YSZ and pore volumes, with diminished influence on surface areas. Perhaps not surprisingly, the exact boundary location had little impact on triple-phase-boundary density. This study highlights the importance of and advantage gained by filling the pores with epoxy, as discussed in section 3.4.3, where pore boundaries are not subject to charging and are easily identifiable.

Table 3.3. Error ranges (in percent) as a result of expansion and contraction of pore segmentation by 2-4 pixels.

	Ni (+/- %)	YSZ (+/- %)	Pore (+/- %)
Phase Volume	0.58	2.22	6.22
Surface Area	0.00	0.83	2.03
Triple-Phase Boundary Density	0.82		

Figure 3.21. From left to right: illustrations of a pore with charging along its border; original segmentation; “fill in” segmentation”; and “fill out” segmentation. The differences between segmentation methods are subtle (2-5 pixel differences) and are better reflected in the calculated parameters given in the discussion.

CHAPTER FOUR

Reconstruction of Mixed Conducting LSC Cathodes

Chapter 4: Reconstruction of Mixed Conducting LSC Cathodes

The work conducted on single-phase LSC cathodes was done in collaboration with Professor Stuart Adler and graduate student Cortney Kreller at the University of Washington. All testing and sample fabrication was done at the University of Washington. The following are two studies that were conducted involving the three-dimensional reconstruction of the electrodes of these samples.

4.1 Sintering Temperature Study

The LSC cathode layers were part of LSC symmetric cells on Gd-doped ceria (GDC) bulk electrolytes. The LSC cathodes were screen printed on both sides of the GDC, and fired at either 1000 or 1150^{o}C. The samples were not epoxy impregnated before imaging with the FIB-SEM, conducted on the Zeiss instrument at Argonne National Laboratory. Figure 4.1 shows an image of the milled region. In this case, the cathode surface was placed normal to the ion beam, and the interface with the GDC electrolyte was revealed by milling down into the cathode about 7 μm deep. Also provided in Figure 4.1 is an example of a cropped image from the sample that is ready for segmentation, along with the segmented image. It can be seen that material within the pores is readily visible, making automatic segmentation extremely difficult. As a result, the cropped images were segmented by hand, making sure to carefully identify only material that is at the polished surface.

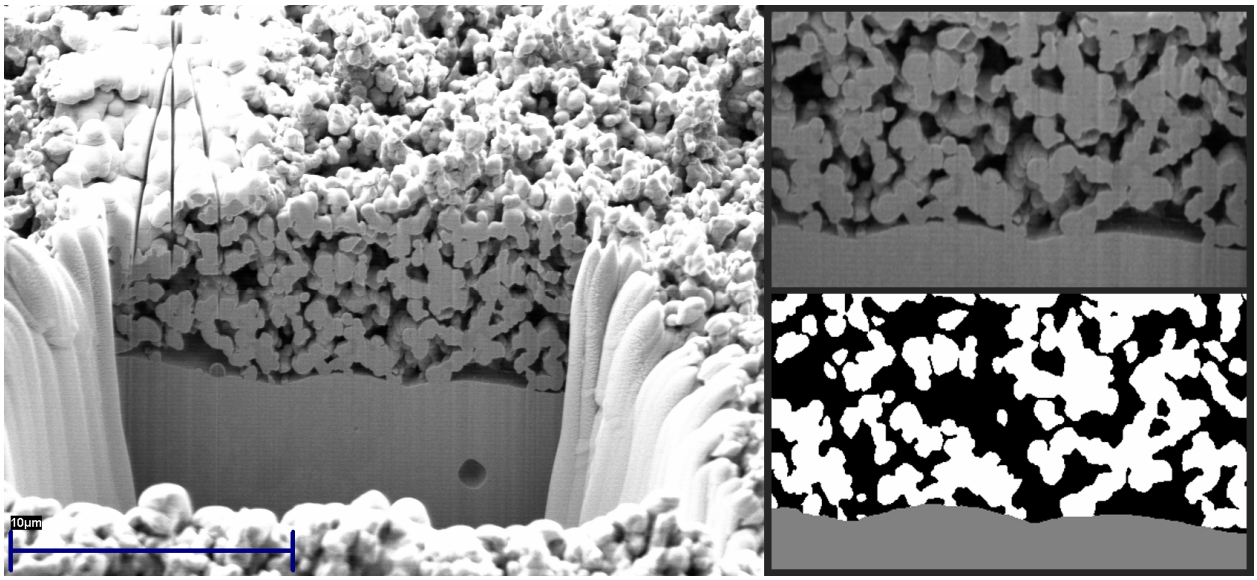

Figure 4.1. A bulk image of an LSC cathode milled from the top down to reveal the GDC electrolyte interface. The scale bar is 10 µm. The resulting cropped and segmented images are shown on the right.

3D reconstructions were performed on two LSC mixed-conducting single-phase cathodes that were sintered at 1000ºC and 1150ºC. Figure 4.2 shows a 3D image of the cathode sintered at 1150ºC, as well as a 3D representation of the interface between the electrolyte and cathode with inverse shading (gray is pore/GDC, black is LSC/GDC). Both samples show a high degree of porosity, sub-micron feature sizes, and a relatively small cathode-electrolyte interfacial area. The cathode-electrolyte interfacial area and cathode-pore surface area, which are both expected to be important in single-phase mixed-conducting cathodes[124], have been determined and are shown in Table 4.1. The data shows lower porosity for the cathode sintered at higher temperature, indicating greater sintering shrinkage. On the other hand, the cathode/electrolyte

contact area decreased slightly with increasing firing temperature; the reasons for this are not known at present. The LSC/pore surface area was slightly higher at the higher temperature, but a more typical measure is to normalize the LSC surface area to the LSC volume (not the total sampled volume), and this decreased slightly with increasing temperature.

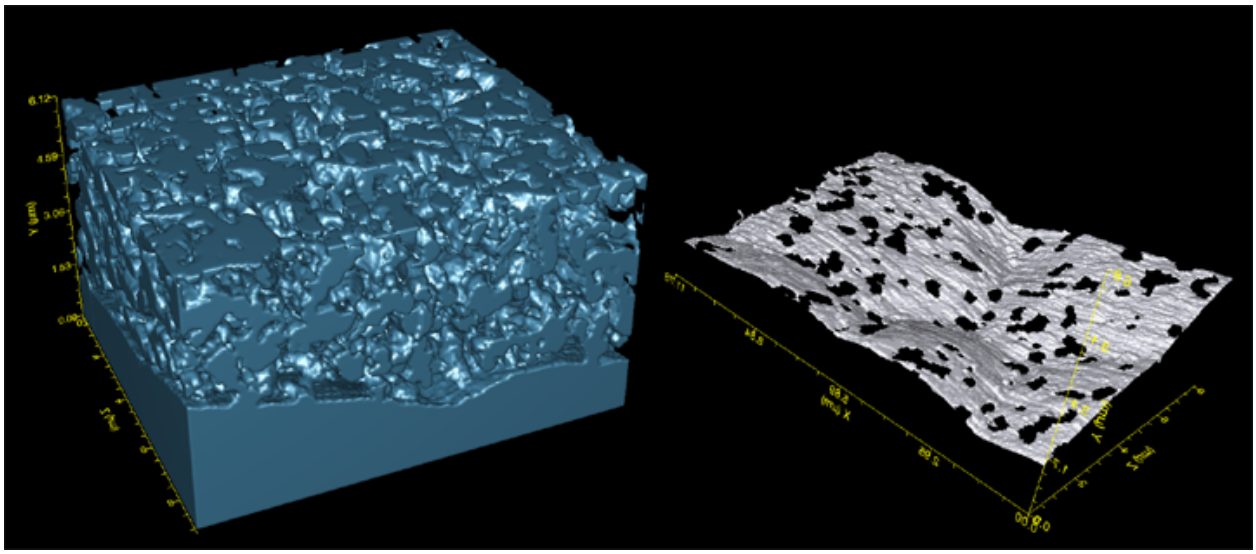

Figure 4.2. A 3D reconstruction of an LSC cathode on a GDC electrolyte, fired at 1150ºC, shown on the left. The interface between LSC and GDC is shown on the right (the black holes represent the LSC/GDC contact areas).

Further analysis of the relationship between the structure and the performance, as measured using non-linear electrochemical impedance spectroscopy (NLEIS), is discussed by Wilson *et al.*[240] This work showed that the reduction of oxygen on LSC cathodes is limited by dissociative adsorption on a limited number of vacant surface oxygen sites. While this step does not involve any charge-transfer barrier, an Arrhenius dependency is predicted due to the

large negative enthalpy involved.[241] Based on this conclusion, the performance of the electrode will be a function of the surface area density, and/or some surface activity per area that both change with processing and operating conditions. The surface area density is a structural component and can be directly measured using the technique developed in this thesis. As shown in Table 4.1, the surface area density does not change much between the two different sintering temperatures, despite the fact that dramatic differences in performance were observed for the two samples. This implies that the processing has greatly affected the surface activity of the LSC electrodes, perhaps altering the number and mobility of vacant oxygen surface sites. This work highlights the utility of having three-dimensional structural information to aid in determining the electrochemical behaviour of SOFC electrodes.

Table 4.1. Three-dimensional calculations for two LSC cathodes sintered at different temperatures.

	Volume %		Cathode-Pore Surface Area (μm^{-1})	Electrolyte Contact Fractions	
	Pore	Cathode		Pore-Elec	Cath-Elec
1000ºC	58.3 %	41.7 %	2.74	77.7 %	22.3 %
1150ºC	54.2 %	45.8 %	2.83	79.5 %	20.5 %

4.2 Reconstruction for Finite-Element Modeling

An additional study was conducted in order to better understand the relationship between the structure and the performance of LSC cathodes. The purpose of this study was to implement finite element modeling using a real microstructure in order to better describe the electrochemical processes involved in oxygen reduction. An LSC sample was analyzed extensively with EIS and non-linear EIS at the University of Washington to fully characterize the performance of the electrode.

The role of the work done in this thesis was to fully analyze the three-dimensional microstructure and provide the 3D structure for conversion to a finite-element mesh for modeling. The sample provided was imaged using the FEI instrument at Northwestern University using the auto-slice-and-view program. The sample was impregnated with epoxy before imaging in order to enhance the contrast between the pore and LSC phases and to eliminate viewable material within the pores, a problem found with the samples in section 4.1. Figure 4.3 shows an image of the milled region revealing the polished LSC cathode and the interface with the GDC electrolyte. The X and Y resolution of the images collected was 25 nm and the slicing resolution (Z direction) was 50 nm. The cathode thickness was only ≈7 μm, so the volume of material reconstructed was limited to ≈400 μm^3, although sufficient electrode area was covered.

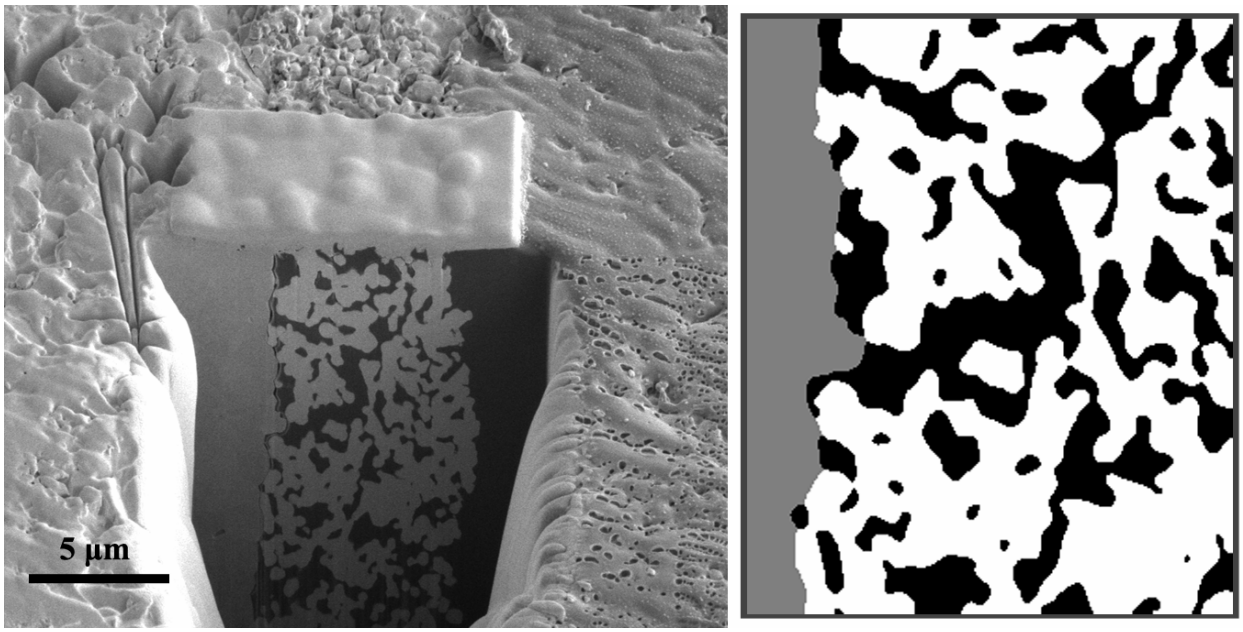

Figure 4.3. A bulk image of the milled region of an LSC cathode revealing the polished surface of the cathode and the GDC electrolyte interface. The resulting segmented image is shown on the right.

The LSC and Pore phases were initially segmented automatically such that the GDC and LSC were identified as the same phase. The GDC was segmented with respect to the LSC phase by hand, as slight contrast was observable between the two phases to allow for identification by eye. Figure 4.4 shows the full reconstruction of the LSC cathode, with separate images of the individual LSC and pore surfaces provided. The three-dimensional macroscopic structural information is provided in Table 4.2.

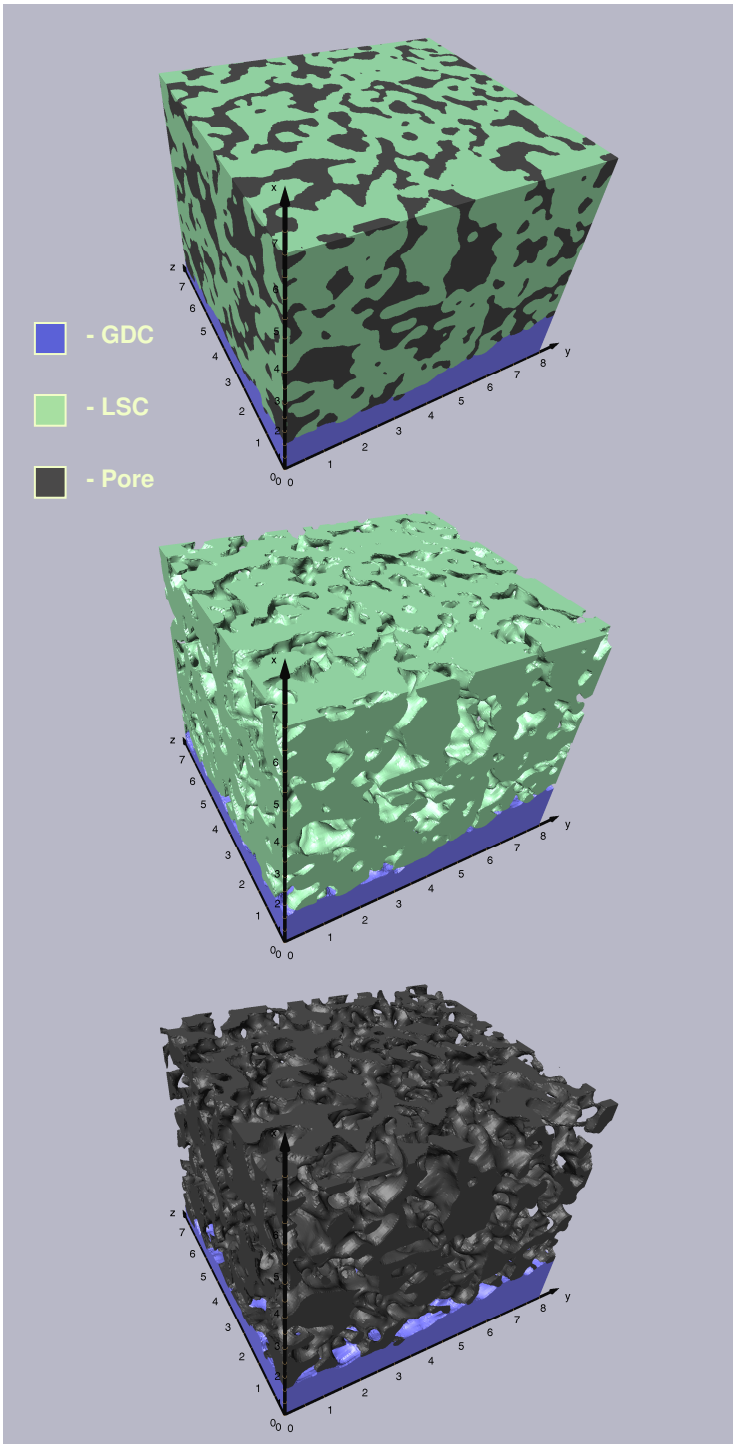

Figure 4.4. Images of the three-dimensional reconstruction of an LSC cathode. The top image shows all three phases, while the bottom two images show the surfaces of the LSC and pore phases, respectively.

Table 4.2. Three-dimensional structural information for a standard LSC cathode provided by the University of Washington.

Volume %		Cathode-Pore Surface Area (μm^{-1})	Electrolyte Contact Fractions	
Pore	Cathode		Pore-Elec	Cath-Elec
38.6	61.4	2.45	63.7	36.3

Figure 4.5 shows different views of the interface between the GDC (blue) and LSC (green). The morphology of the interface is clearly visible; in many cases the GDC surface appears to be raised in a plateau shape where it meets the LSC material. The quality of detail observed in the interface reconstruction is vital to correctly modeling the electrochemical performance. While reconstructions can provide macroscopic structural values important in models such as porous electrode theory, an equally important benefit of reconstructions is that they provide real structures for micro- and nano-scale modeling. The finite-element modeling of this sample is currently underway at the University of Washington, and results have yet to be published.

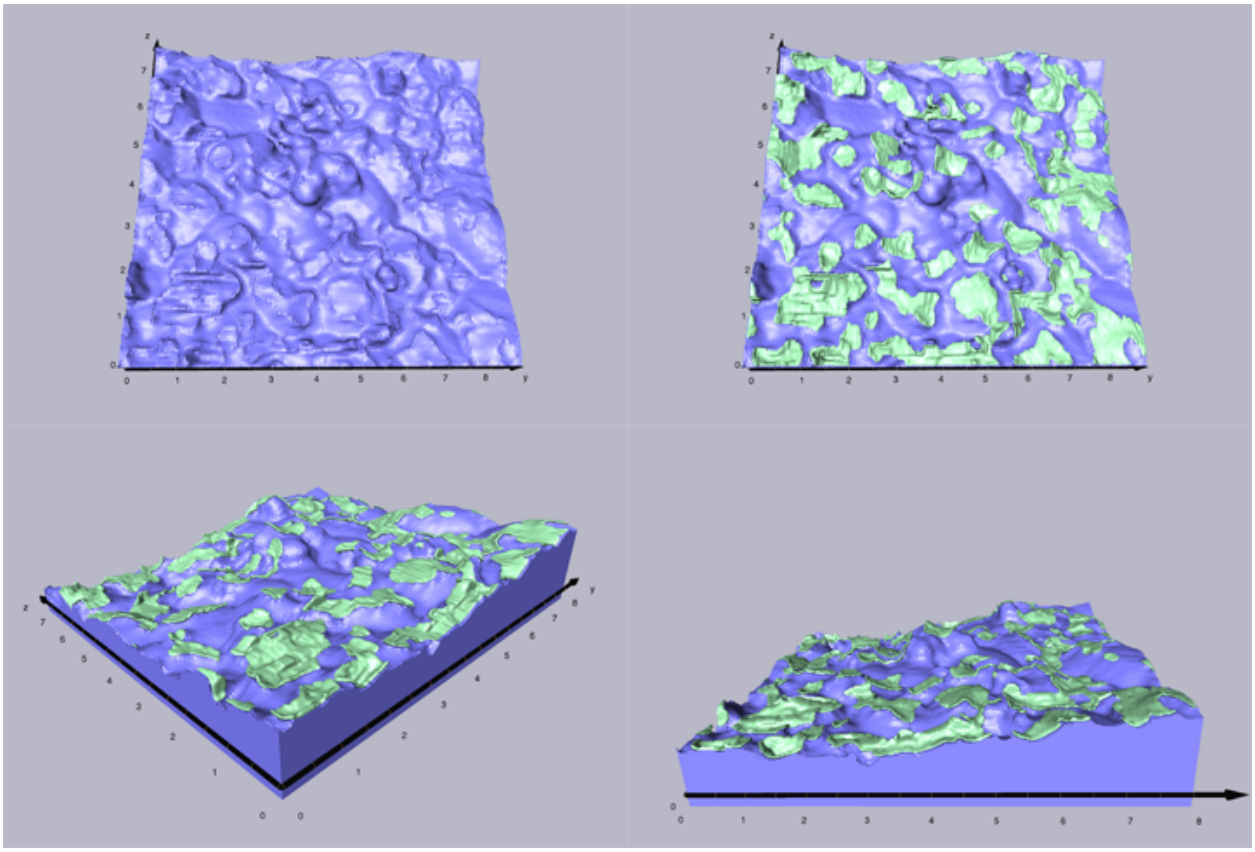

Figure 4.5. Different views of the reconstructed interface between an LSC cathode and GDC (blue) electrolyte. Where the cathode meets the GDC interface is highlighted in green.

CHAPTER FIVE

A Composite Ni-YSZ Anode Reconstruction

Chapter 5: A Composite Ni-YSZ Anode Reconstruction

5.1 Introduction

Numerous quantitative models have been developed to relate SOFC electrode microstructure to performance.[42, 53, 72, 103, 124, 134, 189, 242] These models often make use of porous electrode theory, which assumes the effect of microstructure can be embodied in macrohomogeneous properties such as surface area, three-phase boundary length, volume fraction of the various phases, and tortuosity of gas, ionic, and electronic transport paths.[243] In the absence of a detailed 3D understanding of the microstructure, it can be difficult to justify the assumptions of porous electrode theory rigorously. In addition, the relevant macrohomogeneous parameters can often be difficult to determine independently. For example, the surface area is usually too low to measure accurately using Brunauer-Emmett-Teller (BET) analysis, which in any case is unable to differentiate the surface areas of specific phases. Tortuosity is nearly impossible to measure from two-dimensional (2D) cross sections, since it relies on exactly how and where phases interconnect in three dimensions. While stereological methods can be used to estimate total three-phase boundary (TPB) length from 2D images,[176] such estimates are only accurate for isotropic microstructures. More importantly, 2D images cannot differentiate which portions of a particular phase or TPB are connected to contiguous gaseous, ionic, and electronic transport paths. In many cases, such parameters must be estimated based on specific idealized geometric models[244, 245], or remain adjustable parameters. Finally, under circumstances where porous electrode theory breaks down, the absence of 3D microstructural data makes it difficult to proceed. Although some workers have examined the

role of local microstructure on performance, these models typically assume an idealized (hypothetical) 3D microstructure[136, 211], rather than the actual structure in question.

Here the use of dual-beam focused ion beam scanning electron microscopy (FIB-SEM) for making a complete 3D reconstruction of a solid oxide fuel cell (SOFC) Ni-YSZ composite anode is demonstrated. This data is used to calculate critical microstructural features such as volume fractions and surface areas of specific phases, three-phase boundary length, and the connectivity and tortuosity of specific sub-phases.

5.2 Experimental Procedure

The focus of this initial study was the Ni-yttria-stabilized zirconia (Ni-YSZ) composite anode, typical of an anode-supported SOFC.[209, 246] This system was chosen because it typifies the problem of connecting microstructure to performance in a 3-D microstructural network.[160, 167] The anode-supported, thin-electrolyte SOFC studied was Ni-YSZ/YSZ/LSM-YSZ,LSM (YSZ = 8 mol% Y_2O_3-stabilized ZrO_2 and LSM = $La_{0.8}Sr_{0.2}MnO_3$). The anode substrates, consisting of NiO/YSZ (70/30wt%) with 10% starch filler, were bisque fired at 1000^0C. Thin (10-20 μm) layers of NiO/YSZ (50/50wt%) and YSZ were deposited on the supports using a colloidal deposition technique similar to that described previously.[24] The anode and electrolyte were co-fired at 1400^0C for 6h. LSM-YSZ cathode layers were applied and fired at 1200^0C for 4 h. A second layer of pure LSM slurry was then applied and fired at 1200^0C for 4 h. The colloidal NiO/YSZ layer adjacent to the YSZ electrolyte, which was the electrochemically active portion of the anode, was the region studied in detail here.

The single cell was tested using a standard testing geometry, similar to that reported previously.[28] At the beginning of the test, the Ni-based anode was fully reduced in humidified H_2 at 800^0C. The cell was tested with air at the cathode, while the fuel was humidified hydrogen. Cell electrical testing was carried out at 600-800°C, with a maximum power density of ≈ 1.2 W/cm^2 produced by the cell at 800°C, as shown in Figure 5.1 where the current versus voltage was recorded. This power density is fairly typical of SOFCs tested under these conditions.[28, 34, 209, 246] Thus, the microstructures examined below are believed to be representative of state-of-the-art Ni-YSZ SOFC anodes.

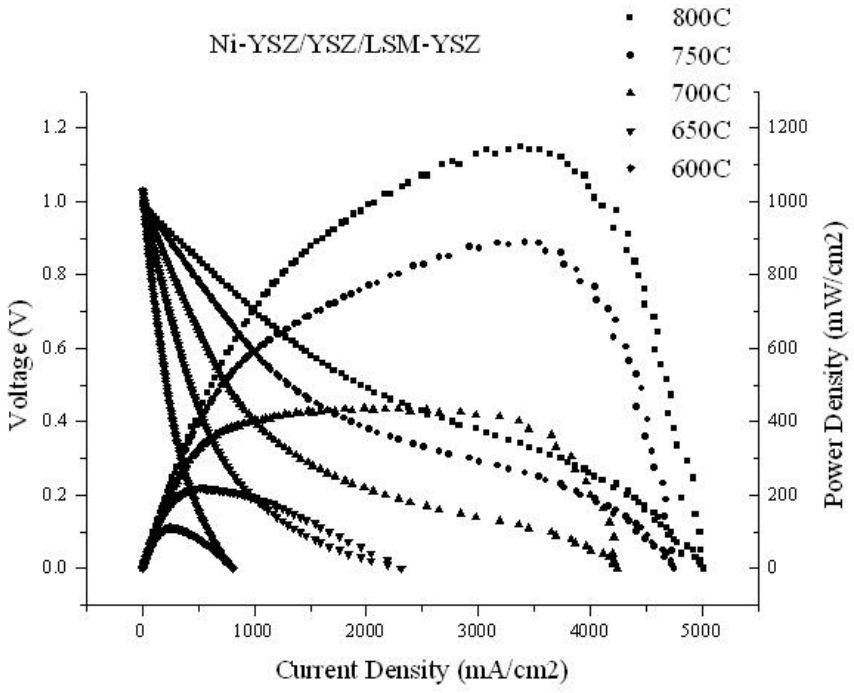

Figure 5.1. Measured voltage and power density versus current density for the SOFC utilized in the present study.

The present images were collected using the Zeiss 1540XB instrument at Argonne National Laboratory. A spacing v = 44nm between consecutive images was calculated from the fixed FIB milling rate and the milling time per image. A total of 82 images were used in the reconstruction, which were segmented manually over a span of a few weeks, much more time than that needed for image acquisition and 3D calculations (a few hours each). Due to the different resolutions in different directions – 13.9 nm in the image plane and 44 nm between images – in the 3D data sets, the desired approximately cube-shaped voxels were obtained by reducing the resolution to 41.7 nm in the images. This loss of resolution was not a serious problem for the present anodes, which were typical of state-of-the-art SOFC anodes, where the feature sizes ranged from ~ 200 nm to 1 μm. The detailed procedures for image collection and image stacking can be found in Chapter 3. Figure 5.2 illustrates the resulting 3D reconstruction showing the Ni (green), YSZ (transparent), and pore phases (blue).

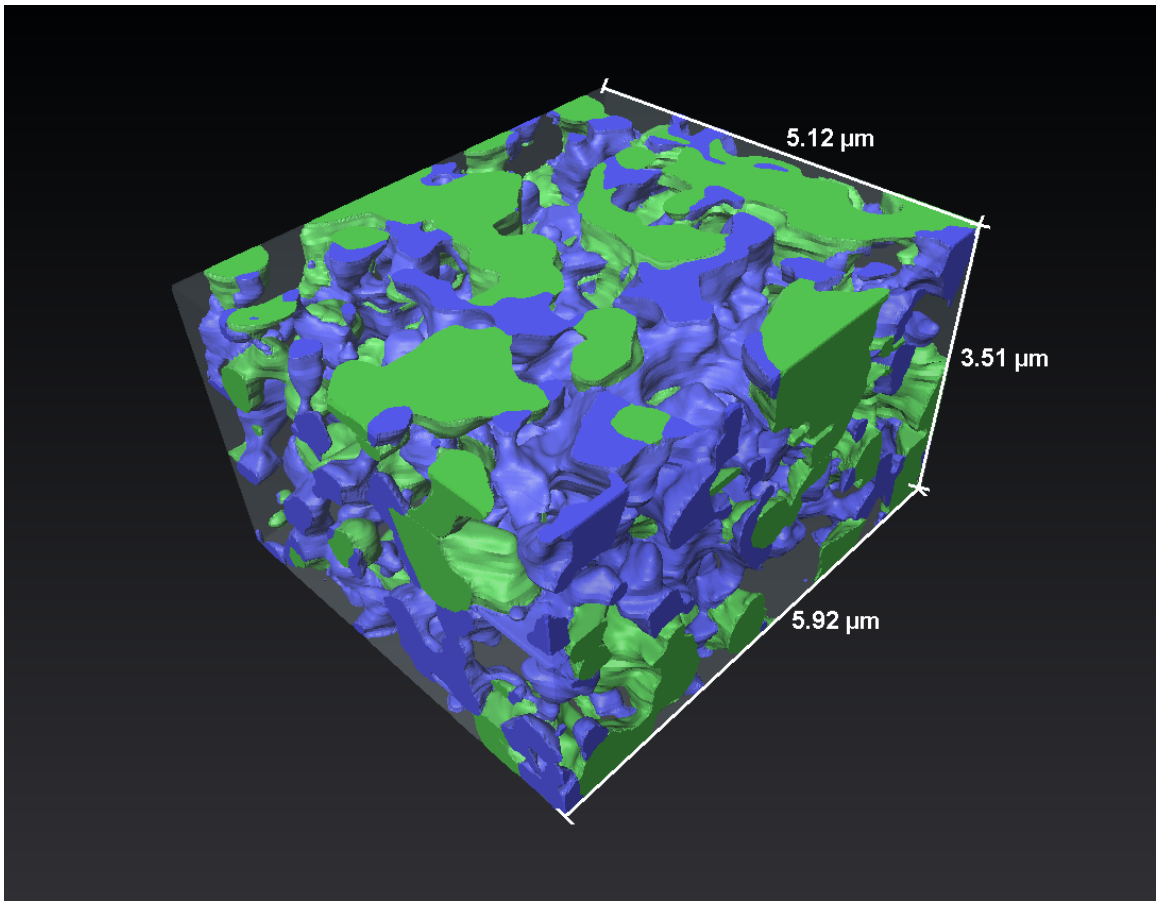

Figure 5.2. A view of the 3D anode reconstruction showing the Ni (green), YSZ (transparent), and pore (blue) phases.

5.3 Experimental Results and Discussion

A key application of 3D reconstruction is to make quantitative correlations between processing and microstructure. A rudimentary example is quantification of phase volume fractions. The volume percentages of Ni, YSZ and pores calculated from the 3D reconstruction were 25.9%, 54.6% and 19.5%, respectively. This gives a Ni-to-YSZ volume ratio of 32:68. Using the starting powder weight ratio of NiO:YSZ = 50:50 (47.61:52.39 by volume),

calculations based on the volume change upon reduction of NiO to Ni yielded a final volume ratio of Ni:YSZ = 35.04:64.96. The agreement between this value and that obtained from the 3D reconstruction indicates that the boundaries between the phases were located accurately from the 2D images. Assuming that the measured Ni plus pore volume (45.4%) was primarily NiO plus some small residual porosity prior to reduction, and using the ≈41% volume reduction on going from NiO to Ni, yields a pre-reduction NiO-YSZ porosity of 1-2%. That is, the as-fired NiO-YSZ anode active layer was nearly dense such that most of the final porosity resulted from NiO reduction.

Similarly, we can determine the interface/surface areas of each phase in the anode. Surface area is often used as a measure of the particle size in particle compacts, and the surface area of a mixed conducting phase can help determine the electrochemical reaction rate.[53] In the present case, the measured total phase-boundary areas per unit volume were 3.0 μm^{-1} for YSZ (including interfaces with Ni and pores), 1.6 μm^{-1} for Ni (including interfaces with YSZ and pores), and 2.4 μm^{-1} for the pores. In order to check the accuracy of these values, we deliberately changed the 3D data set resolution and found a small (≈5%) variation (see supplemental section for details). This suggests that the FIB-SEM resolution was sufficient to avoid significant errors for these anodes. For comparison, the starting YSZ and Ni powders had surface areas of ≈6 m^2/g. Using the volume densities of YSZ and Ni (from the reconstruction) to convert the phase-boundary areas to these units yields ≈ 1 m^2/g. That is, the high temperature firing of the NiO-YSZ anode yielded considerable coarsening/sintering. This approach will be used in the future to systematically examine how the final phase-boundary areas vary with processing conditions, e.g. initial powder area per mass, firing temperature and time, etc.

Another important application of 3D reconstruction is to quantitatively connect microstructure to electrochemical performance. The anode electrochemical performance depends on microstructure in a complex fashion, with factors including surface areas, three-phase boundary lengths, and phase connectivity/tortuosity playing key roles[53, 72, 134, 189, 242] The preliminary analysis below demonstrates use of 3D microstructural data to extract key microstructural features of the Ni-YSZ anode.

It is important to analyze the tortuosity of the ionic, electronic, and gas-phase transport pathways within the electrode network. For example, a high gas-phase tortuosity at the anode inhibits the exchange of H_2O and H_2; this can limit cell performance and is most readily observed as a limiting current behavior at high current densities (e.g. the rapid drop in cell voltage above ≈ 4 A/cm^2 seen in Figure S1). Due to the high conductivity of Ni, the tortuosity of the electronic phase is considered negligible. The tortuosity of the pore structure was calculated as described in section 3.6.4 for the three primary axes, $x_i = x, y, z$, of the sample volume to account for any anisotropy. The gas-phase tortuosity based on this procedure was found to be (τ_x, τ_y, τ_z) = (2.1, 2.2, 1.9). A tortuosity factor of 2 is consistent with typical porous catalysts, and the values are reasonably isotropic.

Three-phase boundary (TPB) length is another widely viewed key electrode structural parameter. For a SOFC anode, this concept can be understood by considering the electrochemical reaction of H_2 with an oxygen ion O^{2-} to produce the product H_2O:

$$H_2(gas) + O^{2-}(YSZ) \rightarrow H_2O(gas) + 2e^-(Ni) \qquad (5.1)$$

This reaction involves gas phase species (present in pores), free electrons (in Ni), and oxygen ions (in the YSZ phase), and hence is expected to occur at a rate correlated to the TPB length. Figure 5.3 shows an inventory of TPBs obtained by analyzing the 3D anode data displayed in Figure 5.2 (the color coding of the TPBs is explained later). The volume-specific TPB length was found to be 4.28×10^6 m/cm^3. Although TPB lengths have previously been estimated from 2D images of LSM-YSZ cathodes[176], this is the first direct measurement published that is known to the author.[180]

A crude assessment can be done to determine if the measured TPB density reported above is consistent with the measured SOFC performance. We can estimate the expected anode area-specific resistance by multiplying the above TPB density by previously measured values of the length-specific resistance (LSR) of the TPB, and an approximate anode active depth (≈10 μm).[160, 247] Based on various studies including point-contact[159, 167] or patterned[164, 166] electrodes, reported LSR values vary in a range from 5×10^4 to 5×10^6 Ω-cm at 700°C, yielding anode area-specific resistance of 0.1~10 Ω-cm^2. Although broad, this range encompasses typical values for this type of SOFC anode[248] and is consistent with our total SOFC area-specific resistance at 700°C (≈0.7 Ω-cm^2, from the data in Figure 5.1, which also included electrolyte and cathode resistances). The large uncertainties in this comparison reinforce the need to separate microstructure from other complicating variables, including utilization gradients, impurities, polarization, and polarization history, all of which have been shown to be important in overall anode performance.[167]

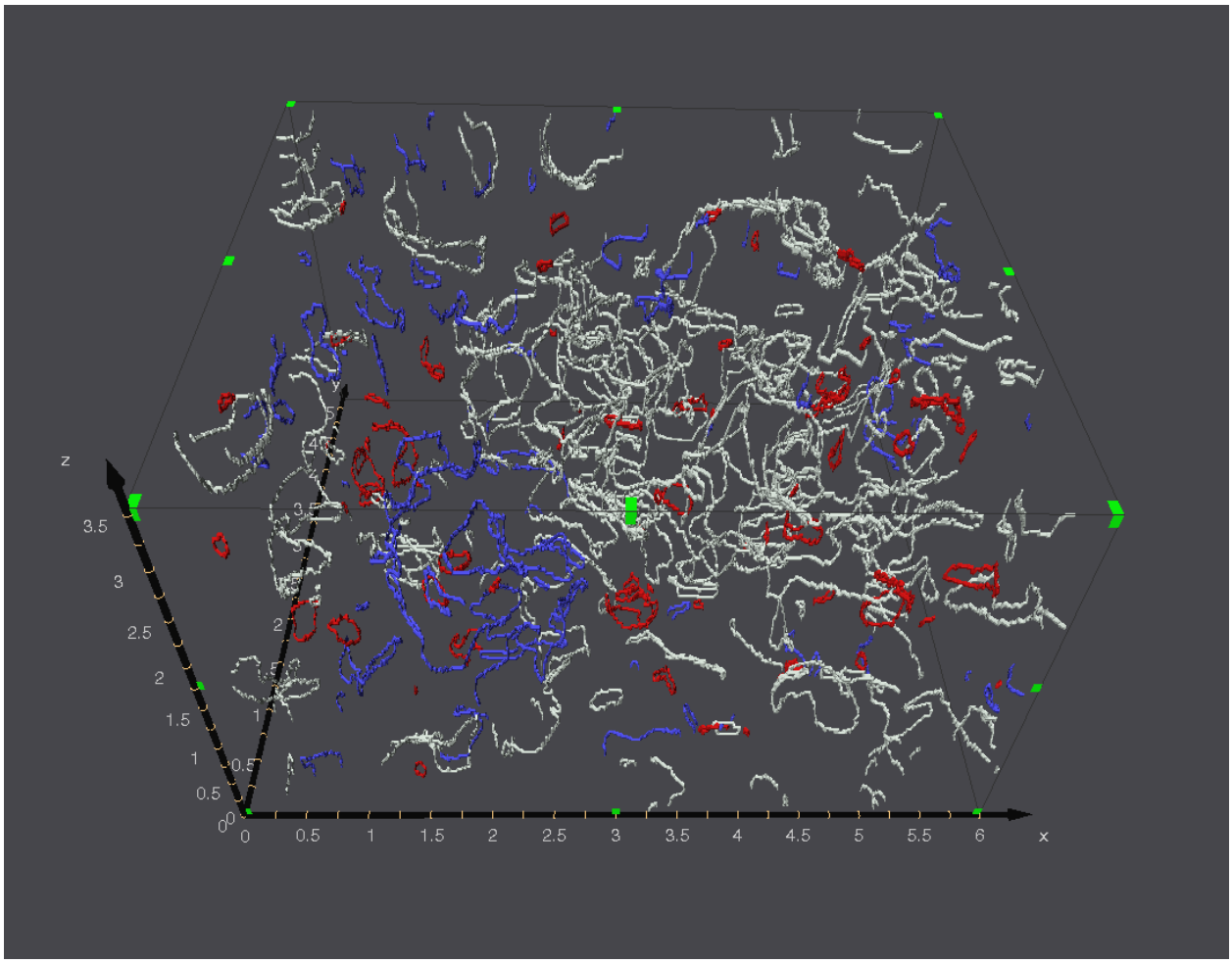

Figure 5.3. Three-dimensional visualization of the anode TPB lines. The "active" TPBs are white, the TPBs of unknown activity are blue, and the inactive TPBs are red. The axis units are microns.

In order for a TPB to contribute to anode electrochemistry (equation 5.1), the gaseous, ionic, and electronic phases adjoining the TPB must have a contiguous connection to the rest of the microstructure. That is, the pore must be connected via the surrounding pore network to the fuel stream, the Ni phase to the external electrical circuit, and the YSZ phase to the bulk YSZ

electrolyte. A lack of phase contiguity was previously used to explain poor electrochemical performance of Ni-rich or YSZ rich Ni-YSZ anode compositions,[249], but contiguity was not directly measured. Methods for extracting phase contiguity data from 3D images have been developed but not applied to fuel cells.[236-238] In this study, the interconnectivity of each of the Ni, YSZ, and pore phases was obtained, allowing for the calculation of the "active" triple-phase boundary density, *i.e.,* the portion of TPB length that is connected to contiguous ionic, electronic, and gaseous transport paths.

Figure 5.4 shows the cumulative size distributions of Ni networks making up the Ni phase in the Ni-YSZ anode for three cases: the unfiltered original segmented data, the same data after one filtering step, as well as after two filtering steps (where the filtering procedure is defined in section 3.5.4). The large number of single-voxel networks, *i.e.,* those with a volume of ~ $7.7*10^4$ nm, present in the unfiltered data, were eliminated after two filtering steps. Furthermore, there was little or no change in the distribution of larger networks, network shapes showed minimal change, and the sample composition by volume was unchanged and agreed with values previously obtained from this data set [250]: 55% YSZ, 26% Ni, and 19% pore. Hence, two filtering steps struck a balance between eliminating very small voxel errors and avoiding changes from the original microstructure, and all the results described below were obtained from this set of images.

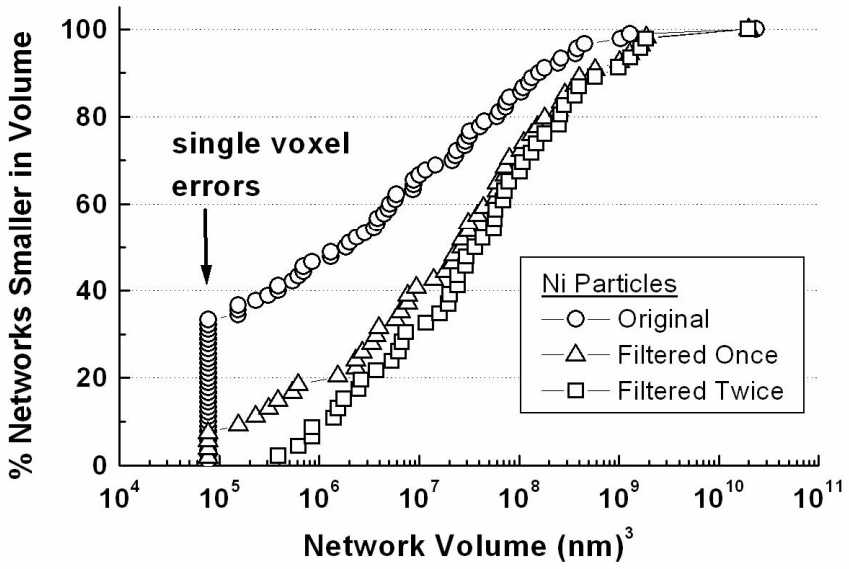

Figure 5.4. Cumulative size distributions of networks constituting the Ni phase in the Ni-YSZ anode, obtained from the original three-dimensional data set and after one or two filtering steps.

Figure 5.5 shows the cumulative size distributions of the networks making up the Ni and pore phases. The YSZ phase was not shown because it was one contiguous network (99.9% of the total YSZ volume). This figure shows that the volume of the largest Ni network was ≈ 10 times that of the next-largest network. That is, the Ni phase was dominated by a single connected structure that included 68% of the total Ni volume. The situation with pores was similar – the largest pore constituted 87.5% of the total pore volume.

Figure 5.5 also indicates which networks were contiguous across the sample volume (labeled "across"), which ones intersected one boundary face and dead-ended within our sample volume (labeled "dead-end"), and which ones were completely isolated within the sample

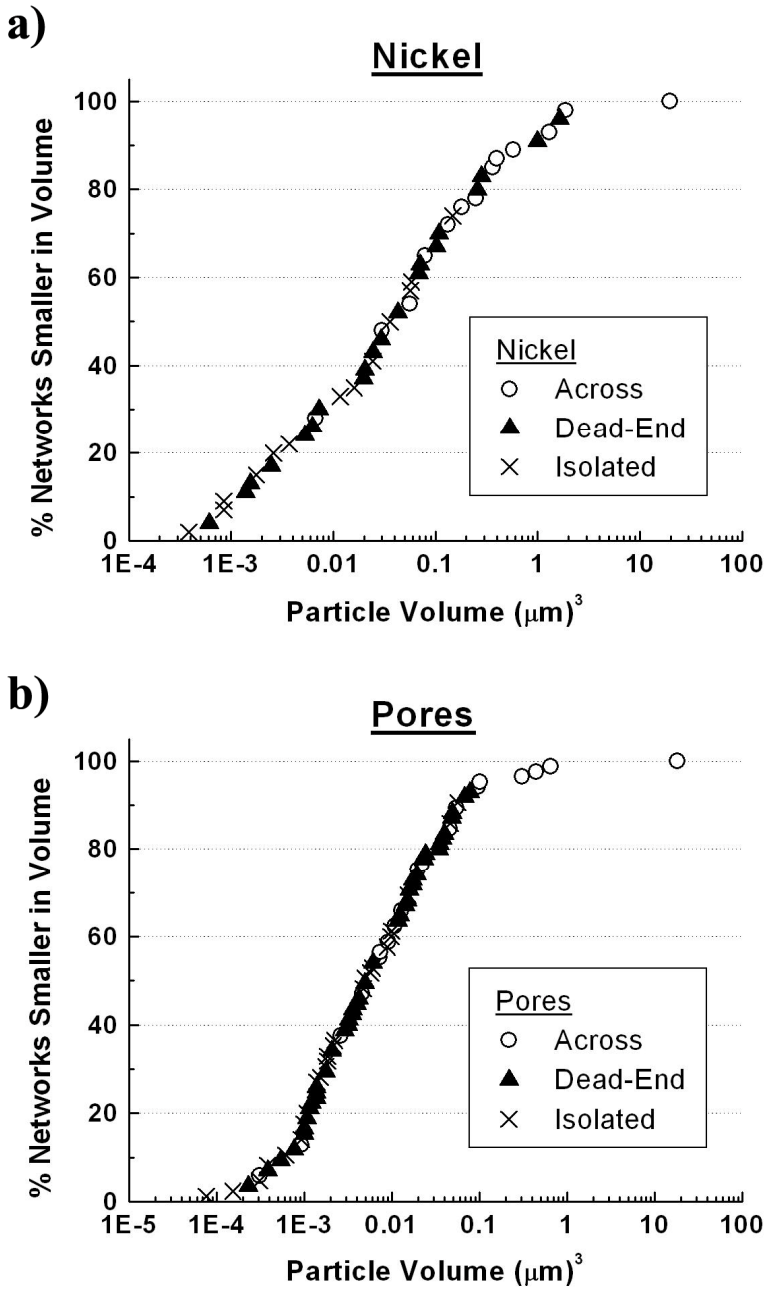

Figure 5.5. Cumulative size distributions of Ni (a) and pore (b) networks in the Ni-YSZ anode. The Y-axis corresponds to the percentage of networks that are smaller than the given volume. YSZ is not shown because it constituted one contiguous network.

volume (labeled “isolated”). Most of the small volume networks were isolated, while the larger networks tended to be connected across the anode structure. The volumes of each type of network were summed and are given in Table 5.1 as a percentage of total phase volume. Contiguous (“across”) networks made up 86 vol% of the Ni phase, 100% of the YSZ phase, and 96% of the pore phase. The high contiguity of the YSZ phase compared to Ni is expected given its higher overall volume fraction (55% versus 26%). On the other hand, it is somewhat surprising that the pore phase, with only 19% total volume, was more well connected than the Ni. This may indicate a tendency of the pores to appear on Ni-YSZ interfaces and to connect with each other in order to minimize interfacial energy. Figure 5.6 provides a visualization of the networks making up the Ni phase. Figure 5.6a shows the entire Ni microstructure, while Figure 5.6b highlights the isolated Ni networks in red, and the dead-end networks in blue.

Table 5.1. Volume percentages of the different connectivity networks making up each anode phase.

	YSZ	Ni	Pore
Connected	100.0	86.0	96.1
Dead-End	0.0	12.7	3.0
Isolated	0.0	1.3	0.9

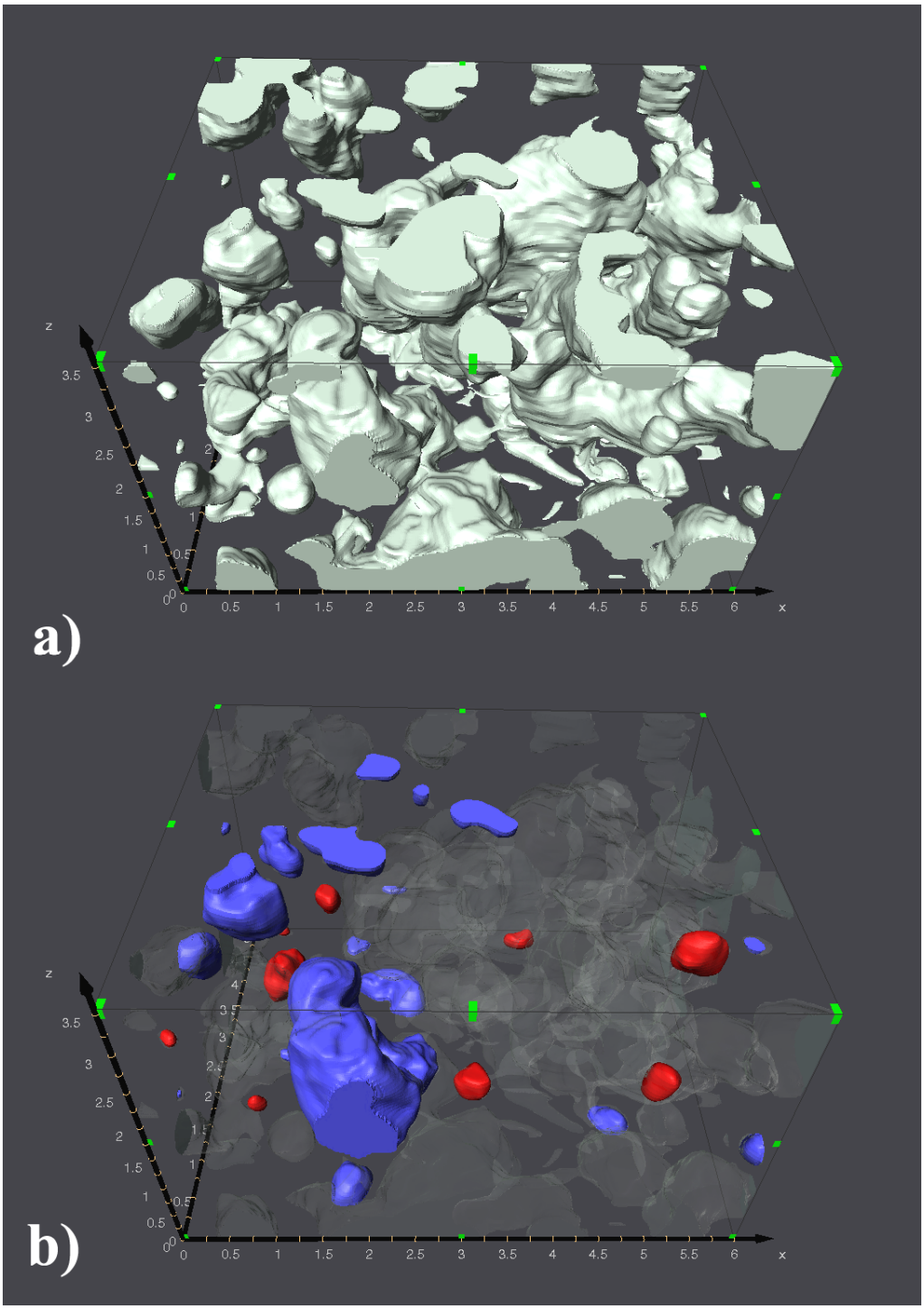

Figure 5.6. Three-dimensional visualization of the networks constituting the Ni phase. Part (a) shows the entire Ni phase, while part (b) highlights the isolated Ni networks in red, and the dead-end networks in blue. The axis units are microns.

In order to assess the effect of phase contiguity on electrochemical kinetics, anode triple phase edges were counted and analyzed to identify the fractions that were on “across” versus “ isolated” or “dead-end” networks, as described previously. The significance of these distinctions is that “isolated” networks contribute only “inactive” triple-phase boundaries to the electrode, whereas TPBs on “across” networks are expected to be electrochemically active, and those on “dead-end” networks are of unknown status. It is found that 5.1% of the total TPB length was on isolated metal networks, 5.3% on isolated pores, and 0% on isolated YSZ. Taking into account that 0.9% of these TPB segments lie on both isolated metal and pores, we calculate the total TPB percentage by length that is electrochemically inactive to be 9.5%.

In a similar manner, the TPBs that lie on “dead-end” pores or Ni were identified to determine the fraction of TPBs for which the activity was unknown. Figure 5.3 shows a 3D visualization of the entire set of TPB lines, where the “active” TPBs are white, the TPBs of unknown activity are blue, and the inactive TPBs are red. The lengths of these different categories of TPB lines are measured and presented in Table 5.2 with respect to the total TPB density.

Table 5.2. Summary of the TPB electrochemical activity showing the percentage of TPB by length that lies on dead-end and isolated networks for the Ni and Pore phases (YSZ is 100% contiguous).

	Ni	Pore	Both	Total
Isolated	5.1	5.3	0.9	9.5
Dead-End	17.6	7.1	0.9	23.8

It is reasonable to assume that the networks that lie on the boundary of our volume will mimic the connectivity of those contained within, such that only a small percentage of the dead-end networks are isolated in actuality. Hence, as ~9.5% of the TPB length lies on isolated networks, we assume that 9.5% of the 23.8% of TPB length that lies on "dead-end" networks is also inactive. This gives us a value of 11.6% for the total length of TPB that is considered inactive. The amended electrochemically active TPB density is then ~3.7 μm^{-2}, from a total density of 4.2 μm^{-2}.

There are limitations to the above-described procedure. It does not provide any information on the degree of connectivity, only whether there is connectivity or not. One could question, for example, why the present anode composition (50:50 wt% NiO:YSZ, yielding 55 vol % YSZ) is widely used in anode active layers; it would appear that somewhat higher Ni and pore volume fractions would improve their connectivity while not decreasing that of YSZ significantly. In reality, however, the very low ionic conductivity of YSZ compared to gas diffusivity in pores and electronic conductivity in Ni must be considered. Thus, a TPB with a connection to the electrolyte via a very narrow YSZ pathway may be effectively equivalent to a disconnected TPB, which is not the case for Ni or pores. The higher YSZ content presumably yields similar effective degrees of connectivity of the three phases, such that transport through one individual phase does not become a dominant rate-limiting step. A full treatment of these effects may require finite element analysis, as in previous pore tortuosity gas diffusion calculations.[250]

5.4 Summary and Conclusions

A technique was implemented for using three-dimensional image data to identify the separate contiguous networks constituting each of the solid and pore phases in SOFC electrodes. The method was used to determine the size distribution and level of connectivity of the Ni, YSZ, and pore phases of a Ni-YSZ anode. Triple-phase boundary edges were identified and the connectivity of each of its three phases was assessed in order to determine the percentage of the TPBs expected to be electrochemically active. Together with phase volume fractions, surface areas, and tortuosities, the present results provide a reasonably complete quantitative description of the electrode microstructure, as needed for utilizing 3D images to determine the links between processing variables, microstructure, and the resulting electrode polarization resistance. While the present results focused on an SOFC anode, this method can be implemented as a general, quantitative technique for analyzing the complex microstructure of fuel cell electrodes, as demonstrated in other Chapters of this thesis.

CHAPTER SIX

Composition Study of Composite Ni-YSZ Anode Microstructure

Chapter 6: Composition Study of Composite Ni-YSZ Anode Microstructure

6.1 Introduction

The choice of Ni-YSZ anode composition determines a number of properties that control solid oxide fuel cell (SOFC) performance. A range of Ni-YSZ compositions provides sufficient electrical conductivity and reasonable thermal expansion match with the YSZ electrolyte.[66, 251] A study of the effect of Ni content on anode electrochemical performance showed that a Ni volume fraction of 40 – 45% (corresponding to ~ 60 wt% NiO) yielded minimum polarization resistance.[252] The anode active layer composition in anode-supported cells is similar, 50:50 to 60:40 wt% NiO:YSZ, and yields low polarization resistance as indicated by relatively large power densities.[61, 248, 253-255] However, there has not been a systematic study to date of the effect of composition on anode performance in anode-supported cells.

Although triple-phase boundary (TPB) density is widely cited as the key microstructural feature that determines Ni-YSZ anode polarization resistance $R_{P,A}$, there is little specific quantitative information available regarding how composition affects TPB density or $R_{P,A}$. Composite-electrode structural models suggest that the composition dependence of the TPB density is strongly dependent on processing-related parameters, especially the relative Ni and YSZ particle sizes.[191, 192] This suggests that the optimal composition will vary depending on the Ni and YSZ powder processing conditions. Furthermore, it is unknown to what extent composition affects phase contiguity, and how this in turn impacts electrochemical performance. In one experimental study, stereological analyses of optical micrographs were employed to determine the phase contiguity of Ni-YSZ microstructures, but the TPB density was not determined and the results were not related to polarization resistance.[256]

Here we present results correlating the structural and electrochemical effects of Ni-YSZ composition. Ni-YSZ / YSZ / LSM-YSZ anode-supported SOFCs were prepared with varying Ni-YSZ active layer compositions. After electrochemical impedance spectroscopy (EIS) characterization of the cells, a focused ion beam – scanning electron microscope (FIB-SEM) was used to obtain anode active layer images.[181, 250] FIB-SEM has the advantage that FIB milling provides high-quality, planar, damage-free cross sections, and the large number of images in a typical data set provides good statistics. Quantitative anode microstructural data was obtained from the images using both stereology methods and full 3D reconstruction calculations.

6.2 Experimental Procedure

SOFC button cells were prepared with a standard anode-supported structure: Ni-YSZ support, Ni-YSZ active layer, thin YSZ (8 mol% Y_2O_3-stabilized ZrO_2) electrolyte, LSM-YSZ cathode active layer, and LSM ($La_{0.8}Sr_{0.2}MnO_3$) current collector.[25] The supports were pressed pellets approximately 700 μm thick prepared from 45 wt% NiO, 45 wt% YSZ, and 10% starch filler that were bisque fired at 1000°C. The Ni-YSZ anode active layer and YSZ electrolyte, each ~10 μm thick, were drop-coated from NiO-YSZ and YSZ colloidal solutions, respectively, after which the structure was co-fired at 1400°C for 4h. LSM-YSZ ink was prepared by mixing the powders with a vehicle (Heraeus), followed by printing and firing at 1200°C for 4h to produce a cathode active layer of ~30 μm thickness with a cell active area of 0.5 cm^2. The LSM layer was then applied in the same way and fired under the same conditions. Cathode porosity was estimated at ~50% based on subsequent results from identically processed cathodes.

A series of cells were prepared in which all layers were processed identically as above, except for the thin (~10 μm) Ni-YSZ anode active layer. The colloidal solutions were prepared with four different NiO:YSZ starting compositions, with the respective weights W set such that the NiO wt% $X_{NIO} = 100 * W_{NiO}/(W_{NiO}+W_{YSZ}) = 40$, 50, 60, and 70. The starting powders were Baker NiO and Tosoh YSZ. For the anode active layers, the powders were ball milled together for 24h, a procedure that should have little effect on particle sizes. Thus, the present results were representative of a widely-used combination of NiO and YSZ powders.

The button cells were tested using a standard testing geometry, similar to that reported previously.[257] At the beginning of each test, the Ni-based anode was fully reduced in humidified H_2 at 800°C. Current-voltage curves and impedance spectroscopy (IS) plots were collected using a Zahner IM6 electrochemical testing station, with stagnant air at the cathode and 50 sccm of humidified hydrogen (97% H_2, 3% H_2O) at the anode.

Two sets of images were collected for each sample using the Zeiss instrument at Argonne National Laboratory implementing the serial-sectioning technique as described in section 3.4.[181, 250] At first, a set of images was collected for each sample with the original open porosity. These images were very difficult to segment due to charging and visible material in the porosity, as shown in Figure 6.1. As a result, the set of images was used primarily for stereological calculations. Concurrently, the samples were impregnated with epoxy and a second set of images for each sample was collected. These images were segmented by hand and used to create full 3D reconstructions of the microstructure. Figure 6.1 shows an example of each of these types of micrographs for the sample with $W_{NiO} = 70$. The images in both sets had an X-Y spatial resolution of 24.8 nm/pixel and a Z-spacing of 25 nm between each consecutive image.

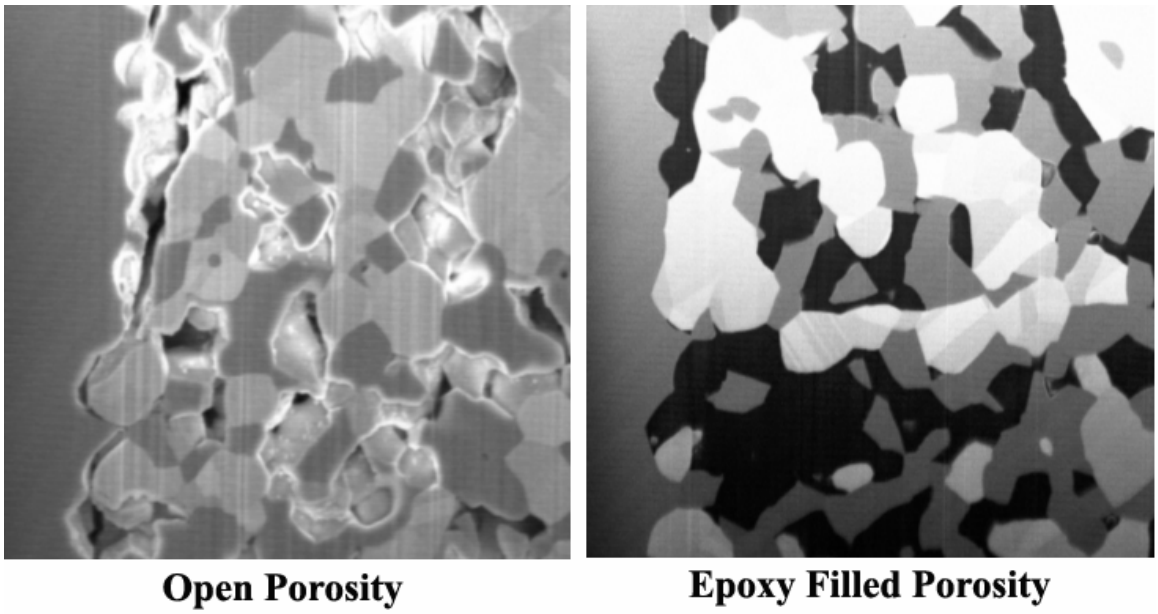

Figure 6.1. Two micrographs from the same Ni-YSZ anode sample. The image on the left is from the set of images collected with open porosity, while the image on the right is from the set collected after the porosity was impregnated with an epoxy.

Standard stereology[176, 239] was initially performed on a total of 33 images for each sample in order to determine volume fractions and triple-phase boundary densities. The area of each image was 7μm x 10μm such that the total surface area analyzed for each sample was 2310 μm^2. The large number of images analyzed was chosen to ensure that there was sufficient electrode surface area to provide good statistics for the stereological analysis.[181] Each image was separated by 125 – 250 nm in the Z direction to ensure that the volumes analyzed were representative of the entire electrode and to reduce errors as a result of structural anisotropy. The Z direction was chosen to be parallel to the electrode-electrolyte interface due to the geometry of the FIB procedure.

For the full 3D reconstructions, every other image of the epoxy impregnated samples was segmented. Thus, the Z-resolution for these sets of data was 50 nm. The segmentation procedure was fully automated except for one stage that was conducted by hand. For this stage, the Ni and YSZ phases were selected using the magic wand feature in Adobe Photoshop because shadowing prevented the automatic selection of the phases. While this procedure is slowed down by the need to treat each image individually, the image processing time for each sample was less than one week, a dramatic improvement over the month long time periods required for full hand segmentation.

Two different volume fraction definitions are used below: Ni solids volume fraction $V_{Ni,Sol} = V_{Ni}^{'} / (V_{Ni}^{'} + V_{YSZ}^{'})$, where the $V^{'}$ terms are the measured volumes, and total volume fraction, e.g., $V_{Ni} = V_{Ni}^{'} / (V_{Ni}^{'} + V_{YSZ}^{'} + V_{Pore}^{'})$.

6.3 Results

6.3.1 Electrochemical Characterization

Three cells were made and tested for each of the four compositions, and in each case the cell with the best performance was used in this study. Note that cell-to-cell performance variations at a given composition were a maximum of ~10%. Figure 6.2a shows the voltage and power density versus current density at 800^0C for each anode active layer composition. The open-circuit voltages were nearly identical, such that variations in power density were due primarily to cell resistance. The cell with $X_{NiO} = 50$ showed the best performance, with a maximum power density of 1.0 W/cm^2, while the $X_{NiO} = 60$ cell was nearly as good, yielding a

maximum power density of 0.98 W/cm^2. The other compositions yielded lower maximum power densities of 0.63 W/cm^2 for X_{NiO} = 40 and 0.77 W/cm^2 for X_{NiO} = 70.

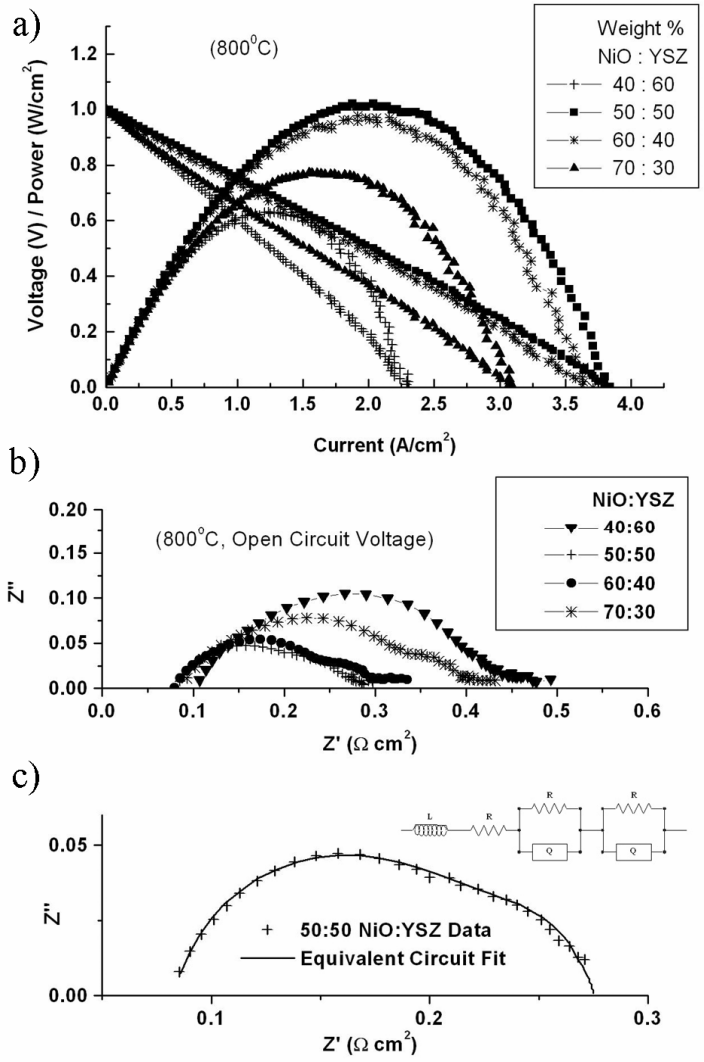

Figure 6.2. (a) Voltage and power density versus current density for cells with each anode composition measured at 800°C in air and humidified hydrogen. (b) Nyquist plots of EIS data measured at open circuit voltage and 800°C in air and humidified hydrogen. (c) An example of the equivalent circuit fit of the EIS data for the X_{NiO} = 50 sample; fits to the other cells were of similar quality.

Figure 6.2b shows EIS data collected at open circuit voltage (OCV) and 800^0C for the same cells as shown in Figure 1a. The EIS data was fitted with a simple equivalent circuit consisting of an inductor, a resistor, and two RQ elements, all in series. Similar circuit elements have been used previously for anode-supported SOFCs.[103, 255] Figure 6.2c displays the fit for the 50-wt%-NiO cell. The resistor accounted for the electrolyte. The high-frequency horizontal-axis intercept was at ~ 0.08 Ωcm^2 in each case, except for the 40-wt%-NiO cell which showed a slightly higher value. This resistance, associated with the resistor in the equivalent circuit, was due to the YSZ electrolyte and other ohmic resistances; the measured value was reasonable for a 10-μm-thick YSZ electrolyte at 800^0C.[35] The higher ohmic resistance in the cell with low Ni content may have been due to limited conductivity in the Ni-YSZ active layer due to the Ni volume fraction V_{Ni} = 0.22 falling below the percolation threshold[10]; however it is difficult to make a definitive conclusion because the additional 0.02 Ωcm^2 observed could also be explained by relatively small variations in electrolyte thickness.

The polarization arcs in Figure 6.2b were fitted by a higher-frequency RQ element, most commonly associated with the anode, and a lower frequency RQ element typically associated with the cathode.[103, 255] The present data supported this association, as the low-frequency arc resistance varied relatively little, from .027 - .032 Ωcm^2, with anode composition, whereas the high-frequency arc resistance varied substantially with composition. In the following discussion, the anode polarization resistance was estimated as $R_{P,A} = R_{P,T}$ - 0.03 Ωcm^2, where the total electrode polarization resistance $R_{P,T}$ was taken as the difference between the two real-axis intercepts of the polarization arc, and 0.03 Ωcm^2 is the cathode polarization resistance estimated from the fitting. Figure 6.3 shows a plot of the $R_{P,A}$ values versus Ni solids volume fraction

$V_{Ni,Sol}$. The cell with $V_{Ni,Sol}$ = 0.42 (50wt% NiO) showed the smallest $R_{P,A}$, with the $V_{Ni,Sol}$ = 0.47 cell being nearly as good. The $V_{Ni,Sol}$ = 0.24 and 0.56 cells showed significantly larger $R_{P,A}$. These trends agreed well with the resistance changes reflected in the I-V curve slopes in Figure 6.2a. EIS data was also taken at other temperatures. The variation of total polarization resistance measured from 600 to 800^{0}C followed Arrhenius dependences for all $V_{Ni,Sol}$ values, with activation energies from 38-42 kJ/mol. Thus, the variation in $R_{P,T}$ versus Ni content at 800^{o}C was similar at the other temperatures. If there was a change in rate-limiting mechanism with anode composition, it was to a mechanism with a similar activation energy.

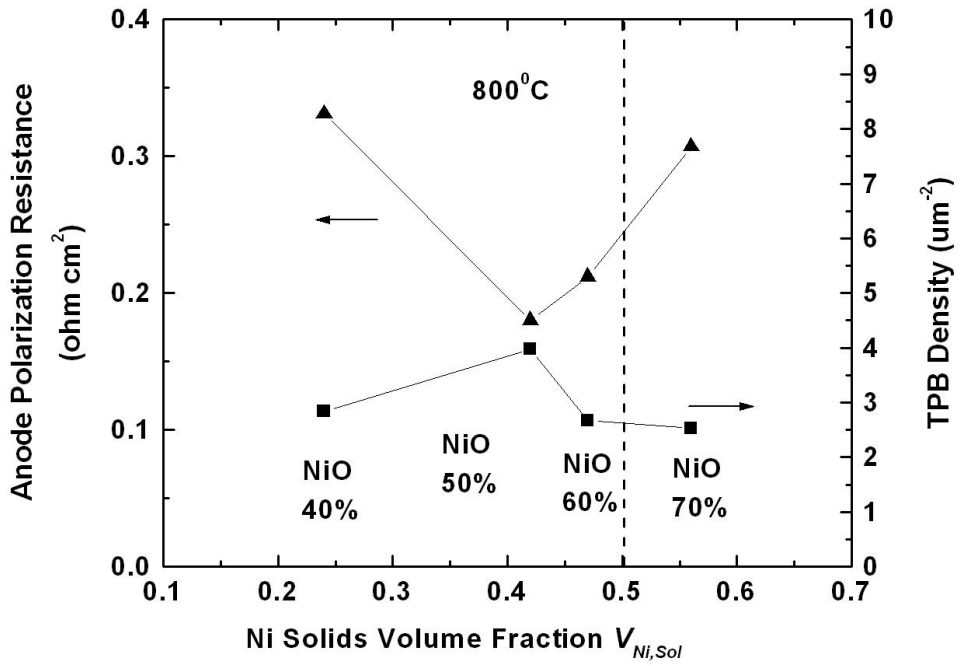

Figure 6.3. Measured anode polarization resistance and measured triple-phase boundary density versus Ni solids volume fraction $V_{Ni:Sol}$. Each data point is also labeled with initial weight percent of NiO, X_{NiO}.

6.3.2 Structural Characterization

Figure 6.4 shows representative images from each of the different anode active layers, with the bottom row being the samples that were impregnated with epoxy. There was clear compositional contrast between the Ni (light grey) and YSZ (dark grey). The images show the expected increase in the Ni phase area and decrease in YSZ area with increasing X_{NiO}. The voids appear primarily at the boundaries between the Ni and YSZ phases; it is not surprising that pores form at these interfaces as the NiO phase is reduced to Ni with a substantial volume reduction, and the high Ni-YSZ interfacial energy favors void formation on the boundary.[250]

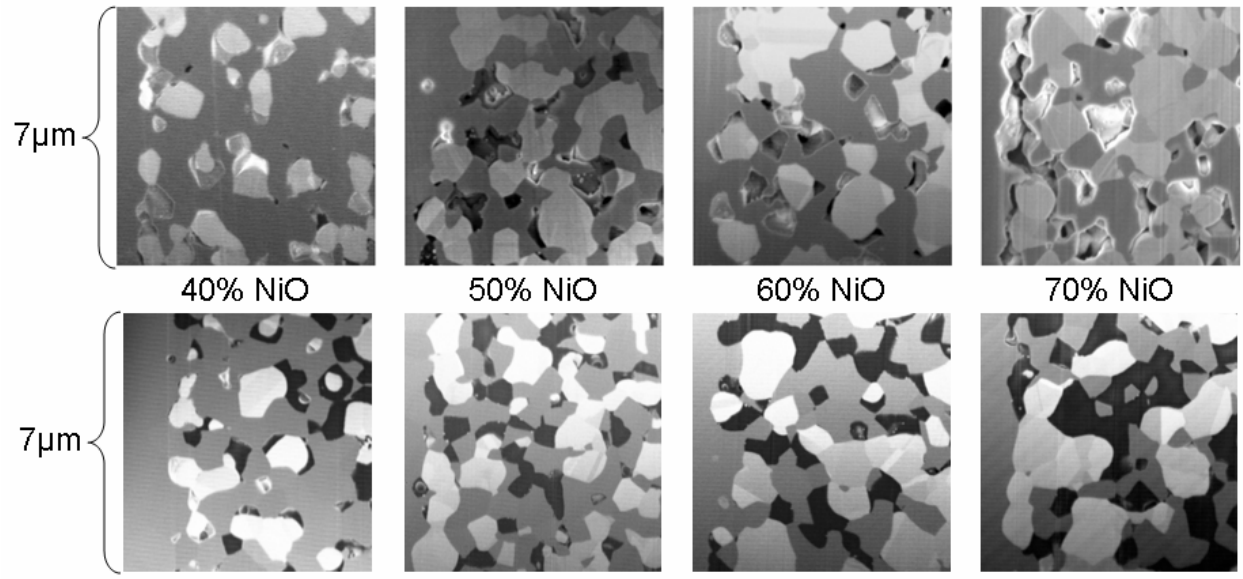

Figure 6.4. Typical FIB-SEM micrographs taken after SOFC electrical testing for each of the anode active layer compositions before any digital filtering is conducted. The bottom row of images are from the samples impregnated with epoxy. The images show the anode active layers with the electrolyte at the extreme left hand side. Ni shows a light gray contrast, YSZ is dark gray, and pores are typically black.

Stereology was initially performed in order to determine the TPB densities of each of the cells. The results are given in Table 6.1. The Ni and YSZ volume fractions calculated from the 3D reconstructions are also listed in Table 6.1. Visual representations of the 3D reconstructions achieved for each epoxy-filled sample are shown in Figure 6.5. The first column shows the Ni and Pore phases together, while the second column shows the YSZ phase. The third column showing the TPB lines will be discussed later. The volume fractions measured give good agreement with the original NiO and YSZ weights, with only the 50 wt% NiO sample showing slightly higher Ni and lower YSZ content than expected (this is why the data for this sample is skewed to the right on the X-axis in Figure 6.3). The measured pore volume increased proportionally with the NiO weight fraction, as expected. The measured TPB densities and bulk surface area densities from the 3D reconstructions are also displayed in Table 6.1. The TPB values are similar to those from stereology, although the lower wt% NiO samples have slightly higher densities comparatively. This highlights, as discussed in section 3.7, that stereological calculations of TPB density can be performed, but some error will be associated with the values. While initial results were published using only the stereological calculations[177], the following analyses will focus solely on the more accurate values taken from the full 3D reconstructions.

Table 6.1. Measured microstructural data and calculated polarization resistance for each of the anode compositions. Volume fractions are given both as the "solids" fraction $V_{Ni,Sol}$ – Ni volume relative to the total solids volume – and "total" fraction V_{Ni} – phase volume relative to the total volume.

Starting Composition	40 wt% NiO 60 wt% YSZ	50 wt% NiO 50 wt% YSZ	60 wt% NiO 40 wt% YSZ	70 wt% NiO 30 wt% YSZ
Ni solids volume fraction $V_{Ni,Sol}$	0.24	0.42	0.47	0.56
Ni total volume fraction V_{Ni}	0.21	0.33	0.36	0.40
YSZ total volume fraction V_{YSZ}	0.65	0.46	0.41	0.32
Pore total volume fraction V_{Pore}	0.15	0.21	0.23	0.27
Ni Surface Area Density (μm^{-1})	1.29	1.78	1.39	1.37
YSZ Surface Area Density (μm^{-1})	2.16	2.88	2.17	2.03
Pore Surface Area Density (μm^{-1})	1.51	2.00	1.72	1.72
TPB length (μm^{-2}) Stereology	2.40	3.12	2.73	2.50
TPB length (μm^{-2}) 3D Reconstruction	2.84	3.97	2.67	2.53
Model Calculated Polarization Resist at 700^0C (Ωcm^2)	0.33	0.24	0.31	0.30

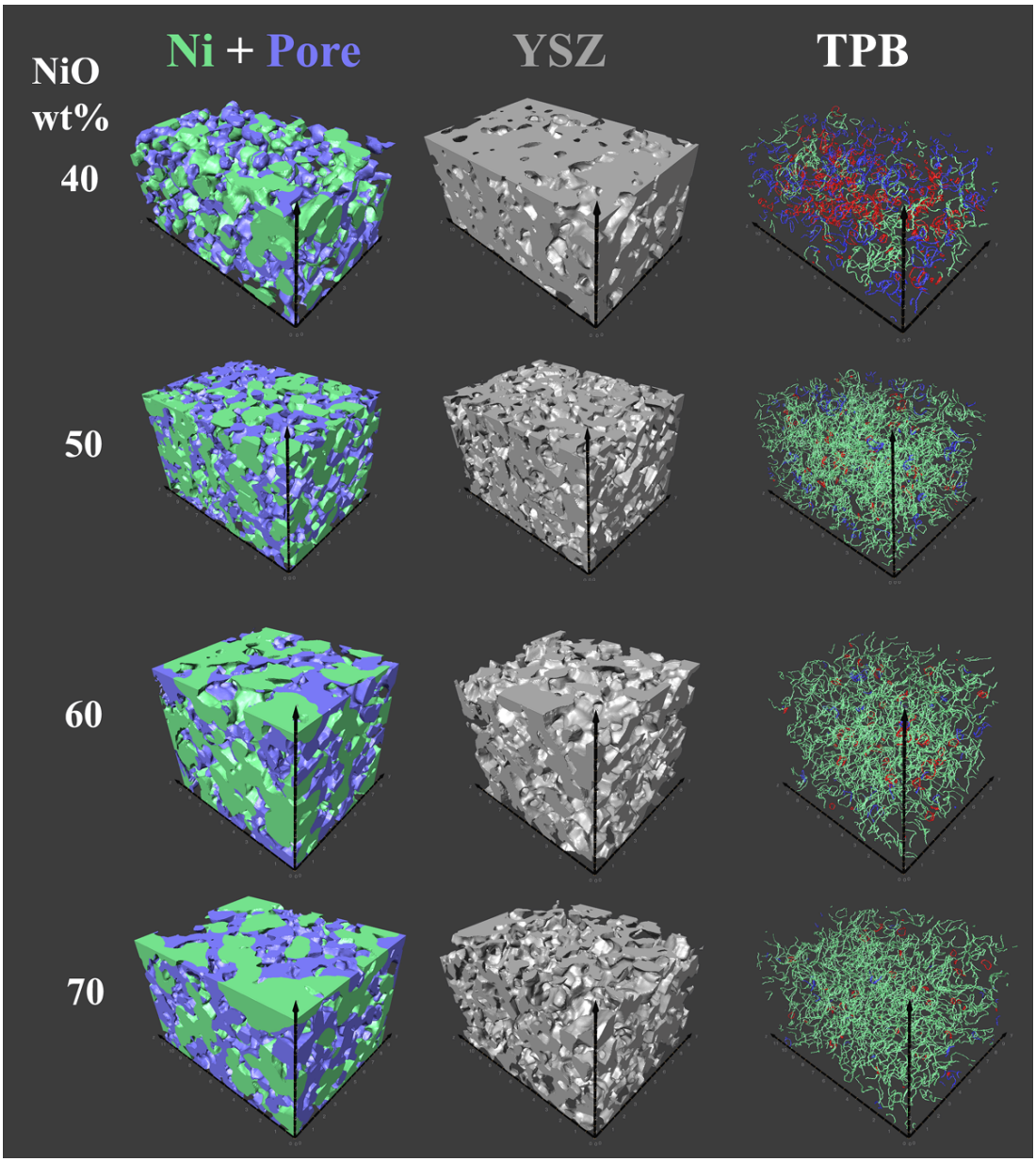

Figure 6.5. The left hand column shows a visual representation of the Ni (green) and pore (blue) phases for each sample composition. The middle column shows a visual representation of the YSZ phase. The right hand column shows the TPB lines for each sample, with the active TPBs shown in green (EA-TPBs), the unknown activity TPBs in blue, and the inactive TPBs in red. The volumes of each reconstruction are 342, 498, 530, and 671 μm^3, for the NiO weight % 40, 50, 60, and 70 samples, respectively.

Figure 6.3 shows the measured TPB densities versus $V_{Ni,Sol}$. The TPB density showed a maximum for the $V_{Ni,Sol}$ = 0.42 anode, the same composition where $R_{P,A}$ was lowest. Thus, polarization resistance qualitatively showed the expected dependence on TPB density. However, the TPB density varied by only ~35%, much smaller than the measured polarization resistance variation of ~100%.

Additional analysis of the connectivity of each of the phases was conducted in the same manner as previously published and described in section 3.6.5.[179] A summary of this data is presented in Figure 6.6a where the percentage of active material by volume for each phase is plotted along with the volume percentage of each phase. The only sample that has significant levels of isolated particles is the 40 wt% NiO sample. This is expected because the volume percentages of Ni and pore are 0.21 and 0.15 respectively, both in the range of the percolation threshold. Figure 6.7 shows a 3D representation of the isolated (red), dead-end (blue), and active (transparent) particle networks for the Ni and pore phases for the 40 wt% NiO sample. For the three other samples, the connectivity of the three phases never drops below 99%. Of note, for the 70 wt% NiO sample the YSZ phase remains highly connected despite the low 0.32 volume percentage.

Determination of the connectivity of each particle network of each phase allowed for the calculation of the electrochemically-active TPB (EA-TPB) density, the portion of TPB segments that are adjacent to contiguous pathways of each of the Ni, YSZ, and pore phases. The EA-TPB densities for each of the samples, calculated based on their respective connectivity data, is plotted in Figure 6.6b and shown visually in Figure 6.7 for the 40 weight % NiO sample. The ≈10% by volume isolated Ni and pore phases in the 40 wt% NiO sample has a significant effect on the EA-TPB density, reducing the original value from 2.84 μm^{-2} to 1.37 μm^{-2}. The other

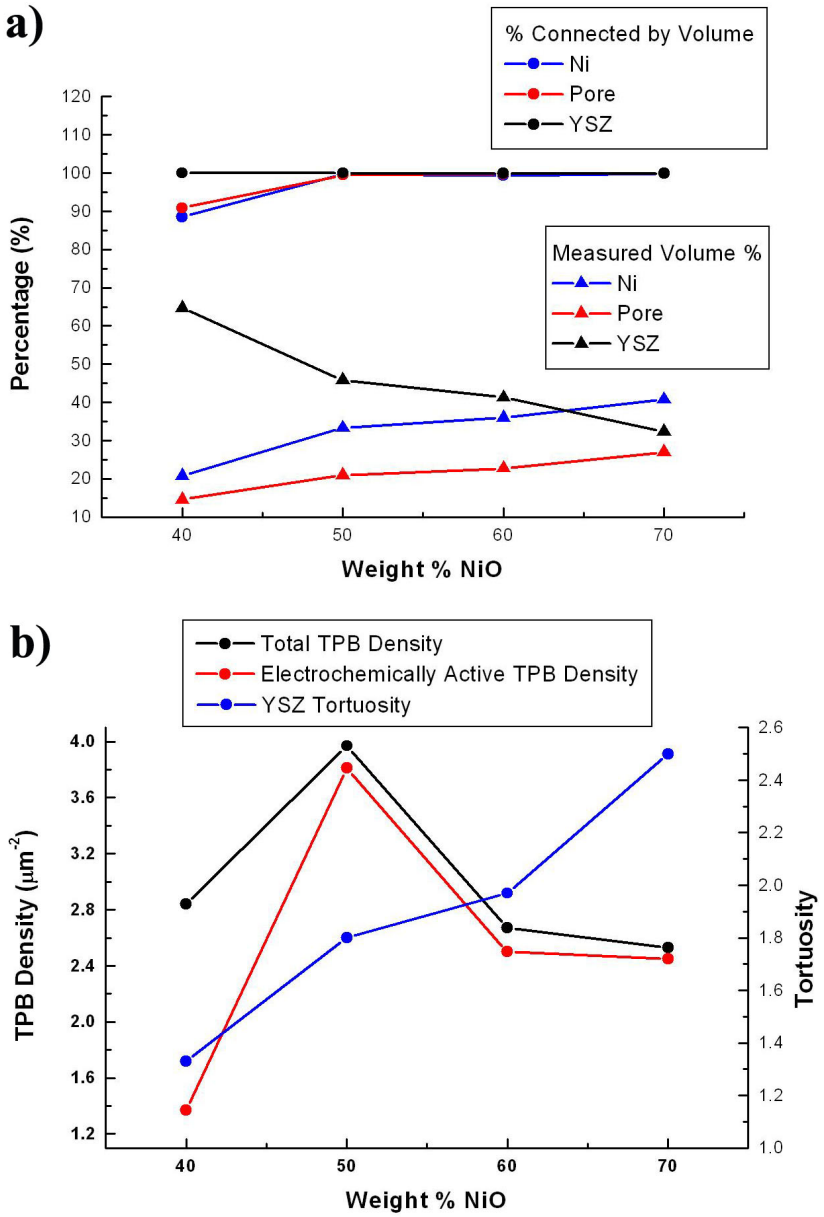

Figure 6.6. (a) A plot of the volume percentage of each phase as well as the percentage of connected material by volume for each phase calculated from the 3D reconstructions. (b) A plot of the total TPB density as well as the resulting EA-TPB density calculated based on the connectivity data. The tortuosity of the YSZ phase is also plotted with respect to the right hand axis.

(next page)

Figure 6.7. A visual representation of the sequence of connectivity calculations performed for the 40 wieght % NiO sample. The total volume of each phase is shown in the top row. The second row shows the isolated (red) and unknown connectivity (blue) particle networks for each phase highlighted within the total phase shown in transparent color. The isolated and unknown particle networks of the Ni and pore phases contribute to a reduction in the EA-TPB density, shown at the bottom of the figure, with the EA-TPBs highlighted in green, the TPBs lying on particle networks of unknown connectivity in blue, and the TPBs lying on isolated particle networks in red.

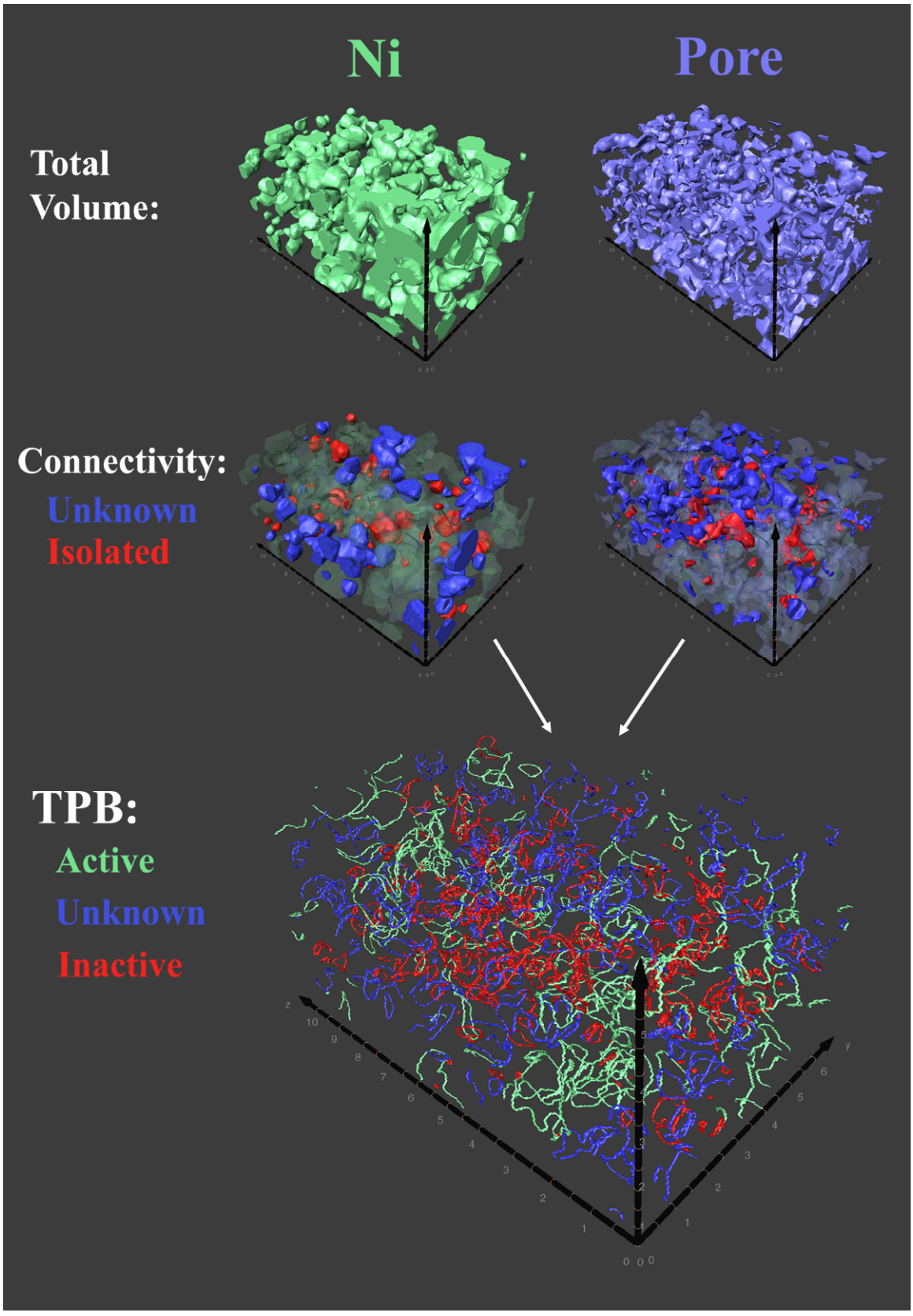
Ni
Pore
Total Volume:
Connectivity:
Unknown
Isolated
TPB:
Active
Unknown
Inactive

three samples showed minimal reduction in EA-TPB density due to their highly connected phases. The 3D visual representation of the TPBs for each sample is shown in the right hand column of Figure 6.5, where the EA-TPBs are shown in green, the unknown activity TPBs are in blue, and the inactive TPBs are in red. The average tortuosity for the YSZ phase is also plotted and is important for electrochemical modeling discussed later. The YSZ tortuosity increases as the amount of YSZ decreases, as would be expected. While not plotted, the pore tortuosity follows the same trend of increasing tortuosity with decreasing volume %, although the magnitude of the tortuosity is much greater, reaching 5.77 for the 40 wt% NiO sample that has only 15% porosity by volume. For the electrochemical modeling discussed later it is assumed that there are no gas transport limitations, which in general do not contribute to the electrode polarization when operating at low currents (the electrode polarizations were measured at OCV). Additionally, the Ni tortuosity is ignored because the conductivity of Ni is orders of magnitude greater than that of YSZ and hence, electronic transport limitations are negligible.

6.4 Discussion

In the following, the effect of composition on TPB density is discussed first, followed by the effect of TPB density on polarization resistance.

6.4.1 Effect of Composition on TPB Density

The results in Figure 6.3 show the highest TPB density for $V_{Ni,Sol}$ = 0.42, a 2:3 Ni:YSZ volume ratio. This asymmetry may result in these Ni-YSZ anodes because the pore volume increases with increasing NiO content. That is, the pore volume is ≈ 70% of the Ni volume

because it derives from the 41% volume loss during reduction from NiO to Ni. In addition, it appears that the Ni grains are larger than the YSZ grains in Figure 6.4. This is expected since the original powder size for the NiO was ~ 2.5 μm, which decreases to ~2.0 μm upon reduction of NiO to Ni, and the original powder agglomeration size for YSZ was on average ~0.5μm.[258]

Two recent models are used here to help determine the effect of these parameters on TPB density. The models are based on the random packing of spheres, and have provided new insights into how variations in particle size, porosity, and composition affect the TPB density in composite electrodes.[191, 192] Figure 6.8 shows plots from each model using three different combinations of particle sizes ((Ni,YSZ) = (2.0μm,0.5μm), (2.0, 1.0), and (1.0, 1.0)). In each case, the measured experimental values of Ni volume fraction and porosity, shown in Table 6.1, were used. The measured total TPB density is shown for comparison. Two conclusions can be drawn from Figure 6.8. First, each model can predict the correct magnitude of the measured TPB density with small modifications of the particle sizes, porosity, coordination number, sphere overlap, etc. For example, the Janardhanan model for particle sizes of Ni = 2.0 μm and YSZ = 1.0 μm. Second, the models are mutually contradictory when trying to describe the *shape* of the curve of the measured values. For the particle sizes of Ni = 2.0 μm and YSZ = 0.5 μm, *i.e.,* those of the present anodes, the two models show opposite trends. In the case of the Janardhanan model, the smaller YSZ particle size shifts the maximum TPB density towards a YSZ-rich composition, while the Zhu model shifts the maximum towards a Ni-rich composition. This discrepancy indicates that the two models treat particle size effects in different ways. However, it also appears to be related to the treatment of porosity. Looking at the two curves for equal Ni and YSZ particle sizes of 1.0μm, the Zhu model shows a slight shift of the maximum TPB length

towards a YSZ-rich composition, while the Janardhanan model shows a larger shift towards a Ni-rich composition. These shifts are due to the increase in porosity with increasing Ni content. (For constant porosity and equal particle sizes, the Janardhanan model predicts a maximum TPB density at $X_{Ni} = 0.5$). The opposing predictions appear to be related to how the models relate the average particle coordination number and porosity [187]. Thus, the exact factors causing the asymmetry in measured TPB density remain undetermined.

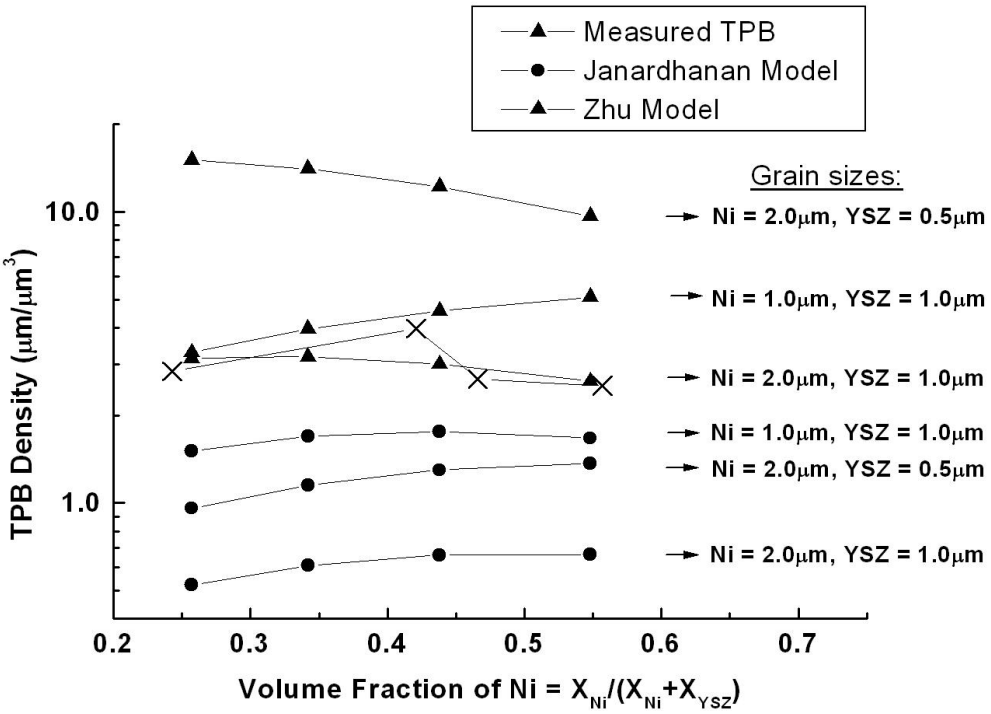

Figure 6.8. Comparison of the present TPB density values with predictions from two different structural models assuming different particle sizes,[191, 192] plotted versus Ni content. For the Zhu et al. model, particle contact angle is assumed to be 15 degrees, an average coordination number of 6 is used, and percolation probability is ignored. For the Janardhanan et al. model, the distance between particle centers is taken as 0.9 times the largest particle radius, the coordination number for different-phase particles is 3, on average is 6, and the fractional overlap is kept at 0.

6.4.2 Effect of Microstructure on Polarization Resistance

The Tanner-Fung-Virkar (TFV) composite electrode model[136] was employed to help relate measured microstructure and polarization resistance. The model assumes an ionically-conducting (YSZ) phase consisting of one-dimensional columns extending vertically from the electrolyte, with the intervening volume containing the electronic-conductor phase (Ni) and porosity. A tacit assumption of this model is that all phases are fully contiguous and that concentration polarization is negligible. In the present calculation, the YSZ column structure was set at 1 μm thickness (unless otherwise indicated), and the distance between YSZ columns was varied to match the measured volume fractions for each anode (Table 6.1). The TFV model assumes an average surface resistance on the ionic-conductor surfaces; in the present case, this surface resistance was calculated by uniformly distributing TPB's on the YSZ column surfaces to match the present measured l_{TPB} (m/m^3) values, and using linear-specific TPB resistance values measured in patterned electrode studies,[166, 167] given by

$$R_P = \frac{\beta}{\ell_{TPB}^{\alpha}} \tag{6.1}$$

The values $\alpha = 0.8$ and $\beta = 340$ Ωm at 700°C (800°C values were not available) from Ref. [166] were used, because this study provided the most complete data set with TPB density varied over three orders of magnitude.

Table 6.1 shows the anode polarization resistances $R_{P,A}$ calculated as indicated above, using the experimentally measured anode active layer thickness of ≈10 μm and the total TPB length per sample, ignoring any connectivity data for the time being. The predicted $R_{P,A}$ magnitudes were in reasonable agreement with the measured polarization resistances and show

the same trends. However, the variation of the calculated $R_{P,A}$ values was only ≈30%, much smaller than that of the measured $R_{P,A}$. A likely explanation for the discrepancy between measured and modeled polarization resistance is that phase connectivity and tortuosity effects impact the polarization resistance. The observed un-connected Ni and pore networks at low Ni content that reduce the EA-TPB density should explain the substantial increase in polarization resistance observed. Furthermore, the model in this case assumes straight columns of YSZ with uniform-thickness, ignoring effects of the observed high-tortuosity ionic transport paths. Given the relatively low conductivity of YSZ (10^6 times lower than that of Ni), these features may increase $R_{P,A}$ as the YSZ volume fraction decreases, even without a significant fraction of un-connected YSZ particles.

Figure 6.9 shows the polarization resistances predicted by the TFV model when the EA-TPB density is used instead of the total TPB density, and when the tortuosity of the YSZ phase is included (values shown in Figure 6.6), plotted in red. The effect of the YSZ tortuosity is implemented in the model by dividing the YSZ conductivity by the tortuosity factor. Because the oxygen ion has τ_{ysz} (the YSZ tortuosity factor) times the distance to travel compared to a straight line normal to the electrolyte, the electrode can be described in the model by straight extensions of YSZ with τ_{ysz} times the resistivity. As can be seen in Figure 6.9, implementation of these two microstructural factors has greatly reduced the polarization resistance of the low Ni content sample, better matching the observed performance of the cell. This is a direct effect of the reduced EA-TPB density for that sample. However, the 70 weight % NiO sample (30 weight % YSZ) did not show much change. In fact, the predicted performance from the TFV model scales very well with the EA-TPB density, implying that the electrodes are not limited by ionic transport in the tortuous YSZ networks.

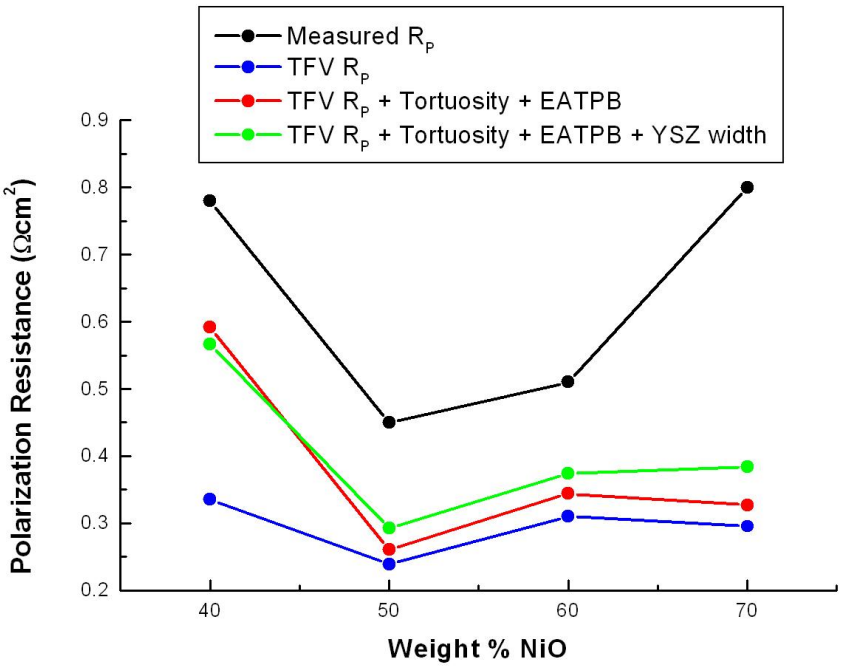

Figure 6.9. Polarization resistances (R_P) estimated from the Tanner-Fung-Virkar (TFV) electrochemical composite electrode model in comparison to the measured R_P. Model parameters used include an electrode thickness of 10 μm, YSZ column thickness of 1 μm, and values $\alpha = 0.8$ and $\beta = 340$ Ωm at 700°C from the Bieberle et al. work.

An additional adjustment that can be made in the model to further test the affect of transport in the YSZ phase is to adjust the YSZ column thickness for each composition (not just the conductivity as a function of the tortuosity) instead of using a constant estimated value of 1 μm. The thickness of the YSZ for each sample was estimated by multiplying the ratio of the YSZ volume to the YSZ surface area by a factor of 4. This is equivalent to the characteristic

diameter of the YSZ if it were made up of cylinders, as it is described in the TFV model. One would expect that this characteristic length would be directly proportional to the YSZ content. The column thicknesses calculated were 1.20 μm, 0.64 μm, 0.76 μm, and 0.64 μm for the samples of YSZ wt% 60, 50, 40, and 30, respectively. Figure 6.9 shows the predicted polarization resistances when this size effect is incorporated, plotted in green. It can be seen that reducing the thickness of the YSZ columns serves to increase the polarization resistance, and that the predicted values better match the shape of the observed performance when this is accounted for. This implies that ionic transport within the YSZ does play a role in the observed polarization.

While reducing the YSZ thickness in the 70 wt% NiO sample increases the polarization resistance in the TFV model, there is still an observable difference with respect to the measured value. There are two other possible explanations that could describe the observed high resistivity in this sample. Firstly, Figure 6.3 (top row) shows possible delamination and/or detrimental porosity formation occurring at the interface of the electrolyte. It is possible that structural defects such as this could cause the high polarization resistance. It is not unreasonable to see something to this effect, as the large volume loss during reduction of NiO to Ni in especially high content NiO samples could cause structural failure in the lower content and thinner YSZ microstructure.

Secondly, the TFV model is limited to calculating the polarization resistance for a given electrode thickness. In reality, however, the anode support will contribute to the performance if the active thickness of the electrode (which is a function of the microstructure) is greater than that of the active layer. The samples with lower YSZ and higher tortuosity (i.e. those with high NiO wt%) will be more prone to transport limitations, and hence their effective thicknesses will

be less. Figure 6.10a shows this effect of the electrode thickness on the predicted polarizations from the TFV model for the four samples in this study. The values are calculated using the EA-TPB density and implementation of the YSZ tortuosity and column thickness. It is clear that the 70 wt% NiO sample reaches its minimum polarization at a larger thickness than the other samples. Figure 6.10b, which is the same data as Figure 6.10a but in this case plotted as a function of weight % NiO, shows that larger thicknesses will tend to decrease the 40 wt% NiO sample polarization resistance more than that of the 70 wt% NiO sample. This serves to make the performance of the series of cells more symmetrical, as was observed, and could explain how inclusion of the anode support layer in the model would help in describing the measured performance.

The above ideas can also help explain why $R_{P,A}$ was minimized for a Ni-YSZ volume ratio of 2:3. The optimal structure is where transport rates for each species – vapor, electrons, and ions – is approximately equal, *i.e.,* no single species limits the resistance. Given that pore gas diffusivity and Ni electron conductivity are much faster than ion transport in YSZ, it is reasonable that a relatively high YSZ volume fraction, providing low tortuosity pathways for oxygen-ion transport, was optimal.

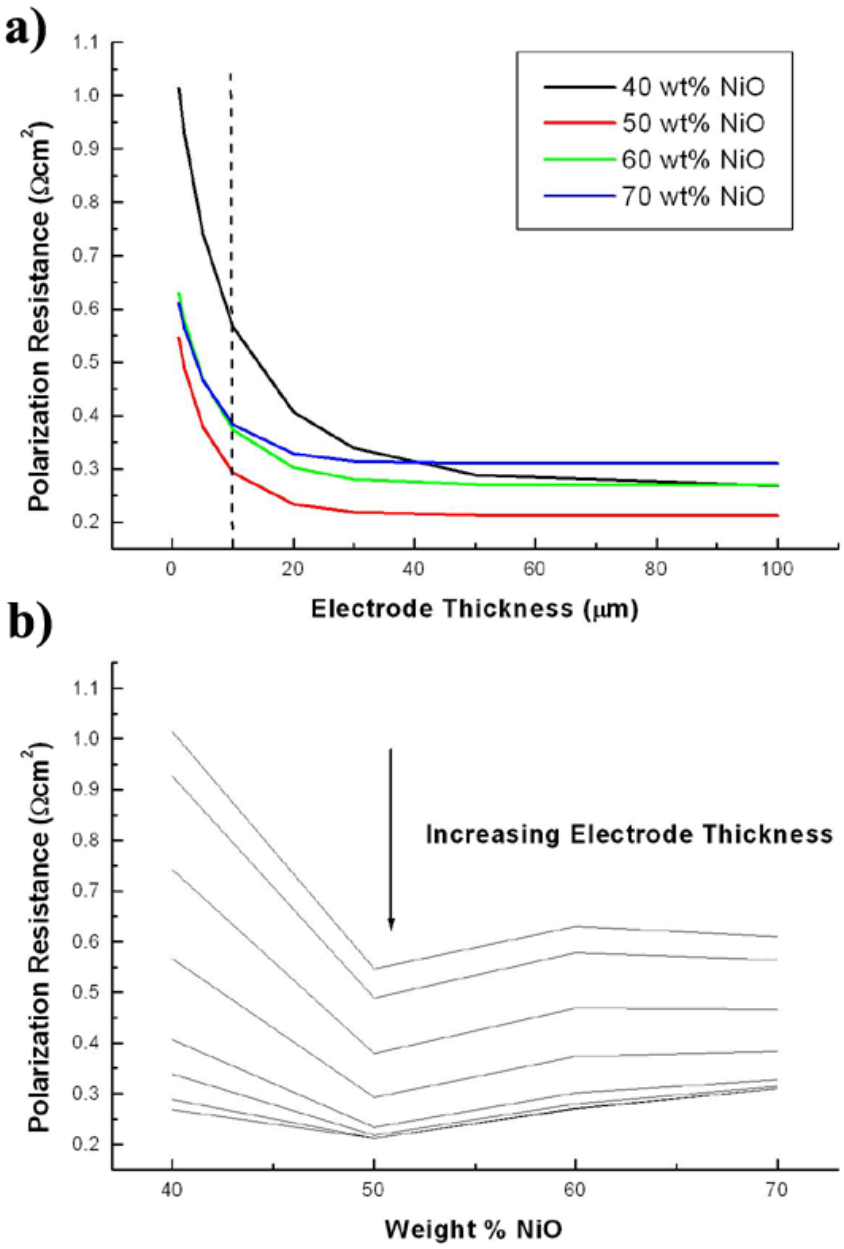

Figure 6.10. (a) Polarization resistance from the TFV model as a function of the electrode thickness. (b) The same data as that in (a) but in this case each thickness is plotted individually as a function of weight % NiO. In both cases, the EA-TPB density, YSZ tortuosity, and varying YSZ column thickness are used in the model, as plotted in green in Figure 6.9.

6.5 Summary and Conclusions

Anode-supported SOFCs with varying Ni-YSZ active-layer compositions were compared structurally using a focused ion beam – scanning electron microscope. Stereological analysis and 3D reconstruction calculations showed that the highest triple-phase boundary (TPB) density was at a Ni solids volume fraction of ≈0.42. The results show reasonable agreement with structural models for predicting TPB density. While the anode polarization resistance was minimized at the same composition where TPB density was maximized, when the observed microstructure including TPB density variation was inserted in a simple electrochemical model, the predicted polarization resistance variation was much smaller than observed experimentally. Connectivity data was obtained for each phase, where appreciable volumes of isolated Ni and pore networks for the 40 weight % NiO sample contributed to a substantial fraction of electrochemically-inactive TPBs, explaining the poor performance observed for this sample. Inclusion of YSZ tortuosity and characteristic feature size in the model only partially explained the poor performance observed in the 70 weight % NiO sample.

Ultimately, finite element analysis of measured 3D microstructures will allow quantitative connection between anode polarization and microstructure.

CHAPTER SEVEN

A Composite LSM-YSZ Cathode Reconstruction

Chapter 7: A Composite LSM-YSZ Cathode Reconstruction

7.1 Introduction

Most state of the art solid oxide fuel cells (SOFCs) utilize a cathode consisting of a porous mixture of $La_{1-x}Sr_xMnO_3$ (LSM) and 8 mol% Y_2O_3-stabilized ZrO_2 (YSZ) to carry out the critical oxygen reduction reaction.[143, 259-261] LSM-YSZ cathodes were an important development that helped allow reduction of SOFC operating temperature from ≈1000°C to ≈800°C.[143, 259-263] Even so, these cathodes contribute substantially to the SOFC electrochemical resistance losses, and questions remain regarding long-term stability.[264] Thus, there is a need for continued study and development. While it is widely believed that the LSM-YSZ composite yields low polarization resistance because of a high density of three-phase boundaries, there have been only very limited attempts to explore this.[176] Indeed, due to the dearth of experimental microstructure measurements, attempts to understand composite cathodes have focused on idealized microstructural models to predict three-phase boundary densities and hence polarization resistance.[136, 189, 190, 212] Given this situation, quantitative microstructural data is needed to enable understanding of electrochemical processes in LSM-YSZ, to aid in development of cathodes with reduced polarization resistance, and for observing and understanding long-term degradation processes.

Microstructural characterization has been hampered by the difficulty of resolving the LSM and YSZ phases using typical imaging methods such as electron microscopy, and the difficulty of quantitatively characterizing the complex interconnected three-component (LSM-YSZ-pore) structures. Recent advances in three-dimensional structural analysis of materials, using data from methods such as focused ion beam – scanning electron microscopy (FIB-SEM),

now make it feasible to analyze SOFC electrodes.[177, 181-183, 226, 250] Here we describe the three-dimensional characterization and quantification of key structural parameters from a LSM-YSZ cathode using focused ion beam – scanning electron microscopy (FIB-SEM). Analysis of the connectivity of the cathode phases allowed for the determination of the electrochemically active triple-phase boundary (TPB) density, the first published measurement of its kind, and in conjunction with electrochemical modeling and tortuosity measurements of the YSZ phase, the effective resistance of the LSM-YSZ-air triple-phase boundary was calculated.

7.2 Experimental Procedure

The present LSM-YSZ cathodes were prepared using standard materials and processing methods, such that the present structural data will be comparable to a majority of the cathodes being used world wide. The samples used in this study consisted of dense 8 mol% Y_2O_3-stabilized ZrO_2 (YSZ) electrolyte pellets, with identical cathodes symmetrically placed on opposite sides of the pellet. The YSZ pellets were prepared by uniaxially dry pressing from a mixture of YSZ powder (Tosoh) and a small amount of PVB binder. The pellets were fired at 1400°C for 4h.

The cathodes in this study were mixtures of LSM-YSZ (LSM = $La_{0.8}Sr_{0.2}MnO_3$, Praxair). The cathodes were applied to dense YSZ electrolyte surfaces by screen-printing. The screen printing inks were prepared by first ball milling the LSM and YSZ powder to thoroughly mix, and then combining with a Heraeus vehicle in a three-roll mill. After printing, the LSM-YSZ layer was fired in air at 1175^0C for 1 hour. Pure LSM current collector layers were then printed (using an ink prepared from LSM powder only) on top of the LSM-YSZ. The samples were then

fired again in air at 1175^0C for 1 hour. Figure 7.1a illustrates a fracture cross-sectional scanning electron microscope image of the LSM-YSZ cathode; this is the most common type of microstructural information reported in the literature. While the porous nature of the cathode is clear, the lack of contrast between the LSM and YSZ components, combined with the complex three-dimensional nature of the structure, makes it impossible to extract quantitative information from this standard cross-sectional image. LSM-YSZ and LSM layers were both ~10-12μm thick. FIB-SEM images were taken from the portion of the LSM-YSZ cathode active layer directly adjacent to the YSZ electrolyte, which should be most relevant to determining the electrochemical performance.

The symmetric LSM-YSZ cathode samples were electrochemically characterized using a Zahner IM6 electrochemical testing station. Figure 7.2 shows a Nyquist plot illustrating typical data measured in air at 800°C with no applied dc voltage. The shape of the impedance arc was similar to that reported previously for LSM-YSZ cathodes.[265] The total polarization resistance (measured as the difference between the real-axis intercepts) at 800°C was $0.51\Omega cm^2$. The polarization resistances versus temperature are plotted in Figure 7.5, discussed later in this chapter. The measured values are in the range normally observed for LSM-YSZ composite cathodes measured in this way.[109, 265] This is perhaps not surprising given that the starting powder sources and processing procedures used here are fairly common. Thus, the present microstructural results are expected to be fairly representative of LSM-YSZ cathodes studied by many groups.

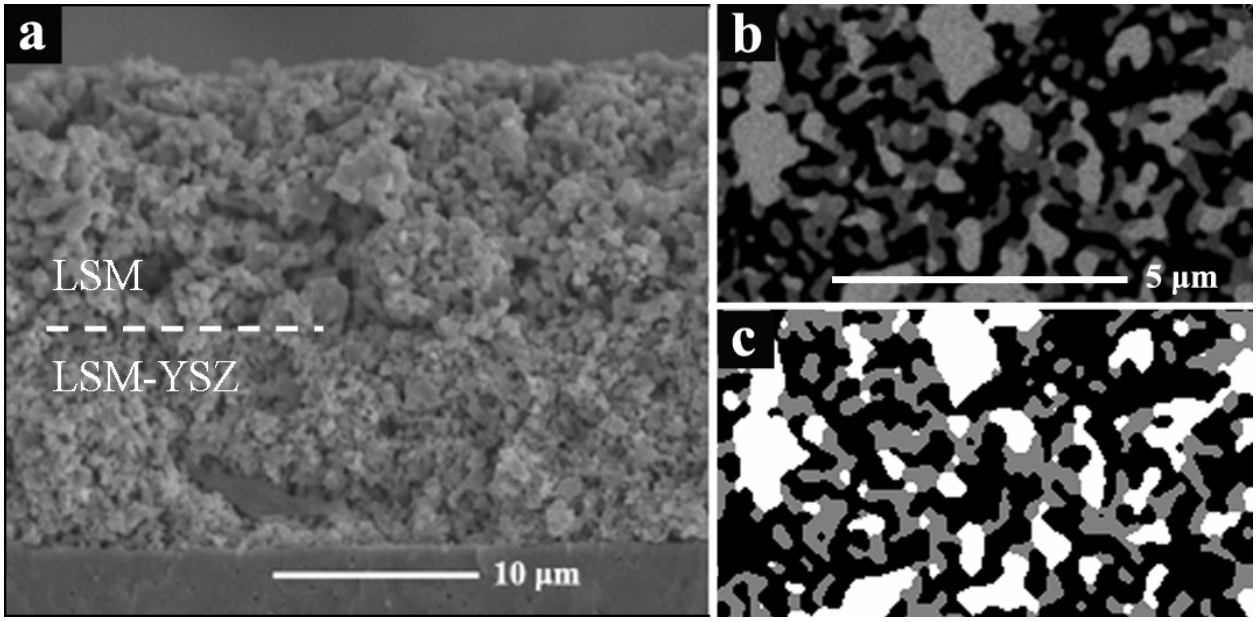

Figure 7.1. (a) A typical SEM micrograph of a SOFC fracture surface showing the composite LSM-YSZ cathode (middle), the dense YSZ electrolyte (bottom), and the pure LSM current collector layer (top). (b) One of 242 serial-section images collected using FIB-SEM with ESB detection. The pores were filled with epoxy and appear as dark black, with the LSM (light grey) showing excellent contrast with respect to the YSZ phase (dark grey). (c) The same image as shown in (b) after segmentation, *i.e.,* assignment of each pixel to a specific phase (YSZ = white, LSM = grey, pore = black).

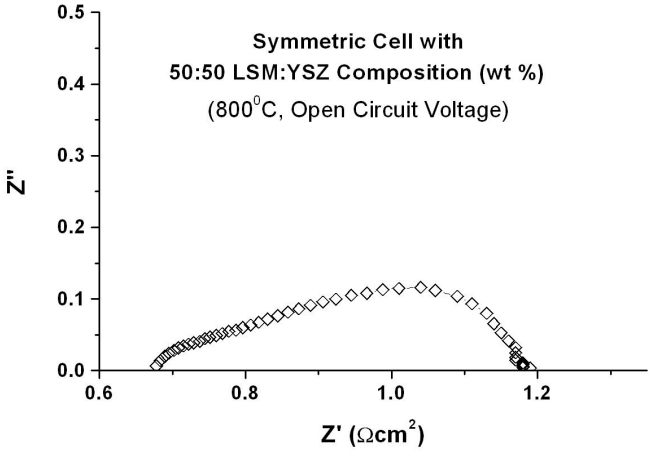

Figure 7.2. Nyquist plot of the LSM-YSZ cathode at 800°C and open circuit voltage.

The cell ohmic resistance (taken from the left real-axis intercept in Figure 7.2) was 0.68 Ωcm^2 at 800°C. This value stems from the YSZ electrolyte, and is consistent with published resistivity values of YSZ prepared from Tosoh powder.[55, 266] Our measured values of the conductivity of YSZ pellets are listed in Table 7.1. These values were used in the LSM-YSZ composite cathode calculations described later.

Table 7.1. Measured conductivity of a pressed YSZ pellet at different temperatures.

Temperature (℃)	YSZ Conductivity (S/cm)
600	0.008
650	0.013
700	0.025
750	0.041
800	0.063

The present FIB-SEM measurements utilized two key measures to produce quantitative three-dimensional images. First, the pores within the electrode structure were filled with an impregnating epoxy prior to the measurements. This allowed the focused ion beam to produce nearly planar sectional surfaces for imaging without the contrast variations associated with charging of the pore edges, and signal emitted from within the pores, that previously made accurate 'reconstruction' of three-dimensional (3D) volumetric data sets difficult. [250] Second, the poor resolution of sub-micron domains and very weak contrast between LSM and YSZ was addressed by using low electron beam energy and an energy-selective (biased) in-lens backscatter detector (as discussed in section 3.4.4). Figure 7.1b shows a typical two-dimensional (2D) FIB-SEM cathode image. The clear contrast between the LSM (light grey), YSZ (dark grey) and pore/epoxy (black) and the uniform contrast within each phase allowed the use of automated procedures to rapidly segment the images. Figure 7.1c illustrates the fully segmented three-color image corresponding to that shown in Figure 7.1b. The data set considered here included 242 such 2D images, each separated by 53.3 nm, that were reconstructed into a 3D volumetric data set.

7.3 Results and Discussion

Figure 7.3a shows a visual representation of the resulting full image volume, with the LSM phase in yellow, the YSZ phase in pink, and the porosity transparent. The total volume in the 3D image was 685 μm^3. Since it is difficult to resolve structural details in such overview images, a thin image section (Figure 7.1b) and a representative zoomed-in portion of the volume (Figure 7.1c) are also shown. These images show the interpenetrating networks of LSM, YSZ,

(next page)

Figure 7.3. The columns in this figure show similar features, while the rows show images with the same dimensions and volumes. (**a**) The full cathode volume (dimensions 6.0 x 8.8 x 12.9 μm) with LSM shown in yellow, YSZ in pink, and the porosity transparent. (**b** and **c**) Smaller volume subsets of the cathode shown in (a) highlighting the microstructure and surfaces of the LSM and YSZ phases. (**d**) The full cathode volume view of electrochemically active TPBs (green), unknown status TPBs (blue), and inactive TPBs (red). (**e**) A thin section showing TPB segments. (**f**) A smaller-volume view of isolated and connected TPB segments on the LSM phase (transparent red). The apparent TPB-solid discontinuity is an artifact of the imaging software used. (**g**) The full cathode volume showing the LSM phase divided into connected networks (transparent yellow), dead-end networks (blue), and isolated networks (red). (**h** and **i**) Smaller volume subsets of the cathode shown in (g) highlighting the connected, dead-end, and isolated networks.

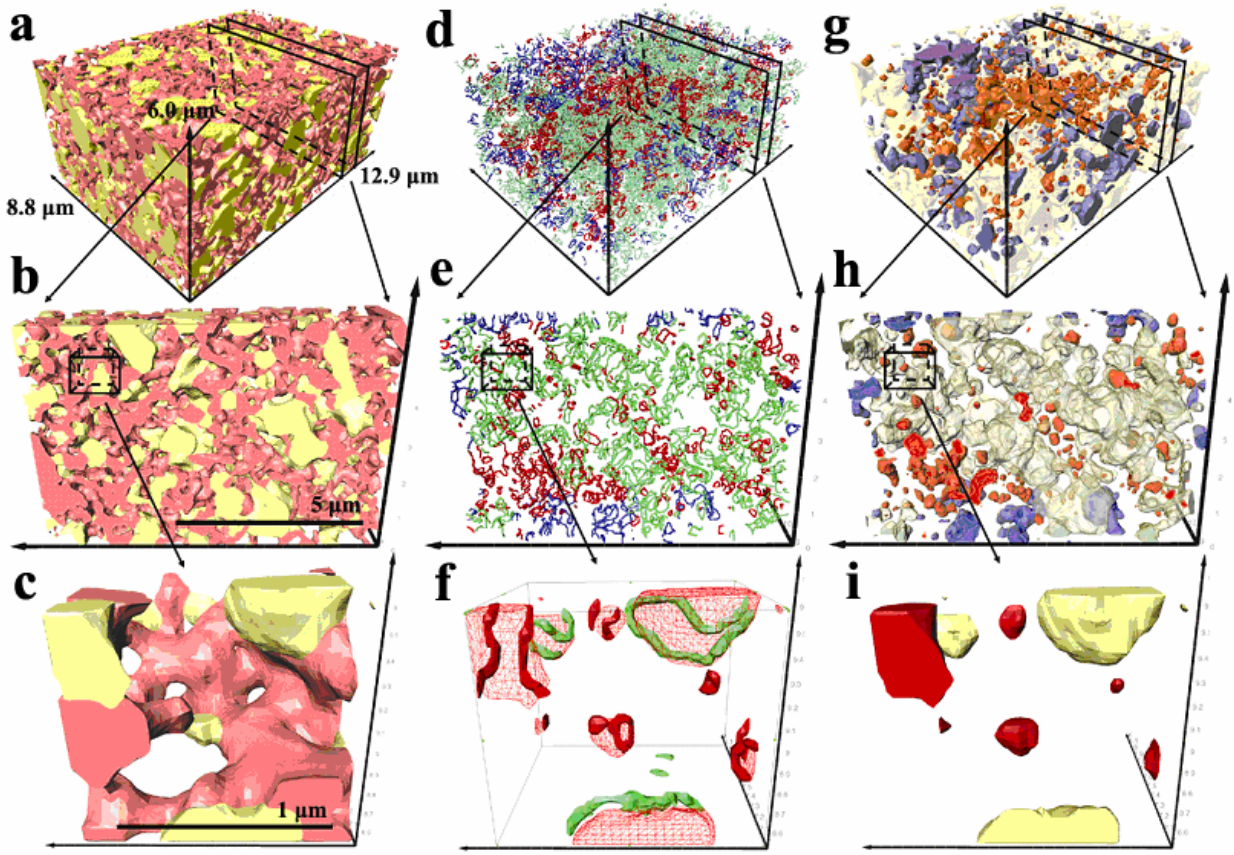
a
6.0 µm
8.8 µm
12.9 µm
b
5 µm
c
1 µm
d
e
f
g
h
i

and pore, and their local surface curvatures. The YSZ particle size and pore size were found to be smaller than that of LSM. This is reasonable given the larger average particle size of the LSM starting powder (≈3.0μm) compared to that of the YSZ powder (≈0.5μm). [258]

A number of different quantities were extracted from the 3D data set. The volume percentages of the phases were 23.2% LSM, 25.3% YSZ, and 51.5% porosity. This yields a solids volume ratio of 47.9% LSM / 52.1% YSZ, in close agreement with the values expected from the cathode LSM/YSZ weight ratio (50 wt% LSM / 50 wt% YSZ) and their densities, which yielded 47.6 vol% LSM / 52.4 vol% YSZ. The good agreement provides evidence that the volume of cathode analyzed was representative and that the imaging/reconstruction process was accurate. The measured interface surface area densities (interface area per unit sample volume) were 1.33μm^{-1} for LSM-pore interfaces, 2.60μm^{-1} for YSZ-pore, and 0.46μm^{-1} for LSM-YSZ. For each bulk phase, these were respectively, 1.79μm^{-1} (LSM), 3.07μm^{-1} (YSZ), and 3.93μm^{-1} (pore). Starting particle size diameters for the LSM and YSZ powders used were ≈3.0μm and ≈0.5μm,[258] respectively, so it is expected that the YSZ surface area would be greater than that of the LSM. In addition, the factor of two greater surface area for YSZ-pore with respect to LSM-pore is comparable to that of their bulk surface densities, implying that there does not appear to be significant preference for wetting of LSM and YSZ. In other words, if LSM and YSZ preferred to wet on each other's surfaces, causing the LSM-YSZ surface area to increase, the YSZ-pore / LSM-pore ratio would increase dramatically. Specific surface areas (surface area of a phase normalized to its volume) were 7.7μm^{-1} for LSM and 12.1μm^{-1} for YSZ; these values indicate that the characteristic length scale of the LSM was larger than that of YSZ by ≈60%, consistent with Figures 7.1b and 7.3a-7.3c and the assessment given above.

Three-phase boundaries (TPBs), defined as the lines of contact between the LSM, YSZ, and pore phases, are believed to be important in determining LSM-YSZ cathode electrochemical properties.[123, 124] In particular, the cathode oxygen reduction reaction,

$$O_2 + 4e^- \rightarrow 2O^{2-}, \quad (7.1)$$

is expected to occur near TPBs where all the species involved – O_2 in pores, electrons in LSM, and oxygen ions in YSZ – are present. Figure 7.3d shows an image of all the TPBs in the 3D image volume. Figures 7.3e and 7.3f are successive zoomed-in views, shown to allow better visualization of the TPBs and their positions in the microstructure. The different TPB colors indicate their connectivity, an important distinction discussed below. The total TPB density obtained was 7.35 μm^{-2}. This density is substantially larger than previously reported values of $\approx$2-4 μm^{-2} for Ni-YSZ anodes.[177, 250] This should be expected, however, because the grain sizes in the cathode are smaller than those observed in the anode, producing a finer microstructure and hence a higher TPB density. In the only other report of TPB density in LSM-YSZ cathodes, obtained from stereological analysis of 2D images,[124, 176] the TPB densities ranged from $\approx$1.7 to $\approx$6.5μm^{-2} (TPB densities were reported as TPB length per cathode area, so a typical cathode thickness of 10μm thick was assumed here to obtain a volumetric TPB density). The present results are reasonably consistent with these prior values, especially given that the compositions and porosities were different.

The LSM-pore interface area adjacent to the TPB's is of special interest because oxygen adsorption on LSM-pore surfaces and surface diffusion to the TPB is believed to be a main reaction path at low overpotential.[149] Figure 2f shows examples of LSM surfaces adjacent to

TPBs. An initial estimate of the length scale of this LSM surface adjacent to TPB's can be obtained by dividing the LSM-pore interface area, given above, by the TPB density, yielding 0.18 μm. The width adjacent to TPB's that contributes to the oxygen reduction process is not known;[124] future studies on cathodes with, *e.g.,* fixed TPB lengths and varied LSM surface areas may provide clues regarding the length scales of these TPB mechanisms.

In order for the oxygen reduction reaction to occur at a TPB, the microstructure must allow the species in equation (7.1) to transport between the TPB and the surrounding phases (*i.e.,* O_2 from the air supply, electrons from the external circuit, and oxygen ions to the YSZ electrolyte). That is, only those TPBs that lie on percolated networks of all three phases will be electrochemically active. Thus, the quantity of interest is not the total TPB density given above, but the portion of the TPBs that meet the connectivity requirement. This electrochemically active triple-phase boundary (EA-TPB) density was determined by first analyzing the connectivity of each of the three phases.[179] The connectivity of the networks (self-connected portions of a phase) making up the 3D microstructure were divided into three categories. If a network did not intersect any of the boundaries of our analyzed sample volume (it was contained completely within the sample volume), it was considered "isolated". Networks that intersected one and only one boundary at one location were considered to "dead-end" within the sample volume – their continuity outside of our sample volume was unknown. Finally, networks that intersected more than one boundary and were contiguous throughout the sample were assumed to be "connected" to the surrounding electrode.

The pore and YSZ phase networks were found to be almost entirely (>99 volume %) in the "connected" category. On the other hand, the LSM phase showed a significant fraction of "isolated" and "dead-end" networks, and the discussion below focuses on LSM. Figure 7.3g

shows the LSM phase (translucent yellow) with the isolated networks highlighted red and the dead-end particles highlighted blue. Figure 7.3h shows a thin section of this volume showing that the dead-end networks appeared only near the boundaries of the volume. Figure 7.3i shows the same zoomed-in volume as in Figure 7.3c, but with the isolated (red) and connected (yellow) LSM particles identified. Table 7.2 shows the volume percentages of isolated, dead-end, and connected particles. The LSM phase contained 9.2% isolated networks by volume, with another 10.4% dead-end networks of unknown status.

Table 7.2. Measured volume percentages of the LSM, YSZ, and pore phases that are isolated connected, or dead-end. Also given are the percentages and densities of TPBs in each of the connectivity categories.

	Pore %	LSM %	YSZ %	TPB %	TPB Density (μm^{-2})
Isolated	0.0	9.2	0.6	28.0	2.06
Dead-End	0.0	10.4	0.6	14.8	1.09
Connected	100.0	80.4	98.8	57.2	4.20
*Overall Connected	100.0	89.6	99.4	67.2	4.93

* Estimated value obtained by assigning the dead-end networks to either the connected or isolated categories as discussed in the text.

Each TPB segment was analyzed to determine whether it was on connected, dead-end, or isolated phases. It was both necessary and sufficient that all three phases be connected in order

for the TPB to be electrochemically active – these TPB lines are green in Figures 7.3d – 7.3f. If any one of the three phases was isolated, the TPB was considered electrochemically inactive and colored red in Figures 7.3d – 7.3f. TPBs that were on dead-end phases were of unknown electrochemical status and colored blue in Figures 7.3d – 7.3f. Figure 7.4, an enlarged view of the same TPB segments shown in Figure 7.3e, highlights the different TPB lines on the surface of the LSM phase. While most of the TPBs are connected (green), there are a number of isolated TPBs (red) distributed throughout the structure. The unknown activity TPBs (blue) were near the boundary of the sample volume. The activity of the TPBs directly correlated to the connectivity of LSM shown in Figure 7.3h. Figure 7.3f shows a zoomed-in view of a few LSM particles decorated with isolated or connected TPBs.

Table 7.2 gives the percentages of the three TPB categories. In order to estimate the total EA-TPB density, it was assumed that dead-end networks were either isolated or connected with respect to the cathode volume outside our image area, in the same proportion as that measured within our sample volume. The ratio of connected to isolated TPBs was 67% : 33%, so 67% of the TPBs of unknown status were taken to be connected. The resulting EA-TPB density value was 4.93 μm^{-2}.

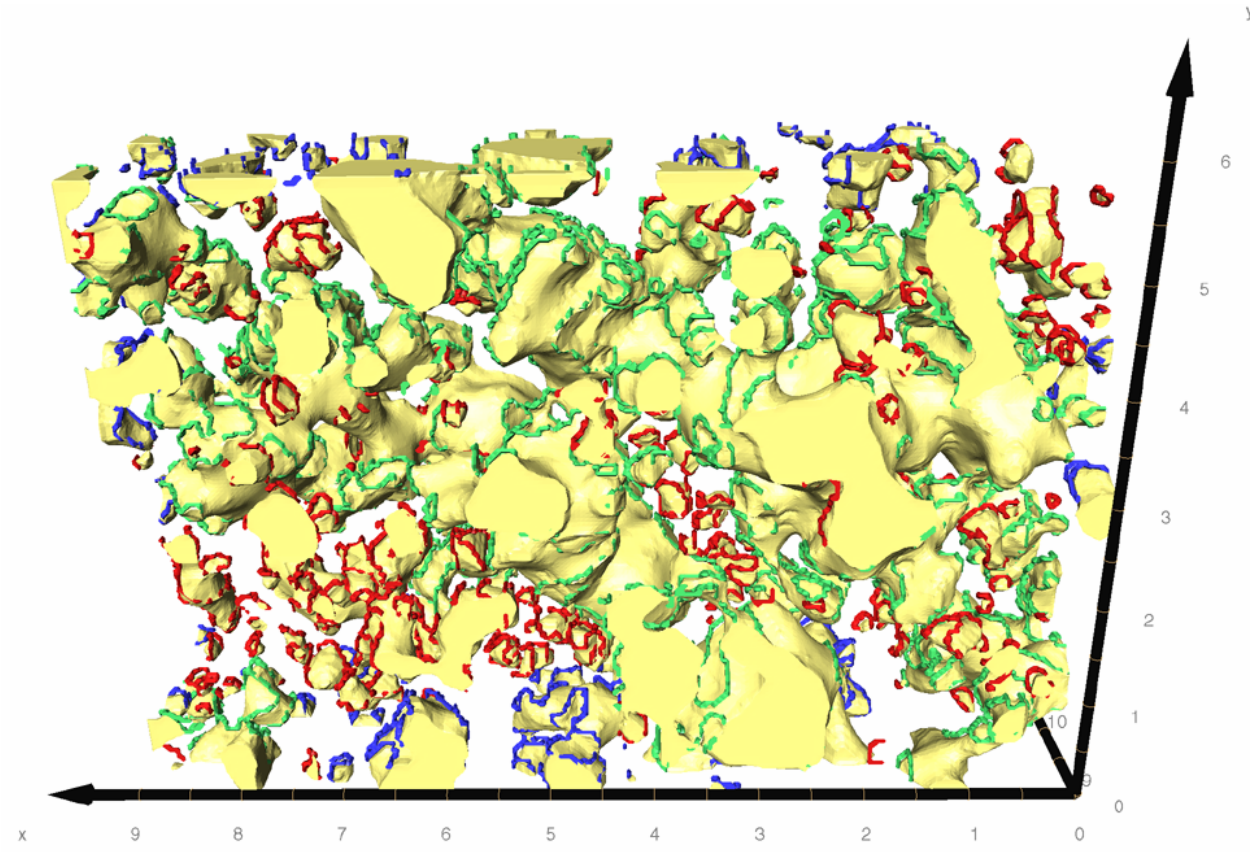

Figure 7.4. The same TPB segments as in Figure 7.3e, enlarged in order to show more clearly their distribution on the surface of the LSM (yellow). Electrochemically active TPBs are green, unknown activity TPBs are blue, and inactive TPBs are red. Dimensions are in microns.

The tortuosities of the pore and YSZ phases were also calculated in the same manner as published previously.[250] In this method, the structure of each phase was imported into a finite element software program and the diffusion flux was calculated under an applied one-dimensional concentration gradient. The tortuosity was obtained as the ratio of the flux calculated for an idealized structure consisting of straight tubes with the same volume percentage as the real structure, to the flux through the real structure. The pore phase tortuosity was measured to be (1.6, 1.6, 1.6) in each of the (x,y,z) orthogonal directions. The YSZ phase tortuosity was calculated as (3.4, 3.4, 3.5). The lack of variation between the three directions indicated that the data set was sufficiently large to avoid major statistical variations in the tortuosity values.

Prior to the FIB-SEM imaging, the LSM-YSZ cathodes were characterized using electrochemical impedance spectroscopy (EIS). These measurements were at low applied potential where LSM does not exhibit reduced oxygen content and enhanced ionic conductivity.[124] The polarization resistance values, plotted versus temperature in Figure 7.5, show the expected Arrhenius temperature dependence with an activation energy of 1.03 eV, similar to some prior reports.[61, 267] The magnitude of the resistance values are similar to prior reports for LSM-YSZ cathodes measured under similar conditions.[103]

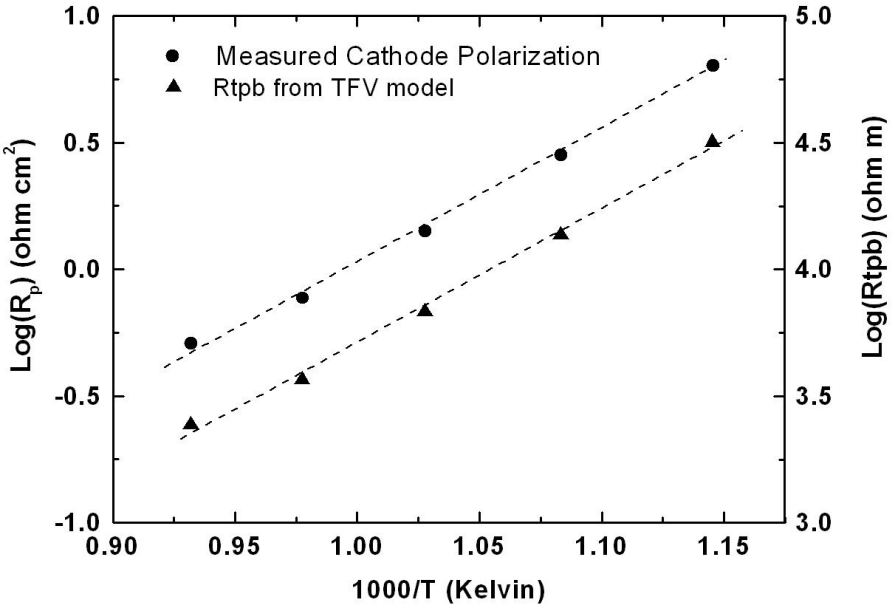

Figure 7.5. Arrhenius plot of the measured cathode polarization resistances using electrochemical impedance spectroscopy plotted with respect to the left hand axis, and the corresponding R_{TPB} values calculated using the Tanner-Fung-Virkar model plotted with respect to the right hand axis.

In order to make a preliminary evaluation of whether the present structural data was consistent with the measured polarization resistances, a composite cathode electrochemical model was applied.[136] Like other similar models,[208, 250] this model assumes idealized microstructures, necessitated by the lack of actual microstructure information. (In the future, data such as that presented here can be used to develop more structurally detailed models.) The model accounts for the resistance associated with oxygen ion transport in the YSZ phase, which is

approximated as columns perpendicular to the electrolyte surface (≈ 0.5 μm wide with a 1.0 μm repeat period and a height of 10 μm, based on the present FIB-SEM data). The model assumes a uniform surface resistance on the YSZ columns; this value was taken to be the product of the TPB density on the columns and the TPB resistance R_{TPB} per unit TPB length. Resistances associated with gas-phase diffusion in pores and electron transport in LSM are neglected in this model. Note, however, that the present EA-TPB value was used in the calculation, accounting for the effect of isolated LSM particles.

The above model idealizes the electrode microstructure by assuming the YSZ phase consists of uniform and straight columns extending from the electrolyte surface. This is clearly not a good approximation of the convoluted and tortuous YSZ phase shown in the above images. The model was thus modified to account for the YSZ tortuosity, which can be thought of as the ratio of the actual oxygen ion path length through the YSZ phase compared to a straight-line path through the cathode.

The effect of tortuosity can be accounted for approximately in the TFV model by one of two changes in the modeled structure. In one case, the structure can be thought of as tortuous tubes that are extended until they are straight (this should increase their length by the tortuosity factor of ≈3.4). This effectively dilutes the TPB density and extends the thickness of the electrode by the same tortuosity factor. In the second case, one describes the electrode with the same macroscopic values for TPB density and volume percentages, but with a proportionally increased YSZ ionic resistivity. This description makes sense in that the TPB reaction sites do not change, but since the oxygen ion has 3.4 times the distance to travel compared to a straight line normal to the electrolyte, the electrode can be described by straight tubes with 3.4 times the resistivity. While both cases produce values within 5% error of each other, the latter case is used

in our analysis in order to avoid issues from artificially increasing the electrode thickness beyond the active electrode thickness. Hence, the YSZ ionic resistivity was increased by a factor of 3.4 for all tortuosity-corrected calculations using the TFV model.

R_{TPB} values were back-calculated from the model using the measured polarization resistances, and the resulting values are plotted in Figure 7.5. Note that the tortuosity effect was relatively small, yielding an ≈5% reduction in the R_{TPB} values. This suggested that ionic transport through the YSZ was not a major limiting process in this cathode. The resulting value of R_{TPB} was ≈ 2.5 x 10^5 Ωcm at 800°C is consistent with prior estimated R_{TPB} values of ≈ 1.0 x 10^5 Ωcm and 1.26 x 10^5 Ωcm.[146, 176] The activation energy (E_a) for R_{TPB} from the slope of Figure 7.5 is 1.05 eV, close to the activation energy of the measured cathode polarization resistance (1.03 eV) in Figure 7.5. While similar polarization resistance activation energy values have been reported previously for LSM-YSZ cathodes,[61, 267] values as high as 1.6 eV have also been reported.[103] Much work has been published attempting to identify rate-limiting steps in the oxygen reduction pathway in LSM-YSZ.[124, 141, 146] In particular, it has been suggested that activation energies can be used to identify specific LSM-YSZ mechanisms (*e.g.,* oxygen dissociation, diffusion, *etc.*), at least for idealized-geometry patterned electrodes.[141] Activation energies similar to the present values have been reported for both an intermediate-frequency EIS arc attributed to surface diffusion,[268] and a high-frequency arc attributed to oxygen ion transfer.[105, 142] However, such identifications should be viewed with some skepticism until a more complete electrochemical characterization is completed.

7.4 Summary and Conclusions

The above work represents the first of its kind; there have not been any published results of quantitative three-dimensional composite cathode structure. In this work, a technique was implemented for using three-dimensional image data to identify pertinent microstructural properties, such as the triple-phase boundary density, and surface area densities and tortuosities of each phase. Analysis of the connectivity of the LSM, YSZ, and pore particle networks allowed for the calculation of the electrochemically-active triple-phase boundary segments. It was found that while the YSZ and pore networks were almost entirely self-connected, the LSM phase, with a characteristic feature size that was larger than that of the YSZ, showed at least 10% isolated particle networks by volume. These un-connected LSM networks contributed to a significant reduction in the EA-TPB density from the total of 7.35 μm^{-2} to 4.93 μm^{-2}. Using the Tanner-Fung-Virkar electrochemical model of composite electrodes, implementing the EA-TPB density and YSZ tortuosity of 3.4, the intrinsic linear-specific charge transfer resistivity of the LSM-YSZ-air triple-phase boundary was estimated to be $\approx 2.5 \times 10^5$ Ωcm at 800°C.

CHAPTER EIGHT

Composition Study of Composite LSM-YSZ Cathode Microstructure

Chapter 8: Composition Study of Composite LSM-YSZ Cathode Microstructure

8.1 Introduction

The most common cathode in state of the art solid oxide fuel cells (SOFCs) utilizes a mixture of $La_{1-x}Sr_xMnO_3$ (LSM) and 8 mol% Y_2O_3-stabilized ZrO_2 (YSZ).[143, 259-261] These LSM-YSZ composites have allowed for a reduction in operating temperature and an increase in performance in cells where oxygen reduction at the cathode so often dominates the internal polarizations.[259, 261-264] The cathode polarization, while dependent on the materials used, is a direct function of the microstructure. Despite this fact, very little work has focused on characterization of cathode microstructure due to the difficulty of resolving the LSM and YSZ phases using typical imaging methods such as electron microscopy. In addition, microstructural analysis through stereology and two-dimensional cross-sectional analysis give limited information about the complex interconnected three-component (LSM-YSZ-pore) structures that can only be fully characterized in three dimensions.[176]

Recent advances in the use of focused ion beam – scanning electron microscopy (FIB-SEM) for three-dimensional structural analysis now make it feasible to analyze the microstructure of SOFC electrodes.[177, 181-183, 226, 250] Additional developments in achieving compositional contrast between LSM and YSZ with energy-selective backscatter (ESB) detection and improvements in three-dimensional data analysis now allow for the full characterization of all microstructural quantities pertinent to SOFC performance.[178, 179] Here we describe the three-dimensional characterization and quantification of key structural parameters using FIB-SEM with ESB for a series of LSM-YSZ cathodes with composition varied between 30-70 weight % YSZ. Implementing established techniques for the

determination of the connectivity of the cathode phases to measure the electrochemically active triple-phase boundary (EA-TPB) density, and in conjunction with tortuosity measurements of the YSZ phase and other microstructural features, the observed cathode performance for the different compositions is explained through electrochemical modeling.

8.2 Experimental Procedure

The present LSM-YSZ cathodes were prepared using the same processing methods as those presented in Chapter 7. To restate these procedures, the samples used in this study consisted of dense 8 mol% Y_2O_3-stabilized ZrO_2 (YSZ) electrolyte pellets, with identical cathodes symmetrically placed on opposite sides of the pellet. The YSZ pellets were prepared by uniaxially dry pressing from a mixture of YSZ powder (Tosoh) and a small amount of PVB binder. The pellets were fired at 1400°C for 4h.

The cathodes in this study were mixtures of LSM-YSZ (LSM = $La_{0.8}Sr_{0.2}MnO_3$, Praxair), where the weight ratio of LSM:YSZ was varied from 30:70 to 70:30 at intervals of 5%, such that a total of 9 different compositions were achieved. The 50:50 sample analyzed in Chapter 7 is the sample used for that composition in this study. The cathodes were applied to dense YSZ electrolyte surfaces by screen-printing. The screen printing inks were prepared by first ball milling the LSM and YSZ powder to thoroughly mix, and then combining with a Heraeus vehicle in a three-roll mill. After printing, the LSM-YSZ layer was fired in air at 1175^0C for 1 hour. Pure LSM current collector layers were then printed (using an ink prepared from LSM powder only) on top of the LSM-YSZ. The samples were then fired again in air at 1175^0C for 1 hour. Figure 8.1 illustrates a fracture cross-sectional scanning electron microscope image of the

30:70 LSM-YSZ cathode. The LSM-YSZ and LSM layers were both ~10-12μm thick, which was consistent throughout the series of compositions. FIB-SEM images were taken from the portion of the LSM-YSZ cathode active layer directly adjacent to the YSZ electrolyte, which should be most relevant to determining the electrochemical performance.

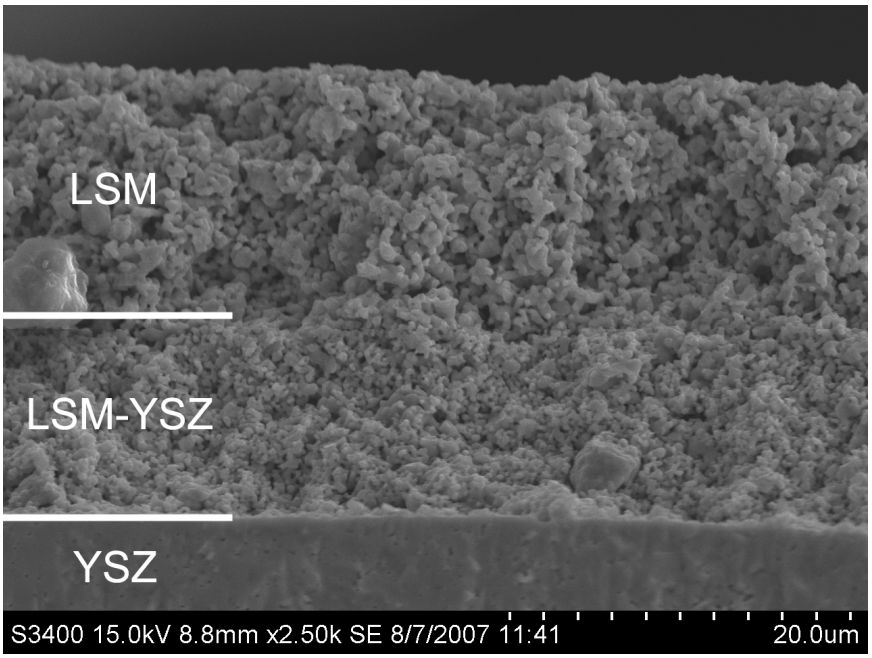

Figure 8.1. SEM cross-sectional image of the LSM and LSM-YSZ layers on top of the dense YSZ electrolyte pellet for the sample with a weight % ratio of 30:70 (LSM:YSZ).

The present FIB-SEM measurements utilized the same two key measures to produce quantitative three-dimensional images as those discussed in Chapter 7 for the 50:50 LSM:YSZ sample. Firstly, the pores within the electrode structure were filled with an impregnating epoxy prior to the measurements to allow for better planar sectioning and for ease of automatic

segmentation. Secondly, contrast between the LSM and YSZ phases was achieved by using low electron beam energy and an energy-selective (biased) in-lens backscatter detector (as discussed in section 3.4.4). The clear contrast between the LSM, YSZ, and pore/epoxy and the uniform contrast within each phase allowed the use of automated procedures to rapidly segment the images for all samples.

8.3 Results

8.3.1 Electrochemical Characterization

The symmetric LSM-YSZ cathode samples were electrochemically characterized using a Zahner IM6 electrochemical testing station. For each composition at least 3 identical samples were fabricated from which the sample with the best performance (performance variation of <10% was observed) was used in this study. Figure 8.2a shows a Nyquist plot illustrating the impedance response of 5 of the 9 compositions in air at 800°C with no applied dc voltage. The shapes of the impedance arcs were similar to that reported previously for LSM-YSZ cathodes.[265] Only 5 samples are shown for clarity in this figure because the other 4 samples whose compositions are symmetric about the 50:50 sample show very similar performance to their converse composition, and hence the impedance arcs overlap. This overlap can be seen in Figure 8.2b, where the polarization resistance is plotted for all 9 compositions at three different temperatures. A very symmetric performance is observed with respect to the 50:50 sample composition. The activation energies for all of the samples were very consistent, ranging randomly from 1.03 eV to 1.14 eV. The magnitudes of the polarization resistances of the cells were in the range normally observed for LSM-YSZ composite cathodes measured in this

way.[109, 265] This is perhaps not surprising given that the starting powder sources and processing procedures used here are fairly common. Thus, the present microstructural results are expected to be fairly representative of LSM-YSZ cathodes studied by many groups.

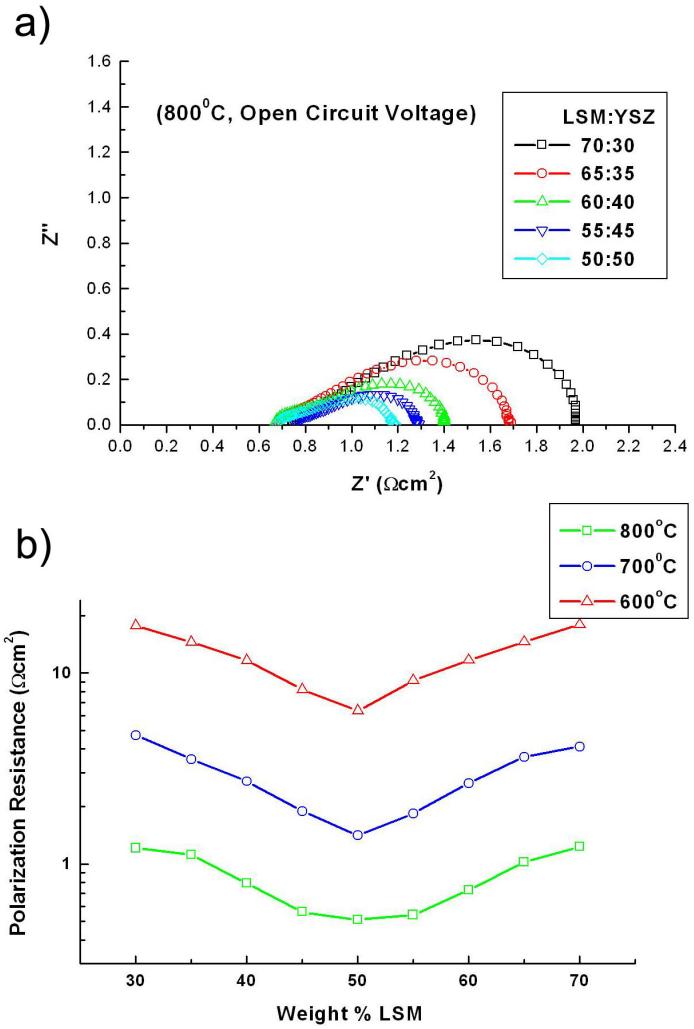

Figure 8.2. (a) A Nyquist plot of the impedance response for 5 of the 9 sample compositions. The other 4 samples are omitted because their impedance curves overlap those displayed. (b) The cathode polarization resistance at three different temperatures for each composition, extracted from the impedance measurements shown in (a).

8.3.2 Structural Characterization

Figure 8.3 shows a compilation of the fully segmented three-color images for each composition (labeled by the weight % YSZ and cropped to all be the same size), where the LSM is white, the YSZ is grey, and the porosity is black. The resolutions and volumes of material analyzed differed slightly between each sample, depending on the conditions set during the microscopy and the level of cropping required as a function of the quality of the images. In all cases, however, the resolutions were better than 50nm in the X-Y and sectional (Z) directions. Figure 8.4 shows the volumes of reconstruction for each sample, where in each case the total volume analyzed was greater than the ≈500 μm^3 minimum estimate required for obtaining statistics representative of the total electrode, as analyzed in section 3.8.1. However, as discussed later, the low volume for the 35 weight % YSZ sample may increase the errors associated with calculations performed.

The full reconstructions of each composition are shown visually in Figure 8.5 in order of increasing weight % YSZ, with the LSM phase in yellow, the YSZ phase in pink, and the porosity fully transparent. From these sets of 3D data a number of microstructural calculations can be made. Figure 8.6a shows the measured volume percentages of each phase for each composition. The level of porosity does not change between the samples, which is a function of the fact that each composition was prepared with the same solids-loading in the screen-printing ink and sintered at the same temperature for the same amount of time. The linear increase and decrease in the YSZ and LSM phases between compositions is expected as the weight % of each phase is varied. Figure 8.6b shows the volume % of solids (i.e. for LSM = $V_{LSM} / V_{LSM}+V_{YSZ}$) for the LSM and YSZ phases. The dashed lines represent the expected solids volume

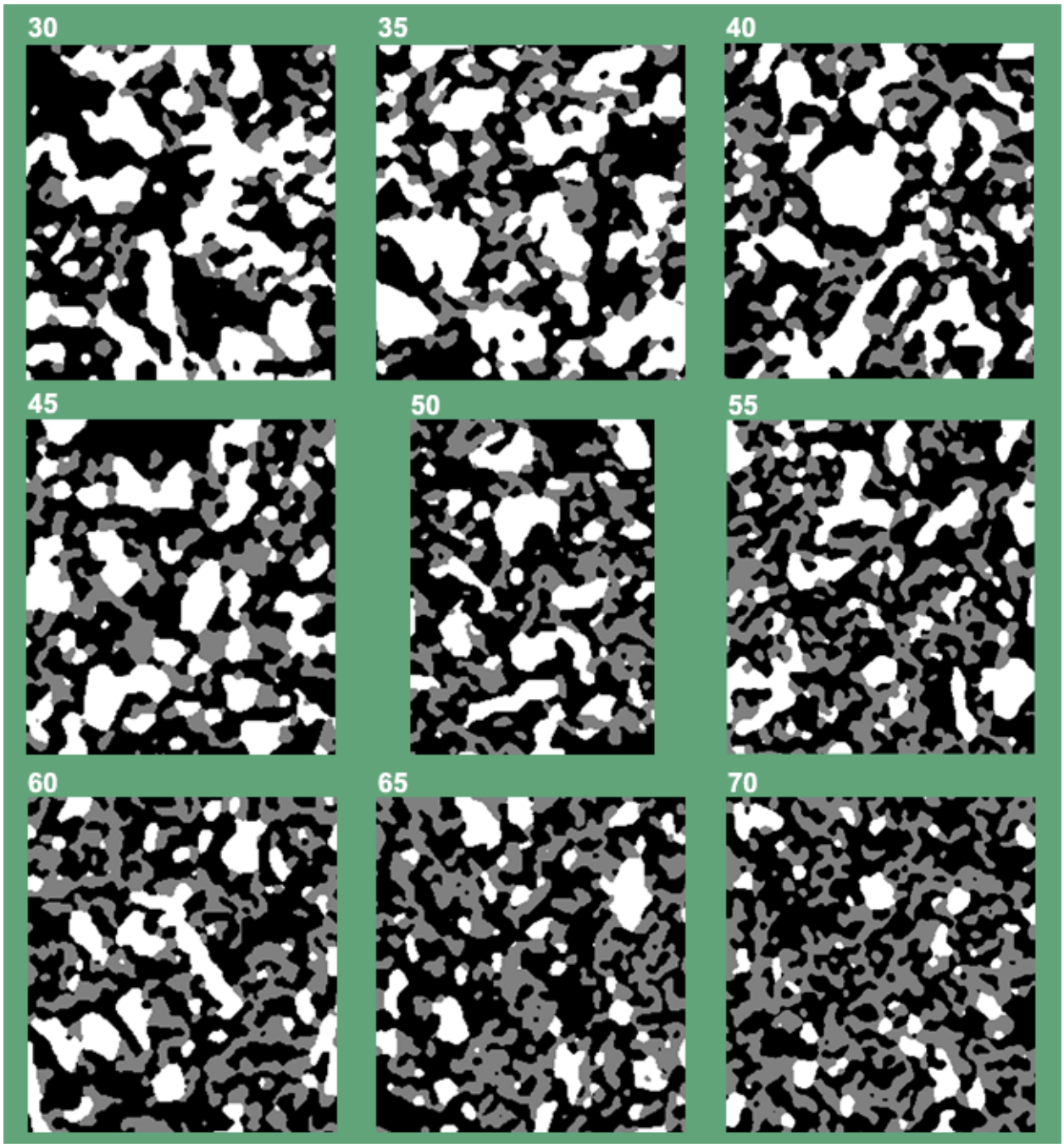

Figure 8.3. A compilation of one segmented 2D image from each composition, labeled by weight % of YSZ in increasing order. LSM is white, YSZ is grey, and porosity is black. Each image is 8.2 μm tall.

percentages calculated based on the starting weight % of each phase. As can be seen, the measured values are very close to these lines, implying that the processing was uniform and consistent, and/or the volumes of the reconstructions were large enough to be representative of the expected electrode composition. The increase in volume % of YSZ and decrease in volume % of LSM can be seen visually in the reconstructions shown in Figure 8.5, where the samples in order of increasing weight % YSZ show continually less yellow LSM phase and more YSZ pink phase.

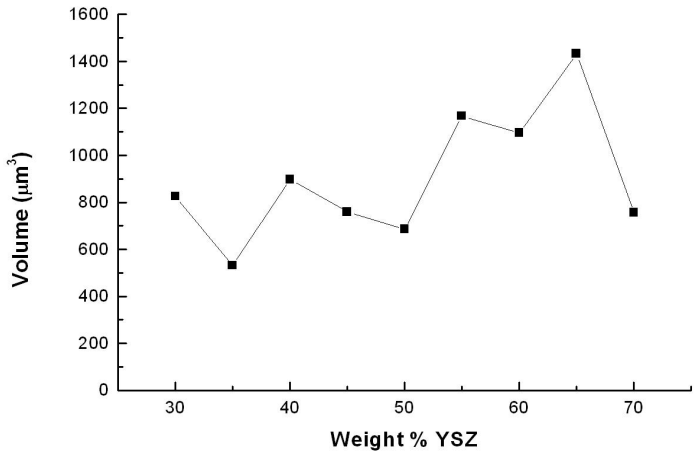

Figure 8.4. Volumes of material reconstructed for each sample composition, plotted as a function of the weight % of YSZ.

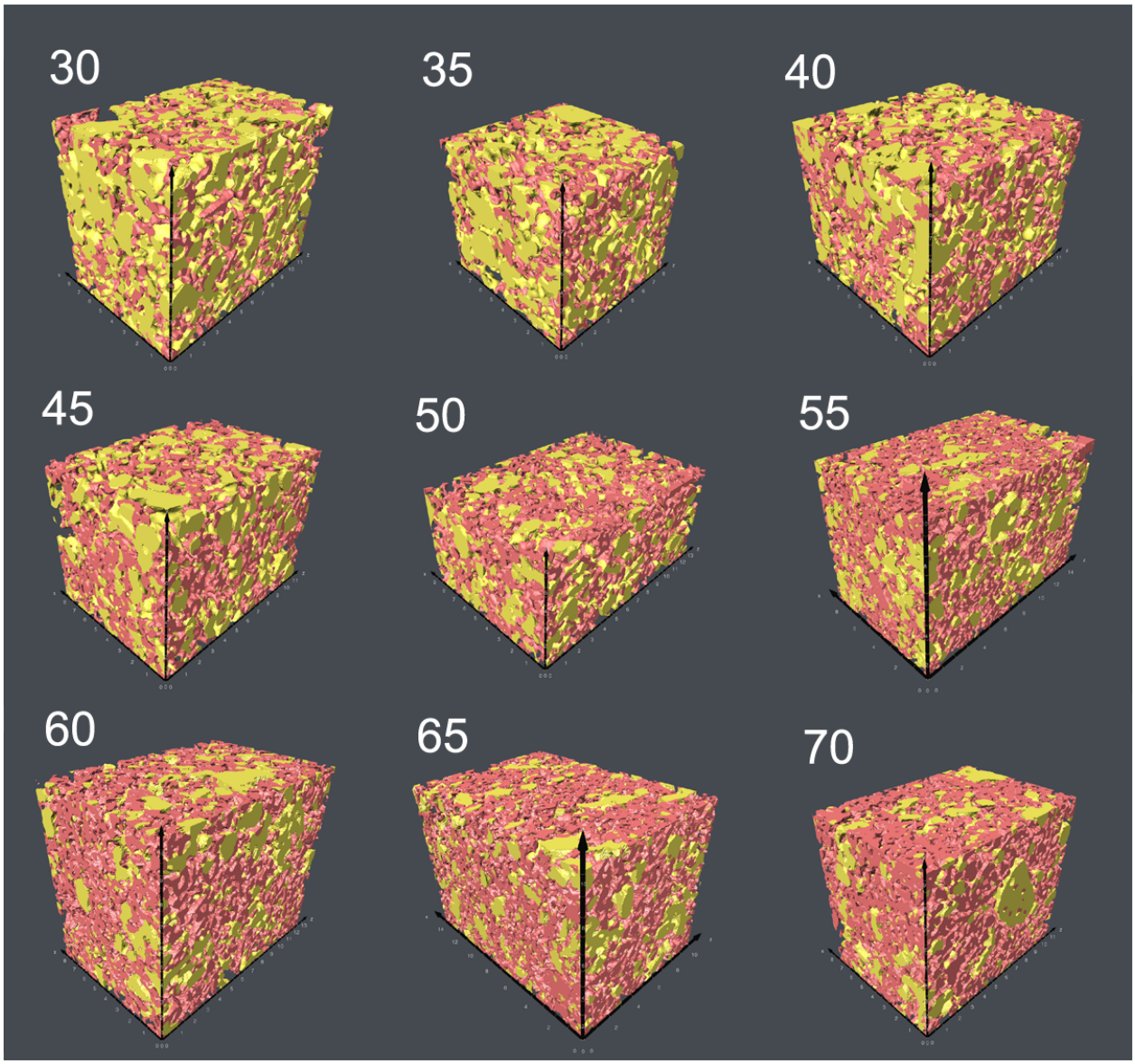

Figure 8.5. Visual representations of the full reconstructions of each sample, labeled by the weight % of YSZ in increasing order. LSM is yellow and YSZ is pink, while the porosity is omitted (transparent). The volumes of each reconstruction are plotted in Figure 8.4.

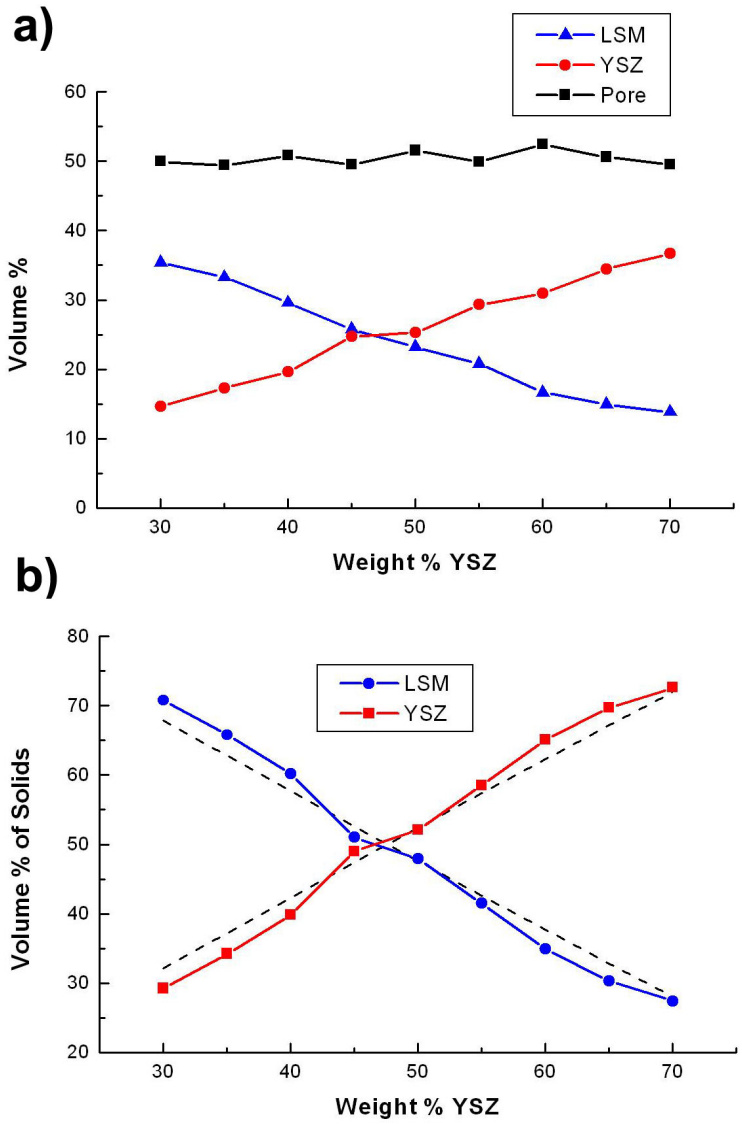

Figure 8.6. (a) The measured volumes percentages of each phase measured from the 3D reconstructions. (b) The volume percentage of LSM and YSZ with respect to the total volume of solid material. The dashed line represents the expected values based on the starting weight ratios of LSM to YSZ showing good agreement with the measured compositions.

The surface area densities were also calculated for each phase and are plotted in Figure 8.7. As is expected, the surface area densities increased with increasing volume percentage for each of the YSZ and LSM phases. The YSZ has a larger surface area density than the LSM relative to their respective volume percentages, implying that the feature size of YSZ is smaller than that of LSM. This was reported earlier for the 50:50 LSM-YSZ sample in Chapter 7, and is reasonable given the larger average particle size of the LSM starting powder (≈3.0μm) compared to that of the YSZ powder (≈0.5μm).[258] This can also be seen in the fact that although the volume percentage of the total solid phases remains constant, the sum of their surface areas densities, which is also proportional to the pore surface area density, increases with increasing YSZ content. This smaller characteristic length scale of YSZ compared to LSM will be important later when implemented with electrochemical and TPB density modeling.

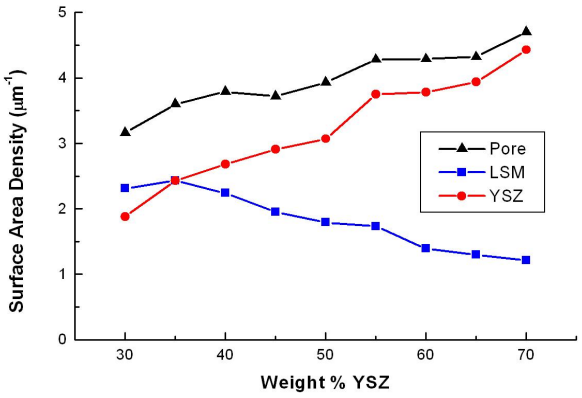

Figure 8.7. Surface area densities measured for each phase from the 3D reconstructions.

The total TPB density was calculated for each sample based on the procedure outlined in section 3.6.3. These values are plotted in red in Figure 8.8 in addition to the measured

polarization resistance. It can be seen that the maximum TPB density is skewed toward an LSM rich composition, most likely due to the difference in particle size between the LSM and YSZ. This effect is discussed in detail later in section 8.4.1. The range of densities between 6-9 μm^{-2} is greater than those reported in Ni-YSZ anodes in Chapter 6, which is a function of the comparatively finer microstructure of the cathodes. Additionally, it is important to note that the 35 wt% YSZ sample, which had the lowest volume of reconstruction, appears slightly high compared to the curved trend of values. This possible error, which is a function of not having enough volume to represent the TPB density of the total electrode, is certainly not large, and plays little effect on the electrochemical modeling conducted in section 8.4.2.

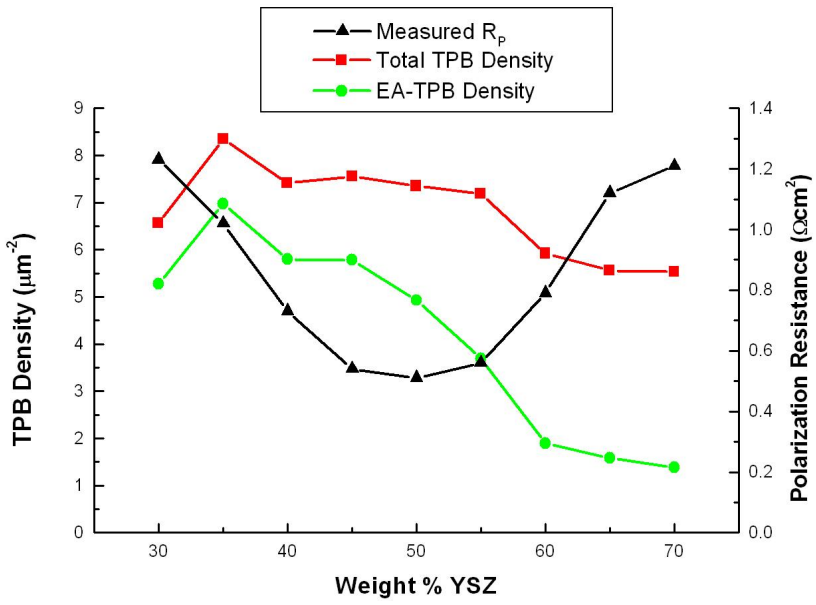

Figure 8.8. The measured TPB and EA-TPB densities for each composition plotted with respect to the left hand axis, and the measured polarization resistance (R_p) at 800°C plotted with respect to the right hand axis.

The connectivity of each of the phases was calculated in the same manner as presented in section 3.6.5 and as performed on the 50:50 LSM-YSZ sample analyzed in Chapter 7. The porosity was found to be 100% connected for all samples, so this phase is ignored in the following analyses. There appeared to a significant particle size effect in the connectivity of the two solid phases. As shown in Figure 8.9, the larger sized LSM showed dramatic decreases in its connectivity as the volume content of LSM was reduced. It appears, as is visible in the images in Figure 8.3, that the LSM morphology involved the formation of larger particles that tended to be isolated within the smaller feature YSZ matrix, which stays almost fully connected down to a measured volume percentage of 25% for the 45 weight % YSZ sample. Figure 8.10 shows a 3D visual representation of the isolated (red) and unknown (blue) particle networks of LSM for each composition, highlighting the increase in volume of unconnected networks as the LSM content decreases. Additionally, Figure 8.11 shows the same representations for the YSZ phase for each composition, which clearly shows consistently very high levels of connectivity. Only at the very low content YSZ compositions do appreciable amounts of isolated YSZ start to form. Even still, at its most extreme, the 30 weight % YSZ sample, with only 14.6% YSZ by volume, remains at least 94.5% connected. This defies common particle packing and percolation theory, which states that a phase with this low a volume percentage would completely consist of isolated particle networks. It is clear that the processing and sintering stage affects the connectivity of the phases, especially that of YSZ, such that connectivity is maintained despite low volume percentages.

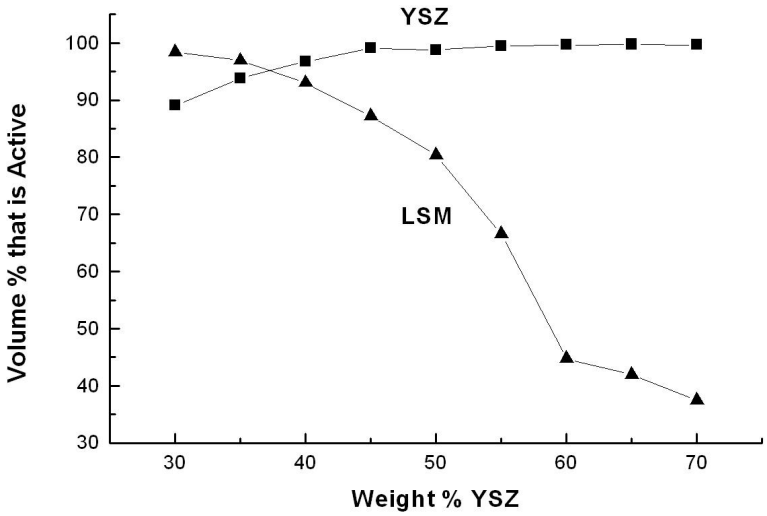

Figure 8.9. Minimum level of connectivity of the YSZ and LSM phases as a percentage of the total phase volume. Values are achieved by subtracting the volume % of isolated and unknown particle networks from the total phase volume.

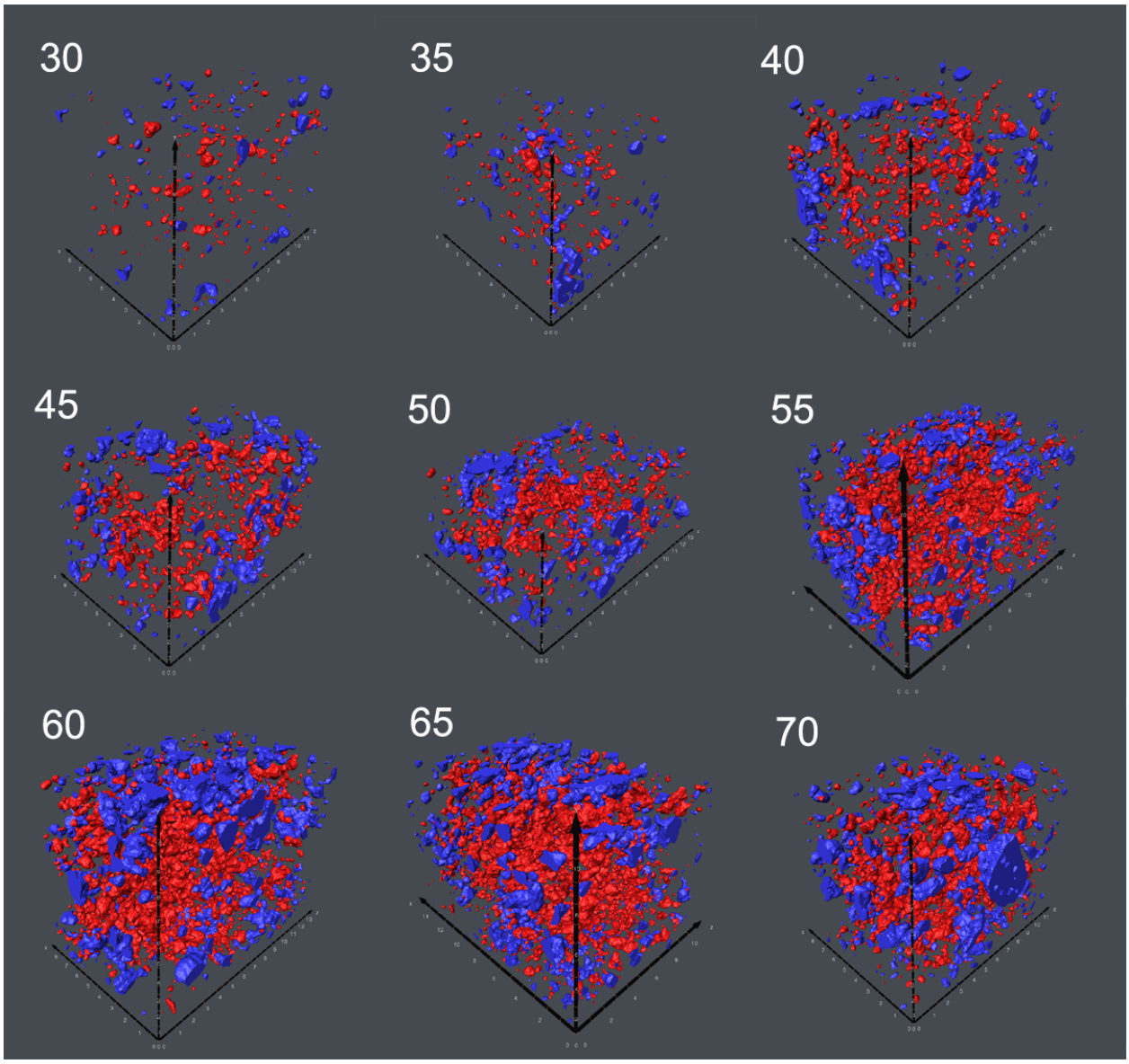

Figure 8.10. 3D visual representations of the isolated (red) and unknown (blue) particle networks for the LSM phase. The samples are labeled by the weight % of YSZ.

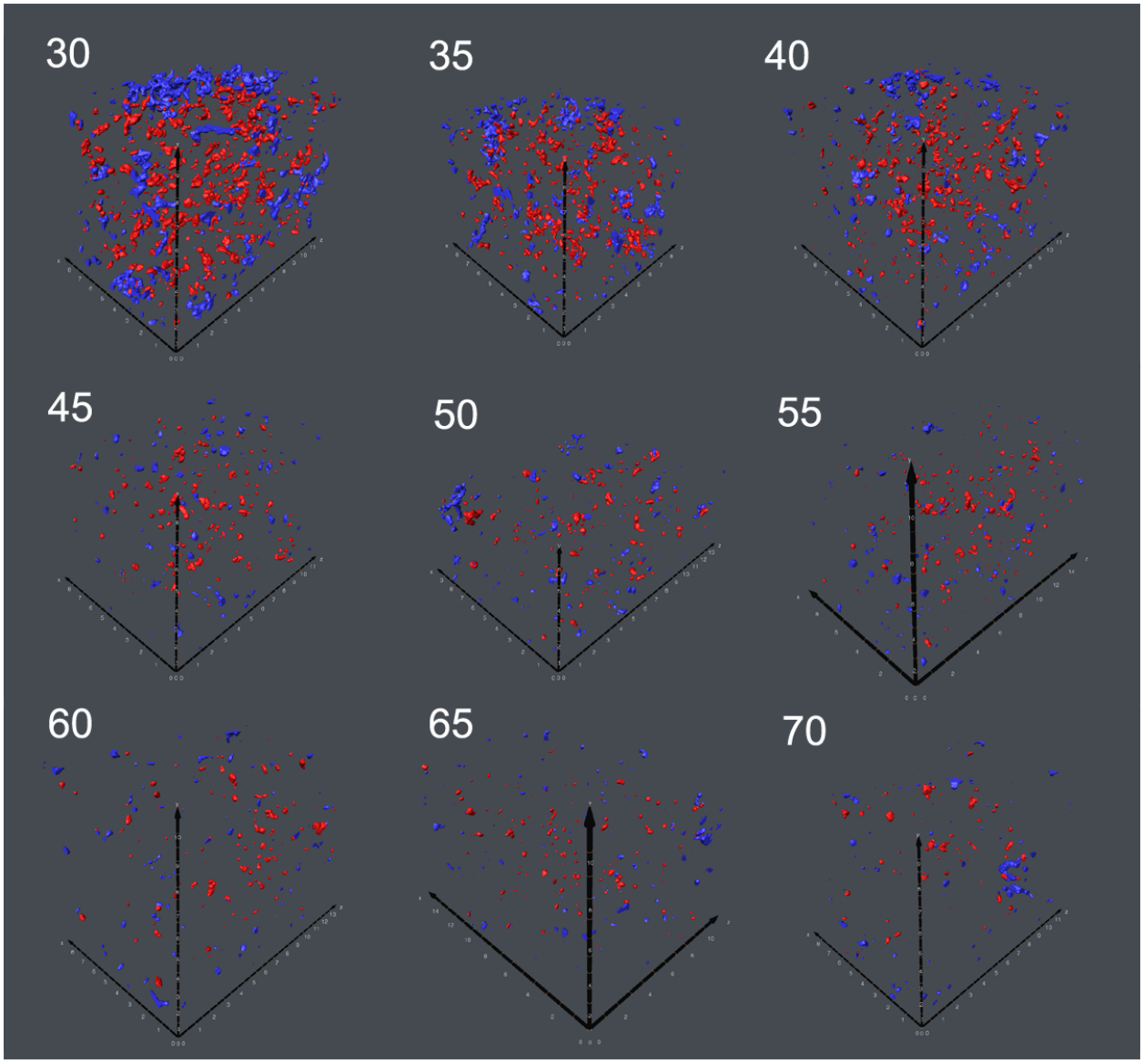

Figure 8.11. 3D visual representations of the isolated (red) and unknown (blue) particle networks for the YSZ phase. The samples are labeled by the weight % of YSZ.

Using the connectivity data of the LSM and YSZ phases calculated above, the electrochemically-active TPB (EA-TPB) density was calculated for each of the compositions. A visual 3D representation of the TPBs for each composition is shown in Figure 8.12, where active TPBs are in green, TPBs of unknown activity are in blue, and in-active TPBs are in red. The influence of the unconnected particle networks displayed in Figures 8.10 and 8.11 is apparent, as the amount of active (green) TPBs dramatically decreases as the LSM content decreases. A plot of the resulting measured EA-TPB densities is shown in green in Figure 8.8. Due to the high levels of unconnected LSM in the high YSZ content compositions, the EA-TPB density is cut by more than half of the total TPB density for the right side of this plot. At the lowest YSZ content compositions, while less pronounced than the effect of unconnected LSM, unconnected YSZ causes an appreciable drop in the EA-TPB density. Figure 8.13 shows a plot describing the percentage of the total in-active TPB density that is due to isolated LSM and YSZ. As described above, most of the compositions are dominated by isolated LSM contributing to inactive TPB length, where at the composition with the very lowest YSZ content, the YSZ becomes the dominant phase responsible for inactive TPBs.

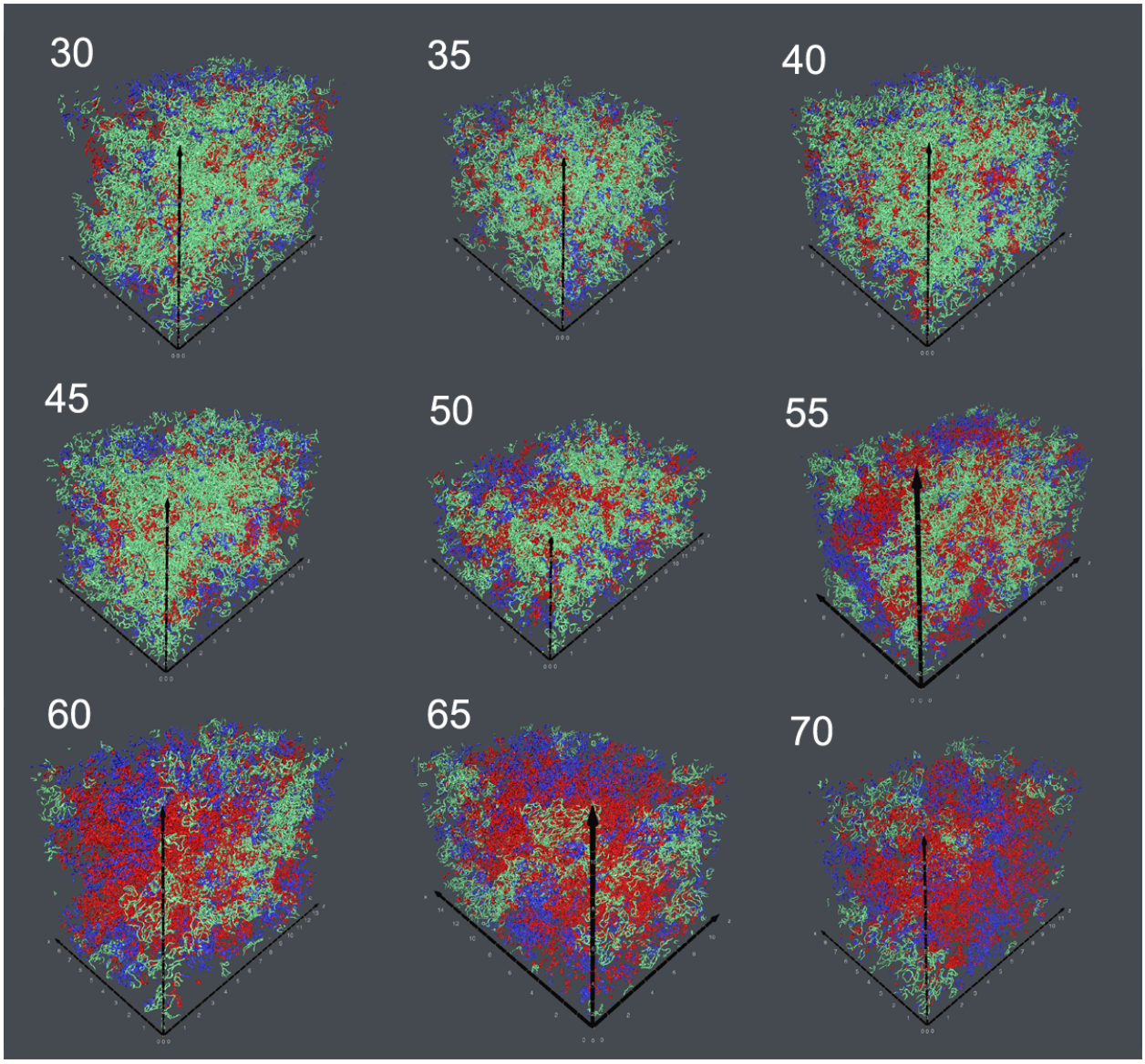

Figure 8.12. Three-dimensional visual representations of the TPB segments for each composition, with the active TPBs in green, the TPBs of unknown activity in blue, and the inactive TPBs in red.

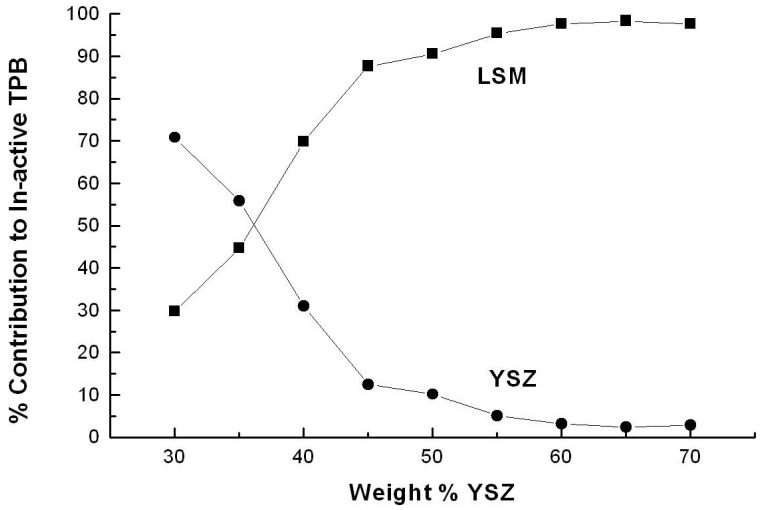

Figure 8.13. A plot showing, of the total in-active TPBs, the percentage by length that lie on isolated LSM or isolated YSZ.

The tortuosity of the YSZ and pore phases were also calculated in order to better understand the bulk transport limitations that might exist in the electrode. Because the conductivity of the LSM is orders of magnitude greater than that of the YSZ, it is assumed that electronic transport within the LSM is not limiting. Figure 8.14 shows a plot of the pore and YSZ tortuosities for each of the compositions. Because the porosity remained at a high volume percentage of ≈50%, and because it was shown to be completely interconnected, a consistent and low tortuosity value of ≈1.6 was calculated for all compositions. Conversely, the YSZ phase showed dramatic increases in tortuosity with decreasing volume percentages of YSZ. A maximum tortuosity of 6.5 was achieved for the 30 weight % YSZ sample, an extremely high

value that will undoubtedly contribute to increases in bulk ionic transport resistances. These values are much higher than those found in Ni-YSZ anodes, which ranged from 1.4-2.5 for the compositions analyzed in Chapter 6. This is a function of the finer microstructure and lower volume percentages of YSZ that is found in the cathodes, compared to the composite anodes. This is most likely a direct result of the fact that the cathodes are only partially sintered, producing higher porosity and lower YSZ volume percentages, while the Ni-YSZ anodes are fully sintered before the porosity is produced from reduction of NiO to Ni.

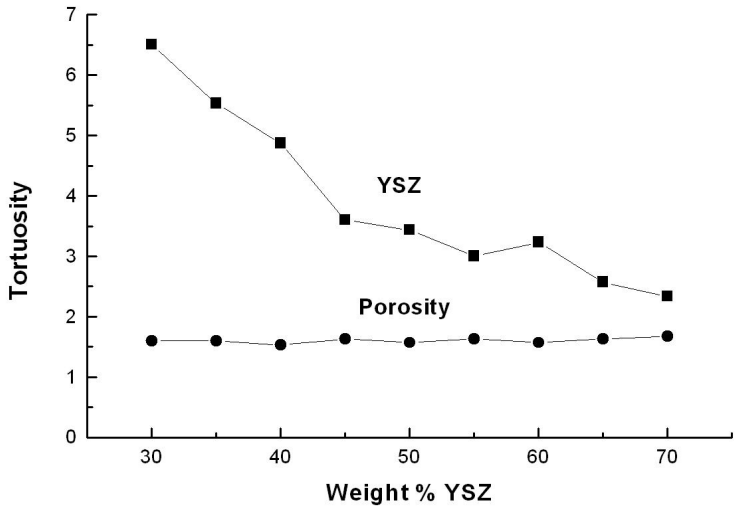

Figure 8.14. Average tortuosity values for the YSZ and pore phases for each of the compositions.

8.4 Discussion

8.4.1 Effect of Composition on TPB Density

The measured total TPB density showed a maximum skewed towards an LSM rich composition. If the particle sizes of the LSM and YSZ phases were equal, this maximum would be expected to occur at a composition with equal volume percentages, as long as the porosity is constant for all compositions. However, because the particle size of the LSM is greater than that of the YSZ, it is logical that having more LSM by volume, to increase the LSM surface area on which YSZ can contact, would increase the TPB density, if all other variables are kept constant. While this effect is observed experimentally in this series of samples, structural models based on random packing of spherical particles can also be implemented in order to test this theory. It should be easier to model these cathodes compared to Ni-YSZ anodes because the porosity is constant between compositions and is close to the often assumed 40% level of porosity common for random packing models. In this case, the Zhu et al. composite electrode structural model was used to calculate the estimated TPB density as a function of the measured volume percentages and particle sizes.[191]

The particles for each phase in the model are assumed to be of a specific diameter. While real interconnected structures don't necessarily mimic a series of connected spheres, their characteristic diameters can be estimated from microstructural features. If a phase is fully connected, it is expected that the structure would best be described by a series of interconnected tubes whose volume to surface area ratio is equal to 4. If a phase consists entirely of isolated spheres, its volume to surface area ratio would equal 6. In reality, electrode structures usually consist of a combination of connected tube-like structures and isolated spherically shaped

particles. The level to which each type of shape contributes to the overall microstructure is estimated based on the connectivity calculations for each phase, where active volume is treated as tubes and isolated phases are treated as spheres. As a result, the characteristic diameter of a real microstructure is estimated to be equal to the ratio of the volume to surface area times the linear extrapolation of the amount of isolated phase between the values of 4 and 6. Calculating the characteristic diameter for each composition based on the measured volumes (Figure 8.6), surface areas (Figure 8.7), and % of connectivity (Figure 8.9), yielded an average diameter of 0.56 μm for LSM and 0.32 for YSZ.

Figure 8.15 shows the estimated TPB densities based on the Zhu model where the measured volume percentages and the characteristic diameters calculated above are used. The TPB maximum occurs at an LSM rich composition, and the overall shape and magnitude of the estimated TPB curve agrees well with the measured total TPB densities that are plotted in the same figure. The ratio of the characteristic diameters of the LSM and YSZ determines the shape of the curve, while the magnitude of the TPB densities is inversely proportional to the magnitude of the characteristic diameters (i.e. smaller particles give rise to higher TPB densities). In this case, except for in the calculation of the diameters, the connectivity of the phases is ignored. However, the model also implements percolation theory to estimate the EA-TPB density. This is also plotted in red in Figure 8.15. While percolation theory overestimates the volume percentage at which the LSM percolation threshold experimentally exists (in the model there is zero connectivity below an LSM volume percentage of 20% which occurs at composition 40:60 LSM:YSZ), the general trend observed in the measured EA-TPB density is seen, where an overall decrease in TPB density occurs at all compositions, with a more dramatic drop in YSZ rich compositions. This result gives great encouragement to the ability of structural models to

accurately describe microstructural properties in cases where there is good agreement between the real structures and the simplified geometric representation.

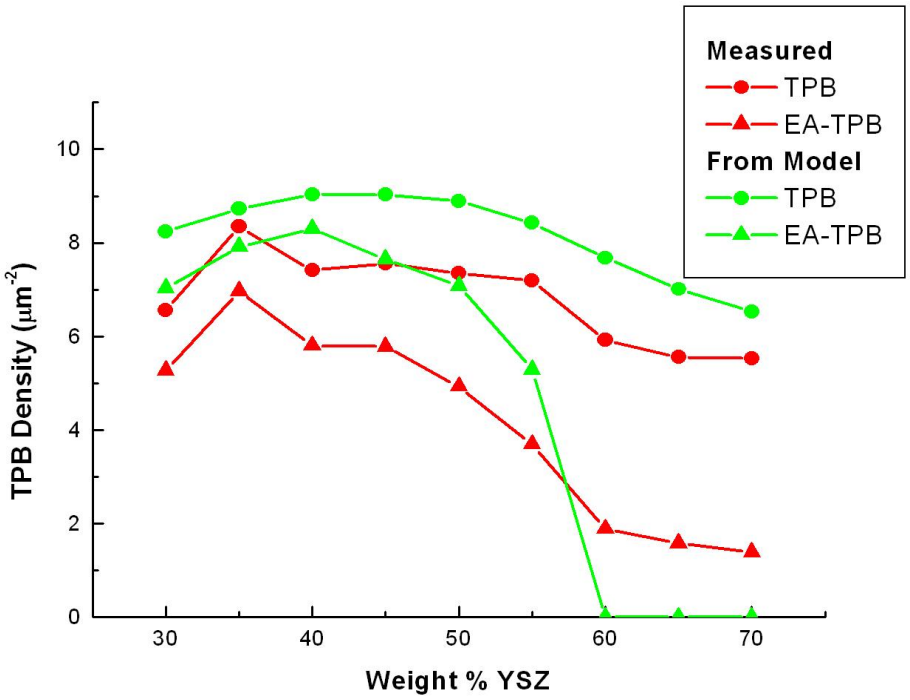

Figure 8.15. The measured TPB and EA-TPB densities plotted in addition to the estimated TPB and EA-TPB densities from the Zhu et al. model. In the model, particle diameters of 0.56 μm for LSM and 0.32 μm for YSZ were used, while the particle contact angle is assumed to be 15 degrees, and an average coordination number of 6 is used.

8.4.2 Effect of Microstructure on Polarization Resistance

In order to better understand the effect of the measured microstructures on the observed performance, the Tanner-Fung-Virkar (TFV) composite electrode model was employed.[136] The model assumes an ionically-conducting (YSZ) phase consisting of one-dimensional columns extending vertically from the electrolyte, where the conducting phase, LSM in this case, is treated as an average surface resistance on the ionic-conductor. A tacit assumption of this model is that all phases are fully contiguous and that concentration polarization is negligible. In the present calculations, the YSZ column structure was set at the characteristic diameter of 0.32 μm, as measured previously. The distance between the YSZ columns was varied to match the measured YSZ volume fractions for each composition. Unless otherwise indicated, an electrode thickness of 10 μm was used in the model based on the experimentally measured active layer thickness. The average surface resistance was calculated by uniformly distributing TPB's on the YSZ column surfaces to match the present measured TPB density values, with the TPBs having the linear-specific TPB resistance of ≈2.5 x 10^5 Ωcm at 800°C (unless otherwise indicated) estimated in Chapter 7 for the sample with 50:50 LSM:YSZ composition.

The estimated polarization resistances (R_p) for each composition with respect to the total TPB density estimated using the TFV model are plotted in red in Figure 8.16. As was the case with the Ni-YSZ anodes studied in Chapter 6, the modeled polarization resistances showed the same general shape as the observed performance, but the magnitude and relative changes in performance between compositions did not match the ≈100% increase in resistance observed between the 50 weight % YSZ sample and the two extremes of 30 weight % LSM or YSZ.

Clearly, microstructural characteristics beyond just the total TPB density are at play to cause such dramatic changes in performance.

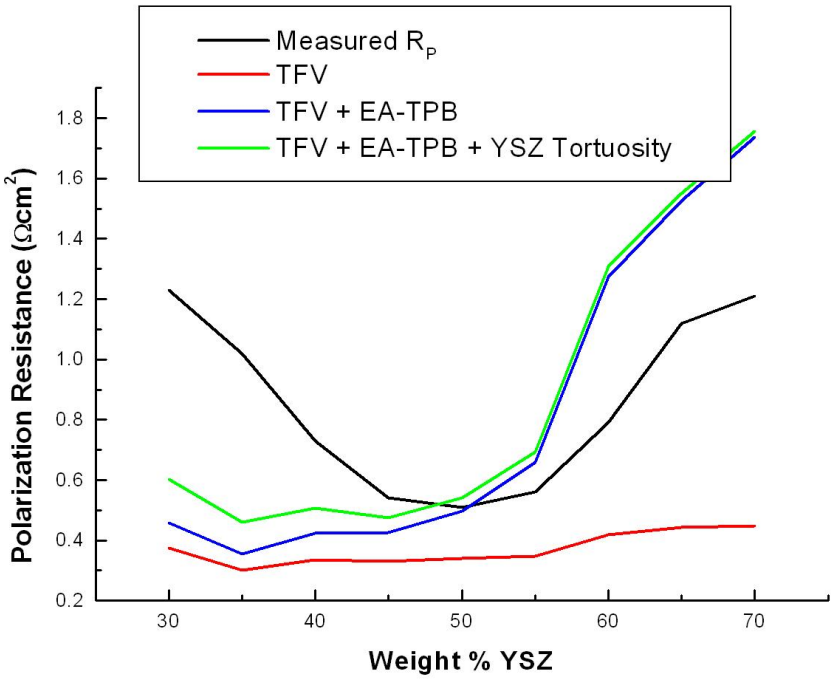

Figure 8.16. Measured and estimated polarization resistances for composite LSM-YSZ cathodes using the TFV electrochemical model for different compositions and model parameters.

While the total TPB density can be roughly estimated from 2D images using stereology, it is the EA-TPB density, only achievable through connectivity calculations from full 3D reconstructions, that must be used in the TFV model, as TPBs that do not have contiguous pathways in all three phases will not contribute to the measured polarization. Re-implementation of the TFV model using the EA-TPB densities calculated for each composition was conducted

and the results are plotted in blue in Figure 8.16. Because the EA-TPB densities were lower than the total TPB densities, the estimated polarizations for each composition increased. This effect, however, dramatically increased with decreasing LSM content. For these low LSM compositions, large amounts of un-connected LSM particle networks led to greatly depleted EA-TPB densities, as discussed previously and shown in Figure 8.8. For the 30 weight % LSM sample, with only 41.4% connectivity (by volume), the reduction of the EA-TPB density to 1.39 μm^{-2} from the total TPB density of 5.53 μm^{-2} served to increase the modeled polarization resistance of this electrode from 0.246 Ωcm^2 to .897 Ωcm^2. Clearly the effect of the connectivity of the phases, manifested in the EA-TPB density, can explain the high polarization resistances observed for the low LSM content compositions. Despite this, there was not significant reduction of the EA-TPB density for low YSZ content compositions, whose observed high polarizations are left to be explained.

Because high YSZ tortuosities occur in the low YSZ content compositions, as shown in Figure 8.14, it is expected that bulk ionic transport limitations will noticeably increase the polarizations for the far left compositions in Figure 8.16. The YSZ tortuosity is implemented in the TFV model by dividing the YSZ conductivity by the tortuosity factor. This serves to equate the ohmic resistances of the straight pathway in the model with that of the tortuous pathway with normal YSZ conductivity in the real structure. The effect of the addition of the YSZ tortuosities into the TFV model (using the EA-TPB values) is plotted in green in Figure 8.16. As postulated, greater increases in resistivity were observed for the compositions with less YSZ. While this effect helps to better match the shape of the measured performances for all compositions, it still falls short of describing the large measured polarizations for the low YSZ content samples.

There are a couple of possible explanations for the inability of the model to explain the observed high resistivity in the low YSZ content samples. Firstly, the TFV model is based on a very simplistic representation of the electrode microstructure, and certainly it is not expected to fully describe the full range of microstructure-performance relationships. With that said, Figure 8.17 shows the effects of electrode thickness and the linear-specific TPB resistivity (R_{TPB}) on the electrode polarization resistance in the model. In either case, an increase in electrode thickness or a decrease in R_{TPB} serves to better match the shape of the measured polarization by creating a more symmetrical curve. What must be considered when using this model is that, while exact matches can not be achieved using the measured structural values, the general trend of high tortuosity and bulk ionic transport limitations in low YSZ content compositions has at least qualitatively been shown to decrease the performance.

Another limitation of the model is that it treats the discrete TPB reaction sites as a diffuse reaction on the surface of the YSZ. While the density of TPBs on the YSZ is large enough to statistically allow for such an approximation (the distance between TPB segments on the YSZ column is approximately half the width of the YSZ column, as calculated from the EA-TPB density and YSZ volume %), two studies using microelectrodes have shown that current constriction in the electrolyte at the TPB also adds a resistance to the electrode.[152, 153] This effect, which is ignored in the TFV model, should certainly increase the measured electrode polarization. This highlights the importance of using finite-element modeling, where structural effects on the nano-scale, such as the reported current constriction at the TPB, can be effectively accounted for. It is possible that the current is restricted enough in the low YSZ content, highly tortuous pathway microstructures to cause the observed high polarizations.

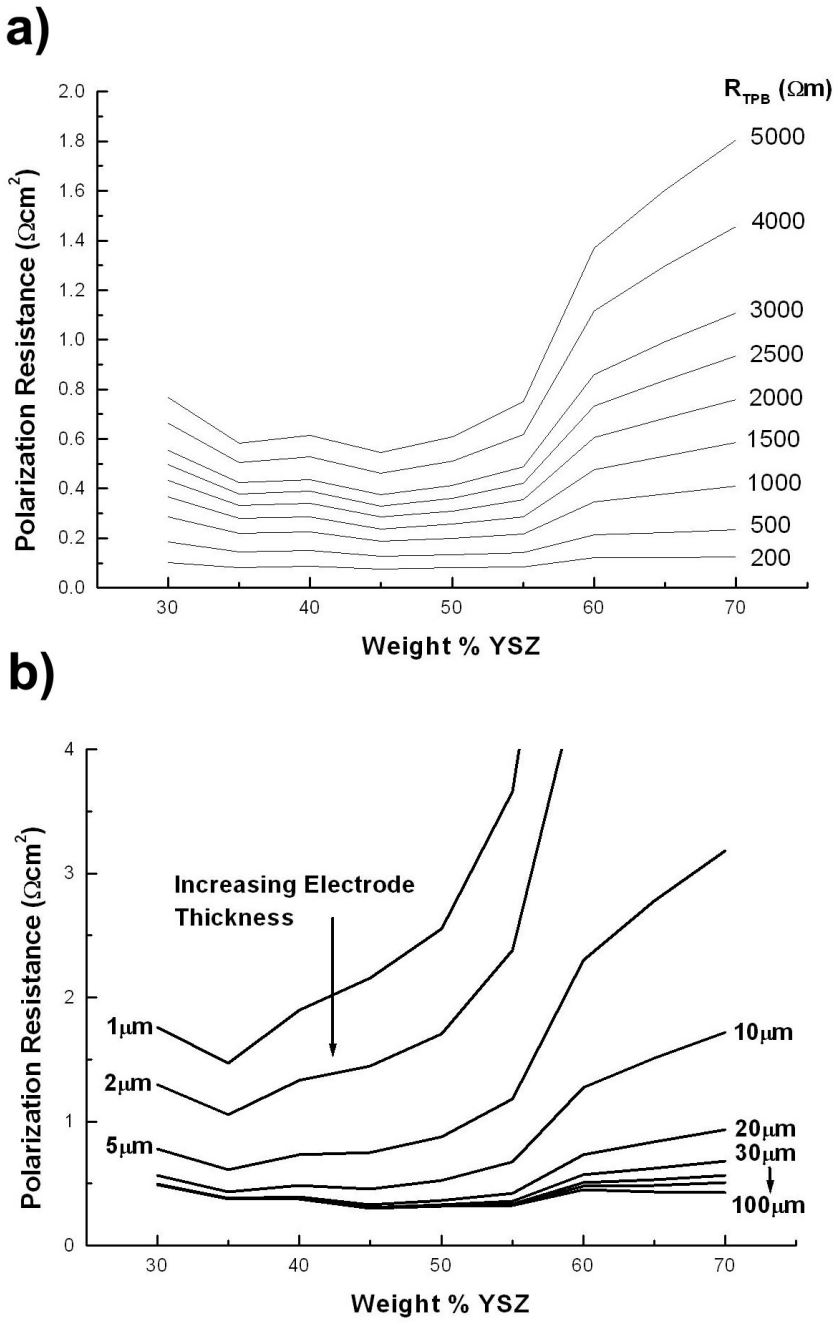

Figure 8.17. (a) Estimated electrode polarizations from the TFV model for different TPB linear-specific resistances using an electrode thickness of 20 μm. (b) Estimated electrode polarizations from the TFV model for different electrode thicknesses using an R_{TPB} of 2500 Ωm.

Lastly, it is important to note that the scaling of polarization with the inverse of the TPB length can be described by co-limitation with adsorption and surface diffusion on LSM. However, the range of this surface reaction from the TPB remains undetermined, although studies have shown in certain conditions that it is less than 1 μm.[98, 154] It is possible then that for the low YSZ content samples, surface reaction limitations may be occurring to further increase the polarization and explain the observed high resistivity. If this were the case, one would expect the amount of LSM surface area (exposed to pore) per length of TPB to decrease with decreasing YSZ content. These are both measurable microstructural characteristics, and this ratio for each composition is plotted in Figure 8.18. As can be seen, the LSM-pore surface area per length of TPB *increases* with decreasing YSZ content, so any surface limitations that could be occurring would have the opposite effect, causing higher resistivities in the low LSM content samples. It is important to note however, that the values are in the range of 0.15-0.25 μm, which is in the range, if not less than the length of the surface reaction, so it is possible that surface limitations are occurring for all the samples equally.

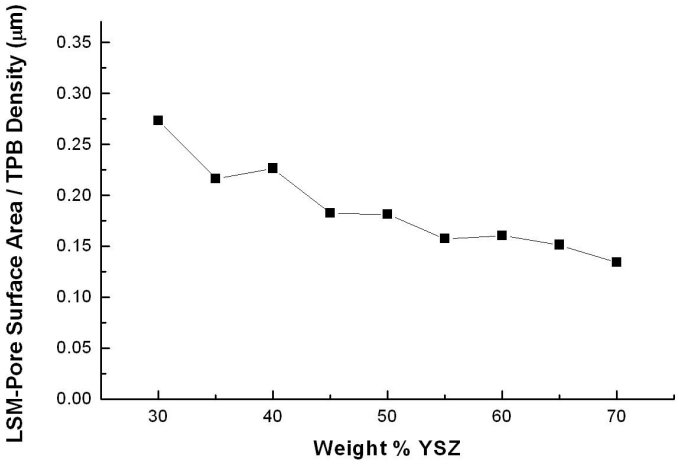

Figure 8.18. The measured LSM-pore surface area divided by the total TPB density, representing the characteristic length of surface area available at each TPB segment.

8.5 Summary and Conclusions

The above work represents the first comprehensive and quantitative study of the effects of varying composition on the microstructure and performance of LSM-YSZ composite electrodes. A serial-sectioning technique using FIB-SEM was implemented to fully reconstruct the microstructure of 9 samples with compositions ranging from 30:70 – 70:30 weight % LSM:YSZ. In addition to calculations of the phase volume fractions, surface area densities, phase tortuosities, and total triple-phase boundary densities, the levels of connectivity of the phases were analyzed in order to determine the electrochemically active triple-phase boundary density. Results showed a large mismatch between the TPB densities and the measured polarization resistances, suggesting microstructural features beyond the total TPB density were

contributing significantly to electrode performance. The effect of low connectivity in the LSM phase to greatly reduce the EA-TPB density explained the observed large polarizations in compositions with low LSM content. Implementation of the Tanner-Fung-Virkar electrochemical model of composite electrodes showed that the YSZ tortuosity contributed to bulk ionic transport limitations at low YSZ content, although the magnitude of the polarization resistance could not be matched. These results highlight the need for full quantization of three-dimensional microstructure in order to understand the underlying effects of structure on performance that would be otherwise misidentified.

CHAPTER NINE

Conclusions

Chapter 9: Conclusions

The goal of this thesis was to better understand the processing-microstructure and microstructure-performance relationships for solid oxide fuel cell electrodes. As a first step, a method of serial-sectioning using a dual-beam FIB-SEM to create continuous 3D structural data was investigated and fully developed in order to quantitatively analyze the microstructure of solid oxide fuel cell electrodes. The use of FIB-SEM as a means for achieving 3D data allowed for resolutions as low as 20nm and total lengths per dimension of reconstruction up to 15μm, a range that was ideally suited for the typical micron and sub-micron scale of SOFC electrodes. Compositional contrast was achieved between Ni and YSZ through an ion-induced charging mechanism, while compositional contrast between LSM and YSZ was achieved through the use of low energy incident electrons coupled with an in-lens energy-selective backscatter detector. Automated procedures for image processing were developed, allowing for rapid production of reliable three-dimensional structural data. Techniques for calculating the triple-phase boundary density, phase tortuosity, and phase connectivity, which in turn allowed for the calculation of the electrochemically-active triple-phase boundary density, were developed. Errors involved in the reconstruction procedure were analyzed, where it was found that errors in image segmentation showed minimal effects with regard to the triple-phase boundary and tortuosity calculations. Additionally, the sensitivities of calculations with respect to the volume of material reconstructed were quantified. The entire reconstruction procedure, once established, was then implemented for both single-phase and composite cathode and anode materials systems.

A Ni-yttria-stabilized zirconia (Ni-YSZ) composite anode consisting of a standard composition of 50:50 weight % Ni:YSZ was first investigated in order to establish proof of

concept of the reconstruction procedure. This system was chosen because it typifies the problem of connecting microstructure to performance in a 3-D microstructural network. For this electrode, the gas-phase tortuosity was found to be $(\tau_x, \tau_y, \tau_z) = (2.1, 2.2, 1.9)$, where a tortuosity factor of 2 is consistent with typical porous catalysts. The volume-specific TPB length was found to be 4.28×10^6 m/cm^3. It was determined that the YSZ phase was 100% connected, whereas at least 86% of the Ni and 96% of the pores were connected. Triple-phase boundary (TPB) segments were identified and evaluated with respect to the contiguity of each of the three phases at their locations. It was found that 11.6% of the TPB length was on one or more isolated phases, and hence was not electrochemically active. Together with phase volume fractions and surface areas, the present results provide a reasonably complete quantitative description of the electrode microstructure, as needed for utilizing 3D images to determine the links between processing variables, microstructure, and the resulting electrode polarization resistance.

As a next step, anode-supported SOFCs with varying Ni-YSZ active-layer compositions were compared structurally using the procedures demonstrated above in order to understand the subsequent effects of processing on microstructure and performance. Calculations from the 3D reconstructions showed that the highest triple-phase boundary (TPB) density was at a Ni solids volume fraction of ≈0.42, which showed reasonable agreement with structural models for predicting TPB density. While the anode polarization resistance was minimized at the same composition where TPB density was maximized, when the observed microstructure including TPB density variation was inserted in a simple electrochemical model, the predicted polarization resistance variation was much smaller than observed experimentally, implying that polarization resistance was determined not only by TPB density, but also by other structural factors, such as phase tortuosity and contiguity. Connectivity data was obtained for each phase, and it was

determined that isolated Ni and pore networks for the 40 weight % NiO sample contributed to a substantial fraction of electrochemically-inactive TPBs, explaining the poor performance observed for this sample. Inclusion of YSZ tortuosity and characteristic feature size in the model, serving to increase the bulk transport resistivity, only partially explained the poor performance observed in the 70 weight % NiO sample.

Three-dimensional reconstructions were performed on two LSC mixed-conducting single-phase cathodes that were sintered at 1000ºC and 1150ºC. The difference in surface area density between the two samples was negligible, despite the fact that dramatic differences in performance were reported for the two samples. This implied that the processing greatly affected the surface activity of the LSC electrodes, perhaps altering the mobility and number of vacant oxygen surface sites. While reconstructions of single-phase cathodes can provide macroscopic structural values important in models such as porous electrode theory, an equally important benefit of reconstructions is that they provide real structures for micro- and nano-scale modeling. Conversion to finite-element meshes of the reconstructions achieved in this thesis for LSC cathodes is currently underway at the University of Washington for the purpose of electrochemical modeling.

Achievement of compositional contrast between LSM and YSZ using low electron beam energy and an energy-selective (biased) in-lens backscatter detector was first demonstrated on a LSM-YSZ composite cathode with 50:50 weight % composition fabricated using standard processing techniques. Subsequently, a set of images was collected to create a three-dimensional reconstruction from which pertinent microstructural properties, such as the triple-phase boundary density, and surface area densities and tortuosities of each phase, were calculated. Analysis of the connectivity of the LSM, YSZ, and pore particle networks allowed for the calculation of the

electrochemically-active triple-phase boundary segments. It was found that while the YSZ and pore networks were almost entirely self-connected, the LSM phase, with a characteristic feature size that was larger than that of the YSZ, showed at least 10% isolated particle networks by volume. These un-connected LSM networks contributed to a significant reduction in the EA-TPB density, calculated to be 4.93 μm^{-2}, compared to the total TPB density of 7.35 μm^{-2}. Using the Tanner-Fung-Virkar electrochemical model of composite electrodes, implementing the EA-TPB density and YSZ tortuosity of 3.4, the intrinsic linear-specific charge transfer resistivity of the LSM-YSZ-air triple-phase boundary was estimated to be $\approx 2.5 \times 10^5$ Ωcm at 800°C. The effect of the YSZ tortuosity in the model was relatively small, yielding an ≈ 5% reduction in the R_{TPB} values, suggesting that ionic transport through the YSZ was not a major limiting process for this cathode composition.

Lastly, a series of nine LSM-YSZ composite cathodes fabricated with compositions ranging from 30:70 – 70:30 weight % LSM:YSZ were tested and reconstructed in order to better understand processing-microstructure relationships and the effect of the subsequent structures on electrode polarization. Comparison of the calculated TPB densities with those estimated from a particle packing model showed excellent agreement, with the maximum TPB density depending heavily on the particle size ratio between LSM and YSZ. Results showed a large mismatch between the TPB densities and the measured polarization resistances, suggesting microstructural features beyond the total TPB density were contributing significantly to electrode performance. The levels of connectivity of the phases were analyzed, showing fully connected porosity existing for all compositions, slightly un-connected YSZ only at the lowest YSZ content compositions, and significant connectivity limitations in the LSM at most compositions, increasing dramatically with decreasing LSM content. Un-connected LSM particle networks

contributed greatly to a reduction in the electrochemically active triple-phase boundary (EA-TPB) density. Implementation of the Tanner-Fung-Virkar electrochemical model of composite electrodes showed that the effect of greatly reduced EA-TPB density as a result of low connectivity in the LSM phase was sufficient to explain the observed large polarizations in compositions with low LSM content. Addition of the YSZ tortuosity to the TFV model showed qualitatively that bulk ionic transport limitations existed in the samples with low YSZ content that could possibly contribute to the observed large polarizations for these compositions.

The results in this thesis highlight the need for full quantization of three-dimensional microstructure in order to understand the underlying effects of microstructure on performance that would otherwise be misidentified. While performance in both Ni-YSZ anodes and LSM-YSZ cathodes showed standard performance curves, the TPB densities in either case did not match the behavior and magnitude expected to produce such polarizations. Properties such as the phase tortuosity and electrochemically active TPB density, calculations only achievable through three-dimensional microstructure reconstruction, were shown to play important roles in non-optimal electrode compositions. While macro-homogeneous descriptors of the microstructure combined with simplified electrochemical models aided greatly in analyzing the effects of microstructure on performance, insertion of the achieved reconstructed microstructures into finite-element models represents a next step towards quantitatively linking microstructure with the electrochemical pathway steps responsible for SOFC electrode polarization.

CHAPTER TEN

Future Work

Chapter 10: Future Work

There is a large amount of work that can be conducted as a follow-up to this thesis. These ideas are summarized below and placed into four categories: SOFC experimental studies, electrode modeling, artificial electrode reconstruction through Monte Carlo simulations, and alternative FIB-SEM uses.

10.1 SOFC Experimental Studies

Having developed the three-dimensional reconstruction procedure, there are many additional experiments investigating the processing-microstructure and microstructure-performance relationships for SOFC electrodes. In this thesis, variations in composition were studied for both anodes and cathodes. Additional fabrication of cells with different particle sizes and particle size ratios would certainly provide a more encompassing picture of the effects of simple processing variables on the microstructure and how that affects the electrode performance. Careful control of pre-cursor particle size can be achieved through stages of attrition milling and coarsening steps.

An alternate processing route that has recently spurred interest may also be explored.[107, 108, 269] Cathodes are constructed by first fabricating a porous YSZ template. Salt solutions containing stoichiometric compositions of electronic-phase elements (such as La, Sr, and Co for LSC) are introduced into the pores through capillary action. Subsequent calcining and firing at lowered temperatures in the range of 800-900˚C prevent formation of detrimental secondary phases. The importance of this processing technique is that it produces a unique microstructure of porous contiguous YSZ with a disbursement of fine electronic-phase particles

on its surface. A similar structure produced by nucleation of nanometer-scale electrocatalyst particles on the surface of oxide anodes has been demonstrated.[90] Accurate study of these microstructures and processing techniques can be conducted using this FIB-SEM reconstruction method and combined with electrochemical modeling to understand performance enhancements.

Investigation of compositional contrast mechanisms in other electrode materials would also prove beneficial, as exotic material combinations are becoming more regular in research attempting to improve efficiency through means of material optimization. With the discovery of the effectiveness of energy-selective backscatter to detect small differences in backscatter coefficients, attempts to maximize contrast between LSM-GDC, LSCF-GDC, and other cathode combinations, previously investigated unsuccessfully, should be conducted. The recent purchase of a Zeiss ESB CrossBeam FIB-SEM by Argonne National Laboratory should aid in this endeavor. Compositional contrast may be achieved by use of different detectors as well. Electron backscatter diffraction (EBSD), while time-consuming and difficult to implement, achieves contrast in almost all materials due to different crystal structures and lattice parameters, additionally providing grain structure information within a single-phase that could aid in finite element modeling. Northwestern University has recently purchased an EBSD detector, although it has not yet been installed on the FIB-SEM.

Lastly, an important additional application of 3D reconstruction will be to track microstructural changes during long-term fuel cell operation, providing important information regarding fuel cell stability. Work in this area has already been started by Scott Cronin in the Barnett research group at Northwestern University, where Ni-YSZ anodes samples annealed in hydrogen for different lengths of time are being reconstructed to investigate the rate of Ni

coarsening. This work can also be combined with phase-field modeling, as discussed in the next section.

10.2 Electrode Modeling

The ability of modeling to quantify intrinsic material properties, reaction rates, kinetic processes, and general electrochemical SOFC electrode performance relies on measurements from, and corroboration with, experimental studies. The ability to use real microstructures in modeling represents a giant leap forward, as microstructural models are inherently limited by their simplified structural assumptions. While the Tanner-Fung-Virkar electrochemical model was used throughout this thesis, development of finite-element modeling based on the structures achieved in this work would provide a much more accurate description of the connections between electrode polarization and microstructure. Additionally, insertion of reconstructed microstructures as starting structures in phase-field modeling allows for the investigation and determination of realistic kinetic and thermodynamic changes in microstructure. The use of phase-field modeling to describe Ni coarsening in SOFC anodes, in conjunction with the experiments described above, is currently being conducted by Hsun-Yi Chen and Prof. Katsuyo Thornton, collaborators at the University of Michigan.

10.3 Monte Carlo Artificial Reconstructions

Recent work has shown that artificial three-dimensional reconstructions of composite electrodes can be achieved through a stochastic Monte Carlo method using the radial distribution function from a 2D image.[270] In this method, the radial distribution of each phase (the

average probability that material of the same phase exists at a certain radius from itself) is measured from a single segmented 2D image. A starting three-dimensional structure consisting of a random distribution of voxels with the same composition as the 2D image is created. Two voxels are randomly switched and the radial distribution in three-dimensions is measured. If the new structure better matches the measured radial distribution from the 2D image, the structure is kept and the process is repeated. In this manner of Monte Carlo simulation, a final three-dimensional structure is eventually achieved that matches the measured radial distributions. Programs have been written in IDL that perform this Monte Carlo reconstruction for LSM-YSZ cathodes. Figure 10.1 shows the radial distribution of a 2D image from a 50:50 weight % LSM:YSZ sample, with cross-sectional images of the starting random structure and resulting 3D microstructure after simulation. Analysis of the effectiveness and limitations of this method should be conducted by comparing the Monte Carlo structure with that of the reconstructed microstructure. This method could certainly provide advantages in future microstructure studies, should it be proven accurate, in that only a single 2D image is necessary, removing the need for a FIB-SEM and widening the options for achieving compositional contrast beyond SEM imaging.

10.4 Alternative Research Areas for FIB-SEM

Lastly, there are a number of areas of research outside of solid oxide fuel cells that could benefit from three-dimensional reconstruction using FIB-SEM. Any porous structure with size-scales on the order of microns requiring nano-scale resolutions are ideal candidates. Collaborations with research in the areas of lithium-ion batteries and thermal barrier coatings are just two examples of possible outreach for the method developed in this thesis.

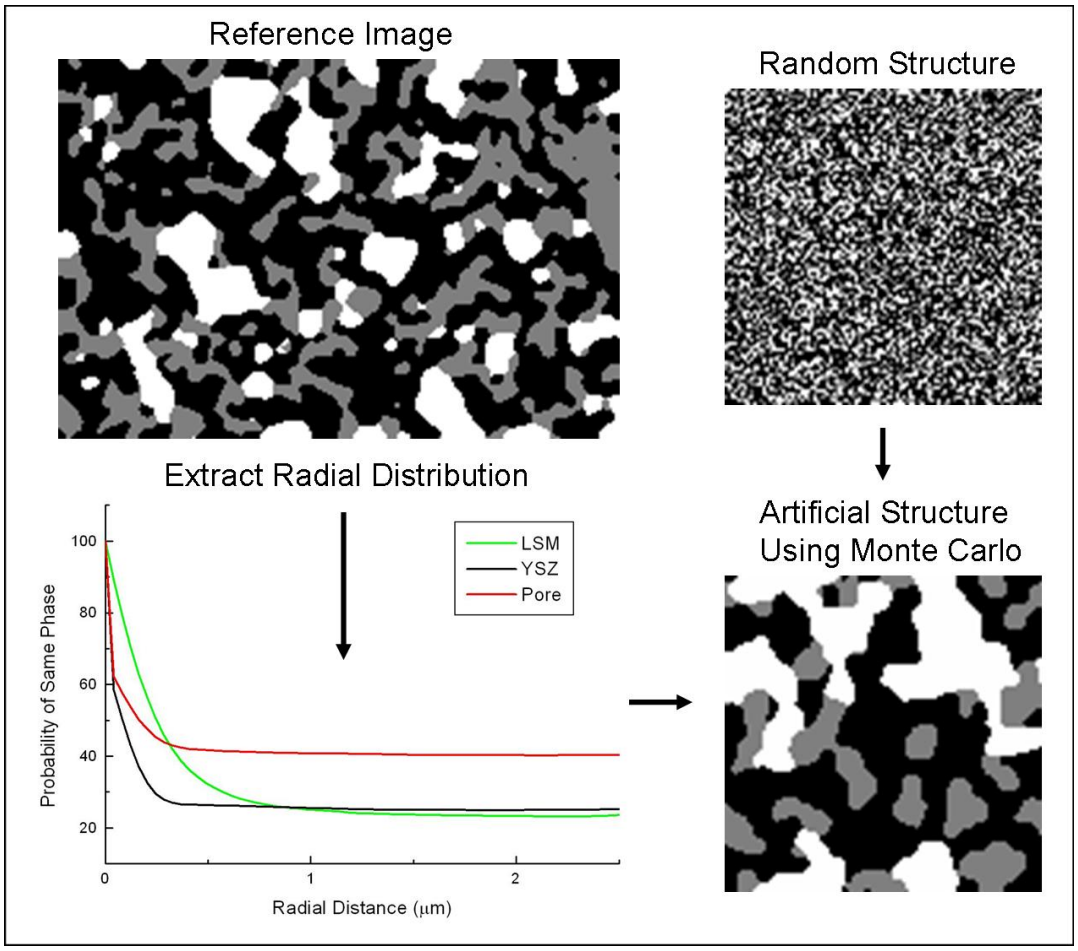

Figure 10.1. Each stage of a stochastic reconstruction method for creating artificial three-dimensional microstructures. The radial distribution for each phase is calculated from a single 2D image. A random 3D structure is driven towards the same radial distribution through Monte Carlo simulation.

References

1. Smil, V., *Energy in Nature and Society - General Energetics of Complex Systems*. 2008, Cambridge, Massachusetts: MIT Press.

2. Lewis, N.S., *Global Energy Consumption*, http://nsl.caltech.edu/files/energy.ppt, Editor. 2008.

3. *Global Carbon Dioxide Emissions and Atmospheric Concentration from 1751-2004*. [cited 2008; Energy Information Administration]. Available from: http://www.eia.doe.gov/bookshelf/brochures/greenhouse/Chapter1.htm.

4. *Estimated Energy Usage in 2006*. 2006, University of California, Lawrence Livermore National Laboratory and the Department of Energy.

5. *U.S. Carbon Dioxide Emissions from Energy Consumption*. 2006, University of California, Lawrence Livermore National Laboratory and the Department of Energy.

6. Grove, W.R., *On Voltaic Series and the Combination of Gases by Platinum.* Phil. Mag. S.3, 1839. **14**(86): p. 127-130.

7. Ostwald, W., Zeitschrift fur Elektrochemie, 1894. **1**: p. 122.

8. Baur, E. and H. Preis, Z. Elektrochem., 1937. **43**: p. 727-732.

9. Nernst, W., *Uber Die Elektrolytische Leitung Fester Korper Bei Sehr Hohen Temperaturen.* Z. Elektrochem., 1899. **6**: p. 41-43.

10. Minh, N.Q., *Ceramic Fuel-Cells.* Journal of the American Ceramic Society, 1993. **76**: p. 563-588.

11. *SOFC Fuel Cell*. [cited; Available from: http://www.eere.energy.gov/hydrogenandfuelcells/fuelcells/images/fcell_diagram_sofc.gif.

12. *Fuel Cell Handbook*. 6th ed. 2002: U.S. Department of Energy.

13. *Fuel Cell Comparison Chart*. [cited 2008; Department of Energy - Energy Efficiency and Renewable Energy]. Available from: http://www1.eere.energy.gov/hydrogenandfuelcells/fuelcells/pdfs/fc_comparison_chart.pdf.

14. Singhal, S.C. and K. Kendall, *High Temperature Solid Oxide Fuel Cells: Fundamentals, Design and Applications*. 2003, New York, Elsevier Inc.

15. Dokiya, M., *SOFC system and technology.* Solid State Ionics, 2002. **152**: p. 383-392.

16. Haile, S.M., *Fuel cell materials and components* Acta Materialia, 2003. **51**(19): p. 5981-6000.

17. Liu, J.A. and S.A. Barnett, *Operation of anode-supported solid oxide fuel cells on methane and natural gas.* Solid State Ionics, 2003. **158**(1-2): p. 11-16.

18. Liu, J., et al., *A fuel-flexible ceramic-based anode for solid oxide fuel cells.* Electrochem. Solid-State Lett., 2002. **5**(6): p. A122-A124.

19. Green, R.D., C.C. Liu, and S.B. Adler, *Carbon dioxide reduction on gadolinia-doped ceria cathodes.* Solid State Ionics, 2008. **179**(17-18): p. 647-660.

20. Jiang, Y. and A.V. Virkar, *A High Performance, Anode-Supported Solid Oxide Fuel Cell Operating on Direct Alcohol.* Journal of The Electrochemical Society, 2001. **148**(7): p. A706-A709.

21. Zhan, Z., J. Liu, and S.A. Barnett, *Operation of anode-supported solid oxide fuel cells on propane-air fuel mixtures.* Appl. Catal. A - Gen, 2004. **262**(2): p. 255-259.

22. McIntosh, S. and R.J. Gorte, *Direct Hydrocarbon Solid Oxide Fuel Cells.* Chemical Review, 2004. **104**: p. 4845-4865.

23. Zhu, W.Z. and S.C. Deevi, *A review on the status of anode materials for solid oxide fuel cells.* Mat. Sci. Engr. A, 2003. **362**(1-2): p. 228-239.

24. Zhan, Z. and S.A. Barnett, *Solid Oxide Fuel Cells Operated By Internal Partial Oxidation Reforming of iso-Octane.* J. Power Sources, 2006. **155**: p. 353-357.

25. Pillai, M.R., D.M. Bierschenk, and S.A. Barnett, *Electrochemical Partial Oxidation of Methane in Solid Oxide Fuel Cells: Effect of Anode Reforming Activity.* Catalysis Letters, 2008. **121**(1-2): p. 19-23.

26. Park, S.D., J.M. Vohs, and R.J. Gorte, *Direct oxidation of hydrocarbons in a solid-oxide fuel cell.* Nature, 2000. **404**: p. 265-267.

27. Lu, C., et al., *Development of solid oxide fuel cells for the direct oxidation of hydrocarbon fuels.* Solid State Ionics, 2002. **152**: p. 393-397.

28. Lin, Y.B., et al., *Direct operation of solid oxide fuel cells with methane fuel.* Solid State Ionics, 2005. **176**(23-24): p. 1827-1835.

29. Ishihara, T., *Novel electrolytes operating at 400-600 C*, in *Handbook of Fuel Cells-Fundamentals, Technology and Applications*, W. Vielstich, A. Lamm, and H.A. Gasteiger, Editors. 2003, West Sussex: John Wiley & Sons Ltd.: Hoboken, NJ.

30. Singhal, S.C., *Advances in Solid Oxide Fuel Cell Technology.* Solid State Ionics, 2000. **135**: p. 305-303.

31. Arachi, Y., et al., *Electrical conductivity of the ZrO –Ln_2O_3 (Ln = Lanthanides) system.* Solid State Ionics, 1999. **121**(1-4): p. 133-139.

32. Will, J., et al., *Fabrication of thin electrolytes for second-generation solid oxide fuel cells.* Solid State Ionics, 2000. **131**(1-2): p. 79-96.

33. Chen, X.J., et al., *Influence of microstructure on the ionic conductivity of yttria-stabilized zirconia electrolyte.* Materials Science and Engineering a-Structural Materials Properties Microstructure and Processing, 2002. **335**(1-2): p. 246-252.

34. Liu, J. and S.A. Barnett, *Thin Yttrium-Stabilized Zirconia Electrolyte Solid Oxide Fuel Cells by Centrifugal Casting.* J. Am. Cer. Soc., 2002. **85**(12): p. 3096-3098.

35. VonDollen, P. and S.A. Barnett, *A Study of Screen Printed Yttria-Stabilized Zirconia Layers for Solid Oxide Fuel Cells.* Journal of the American Ceramic Society, 2005. **88**: p. 3361-3368.

36. Souza, S.d., S.J. Visco, and L.C.D. Jonghe, *Reduced-Temperature Solid Oxide Fuel Cell Based on YSZ Thin-Film Electrolyte.* J. Electrochem. Soc., 1997. **144**(3): p. L35-L37.

37. Perednis, D. and L.J. Gauckler, *Solid oxide fuel cells with electrolytes prepared via spray pyrolysis.* Solid State Ionics, 2004. **166**(3-4): p. 229-239.

38. Ruddell, D.E., B.R. Stoner, and J.Y. Thompson, *The effect of deposition parameters on the properties of yttria-stabilized zirconia thin films.* Thin Solid Films, 2003. **445**(1): p. 14-19.

39. Zhang, Y.L., et al., *Production of dense yttria-stabilized zirconia thin films by dip-coating for IT-SOFC application.* Journal of Applied Electrochemistry, 2004. **34**(6): p. 637-641.

40. Mogensen, M., N.M. Sammes, and G.A. Thompsett, *Physical, Chemical and Electrochemical Properties of Pure and Doped Ceria.* Solid State Ionics, 2000. **129**: p. 63-94.

41. Steele, B.C.H., *Appraisal of $Ce_{1-y}Gd_yO_{2-y/2}$ electrolytes for IT-SOFC operation at 500°C.* Solid State Ionics, 2000. **129**(1-4): p. 95-110.

42. Brandon, N.P., S. Skinner, and B.C.H. Steele, *Recent advances in materials for fuel cells.* Annual Review of Materials Research, 2003. **33**: p. 183-213.

43. Ishihara, T., H. Matsuda, and Y. Takita, *Doped $LaGaO_3$ Perovskite-Type Oxide as a New Oxide Ionic Conductor.* J. Am. Cer. Soc., 1994. **116**(9): p. 3801-3803.

44. Feng, M. and J.B. Goodenough, *A Superior Oxide-Ion Electrolyte.* Eur. J. Solid State Inorg. Chem., 1994. **31**(8-9): p. 663-67.

45. Feng, M., et al., *Fuel cells with doped lanthanum gallate electrolyte.* J. Power Sources, 1996. **63**(1): p. 47-51.

46. Dees, D.W., et al., *Conductivity of Porous Ni/ZrO_2-Y_2O_3 Cermets* J. Electrochem. Soc., 1987. **134**(9): p. 2141-2146.

47. Iwata, T., *Characterization of Ni-YSZ Anode Degradation for Substrate-Type Solid Oxide Fuel Cells.* J. Electrochem. Soc., 1996. **143**(5): p. 1521-1525.

48. Itoh, H., et al., *Configurational and Electrical Behavior of Ni-YSZ Cermet with Novel Microstructure for Solid Oxide Fuel Cell Anodes.* J. Electrochem. Soc., 1997. **144**(2): p. 641-646.

49. Itoh, H., et al. in *Proceedings of the Second European Solid Oxide Fuel Cell Forum.* 1996. Oslo, Norway.

50. Jiang, S.P., *Sintering behavior of Ni/Y2O3-ZrO2 cermet electrodes of solid oxide fuel cells.* J. Mat. Sci., 2003. **38**: p. 3775-3782.

51. Simwonis, D., F. Tietz, and D. Stöver, *Nickel coarsening in annealed Ni/8YSZ anode substrates for solid oxide fuel cells.* Solid State Ionics, 2000. **132**(3-4): p. 241-251.

52. Matsushima, T., H. Ohrui, and T. Hirai, *Effects of sinterability of YSZ powder and NiO content on characteristics of Ni-YSZ cermets.* Solid State Ionics, 1998. **111**: p. 315-321.

53. Jiang, S.P. and S.H. Chan, *A review of anode materials development in solid oxide fuel cells.* J. Materials Science, 2004. **39 (14)**: p. 4405-4439.

54. Tietz, F., et al., Journal of the European Ceramic Society, 2000. **20**.

55. Ciacchi, F.T., K.M. Crane, and S.P.S. Badwal, *Evaluation of Commercial Zirconia Powders for Solid Oxide Fuel-Cells.* Solid State Ionics, 1994. **73**(1-2): p. 49-61.

56. Van Herle, J., R. Ihringer, and A.J. McEvoy. in *SOFC-V.* 1997: Electrochemical Society.

57. Cho, H.J. and G.M. Choi, *Effect of milling methods on performance of Ni-Y2O3-stabilized ZrO2 anode for solid oxide fuel cell.* Journal of Power Sources, 2008. **176**: p. 96-101.

58. Jiang, S.P., P.J. Callus, and S.P.S. Badwal, *Fabrication and performance of Ni/3 mol% Y2O3-ZrO2 cermet anodes for solid oxide fuel cells.* Solid State Ionics, 2000. **132**(1-2): p. 1-14.

59. Sanson, A., P. Pinasco, and E. Roncari, *Influence of pore formers on slurry composition and micrstructure of tape cast cupporting anodes for SOFCs.* Journal of the European Ceramic Society, 2008. **28**: p. 1221-1226.

60. Souza, S.d., S.J. Visco, and L.C.d. Jonghe. *YSZ Thin-Film Electrolytes for High Power Reduced Temperature Solid Oxide Fuel Cells*. in *EPRI/GRI Fuel Cell Workshop Proceedings*. 1996. Tempe, AZ.

61. Kim, J.W., et al., *Polarization effects in intermediate temperature, anode-supported solid oxide fuel cells.* J. Electrochem. Soc., 1999. **146**: p. 69-78.

62. Huebner, W., D.M. Reed, and H.U. Anderson. *Solid Oxide Fuel Cell Performance Studies: Anode Development*. in *Solid Oxide Fuel Cells VI*. 1999. The Electrochemical Society Proceedings: The Electrochemical Society, Pennington, NJ.

63. Lee, J.-H., et al., *Quantitative analysis of microstructure and its related electrical property of SOFC anode, Ni–YSZ cermet.* Solid State Ionics, 2002. **148**(1-2): p. 15-26.

64. Murakami, S., et al. in *The Second International Symposium on Solid Oxide Fuel Cells (SOFC-II)*. 1991.

65. Lee, C.H., et al., *Microstructure and anodic properties of Ni/YSZ cermets in solid oxide fuel cells.* Solid State Ionics, 1997. **98**(1-2): p. 39-48.

66. Koide, H., et al., *Properties of Ni/YSZ cermet as anode for SOFC.* Solid State Ionics, 2000. **132**(3-4): p. 253-260.

67. Lee, J.-H., et al., *The impact of anode microstructure on the power generating characteristics of SOFC.* J. Electrochem. Soc., 2003. **158**(3-4): p. 225-232.

68. Suciu, C., et al., *NiO/YSZ nanoparticles obtained by new sol-gel route.* Chemical Engineering Journal, 2008. **140**(1-3): p. 586-592.

69. Ringuede, A., D. Bronine, and J.R. Frade, *Assessment of Ni/YSZ anodes prepared by combustion synthesis.* Solid State Ionics, 2002. **146**(3-4): p. 219-224.

70. Marinsek, M., K. Zupan, and J. Maeek, *Ni-YSZ cermet anodes prepared by citrate/nitrate combustion synthesis.* Journal of Power Sources, 2002. **106**(1-2): p. 178-188.

71. Muller, A.C., D. Herbstritt, and E. Ivers-Tiffee, *Development of a multilayer anode for solid oxide fuel cells.* Solid State Ionics, 2002. **152**: p. 537-542.

72. Virkar, A.V., et al., *The role of electrode microstructure on activation and concentration polarizations in solid oxide fuel cells.* Solid State Ionics, 2000. **131**(1-2): p. 189-198.

73. Mogensen, M., et al., *Progress in understanding SOFC electrodes.* Solid State Ionics, 2002. **150**: p. 123-129.

74. Liu, Y.L., S. Primdahl, and M. Mogensen, *Effects of impurities on microstructure in Ni/YSZ-YSZ half-cells for SOFC.* Solid State Ionics, 2003. **161**: p. 1-10.

75. Vels Jensen, K., et al., *Microstructural and chemical changes at the Ni/YSZ interface.* Solid State Ionics, 2001. **144**: p. 197-209.

76. Weber, A., et al., *Oxidation of H_2, CO and methane in SOFCs with Ni/YSZ-cermet anodes.* Solid State Ionics, 2002. **152-153**: p. 543-550.

77. Madsen, B.D. and S.A. Barnett. *The influence of Ni Content on Ceramic-Based Solid Oxide Fuel Cell Anodes*. in *Solid Oxide Fuel Cells IX*. 2005. The Electrochemical Society Proceedings Series: The Electrochemical Society: Pennington NJ.

78. Hibino, T., et al., *High Performance Anodes for SOFCs Operating in Methane-Air Mixture at Reduced Temperatures.* Journal of The Electrochemical Society, 2002. **149**(2): p. A133-A136.

79. Mogensen, M., et al., *Physical Properties of Mixed Conductor Solid Oxide Fuel Cell Anodes of Doped CeO_2.* J. Electrochem. Soc., 1994. **141**(8): p. 2122-2128.

80. Fukui, T., et al., *Performance of intermediate temperature solid oxide fuel cells with La(Sr)Ga(Mg)O-3 electrolyte film.* Journal of Power Sources, 2002. **106**(1-2): p. 142-145.

81. Park, S., R.J. Gorte, and J.M. Vohs, *Tape cast solid oxide fuel cells for the direct oxidation of hydrocarbons.* Journal of the Electrochemical Society, 2001. **148**(5): p. A443-A447.

82. McIntosh, S., J.M. Vohs, and R.J. Gorte, *Role of Hydrocarbon Deposits in the Enhanced Performance of Direct-Oxidation SOFCs.* J. Electrochem. Soc., 2003. **150**(4): p. A470-A476.

83. McEvoy, A.J., *Innovations for anodes oxidation - catalysis and direct oxidation.* Materialwissenschaft Und Werkstofftechnik, 2002. **33**(6): p. 331-334.

84. Hui, S. and A. Petric, *Evaluation of Yttrium-doped SrTiO3 as an Anode for Solid Oxide Fuel Cells.* J. Eur. Ceram. Soc., 2002. **22**: p. 1673-1681.

85. Hui, S.Q. and A. Petric, *Electrical properties of yttrium-doped strontium titanate under reducing conditions.* J. Electrochem. Soc., 2002. **149**: p. J1-J10.

86. Vernoux, P., E. Djurado, and M. Guillodo, *Catalytic and Electrochemical Properties of Doped Lanthanum Chromites as New Anode Materials for Solid Oxide Fuel Cells.* J. Am. Ceram. Soc., 2001. **84**(10): p. 2289-2295.

87. Madsen, B.D. and S.A. Barnett, *La0.8Sr0.2Cr0.98V0.02O3-delta Ce0.9Gd0.1O1.95-Ni anodes for solid oxide fuel cells - Effect of microstructure and Ni content.* Journal of the Electrochemical Society, 2007. **154**(6): p. B501-B507.

88. Atkinson, A., et al., *Advanced anodes for high-temperature fuel cells.* Nature Materials, 2004. **3**: p. 17-27.

89. Sauvet, A.-L., et al., *Surface properties and physicochemical characterizations of a new type of anode material, $La_{1-x}Sr_xCr_{1-y}Ru_yO_{3-\delta}$ for a solid oxide fuel cell under methane at intermediate temperature.* J. Catalysis, 2002. **209**: p. 25-34.

90. Madsen, B.D., et al., *Nucleation of nanometer-scale electrocatalyst particles in solid oxide fuel cell anodes.* Journal of Power Sources, 2007. **166**(1): p. 64-67.

91. Marina, O.A. and L.R. Pederson, *Novel Ceramic Anodes for SOFCs Tolerant to Oxygen, Carbon and Sulfur*, in *The Fifth European Solid Oxide Fuel Cell Forum*, J. Huijismans, Editor. 2002, European Fuel Cell Forum: Lucerne, Switzerland. p. 481-489.

92. Kunifusa, Y., et al., *Formation and electrical conductivity of air-sinterable Nd(Cr1-xMgx)O-3.* Solid State Ionics, 2002. **149**(1-2): p. 107-113.

93. Ullmann, H., et al., *Correlation Between Thermal Expansion and Oxide Ion Transport in Mixed Conducting Perovskite-Type Oxides for SOFC Cathodes.* Solid State Ionics, 2000. **138**: p. 79-90.

94. Yokokawa, H. and T. Horita, *Cathodes*, in *High Temperature Solid Oxide Fuel Cells: Fundamentals, Design and Applications*, S.C. Singhal and K. Kendall, Editors. 2003, Elsevier Advanced Technology: Oxford, UK. p. 119-147.

95. Mizusaki, J., et al. in *2nd Ionic and Mixed Conducting Ceramics*. 1994: The Electrochemical Society.

96. Adler, S.B., J.A. Lane, and B.C.H. Steele, *Electrode kinetics of porous mixed-conducting oxygen electrodes.* Journal of the Electrochemical Society, 1996. **143**(11): p. 3554-3564.

97. De Souza, R.A., J.A. Kilner, and J.F. Walker, Materials Letters, 2000. **43**: p. 43-52.

98. Horita, T., et al., *Active Sites Imaging for Oxygen Reduction at the La[sub 0.9]Sr[sub 0.1]MnO[sub 3 - x]/Yttria-Stabilized Zirconia Interface by Secondary-Ion Mass Spectrometry.* Journal of The Electrochemical Society, 1998. **145**(9): p. 3196-3202.

99. Kamata, H., et al., *High temperature electrocatalytic properties of the SOFC air electrode La0.8Sr0.2MnO3/YSZ.* Solid State Ionics, 1998. **106**(3-4): p. 237-245.

100. Jiang, S.P. and W. Wang, *Sintering and grain growth of (La,Sr)MnO_3 electrodes of solid oxide fuel cells under polarization.* Solid State Ionics, 2005. **176**(13-14): p. 1185-1191.

101. Skinner, S.J., *Recent advances in perovskite-type materials for solid oxide fuel cell cathodes.* Int. J. Inorg. Mater., 2001. **3**: p. 113-121.

102. Rietveld, G., P. Nammensma, and J.P. Ouweltjes. *Status of SOFC component development at ECN*. in *Seventh International Symposium on Solid Oxide Fuel Cells (SOFC-VII)*. 2001. Pennington, NJ: The Electrochemical Society, Inc.

103. Murray, E.P., T. Tsai, and S.A. Barnett, *Oxygen Transfer Processes in (La,Sr)MnO3/Y2O3-Stabilized ZrO2 Cathodes: An Impedance Spectroscopy Study.* Solid State Ionics, 1998. **110**: p. 235.

104. Jiang, S.P. and W. Wang, *Fabrication and performance of GDC-impregnated (La,Sr)MnO3 cathodes for intermediate temperature solid oxide fuel cells.* Journal of the Electrochemical Society, 2005. **152**(7): p. A1398-A1408.

105. Leng, Y.J., et al., *Performance evaluation of anode-supported solid oxide fuel cells with thin film YSZ electrolyte.* International Journal of Hydrogen Energy, 2004. **29**(10): p. 1025-1033.

106. Schiller, G., et al., *Development of Solid Oxide Fuel Cells (SOFC) for Stationary and Mobile Applications by Applying Plasma Deposition Processes.* Materials Science Forum, 2003. **426**(4): p. 2539-2544.

107. Jiang, S.P., *A review of wet impregnation--An alternative method for the fabrication of high performance and nano-structured electrodes of solid oxide fuel cells.* Materials Science and Engineering: A, 2006. **418**(1-2): p. 199-210.

108. Sholklapper, T.Z., et al., *LSM-infiltrated solid oxide fuel cell cathodes.* Electrochemical and Solid State Letters, 2006. **9**(8): p. A376-A378.

109. Jiang, S.P., et al., *Development of (La, Sr)MnO3-based cathodes for intermediate temperature solid oxide fuel cells.* Electrochemical and Solid State Letters, 2003. **6**(4): p. A67-A70.

110. Sholklapper, T.Z., et al., *Nanostructured solid oxide fuel cell electrodes.* Nano Letters, 2007. **7**(7): p. 2136-2141.

111. Tsai, T. and S.A. Barnett, *Effect of LSM-YSZ Cathode on Thin-Electrolyte Solid Oxide Fuel Cell Performance.* Solid State Ionics, 1997. **93**: p. 207.

112. Yang, C.C.T., W.C.J. Wei, and A. Roosen, *Electrical conductivity and microstructures of La0.65Sr0.3MnO3-8 mol% yttria-stabilized zirconia.* Materials Chemistry and Physics, 2003. **81**(1): p. 134-142.

113. Piao, J., et al., *A study of process parameters of LSM and LSM-YSZ composite cathode films prepared by screen-printing.* Journal of Power Sources, 2008. **175**: p. 288-295.

114. Wang, W.G., et al., Electrochemical and Solid State Letters, 2005. **8**(12): p. A619-A621.

115. Kim, J.Y., et al., *Effects of Chrome Contamination on the Performance of La0.6Sr0.4Co0.2Fe0.8O3 Cathode Used in Solid Oxide Fuel Cells.* J. Electrochem. Soc., 2006. **153**: p. A880.

116. Choi, J.H., J.H. Jang, and S.M. Oh, *Microstructure and cathodic performance of La0.9Sr0.1MnO3/yttria-stabilized zirconia composite electrodes.* Electrochimica Acta, 2001. **46**(6): p. 867-874.

117. Murray, E.P. and S.A. Barnett, *(La,Sr)MnO3-(Ce,Gd)O2-x composite cathodes for solid oxide fuel cells.* Solid State Ionics, 2001. **143**: p. 265-273.

118. Kim, J.D., et al., *Characterization of LSM-YSZ composite electrode by ac impedance spectroscopy.* Solid State Ionics, 2001. **143**(3-4): p. 379-389.

119. Barbucci, A., et al., *Characterization of composite SOFC cathodes using electrochemical impedance spectroscopy. Analysis of Pt/YSZ and LSM/YSZ electrodes.* Electrochimica Acta, 2002. **47**: p. 2183-2188.

120. Jørgensen, M.J., et al., *Effect of sintering temperature on microstructure and performance of LSM- YSZ composite cathodes.* Solid State Ionics, 2001. **139**(1-2): p. 1-11.

121. Choi, J.H., et al., *Microstructure and cathodic performance of LSM electrodes according to particle size of starting powder.* Journal of Power Sources, 2000. **87**: p. 92-100.

122. Song, H.S., et al., *Effect of starting particulate materials on microstructure and cathodic performance of nanoporous LSM-YSZ composite cathodes.* Journal of Power Sources, 2007. **167**: p. 258-264.

123. Fukunaga, H., et al., *The relationship between overpotential and the three phase boundary length.* Solid State Ionics, 1996. **86-88**(2): p. 1179-1185.

124. Adler, S.B., *Factors Governing Oxygen Reduction in Solid Oxide Fuel Cell Cathodes.* Chemical Reviews, 2004. **104**(10): p. 4791-4843.

125. Wang, S., et al., *Performance of a La0.6Sr0.4Co0.8Fe0.2O3-Ce0.8Gd0.2O1.9-Ag Cathode for Ceria Electrolyte SOFCs.* Solid State Ionics, 2002. **146**: p. 203-210.

126. Murray, E.P., M.J. Sever, and S.A. Barnett, *Electrochemical performance of $(La,Sr)(Co,Fe)O_3$-$(Ce, Gd)O_3$ composite cathodes.* Solid State Ionics, 2002. **148**(1-2): p. 27-34.

127. Shao, Z. and S.M. Haile, *A high-performance cathode for the next generation of solid-oxide fuel cell.* Nature, 2004. **431**: p. 170-173.

128. Xia, C. and M. Liu, *Novel Cathodes for Low-Temperature Solid Oxide Fuel Cells.* Adv. Mater., 2002. **14**(7): p. 521-523.

129. Ullmann, H., et al., *Correlation between thermal expansion and oxide ion transport in mixed conducting perovskite-type oxides for SOFC.* Solid State Ionics, 2000. **138**(1-2): p. 79-90.

130. Holtappels, P. and C. Bagger, *Fabrication and Performance of Advanced Multi-Layer SOFC Cathodes.* J. Eur. Ceram. Soc., 2002. **22**: p. 41-48.

131. Nagata, M., H. Hotta, and H. Iwahara, *Synthesis and Electrochemical Properties of an Oxide Electrode Layer Prepared by a New Electroless Plating Technique.* Journal of Applied Electrochemistry, 1994. **24**(5): p. 411-419.

132. Sasaki, K., et al., *Microstructure-property relations of solid oxide fuel cell cathodes and current collectors.* Journal of the Electrochemical Society, 1996. **143**(2): p. 530-543.

133. Mogensen, M., et al., *Composite electrodes in solid oxide fuel cells and similar solid state devices.* Journal of Electroceramics, 2000. **5:2**: p. 141-152.

134. Kenjo, T. and M. Nishiya, *LaMnO3 air cathodes containing ZrO2 electrolyte for high temperature solid oxide fuel cells.* Solid State Ionics, 1992. **57 (3-4)**: p. 295-302.

135. Mizusaki, J., et al., *Reaction-Kinetics and Microstructure of the Solid Oxide Fuel-Cells Air Electrode La0.6ca0.4mno3/Ysz.* Journal of the Electrochemical Society, 1991. **138**(7): p. 1867-1873.

136. Tanner, C.W., K.Z. Fung, and A.V. Virkar, *The Effect of Porous Composite Electrode Structure on Solid Oxide Fuel Cell Performance: Part I - Theoretical Analysis.* J. Electrochem. Soc., 1997. **144**: p. 21-30.

137. Ivers-Tiffee, E. and A.V. Virkar, *Electrode Polarizations*, in *High Temperature Solid Oxide Fuel Cells: Fundamentals, Design and Applications*, S.C. Singhal and K. Kendall, Editors. 2003, Elsevier Advanced Technology: Oxford, UK. p. 229-260.

138. Adler, S.B., *Mechanism and kinetics of oxygen reduction on porous La1-xSrxCoO3-delta electrodes.* Solid State Ionics, 1998. **111**: p. 125-134.

139. Liu, M. and Z. Wu, *Significance of Interfaces in Solid-State Cells with Porous Electrodes of Mixed Ionic-Electronic Conductors.* Solid State Ionics, 1998. **107**: p. 105-110.

140. Kuznecov, M., et al., *Diffusion controlled oxygen transport and stability at the perovskite/electrolyte interface.* Solid State Ionics, 2003. **157**(1-4): p. 371-378.

141. la O, G.J., et al., *Probing oxygen reduction reaction kinetics of Sr-doped LaMnO3 supported on Y2O3-stabilized ZrO2.* Journal of the Electrochemical Society, 2007. **154**(4): p. B427-B438.

142. Chen, X.J., K.A. Khor, and S.H. Chan, *Identification of O2 reduction processes at yttria stabilized zirconia|doped lanthanum manganite interface.* J. Power Sources, 2003. **123**: p. 17.

143. Jorgensen, M.J. and M. Mogensen, *Impedance of solid oxide fuel cell LSM/YSZ composite cathodes.* J. Electrochem. Soc., 2001. **148 (5)**: p. A433-A442.

144. Inoue, T., et al., *Cathode and anode materials and the reaction kinetics for the solid oxide fuel cell.* Solid State Ionics, 1990. **40-41**(1): p. 407-410.

145. Herle, J.V., A.J. McEvoy, and K.R. Thampi, *A study on the $La_{1-x}Sr_xMnO_3$ oxygen cathode.* Electrochimica Acta, 1996. **41**(9): p. 1447-1454.

146. Radhakrishnan, R., A.V. Virkar, and S.C. Singhal, *Estimation of charge-transfer resistivity of La0.8Sr0.2MnO3 cathode on Y0.16Zr0.84O2 electrolyte using patterned electrodes.* Journal of the Electrochemical Society, 2005. **152**(1): p. A210-A218.

147. Fleig, J., et al., *Oxygen Reduction Kinetics of Lanthanum Manganite (LSM) Model Cathodes: Partial Pressure Dependence and Rate-Limiting Steps.* Fuel Cells, 2008. **In Press**.

148. Fleig, J., et al., *Thin film microelectrodes in SOFC electrode research.* Fuel Cells, 2006. **6**(3-4): p. 284-292.

149. Brichzin, V., et al., *The geometry dependence of the polarization resistance of Sr-doped LaMnO3 microelectrodes on yttria-stabilized zirconia.* Solid State Ionics, 2002. **152**: p. 499-507.

150. Brichzin, V., et al., *Geometry dependence of cathode polarization in solid oxide fuel cells investigated by defined Sr-doped LaMnO3 microelectrodes.* Electrochemical and Solid State Letters, 2000. **3**(9): p. 403-406.

151. Baumann, F.S., et al., *Quantitative comparison of mixed conducting SOFC cathode materials by means of thin film model electrodes.* Journal of the Electrochemical Society, 2007. **154**(9): p. B931-B941.

152. Hertz, J.L. and H.L. Tuller, *Measurement and finite element modeling of triple phase boundary-related current constriction in YSZ.* Solid State Ionics, 2007. **178**(13-14): p. 915-923.

153. Fleig, J., *A way for determining the effective three phase boundary width of solid state electrochemical reactions from the primary and secondary current distribution at microelectrodes.* Z. Phys. Chem., 2007. **221**: p. 1149-1159.

154. van Heuveln, F.H., H.J.M. Bouwmeester, and F.P.F. van Berkel, *Electrode Properties of Sr-Doped LaMnO3 on Yttria-Stabilized Zirconia.* Journal of the Electrochemical Society, 1997. **144**(1): p. 126-133.

155. Jiang, S.P. and S.P.S. Badwal, *An electrode kinetics study of H-2 oxidation on Ni/Y2O3-ZrO2 cermet electrode of the solid oxide fuel cell.* Solid State Ionics, 1999. **123**(1-4): p. 209-224.

156. Primdahl, S. and M. Mogensen, *Mixed conductor anodes: Ni as electrocatalyst for hydrogen conversion.* Solid State Ionics, 2002. **152-153**: p. 597-608.

157. Primdahl, S. and M. Mogensen, *Oxidation of Hydrogen on Ni/Yttria-Stabilized Zirconia Cermet Anodes.* J. Electrochem. Soc., 1997. **144**(10): p. 3409-3419.

158. Primdahl, S. and M. Mogensen, *Gas Conversion Impedance: A Test Geometry Effect in Characterization of Solid Oxide Fuel Cell Anodes.* J. Electrochem. Soc., 1998. **145**(7): p. 2431-2438.

159. Norby, T. *Electrochemical Behavior of Ni/YSZ Electrodes*. in *The 2nd European Solid Oxide Fuel Cell Forum*. 1996. Oslo, Norway.

160. Brown, M., S. Primdahl, and M. Mogensen, *Structure/Performance Relations for Ni/Yttria-Stabilized Zirconia Anodes for Solid Oxide Fuel Cells.* J. Electrochem. Soc., 2000. **147 (2)**: p. 475-485.

161. Sun, C. and U. Stimming, *Recent anode advances in solid oxide fuel cells.* Journal of Power Sources, 2007. **171**(2): p. 247-260.

162. de Boer, B., et al., *The effect of the presence of fine YSZ particles on the performance of porous nickel electrodes.* Solid State Ionics, 2000. **127**: p. 269-276.

163. Holtappels, P., et al., *Reaction of hydrogen/water mixtures on nickel-zirconia cermet electrodes - II. AC polarization characteristics.* Journal of the Electrochemical Society, 1999. **146**(8): p. 2976-2982.

164. Mizusaki, J. and et al., *Preparation of Nickel Pattern Electrodes on YSZ and Their Electrochemical Properties in H2-H2O Atmospheres.* J. Electrochem. Soc., 1994. **141**: p. 2129-2134.

165. Mogensen, M. and S. Skaarup, *Kinetic and geometric aspects of solid oxide fuel cell electrodes.* Solid State Ionics, 1996. **86-88**: p. 1151-1160.

166. Bieberle, A., L.P. Meier, and L.J. Gauckler, *The electrochemistry of Ni pattern anodes used as solid oxide fuel cell model electrodes.* J. Electrochem. Soc., 2001. **148 (6)**: p. A646-A656.

167. Hansen, K.V., K. Norrman, and M. Mogensen, *H2-H2O-Ni-YSZ Electrode Performance: Effect of Segregation to the Interface.* J. Electrochem. Soc., 2004. **151 (9)**: p. A1436-A1444 (and refs.).

168. Horita, T., et al., *Materials and reaction mechanisms at anode/electrolyte interfaces for SOFCs.* Solid State Ionics, 2006. **177**: p. 1941-1948.

169. Jiang, S.P. and S.P.S. Badwal, Journal of the Electrochemical Society, 1997. **144**: p. 3777-3784.

170. Bieberle, A. and L.J. Gauckler, *Reaction mechanism of Ni pattern anodes for solid oxide fuel cells.* Solid State Ionics, 2000. **135**(1-4): p. 337-345.

171. Norby, T., et al. *Reaction resistance in relation to three phase boundary length of Ni/YSZ electrodes*. in *Solid Oxide Fuel Cells*. 1993: The Electrochemical Society Proceedings Series.

172. Liu, Y.L. and C. Jiao, *Microstructure degradation of an anode/electrolyte interface in SOFC studied by transmission electron microscopy.* Solid State Ionics, 2005. **176**: p. 435-442.

173. Hauch, A., et al., *Nanoscale chemical analysis and imaging of solid oxide cells.* Electrochemical and Solid State Letters, 2008. **11**(3): p. B38-B41.

174. Lee, K.R., et al., *Viable image analyzing method to characterize the microstructure and the properties of the Ni/YSZ cermet anode of SOFC.* Journal of Power Sources, 2005. **140**(2): p. 226-234.

175. Lee, K.R., et al., *Interpretation of the interconnected microstructure of an NiO-YSZ anode composite for solid oxide fuel cells via impedance spectroscopy.* Journal of Power Sources, 2006. **158**(1): p. 45-51.

176. Zhao, F., Virkar, A.V., *The effect of electrode microstructure on cathodic polarization*, in *Solid Oxide Fuel Cell VII (SOFC-VII)*, S.C. Singhal, Editor. 2001, The Electrochemical Society: Paris. p. 501-510.

177. Wilson, J.R. and S.A. Barnett, *Solid oxide fuel cell Ni-YSZ anodes: Effect of composition on microstructure and performance.* Electrochemical and Solid State Letters, 2008. **11**(10): p. B181-B185.

178. Wilson, J.R., et al., *Quantitative three-dimensional microstructure of a solid oxide fuel cell cathode.* Nature Materials, 2008: p. In Submission.

179. Wilson, J.R., et al., *Three-dimensional analysis of solid oxide fuel cell Ni-YSZ anode interconnectivity.* Microscopy and Microanalysis, 2008: p. In Press.

180. Wilson, J.R., et al., *Three-dimensional reconstruction of a solid-oxide fuel-cell anode.* Nature Materials, 2006. **5**(7): p. 541-544.

181. Wilson, J.R., et al., *Three Dimensional Reconstruction of Solid Oxide Fuel Cell Electrodes Using Focused Ion Beam - Scanning Electron Microscopy* in *Solid Oxide Fuel Cells 10 (SOFC-X)*, K. Eguchi, Singhal, S.C., Yokokawa, H., Mizusaki, J., Editor. 2007, The Electrochemical Society: Nara, Japan. p. 1879-1887.

182. Gostovic, D., et al., *Three-dimensional reconstruction of porous LSCF cathodes.* Electrochemical and Solid State Letters, 2007. **10**(12): p. B214-B217.

183. Izzo, J.R., et al., *Nondestructive reconstruction and analysis of SOFC anodes using x-ray computed tomography at sub-50 nm resolution.* Journal of the Electrochemical Society, 2008. **155**(5): p. B504-B508.

184. Deng, X. and A. Petric, *Geometrical modeling of the triple-phase boundary in solid oxide fuel cells.* J. Power Sources, 2005. **140**: p. 297-303.

185. Jorgensen, M.J., et al., *Effect of sintering temperature on microstructure and performance of LSM-YSZ composite cathodes.* Solid State Ionics, 2001. **139**: p. 1-11.

186. Bouvard, D. and F.F. Lange, *Relation between Percolation and Particle Coordination in Binary Powder Mixtures.* Acta Metallurgica Et Materialia, 1991. **39**(12): p. 3083-3090.

187. Suzuki, M. and T. Oshima, *Estimation of the Coordination-Number in a Multicomponent Mixture of Spheres.* Powder Technology, 1983. **35**(2): p. 159-166.

188. Kuo, C.H. and P.K. Gupta, *Rigidity and conductivity percolation thresholds in particulate composites.* Acta Metallurgica Et Materialia, 1995. **43**(1): p. 397-403.

189. Sunde, S., *Simulations of composite electrodes in fuel cells.* Journal of Electroceramics, 2000. **5 (2)**: p. 153-182.

190. Chen, X.J., S.H. Chan, and K.A. Khor, *Simulation of a composite cathode in solid oxide fuel cells.* Electrochimica Acta, 2004. **49**(11): p. 1851-1861.

191. Zhu, W., D. Ding, and C. Xia, *Enhancement in Three-Phase Boundary of SOFC Electrodes by an Ion Impregnation Method: A Modeling Comparison.* Electrochemical and Solid-State Letters, 2008. **11**(6): p. B83-B86.

192. Janardhanan, V.M., V. Heuveline, and O. Deutschmann, *Three-phase boundary length in solid-oxide fuel cells: A mathematical model.* Journal of Power Sources, 2008. **178**(1): p. 368-372.

193. Fleig, J., *Solid Oxide Fuel Cell Cathodes: Polarization Mechanism and Modeling of the Electrochemical Performance.* Ann. Rev. Matsci, 2003.

194. Costamagna, P., P. Costa, and V. Antonucci, *Micro-modelling of solid oxide fuel cell electrodes.* Electrochimica Acta, 1998. **43**(3-4): p. 375-394.

195. Costamagna, P., P. Costa, and E. Arato, *Some more considerations on the optimization of cermet solid oxide fuel cell electrodes.* Electrochimica Acta, 1998. **43**(8): p. 967-972.

196. Gewies, S. and W.G. Bessler, *Physically based impedance modeling of Ni/YSZ cermet anodes.* Journal of the Electrochemical Society, 2008. **155**(9): p. B937-B952.

197. Deseure, J., et al., *Modelling of a SOFC graded cathode.* Journal of the European Ceramic Society, 2005. **25**: p. 2673-2676.

198. Sunde, S., *Calculation of Conductivity and Polarization Resistance of Composite Sofc Electrodes from Random Resistor Networks.* Journal of the Electrochemical Society, 1995. **142**(4): p. L50-L52.

199. Sunde, S., *Monte Carlo simulations of conductivity of composite electrodes for solid oxide fuel cells.* Journal of the Electrochemical Society, 1996. **143**(3): p. 1123-1132.

200. Sunde, S., *Monte Carlo simulations of polarization resistance of composite electrodes for solid oxide fuel cells.* Journal of the Electrochemical Society, 1996. **143**(6): p. 1930-1939.

201. Deseure, J., et al., *Theoretical optimisation of a SOFC composite cathode.* Electrochimica Acta, 2005. **50**(10): p. 2037-2046.

202. Chan, S.H. and Z.T. Xia, *Anode micro model of solid oxide fuel cell.* Journal of the Electrochemical Society, 2001. **148**(4): p. A388-A394.

203. Xia, Z.T., S.H. Chan, and K.A. Khor, *An improved anode micro model of SOFC.* Electrochemical and Solid State Letters, 2004. **7**(3): p. A63-A65.

204. Abbaspour, A., et al., *A novel approach to study the structure versus performance relationship of SOFC electrodes.* Journal of Power Sources, 2006. **161**: p. 965-970.

205. Schneider, L.C.R., et al., *Discrete modelling of the electrochemical performance of SOFC electrodes.* Electrochimica Acta, 2006. **52**(1): p. 314-324.

206. Schneider, L.C.R., et al., *Percolation effects in functionally graded SOFC electrodes.* Electrochimica Acta, 2007. **52**(9): p. 3190-3198.

207. Chan, S.H., X.J. Chen, and K.A. Khor, *Cathode micromodel of solid oxide fuel cell.* Journal of the Electrochemical Society, 2004. **151**(1): p. A164-A172.

208. Kenjo, T., S. Osawa, and K. Fujikawa, *High temperature air cathodes containing ion conductive oxides.* J. Electrochem. Soc., 1991. **138**: p. 349-355.

209. Kim, J.W., et al., *Polarization effects in intermediate temperature, anode-supported solid oxide fuel cells.* Journal of the Electrochemical Society, 1999. **146**(1): p. 69-78.

210. Herbstritt, D., A. Weber, and E. Ivers-Tiffee, *Modelling and DC-Polarization of a Three Dimensional Electrode/Electrolyte Interface.* Journal of the European Ceramic Society, 2001. **21**: p. 1813-1816.

211. Fleig, J. and J. Maier, *The influence of laterally inhomogeneous contacts on the impedance of solid materials: a three-dimensional finite-element study.* J. Electroceramics, 1997. **1 (1)**: p. 73-89.

212. Janardhanan, V.M. and O. Deutschmann, *Modeling of Solid-Oxide Fuel Cells.* Z. Phys. Chem., 2007. **221**: p. 443-478.

213. Holm, E.A. and P.M. Duxbury, *Three-dimensional materials science.* Scripta Materialia, 2006. **54**: p. 1035-1040.

214. Mobus, G. and B.J. Inkson, *Nanoscale tomography in materials science.* Materials Today, 2007. **10**(12): p. 18-25.

215. Uchic, M.D., et al., *Three-dimensional microstructural characterization using focused ion beam tomography.* Mrs Bulletin, 2007. **32**(5): p. 408-416.

216. Alkemper, J. and P.W. Voorhees, *Quantitative serial sectioning analysis.* Journal of Microscopy, 2001. **201**(3): p. 388-394.

217. Mendoza, R., et al., *Topological complexity and the dynamics of coarsening.* Nature Materials, 2004. **3**(6): p. 385-388.

218. Kammer, D. and P.W. Voorhees, *The morphological evolution of dendritic microstructures during coarsening.* Acta Materialia, 2006. **54**(6): p. 1549-1558.

219. Kammer, D. and P.W. Voorhees, *Analysis of complex microstructures: Serial sectioning and phase-field simulations.* Mrs Bulletin, 2008. **33**(6): p. 603-610.

220. Griesser, S., et al., *Characterization of fuel cells and fuel cell systems using three-dimensional x-ray tomography.* Journal of Fuel Cell Science and Technology, 2007. **4**: p. 84-87.

221. Feser, M., et al., *Sub-micron resolution CT for failure analysis and process development.* Measurement Science & Technology, 2008. **19**(9): p. 8.

222. Midgley, P.A. and M. Weyland, *3D electron microscopy in the physical sciences: the development of Z-contrast and EFTEM tomography.* Ultramicroscopy, 2003. **96**: p. 413-431.

223. Seidman, D.N., *Three-dimensional atom-probe tomography: Advances and applications.* Annual Review of Materials Research, 2007. **37**: p. 127-158.

224. Perea, D.E., et al., *Three-Dimensional Nanoscale Composition Mapping of Semiconductor Nanowires.* Nano Letters, 2006. **6**(2): p. 181-185.

225. Holzer, L., et al., *Cryo-FIB-nanotomography for quantitative analysis of particle structures in cement suspensions.* Journal of Microscopy-Oxford, 2007. **227**(3): p. 216-228.

226. Holzer, L., et al., *Three-dimensional analysis of porous BaTiO3 ceramics using FIB nanotomography.* Journal of Microscopy-Oxford, 2004. **216**: p. 84-95.

227. Holzer, L., et al., *FIB-Nanotomography of particulate systems - Part I: Particle shape and topology of interfaces.* Journal of the American Ceramic Society, 2006. **89**(8): p. 2577-2585.

228. Bansal, R.K., et al., *High-resolution three-dimensional reconstruction: A combined scanning electron microscope and focused ion-beam approach.* Journal of Vacuum Science & Technology B, 2006. **24**(2): p. 554-561.

229. Uchic, M.D., et al., *3D microstructural characterization of nickel superalloys via serial-sectioning using a dual beam FIB-SEM.* Scripta Materialia, 2006. **55**(1): p. 23-28.

230. Groeber, M., et al., *Developing a robust 3-d characterization representation framework for modeling polycrystalline materials.* Jom, 2007. **59**(9): p. 32-36.

231. Groeber, M.A., et al., *3D reconstruction and characterization of polycrystalline microstructures using a FIB-SEM system.* Materials Characterization, 2006. **57**(4-5): p. 259-273.

232. Thyden, K., Y.L. Liu, and J.B. Bilde-Sorensen, *Microstructural characterization of SOFC Ni-YSZ anode composites by low-voltage scanning electron microscopy.* Solid State Ionics, 2008. **178**(39-40): p. 1984-1989.

233. Bhandari, Y., et al., *3D polycrystalline microstructure reconstruction from FIB generated serial sections for FE analysis.* Computational Materials Science, 2007. **41**(2): p. 222-235.

234. Munch, B., et al., *FIB-nanotomography of particulate systems - Part II: Particle recognition and effect of boundary truncation.* Journal of the American Ceramic Society, 2006. **89**(8): p. 2586-2595.

235. Zalc, J.M., S.C. Reyes, and E. Iglesia, *The effects of diffusion mechanism and void structure on transport rates and tortuosity factors in complex porous structures.* Chemical Engineering Science, 2004. **59**: p. 2947-2960.

236. Roberts, N., M. Reed, and G. Nesbitt, *Estimation of the connectivity of a synthetic porous medium.* Journal of Microscopy-Oxford, 1997. **187**: p. 110-118.

237. Odgaard, A. and H.J.G. Gundersen, *Quantification of Connectivity in Cancellous Bone, with Special Emphasis on 3-D Reconstructions.* Bone, 1993. **14**(2): p. 173-182.

238. Jernot, J.P. and C. Lantuejoul, *Letters to the Editor: Estimation of the connectivity of a synthetic porous medium.* Journal of Microscopy-Oxford, 1999. **193**: p. 97-99.

239. Howard, C.V. and M.G. Reed, *Unbiased Stereology: Three-Dimensional Measurement in Microscopy.* 2nd ed. 2005, New York, NY: BIOS Scientific.

240. Wilson, J.R., et al. *Studies of oxygen exchange on thin-film La0.6Sr0.4CoO3-δ using nonlinear electrochemical impedance spectroscopy (NLEIS).* in *The 10th International Symposium on Solid Oxide Fuel Cells (SOFC-X).* 2007. Nara, Japan: ECS Transactions.

241. Adler, S.B., X.Y. Chen, and J.R. Wilson, *Mechanisms and rate laws for oxygen exchange on mixed-conducting oxide surfaces.* Journal of Catalysis, 2007. **245**: p. 91-109.

242. Svensson, A.M., S. Sunde, and K. Nisancioglu, *A mathematical model of the porous SOFC electrode.* Solid State Ionics, 1996. **86-8**: p. 1211-1216.

243. Tiedemann, W.H. and J.S. Newman, *Porous Electrode Theory with Battery Applications.* AIChE Journal, 1975. **21 (1)**: p. 25-41.

244. Deng, X.H. and A. Petric, *Geometrical modeling of the triple-phase-boundary in solid oxide fuel cells.* Journal of Power Sources, 2005. **140**(2): p. 297-303.

245. Wang, C.T. and J.M. Smith, *Tortuosity factors for diffusion in catalyst pellets.* AIChE Journal, 1983. **29 (1)**: p. 132-136.

246. Stevenson, J.W. *Solid oxide Fuel Cell development in PNNL.* in *Solid Oxide Fuel Cells VIII*. 2003. The Electrochemical Society Proceedings Series: The Electrochemical Society: Pennington NJ.

247. Sakamoto, S., H. Taira, and H. Takagi, *Effective electrode reaction area of cofired type planar SOFC.* Denki Kagaku, 1996. **64**: p. 609-613.

248. Zhao, F. and A.V. Virkar, *Dependence of polarization in anode-supported solid oxide fuel cells on various cell parameters.* J. Power Sources, 2005. **141**: p. 79-95.

249. Wilson, J.R. and S.A. Barnett, *Solid Oxide Fuel Cell Ni-YSZ Anodes: Effect of Composition on Microstructure and Performance.* Electrochemical and Solid-State Letters, 2008. **11**(10): p. in press.

250. Wilson, J.R., et al., *Three-dimensional reconstruction of a solid-oxide fuel-cell anode.* Nat. Mater., 2006. **5**(7): p. 541-544.

251. Zhu, W.Z. and S.C. Deevi, *A review on the status of anode materials for solid oxide fuel cells.* Materials Science and Engineering A, 2003. **362**(1-2): p. 228-239.

252. Huebner, W., D.M. Reed, and H.U. Anderson. in *Proceedings of the Sixth International Symposium on Solid Oxide Fuel Cells (SOFC-VI).* 1999. Honolulu, Hawaii.

253. Souza, S., S.J. Visco, and L.C. DeJonghe, *Thin-film solid oxide fuel cell with high performance at low temperature.* Solid State Ionics, 1997. **98**: p. 57-61.

254. Virkar, A.V., et al., *The role of electrode microstructure on activation and concentration polarizations in solid oxide fuel cells.* Solid State Ionics, 2000. **131 (1, 2)**: p. 189-198.

255. Lin, Y., et al., *Direct Operation of Solid Oxide Fuel Cells with Methane Fuel.* Solid State Ionics, 2005. **176**: p. 1827-1835.

256. Lee, J.H., et al., *Quantitative analysis of microstructure and its related electrical property of SOFC anode, Ni-YSZ cermet.* Solid State Ionics, 2002. **148**(1-2): p. 15-26.

257. Zhan, Z., et al., *High-rate electrochemical partial oxidation of methane in solid oxide fuel cells.* Journal of Power Sources, 2006. **161**(1): p. 460-465.

258. Trunec, M., *Fabrication of zirconia- and ceria-based thin-wall tubes by thermoplastic extrusion.* Journal of the European Ceramic Society, 2004. **24**(4): p. 645-651.

259. Jiang, S.P., et al., *The electrochemical performance of LSM/zirconia-yttria interface as a function of a-site non-stoichiometry and cathodic current treatment.* Solid State Ionics, 1999. **121**: p. 1-10.

260. Lu, Z.G., et al., *Study of LSM-YSZ composite cathodes by ac impedance and polarization.* Gaodeng Xuexiao Huaxue Xuebao, 2001. **22**: p. 791-795.

261. Tsai, T., Barnett, S.A., *Effect of LSM-YSZ cathode on thin-electrolyte solid oxide cell performance.* Solid State Ionics, 1997. **93**: p. 207.

262. McIntosh, S., et al., *Effect of Polarization on and Implications for Characterization of LSM-YSZ Composite Cathodes.* Electrochem. Solid State Lett., 2004. **7**: p. A111.

263. Leng, Y.J., et al. *Development of LSM/YSZ composite electrodes for thin film solid oxide fuel cells*. in *8th International Symposium on Solid Oxide Fuel Cells (SOFC-VIII)*. 2003: The Electrochemical Society, Inc.

264. Yokokawa, H., et al., *Fundamental mechanisms limiting solid oxide fuel cell durability.* Journal of Power Sources, 2008. **182**(2): p. 400-412.

265. Murray, E.P. and S.A. Barnett, *(La,Sr)MnO3--(Ce,Gd)O(2-x) Composite Cathodes for Solid Oxide Fuel Cells.* Solid State Ionics, 2001. **143**: p. 265-273.

266. Yamamoto, O., et al., *Electrical-Conductivity of Polycrystalline Tetragonal Zirconia Zro2-Sc2o3, Zro2-Y2o3, Zro2-Yb2o3.* Journal of Materials Science Letters, 1989. **8**(2): p. 198-200.

267. Zhang, M., et al., *A bi-layered composite cathode of La0.8Sr0.2MnO3-YSZ and La0.8Sr0.2MnO3-La0.4Ce0.6O1.8 for IT-SOFCs.* Electrochimica Acta, 2008. **53**(15): p. 4998-5006.

268. Kim, J.D., et al., *Characterization of LSM-YSZ Composite Electrode by AC Impedance Spectroscopy.* Solid State Ionics, 2001. **143**: p. 379-389.

269. Wang, W.S., et al., *The stability of LSF-YSZ electrodes prepared by infiltration.* Journal of the Electrochemical Society, 2007. **154**(5): p. B439-B445.

270. Suzue, Y., N. Shikazono, and N. Kasagi, *Micro modeling of solid oxide fuel cell anode based on stochastic reconstruction.* Journal of Power Sources, 2008. **184**(1): p. 52-59.